

---

# Phase transitions in “small” systems

## Inaugural–Dissertation

Dissertation zur Erlangung der Doktorwürde am Fachbereich Physik der

**Freien Universität Berlin**

Olivier Fliegans

1. *Gutachter* : Prof. D. H. E. Groß    Freien Universität, Berlin

2. *Gutachter* : Prof. A. Hüller        Universität Erlangen-Nürnberg

*To Aline, Paul and Théo.*



## Acknowledgments

First of all, I would like to thank Prof. D. H. E. Groß for giving me the opportunity to work in this very interesting field, for drawing my attention to new physical problems, and for his generous and continuous support.

Also, I wish to thank T. Klotz with whom I worked closely on the cluster model during almost two years. I gained a lot from this collaboration. At least, the whole cluster part of this work benefits from his inputs.

I thank D. Valls-Gabaud who invited me several times in Strasbourg and in Toulouse in order to keep me in touch with the astrophysical community. I thank him also for sharing his wisdom with me.

I would like to thank those who read the manuscript of this thesis and helped very much to improve it: D. Valls-Gabaud, T. Klotz, T. Brunne, V. Lalièna-Bielsa and Prof. Groß.

I acknowledge interesting discussions or contacts over the last few years with E. Votyakov, V. Lalièna-Bielsa, P.-H. Chavanis and E. Follana.

Thanks to Tim Brunne who could stand patiently what became “the stupid question of the day”.

I thank the Hahn-Meitner-Institut of Berlin for financial support.

I wish to thank my friends, Nicolas, Raphaël, Pierre, Thierry and Yann for their friendship, and their continuous support.

Last but not least, I would like to thank Aline who took care of our children while I was “far away”.



# Content

<b>General introduction</b>	<b>ix</b>
<b>List of figures</b>	<b>xiii</b>
<b>List of tables</b>	<b>xv</b>

---

---

## Part I Thermostatistics of “small” systems

---

---

<b>Chapter 1 Introduction and definitions</b>	<b>3</b>
1.1 Microcanonical ensemble . . . . .	3
1.1.1 Definitions . . . . .	3
1.1.2 On the choice of $X$ . . . . .	5
1.2 Canonical ensemble . . . . .	7
1.2.1 Definitions . . . . .	7
1.2.2 Link between ME and CE . . . . .	8
1.2.3 Equivalence conditions . . . . .	10
1.3 Microcanonical or canonical ensemble? . . . . .	11
1.4 Toy models . . . . .	12
1.4.1 1–D toy model . . . . .	12
1.4.2 2–D toy model: the van der Waals approximation . . . . .	13

<b>Chapter 2 Thermostatistics of small systems</b>	<b>17</b>
2.1 Pure phases . . . . .	17
2.1.1 Definition . . . . .	17
2.1.2 Example . . . . .	17
2.2 First order phase transitions . . . . .	18
2.2.1 Definitions . . . . .	18
2.2.2 Example . . . . .	22
2.2.3 Transition parameters . . . . .	27
2.3 Second order phase transitions . . . . .	30
2.3.1 Definition . . . . .	30
2.3.2 Example . . . . .	30
2.4 Single event as a signal for phase transition? . . . . .	32
2.5 Alternative theories . . . . .	33
2.5.1 Distribution of zeros . . . . .	33
2.5.2 Tsallis entropy . . . . .	35
2.6 Conclusions . . . . .	36

---



---

**Part II Liquid–gas transition of metallic clusters**

---



---

<b>Chapter 3 Low pressure and scaling properties</b>	<b>39</b>
3.1 Introduction . . . . .	39
3.2 Model . . . . .	40
3.3 Simulation method . . . . .	46
3.4 Results . . . . .	50
3.4.1 $N_a 200, 1 \text{ atm.}$ . . . . .	50
3.4.2 Scaling properties . . . . .	61
3.5 Summary . . . . .	64

---

<b>Chapter 4 Towards the critical point</b>	<b>69</b>
4.1 Introduction . . . . .	69
4.2 MMC results . . . . .	69
4.3 Lattice model (CL) . . . . .	73
4.3.1 Model . . . . .	73
4.3.2 Simulation method . . . . .	75
4.3.3 Results . . . . .	77
4.4 Conclusions . . . . .	83

---



---

## Part III Self-gravitating systems

---



---

<b>Chapter 5 Introduction</b>	<b>87</b>
<b>Chapter 6 Microcanonical properties</b>	<b>89</b>
6.1 Microcanonical definitions . . . . .	89
6.2 Momentum average and dispersion . . . . .	90
6.3 Numerical method . . . . .	92
6.4 Results . . . . .	93
6.4.1 Entropy and its derivatives . . . . .	93
6.4.2 Mass distribution . . . . .	94
6.4.3 Phase diagram . . . . .	100
6.4.4 Loss of information in CE . . . . .	102
6.5 Discussion and conclusions . . . . .	104
<b>General conclusions</b>	<b>107</b>
<b>Appendices</b>	<b>109</b>
<b>Appendix A Avoided volume</b>	<b>109</b>
A.1 Analytical expressions — EOS ansatz . . . . .	109
A.1.1 Exact expressions . . . . .	109
A.1.2 Approximations . . . . .	111
A.2 Numerical estimates . . . . .	115

A.2.1	Simple Monte–Carlo scheme . . . . .	116
A.2.2	Advanced Monte–Carlo scheme . . . . .	117
A.2.3	Further improvements . . . . .	118
	<b>Appendix B Technical “details”</b>	<b>123</b>
B.1	Introduction . . . . .	123
B.2	Monte–Carlo sampling . . . . .	123
B.2.1	Partitioning factor . . . . .	124
B.2.2	Excitation energy sampling . . . . .	126
B.3	Multicanonical algorithm . . . . .	128
	<b>Appendix C Momentum distribution</b>	<b>133</b>
	<b>Appendix D Temperature at constant pressure</b>	<b>137</b>
	<b>Bibliography</b>	<b>139</b>
	<b>Curriculum vitae</b>	<b>153</b>

# General introduction

Holy Entropy! It's boiling!  
Mr Tompkins (G. Gamow [GAM65])

Historically, statistical mechanics (or thermostatics) has been developed to give thermodynamics mechanical foundation. This program was more than successful, and thermostatics has even been applied to models which was not studied by thermodynamics. Nowadays, statistical mechanics is used in almost (if not) all physical fields. It is even used outside physics, e.g. in economics and social sciences.

Thermodynamics deals with *extensive* systems composed of a very large (physically *infinite*) number of particles  $N$ . Hence, the tools developed in statistical mechanics are marked by these properties. In statistical mechanics the limit  $N \rightarrow \infty$  for an extensive system is called the thermodynamical limit. As an example, phase transitions are defined as Yang-Lee singularities of the canonical potential of the considered system. It is easy to show that these singularities show up only at the thermodynamical limit. In other words, systems far from this limit, or “small” system, *cannot* exhibit the usual signals (Yang-Lee singularities) of phase transitions. Systems are considered to be “small” if the range of their forces is at least of the order of the size of the system.

Because the conventional signals rely on the thermodynamical limit they are absent in “small” systems. But does it mean that there is actually no phase transition at all in these systems?

In fact, in experiments (real or numerically simulated) one can observe that “small” systems do have some behaviors that would be called phase transitions if they were infinite. E.g. atomic clusters composed of a few hundreds of atoms have solid-like properties at low energies, then liquid-like at higher energies to eventually be a gas of atoms at high energies. Spin systems are “ordered” at small energies and completely “disordered” at very high energies. Nevertheless, in the conventional sense, these different macroscopic states and the intermediate stages between them cannot be called phases and phase transitions because the systems do not show any of the “correct” signals of phase transitions.

The facts mentioned above are clear indications that the phase transitions do not appear at the thermodynamical limit but only their usual signals. Therefore, it is natural to ask whether one can redefine phases and phase transitions without invoking the thermodynamical limit. Of course, these new definitions should converge to the usual ones in the limit  $N \rightarrow \infty$ , if it exists.

A thermostatics of “small” systems has been developed by D.H.E. Gross and its collaborators for many years now [GRO01, GRO97]. In this theory, phases and phase transitions are defined by means of *local* properties of the *microcanonical entropy*, where the latter is a function of the *dynamically conserved* quantities of the system.

The microcanonical ensemble is based on the mechanical properties of the studied

system. The entropy is defined by means of Boltzmann's principle and hence is a purely mechanical based quantity. Boltzmann's principle does not impose (or require) properties like extensivity or infinite number of particles. Hence, the microcanonical ensemble is the proper ensemble to study "small" systems. On the contrary, the canonical ensemble does not provide an accurate description of "small" systems, because it is based on assumptions (extensivity, small interactions with a heat bath) which are not true for these systems. The statistical descriptions of "small" systems, provided by the different ensembles, are not equivalent.

The aim of this thesis is, first to collect and summarize theoretical results, and convince the reader of the physical relevance of the microcanonical thermostatics of "small" systems. Then, some concrete applications of this theory to different models of "small" systems are presented. It is shown that these systems have rich phase diagrams and that almost all their finite-size peculiarities are overlooked by the canonical ensemble.

This thesis is organized as follows.

The first part tries to give an almost exhaustive overview of the present status of the statistical mechanics of "small" systems from a theoretical point of view. This description is illustrated with some original applications to analytical entropy-models.

The first chapter is a remainder of notions that are used throughout this thesis. Most of them are known from standard statistical mechanics. However, some of them have to be redefined in order to be adapted to the peculiarities of "small" systems. The definitions of the microcanonical and canonical ensemble used in this work are given in sections 1.1 and 1.2. The choice of the microcanonical ensemble among the different statistical descriptions is discussed in section 1.3. Simple analytical entropy-models are introduced in sec. 1.4. They are mainly used in chap. 2. The microcanonical entropy of a gas in the van der Waals approximation is one of them. In chapter 2 the definitions of phases and phase transitions are given (sections 2.1, 2.2 and 2.3). The fact that these definitions apply to an ensemble of systems is stressed in sec. 2.4. Finally, alternative statistical descriptions of "small" (or non-extensive) systems are reviewed and compared with the one used in this work (sec. 2.5).

The two other parts show original results of studies of some "small" systems.

In part II, the liquid-gas transition of sodium clusters composed of a few hundreds of atoms is discussed. This work continues the one done by many authors of Gross' group.

In chapter 3 the transition is studied at atmospheric pressure. After a short introduction (sec. 3.1), the cluster model (sec. 3.2) and the numerical method (sec. 3.3) are described. The numerical results are shown in sec. 3.4. Caloric curves and their relation to the mass distribution of the system are discussed. The transition parameters are derived from the Maxwell construction. Finally, the scaling behavior of all these observable is described. The results are summarized in sec. 3.5.

In chapter 4 the system is studied at very high pressures. Here, the goal is to reach the critical point of the liquid-gas transition. In the introduction sec. 4.1, the bulk critical parameters are recalled. Then several attempts to observe a second order phase transition within the cluster models used in chap. 3 are presented. They all suggest that if the critical point of finite size sodium clusters it exists, then it is located at higher pressure than its bulk counter-part. In sec. 4.3 a new model for clusters is presented. It is inspired from lattice gas models. This models shows for the first time the critical point of the liquid-gas transition of sodium clusters. In this model the critical pressure is much higher compared to the critical pressure in the corresponding thermodynamical limit. The finite size critical pressure decreases with increasing total mass of the system.

---

The third and last part is devoted to self-gravitating systems. These systems are “small”. They exhibit *negative* specific heat capacity regions for any number of particles. This fact has been pointed out to the astrophysical community by the seminal work of Antonov. The equilibrium properties of these systems have mainly been studied as a function of the total energy  $E$ . However, in astrophysical context, the energy is not the only relevant constant of motion. In this part of this thesis the influence of the conservation of total angular momentum  $L$  on the statistical properties of a self-gravitating system is presented.

In chapter 5 a very short introduction on the statistical description of self-gravitating systems is given. The assumptions that have to be made in order to make possible a statistical description of  $N$ -body systems interacting via Newtonian potential are briefly discussed. Contrary to previous works, no assumptions are made about the spatial symmetry of the mass distribution and a more “realistic” potential is used.

The study of this system is presented in chapter 6. First, some microcanonical definitions are given (sec. 6.1). Then the average and the dispersion of the linear momentum of a particle at a given position is discussed (sec. 6.2). A numerical method, suitable to integrate observables over the whole parameter space, is described in sec. 6.3. The numerical results are presented in sec. 6.4. The entropy, its derivatives (temperature, angular velocity) and observables probing the mass distributions are discussed for the whole parameter space. The definitions of phase transitions, given in chap. 2, are used in order to construct the phase diagram of the system. It is surprisingly rich, showing first order and many second order phase transitions. All the properties of astrophysical interest are lost in the canonical ensemble as shown in sec. 6.4.4. The results are summarized and an outlook on future works is given in sec. 6.5.

The main results of this thesis are collected and discussed in the general conclusions.



# List of figures

1.1	Schematic view of $W$ the accessible phase-space . . . . .	6
1.2	Schematic illustration of the integral (1.12) . . . . .	9
1.3	Specific entropy $s_1(\epsilon)$ . . . . .	13
1.4	Specific entropy surface of the van der Waals model . . . . .	14
1.5	Isotherms and isobars of the van der Waals model. . . . .	15
2.1	Sign of $\lambda_1$ for the van der Waals entropy-model . . . . .	18
2.2	Contour plot of $f$ for the vdW entropy-model: $\lambda_1(X_0) < 0$ (pure phase) . .	19
2.3	Distribution functions $P(\epsilon, \epsilon_0)$ for two values of $N$ and of temperatures . . .	20
2.4	Inverse temperature as a function of $\epsilon$ (ME), $\langle \epsilon \rangle$ (CE) and $N$ . . . . .	21
2.5	Contour plot of $f$ for the vdW entropy-model: $\lambda_1(X_0) > 0$ . . . . .	23
2.6	Vector field $\mathbf{v}_1$ for the vdW entropy-model . . . . .	24
2.7	Parametric plots $(\epsilon(t), \alpha_\beta(t))$ and $(\epsilon(t), \alpha_p(t))$ . . . . .	25
2.8	Vector field $\mathbf{v}_1$ plus isotherms and isobars for the vdW entropy-model . . .	26
2.9	Maxwell construction and surface tension $\mathcal{M} = 1$ for $s_1$ . . . . .	28
2.10	Specific entropy $s'_1(\epsilon) = s_1(\epsilon) + \frac{1}{5} \exp(-20\epsilon^2)$ . . . . .	29
2.11	Contour plot of $f$ for the vdW entropy-model: towards the critical point . .	31
2.12	Criteria for second order phase transition applied to the vdW entropy-model	32
2.13	Schematic representation of the distribution of zeros . . . . .	34
3.1	Specific binding energy as a function of the cluster size . . . . .	42
3.2	Specific heat capacity of bulk sodium at atmospheric pressure . . . . .	44
3.3	Specific entropy and temperature of bulk sodium at atmospheric pressure .	44
3.4	Schematic cluster model: surface and volume dofs . . . . .	45
3.5	Entropy and $N_s^*$ versus $N^*$ . . . . .	45
3.6	Pressure vs volume at fixed total energy and for different total masses. . . .	50
3.7	Summary of the results for $N_{a\ 200}$ at 1 atm . . . . .	51
3.8	Summary of the results for $N_{a\ 200}$ at 1 atm, without exp. binding energies .	53
3.9	Summary of the results for $N_{a\ 200}$ at 1 atm, without $\omega_{sym}$ . . . . .	54
3.10	$N_{\text{eff}}$ based on different definitions: $A = 200$ . . . . .	56
3.11	$N_{\text{eff}}$ based on different definitions: $A = 1000$ . . . . .	56
3.12	$N_{a\ 200}$ at 1 atm from [GM97, GROA] . . . . .	58
3.13	Caloric curves $N_{a\ 200}$ : comparison with [GM97]. . . . .	59
3.14	Summary of the results for $N_{a\ 200}$ at 1 atm, without surface entropy . . . .	60
3.15	Summary of the results for $N_{a\ 1000}$ at 1 atm . . . . .	62
3.16	Relative weight of $p_{NCC}$ in the total pressure versus $\epsilon$ for $A = 200$ and 1000	63
3.17	Caloric curves versus $h$ for several system total masses . . . . .	64

3.18	Scaling of some transition parameters . . . . .	66
4.1	Temperature versus density $\rho$ . . . . .	70
4.2	Scatter plot of the temperature and the pressure as functions of $h$ . . . . .	71
4.3	Scatter plot of $p_{NCC}/p$ versus $p$ . . . . .	72
4.4	Schematic 2D illustration of a cluster in CL . . . . .	74
4.5	Temperatures from MMMC and CL at <i>constant volume</i> . . . . .	78
4.6	Comparisons of mass distributions of CL and MMMC95 . . . . .	79
4.7	$\beta$ curves at constant volume for several system volumes . . . . .	80
4.8	Critical points of CL model for several system masses . . . . .	81
4.9	Relative fluctuations of the big cluster shape toward the critical point . . . . .	82
6.1	Entropy surface $S(\epsilon, \Omega = l^2)$ . . . . .	94
6.2	Inverse temperature $\beta(\epsilon, \Omega = l^2)$ surface . . . . .	95
6.3	Microcanonical angular velocity $\omega(\epsilon, \Omega = l^2)$ surface . . . . .	96
6.4	Density as a function of the distance from the center $r$ for different $\epsilon$ and $\Omega$ . . . . .	97
6.5	Distance distribution $P(d)$ for different simulated spatial configurations . . . . .	98
6.6	Distance distribution $P(d)$ for different values of $(\epsilon, \Omega)$ . . . . .	99
6.7	Sign of $\lambda_1(\epsilon, \Omega)$ . . . . .	100
6.8	Locus of second order phase transitions . . . . .	101
6.9	$f(\epsilon, \Omega, \beta_0, \gamma_0)$ in the $G$ -region . . . . .	103
6.10	Entropy surface as function of $l = \sqrt{\Omega}$ and $\epsilon$ . . . . .	104
6.11	$f(\epsilon, l, \beta_0, \omega_0)$ in the $G$ -region . . . . .	105
A.1	Illustration of the avoided volume for two particles near the boundary. . . . .	111
A.2	Comparison of $NCC$ s from EOS and from numerical computations . . . . .	116
A.3	CPU-time needed to compute $NCC$ , for different mass distributions . . . . .	117
A.4	Number of possible mass distributions as a function of the total mass $A$ . . . . .	118
A.5	Representation of a set of mass distributions on a tree . . . . .	119
A.6	Mass distributions on the $(\hat{\mu}_1, \hat{\mu}_2, \hat{\mu}_4)$ space at fixed $\hat{\mu}_0$ : $A = 200$ . . . . .	120
B.1	Illustration of the repartitioning procedure . . . . .	126
B.2	Schematic illustration of the blocking mechanism . . . . .	129
B.3	Estimates of the density of state $Bg$ and histograms $C$ . . . . .	130
B.4	Final estimate of $Bg$ for $N = 20$ . . . . .	131

# List of tables

3.1	Experimental and theoretical input values for MMMC95 . . . . .	46
3.2	Transition parameters: cluster internal entropy with surface term. . . . .	65
3.3	Transition parameters: cluster internal entropy without surface term. . . . .	65
4.1	Critical parameters as functions of the system total mass . . . . .	82
A.1	Set of mass distributions #1. . . . .	119
A.2	Set of mass distributions #2. . . . .	120
B.1	List of $\mu_s$ for $A = 6$ and their resp. symmetrization weight $\omega_{sym}$ . . . . .	127
B.2	Comparison of analytical and numerical results for different observables. . .	127



**Part I**

**Thermostatistics of “small”  
systems**



# Chapter 1

## Introduction and definitions

The aim of this chapter is to recall and introduce notions and terms that are used throughout the rest of this thesis. Most of them are known in the framework of standard statistical mechanics. However, some of them have to be redefined (extended) in order to be of use for small <sup>a</sup> systems. Most of these notions recover their usual sense at the thermodynamical limit. It is by no means an exhaustive overview of thermostatics' realm. Moreover, dynamical issues like ergodicity, mixing or “approach to equilibrium” [SAS85, KRY79] are out of the scope of the present thesis, though arguments based on dynamics and time-scales are used. Finally, for simplicity the definitions are worked out within the classical mechanics framework although the basement of thermostatics on quantum mechanics is needed as it is done in standard textbooks on statistical mechanics, viz. [LL94, CAL85, DGLR89, BAL82, HIL56]. Nevertheless, once the phase-space volume is given the type of mechanics (either classical or quantum) plays only a marginal role in the rest of the theory as it is shown below.

### 1.1 Microcanonical ensemble

#### 1.1.1 Definitions

Let us consider an isolated physical system whose (microscopic) state at a given time  $t$  is described by a set of  $N$  generalized positions and momenta

$$\{\mathbf{q}, \mathbf{p}\}(t) \equiv \{\mathbf{q}_1(t), \dots, \mathbf{q}_N(t), \mathbf{p}_1(t), \dots, \mathbf{p}_N(t)\}. \quad (1.1)$$

The set over which  $\{\mathbf{q}, \mathbf{p}\}$  is defined is called the *total phase space*  $\Omega$ . Its dimension is usually huge even for a small system, e.g. for a system of  $N$  classical particles the dimension of  $\Omega$  is  $6N$ . The dynamical evolution of the system is described by its Hamiltonian  $\mathcal{H}(\{\mathbf{q}, \mathbf{p}\})$ . For a time-independent (conservative) Hamiltonian <sup>b</sup>, this Hamiltonian and an initial state say  $\{\mathbf{q}_0, \mathbf{p}_0\} \doteq \{\mathbf{q}, \mathbf{p}\}(t=0)$  define a unique trajectory of the microscopic state  $\{\mathbf{q}, \mathbf{p}\}$  in  $\Omega$  <sup>c</sup>. This trajectory does not span the whole phase space  $\Omega$  but it is dense only on a sub-manifold of  $\Omega$  noted by  $W$ . The dimension of  $W$  depends on the number and type of the (macroscopic) “*extensive*” dynamical conserved quantities noted

---

<sup>a</sup>In the following, the quotation marks around small are dropped if there is no ambiguity.

<sup>b</sup>Here and hereafter only time-independent Hamiltonian are considered.

<sup>c</sup>Since the Hamiltonian is time-independent any point of the trajectory can be taken as the initial state.

by  $X \equiv \{X_1, \dots, X_{\mathcal{M}}\}$ <sup>d,e</sup>. The number of conserved quantities and their nature depend on the system considered. E.g. the total energy  $E$ <sup>f</sup>, the total linear momentum  $\mathbf{P}$  (if  $\mathcal{H}$  is invariant by translation), the total angular momentum with respect to the system center of mass  $\mathbf{L}$  (if  $\mathcal{H}$  is invariant by translation and by rotation), the number of classical particles  $N$ , the total charge  $\mathcal{Q}$ , the system volume  $V$  which can be included in the Hamiltonian as a static potential is also a macroscopic conserved quantity<sup>g</sup>.

Now if one assumes *ergodicity* [HIL56, LL94, KRY79], i.e. that the time average  $\langle \mathcal{O} \rangle_t$  of an observable  $\mathcal{O}$  along a trajectory defined by  $\{\mathbf{q}_0, \mathbf{p}_0\}$  and  $\mathcal{H}$  is equal to  $\langle \mathcal{O} \rangle_{W(X_0)}$  the average over  $W(X_0)$ , where  $X_0 \doteq X(\{\mathbf{q}_0, \mathbf{p}_0\})$ ,

$$\begin{aligned} \langle \mathcal{O} \rangle_t &\doteq \lim_{t \rightarrow \infty} \frac{1}{t} \int_0^t d\tau \mathcal{O}(\tau) \\ &\equiv \frac{\int_{\Omega} d\mathbf{q} d\mathbf{p} \mathcal{O}(\{\mathbf{q}, \mathbf{p}\}) \delta(X(\{\mathbf{q}, \mathbf{p}\}) - X_0)}{\int_{\Omega} d\mathbf{q} d\mathbf{p} \delta(X(\{\mathbf{q}, \mathbf{p}\}) - X_0)} \doteq \langle \mathcal{O} \rangle_{W(X_0)}. \end{aligned} \quad (1.2)$$

I.e. the temporal averaging  $\langle \cdot \rangle_t$  for a single state can be replaced by an ensemble of (infinitely) many states averaging  $\langle \cdot \rangle_{W(X(t=0))}$  over the accessible phase-space  $W(X_0)$ . The density probability of the microstates  $\{\mathbf{q}, \mathbf{p}\} \in W(X_0)$  is *uniform*, i.e.<sup>h</sup>

$$P(\{\mathbf{q}, \mathbf{p}\}) = \frac{\delta(X(\{\mathbf{q}, \mathbf{p}\}) - X_0)}{\mathcal{W}(X_0)}, \quad (1.3)$$

where  $\mathcal{W}$  is the volume of the accessible phase-space  $W$ .

**Definition 1.** A collection of systems whose probability distribution follows eq. (1.3) is called a *microcanonical ensemble*.

Boltzmann's principle

$$\boxed{S(X) \doteq k_B \ln \mathcal{W}(X)}, \quad (1.4)$$

defines the system entropy  $S$  as the logarithm of  $\mathcal{W}$  times Boltzmann's constant  $k_B$ <sup>i</sup>.

Note that so far no assumption has been made on the extensive nature of  $S$ <sup>j</sup> nor the thermodynamical limit  $N \rightarrow \infty$ ,  $N/V = \text{const}$  has been invoked.  $S$  is a purely “mechanical based” quantity defined for any system size.  $S$  *may or may not* be extensive.

<sup>d</sup>This definition of an extensive variable, say  $X$ , is different from the conventional one: consider a system where  $X = X_0$  and divide it in two equal pieces  $A$  and  $B$ .  $X$  is extensive if  $X_A = X_B = \frac{X_0}{2}$  [DGLR89]. At the thermodynamical limit, if it exists, both definitions are equivalent (see sec. 1.2.1). In the following, to avoid cumbersome notations, the dynamical conserved quantities are called “extensive”.

<sup>e</sup>To avoid cumbersome notations  $X$  refers also to a single “extensive” variable.

<sup>f</sup>As only conservative Hamiltonian are considered,  $E = \mathcal{H}$  is a constant of motion. Therefore  $E$  is *always* an element of  $X$ ;  $X_1 \equiv E$ .

<sup>g</sup>Contrary to e.g.  $E$ , the conservation of the volume does not necessarily decrease the dimension of  $W$ .

<sup>h</sup>For a quantum system the discrete nature of  $X$  leads to [DGLR89]

$$P(\{\mathbf{q}, \mathbf{p}\}) = \frac{1}{\mathcal{W}(X_0)}.$$

<sup>i</sup> $k_B$  is set from now on to 1.

<sup>j</sup>In the classical sense  $S(X)$  is said to be extensive if  $X$  is extensive (see footnote (d)) and if for any  $\lambda > 1$

$$S(\lambda X) = \lambda S(X).$$

From now on, the “extensive” variables  $X$  are assumed to be continuous<sup>k</sup> (since the following does not apply to discontinuous variables), and  $S$  is assumed to be a smooth many time differentiable (at least three times) function of  $X$ . Moreover, the nature of the mechanics (classical or quantum) governing the system does not matter it is “hidden” in  $\mathcal{W}$ , the measure of the accessible phase-space [GRO01].

Once the entropy is defined one can introduce new, auxiliary, variables. These *intensive* variables  $x \equiv \{x_1, \dots, x_{\mathcal{M}}\}$  are the conjugate of  $X \equiv \{X_1, \dots, X_{\mathcal{M}}\}$  with respect to the entropy

$$x_i \doteq \frac{\partial S}{\partial X_i}, \quad i = 1, \dots, \mathcal{M}. \quad (1.5)$$

E.g. the conjugate of  $E$  is  $\beta$  which is *defined* as the inverse temperature, the conjugate of the system volume  $V$  is  $\beta P$  where  $P$  is *defined* as the pressure.

There is a clear hierarchy among the quantities mentioned above

- i. first, the “extensive” dynamically conserved quantities  $X$ ;
- ii. then, the entropy  $S$  which is proportional to the logarithm of the space-phase volume accessible to the system at fixed  $X$  (i);
- iii. finally, the intensive variables derived from  $S$  (ii) with respect to the mechanical conserved quantities (i).

All this quantities are well defined and there is no quantity defined *a priori*.

It is worth to notice that the sign of  $C_V^{-1} \doteq \frac{\partial \beta^{-1}}{\partial E}$ , the microcanonical heat capacity, depends on the sign of the second derivative of  $S$  with respect to the energy

$$C_V^{-1} \doteq \frac{\partial \beta^{-1}}{\partial E} = -\frac{\frac{\partial^2 S}{\partial E^2}}{\left(\frac{\partial S}{\partial E}\right)^2}. \quad (1.6)$$

At the thermodynamical limit van Hove’s theorem [vH49] states that  $\frac{\partial^2 S}{\partial E^2} \leq 0$  for all  $E$ <sup>1</sup>, i.e.  $S$  is a *concave* function of  $E$ . The proof of this theorem relies on the thermodynamical limit. Therefore, it does not apply to small systems. *A priori*, for these systems  $\frac{\partial^2 S}{\partial E^2}$  can either be positive or negative, i.e. in small systems there is nothing that forbids negative specific heat capacity regions. This point is of great importance and is further discussed in chapter 2.

### 1.1.2 On the choice of $X$

Following the discussion in the previous section one should incorporate in  $X$  all and only all the conserved quantities of the considered system. However, in practice one has often to loosen this constraint:

- An isolated system of  $N$  classical particles has  $6N - 1$  constant of motions. For  $N > 2$  their functional form are known only when the system equations of motion are integrated [FER65], which is usually an impossibly difficult task. So, all the

---

<sup>k</sup>Or quasi-continuous, e.g. the number of particles  $N$  when  $N$  is sufficiently large, or any other conserved quantity when the system is described by quantum physics.

<sup>1</sup>In fact, the constraint applies to all  $X$ , i.e.  $\frac{\partial^2 S}{\partial X_i^2} \leq 0$ ,  $i = 1, \dots, \mathcal{M}$  for all the values taken by  $X$ , see sec. 1.2.3.

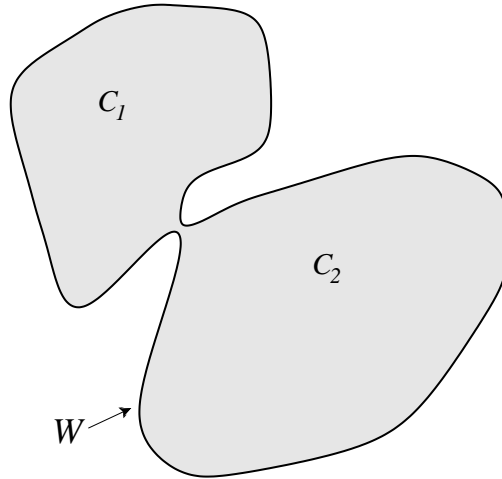


Figure 1.1: Schematic view of  $W$ .  $C$  can have two “macroscopic” values:  $C_1$  and  $C_2$ .

constant of motions cannot be in practice incorporated in  $X$ . Nevertheless, seven of these constants are known: the energy, three components for the total linear and the total angular momentum [PAD90]. Moreover, some of them can be less relevant. For example, the total linear momentum can be set to zero by a suitable choice of frame coordinates. Finally, for practical use one is forced to study the system with a small number of parameters. This is the basic historical reason of introducing statistical mechanics.

- In some systems there exist several processes (degrees of freedom) with very different time-scales. Hence, some quantities might be considered as constant though there are not formally, i.e. some degrees of freedom may relax very quickly compared to other ones. Then, as an approximation one can build a ME where the degrees of freedom with long relaxation time are considered as fixed. This kind of argument is used in part III and in general to define the statistical mechanics of self-gravitating systems, see for example [HK77, SAS85, CP01]. Of course, terms like “majority”, “sensibly”, “quickly”, etc. have to be carefully discussed and defined for each system depending on e.g. the precision asked.
- It can also happen that the phase space is made of two (or more) “basins” connected with each other by “tunnels” (see Fig. 1.1). If the system is ergodic, the time spent in each basin is simply proportional to their respective volume. In some cases, these basins can unambiguously be labeled with a quantity say  $\mathcal{C}$ , for example a symmetry [JG00]. Strictly taken the definition of the microcanonical ensemble given in the previous section, one should not use  $\mathcal{C}$  as a new parameter in  $X$ . However, it is again a matter of time-scales. If in an experiment, one can control  $\mathcal{C}$  and prepare a collection of systems having all the same value of  $\mathcal{C}$ , and if the time of experimentation is smaller than the typical time over which this quantity is conserved (the typical time that the system spends in the corresponding basin), then just like in the previous point, one may consider  $\mathcal{C}$  as quasi-conserved and add it in  $X$ .

## 1.2 Canonical ensemble

### 1.2.1 Definitions

Consider a large isolated system called hereafter  $HT$ . Its Hamiltonian and the value of the constant of motions are noted by  $\mathcal{H}_{HT}$  and  $X_{HT}$ , respectively. Now consider a part of  $HT$ , say  $A$ , and the rest of  $HT$ , say  $B$ .  $\mathcal{H}_{HT}$  can be written as

$$\mathcal{H}_{HT} = \mathcal{H}_A + \mathcal{H}_B + \mathcal{H}_{AB}, \quad (1.7)$$

where  $\mathcal{H}_A$  and  $\mathcal{H}_B$  are the Hamiltonian of  $A$  and  $B$  resp., and  $\mathcal{H}_{AB}$  describes the interactions between  $A$  and  $B$ .

If  $\mathcal{H}_{AB}$  can be neglected compared to  $\mathcal{H}_A$  and  $\mathcal{H}_B$ , i.e. if

$$\mathcal{H}_{HT} \simeq \mathcal{H}_A + \mathcal{H}_B, \quad (1.8)$$

then  $HT$  can be seen as the union of two independent systems  $HT = A \cup B$ . The following relation holds

$$X_{HT} = X_A + X_B, \quad (1.9)$$

where  $X_A$  and  $X_B$  are the values taken by  $X$  in  $A$  and  $B$ . Therefore,  $X$  is a set of extensive variables in the conventional sense (see footnote d on page 4). A priori  $X_A$  and  $X_B$  are not fixed, they can both fluctuate<sup>m</sup>. The volume of the phase space  $\mathcal{W}_{HT}$  accessible to  $HT$  is written as a folding product

$$\mathcal{W}_{HT}(X_{HT}) = \int_{X_A^{min}}^{X_A^{max}} \mathcal{W}_A(X_A) \mathcal{W}_B(X_{HT} - X_A) dX_A, \quad (1.10)$$

where  $\mathcal{W}_A$  and  $\mathcal{W}_B$  are the phase space volumes of  $A$  and  $B$ , respectively. The bounds of the integral in eq. (1.10) depend on the domains of definition of  $A$  and  $B$ .

Now if  $A$  is small compared to  $B$ , i.e. if  $\mathcal{H}_A \ll \mathcal{H}_B$  and  $X_A \ll X_B$ , then  $B$  can be seen as a reservoir of  $X$  for  $A$ , i.e. the exchange of amounts of  $X$  between  $A$  and  $B$  does neither change notably the entropy of  $B$  ( $\frac{\partial^k S_B}{\partial X^k}|_{X_B} = 0$  for  $k = 2, 3, \dots$ ) nor the value of  $X_B$ . Under those conditions, the probability  $P(X_A)$  for the subsystem  $A$  to have a given value of  $X_A$  is [LL94]

$$P(X_A) = \frac{1}{\mathcal{Z}(x_0)} \exp(-x_0 \cdot X_A + S_A(X_A)), \quad (1.11)$$

where  $\mathcal{Z}(x_0)$  is the normalization constant called the partition function

$$\mathcal{Z}(x) = \int_{X_A^{min}}^{X_A^{max}} dX \exp(-x \cdot X + S_A(X)), \quad (1.12)$$

$x_0 = \frac{\partial S_B}{\partial X_B}|_{X_B} \simeq \frac{\partial S_{HT}}{\partial X_{HT}}|_{X_{HT}}$  is imposed to  $A$  by the reservoir.  $S_A(X)$  is the entropy that  $A$  would have if it was isolated. The domain of definition of  $S_A$  is  $[X_A^{min}, X_A^{max}]$ . Thus the values of the intensive variables are imposed by the reservoir  $HT$  on  $A$  while its extensive variables are free to fluctuate according to the distribution (1.11). The probability distribution  $P$  depends explicitly on  $x_0$ . Therefore, in the following, it is noted  $P(X, x_0)$ .

<sup>m</sup>For simplicity, all the components of  $X$  are assumed to fluctuate. Of course, depending on the context some of them might be fixed.

**Definition 2.** A collection of systems whose extensive variables  $X$  are distributed according to the distribution (1.11) is called a canonical ensemble <sup>n</sup>.

In most of the cases the range of  $X_A$  in the integral (1.12) can be changed to  $[0, +\infty[$ . Then  $\mathcal{Z}(x)$  becomes the Laplace transform of  $\exp(S(X))$ . For simplicity, in the following  $\mathcal{Z}(x)$  is called the Laplace transform of  $\exp(S(X))$ . Hereafter, the argument of the exponential in eq. (1.12) is noted by  $f(X, x) = -x \cdot X + S(X)$ ; and  $F(x) \equiv -\frac{1}{\beta} \ln(\mathcal{Z}(x))$  is called the free energy, or the thermodynamical potential in CE. Note that one can alternatively write the previous functions of the intensive parameters  $x$  (i.e.  $P, \mathcal{Z}, f, F$ ) as functions of the “extensive” parameters  $X_0$  provided that  $x_0 = \frac{\partial S}{\partial X}|_{X_0}$ . Hence, in the following,  $f(X, x_0)$  is also noted  $f(X, X_0)$ . Note that  $X_0$  is not necessarily unique, i.e. a priori, nothing forbids  $X_1 \neq X_0$  from satisfying  $x_0 = \frac{\partial S}{\partial X}|_{X_1}$ .

### 1.2.2 Link between ME and CE

Equation (1.12) shows that the main mathematical ingredient that transforms ME to CE is a Laplace transform. In order to facilitate the following discussions it is worth to spend some time to acquire a “pictorial” representation of this transform.

For sake of simplicity let us suppose that  $E$  is the only parameter ( $X = E$ ) and that the entropy  $S(X)$  is a concave function for all values of  $X$  as required by conventional thermodynamics.

Fig 1.2(a) shows the entropy (thick plain line) and the line  $x_0 \cdot X$  (thick dashed line). The value of  $x_0$  ( $\equiv \beta$ ) has been set to  $x_0 = \frac{\partial S}{\partial X}|_{X_0}$ . The plain line is just  $x_0 \cdot X + K$  where  $K$  is a constant chosen so that this line touches  $S(X)$  at  $X_0$ . *By definition* the line  $x_0 \cdot X + K$  is tangent to  $S(X)$  at  $X_0$

$$\frac{\partial}{\partial X}(x_0 \cdot X + K)|_{X_0} = x_0 = \frac{\partial S}{\partial X}|_{X_0}.$$

$f(X, X_0) = f(X, x_0) = -x_0 \cdot X + S(X)$  is plotted in Fig. 1.2(b). It is the result of the shearing of  $S$  by the line of equation  $x_0 \cdot X = 0$ . By construction,  $f(X, x_0)$  has an extremum at  $X_0$

$$\frac{\partial f}{\partial X}|_{X_0} = -x_0 + \frac{\partial S}{\partial X}|_{X_0} = 0.$$

For the present example this extremum is even a maximum since  $\frac{\partial^2 f}{\partial X^2}|_{X_0} = \frac{\partial^2 S}{\partial X^2}|_{X_0} < 0$ . Note that this extremum is a maximum because  $S$  is concave at  $X_0$ .

In Fig. 1.2(c) the argument of the integral in Eq. (1.12), i.e.  $\exp(f(X, X_0)) \propto P(X, X_0)$  is plotted. As one can see, it is a peaked function with a maximum at  $X_0$ . In the canonical ensemble and for this system, the most probable value of  $X$  is  $X_0$ . The most probable value of  $X$  is always  $X_0$  if the entropy  $S$  is a strictly concave function of  $X$ , i.e.  $\frac{\partial^2 S}{\partial X^2} < 0$  for all values of  $X$ . It can be shown that in the Gaussian approximation the width of this distribution is proportional to  $\beta^{-2} C_V$ , where  $C_V$  is the heat capacity.  $C_V$  is defined in CE in the following way

$$C_V \doteq \frac{\partial \langle E \rangle}{\partial T} \propto \langle E^2 \rangle - \langle E \rangle^2, \quad (1.13)$$

---

<sup>n</sup>In the conventional canonical ensemble, the only fluctuating extensive parameter is the subsystem energy  $E_A$ .

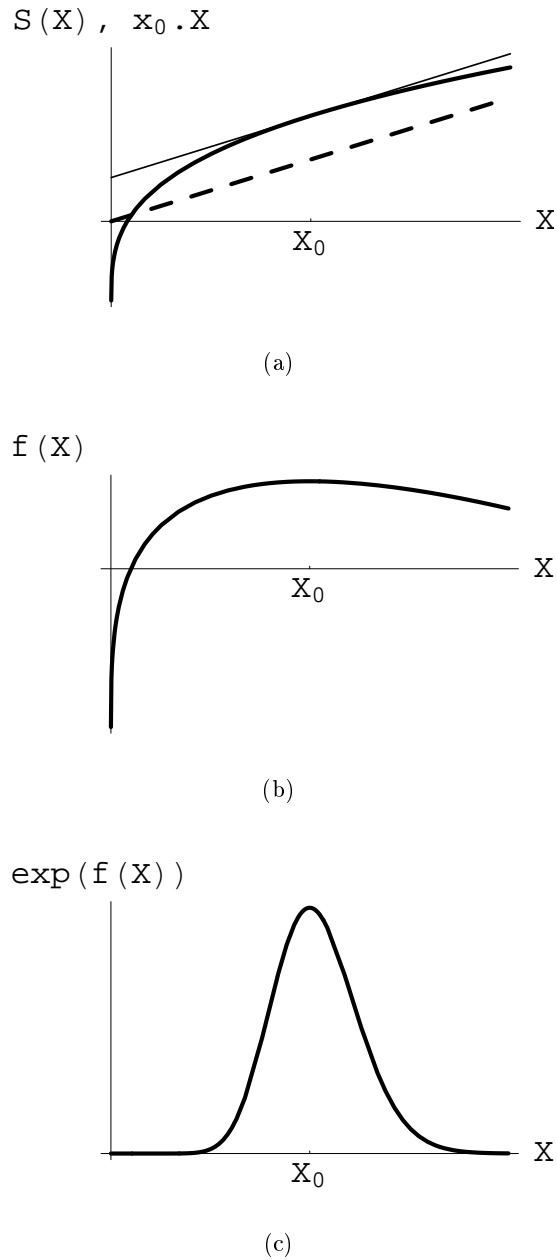


Figure 1.2: Schematic illustration of the integral in Eq. (1.12) on page 7 (see text). (a) Entropy  $S(X)$  (thick line);  $x_0 \cdot X \doteq \frac{\partial S}{\partial X}|_{X_0} \cdot X$  (dashed line) and  $x_0 \cdot X + K$  (thin line) where  $K$  is chosen so that  $x_0 \cdot X_0 + K = S(X_0)$ . (b) Result of the shearing of  $S$  by  $-x_0 \cdot X$ , i.e.  $f(X) = -x_0 \cdot X + S(X)$ . (c) Unnormalized probability distribution of  $X$   $P(X, X_0) \propto \exp(f(X, X_0))$ .

where

$$\langle E \rangle \equiv -\frac{1}{Z} \frac{\partial Z}{\partial \beta} \quad (1.14)$$

is the mean value of the energy in CE, and

$$\langle E^2 \rangle \equiv \frac{1}{\mathcal{Z}} \frac{\partial^2 \mathcal{Z}}{\partial \beta^2} \quad (1.15)$$

is the mean value of the energy squared in CE. From the definition of the canonical heat capacity eq. (1.13), it immediately follows that it is a *positive* quantity. This is in sharp contrast with ME where nothing forbids *a priori* the entropy to have a convex part for finite size systems and consequently a region of *negative* heat capacity. If one identifies the two definitions of  $C_V$  then  $S$  *must* be a concave function of  $X$ . However, when CE and ME are not equivalent this identification is simply no longer legitimated (see sec. 1.2.3).

In order to generalize the previous results to multidimensional parameter spaces, first  $H_S$  is defined as the Hessian matrix of  $S$

$$H_s \doteq \left\| \frac{\partial^2 S}{\partial X_i \partial X_j} \right\|, \quad i, j = 1, \dots, \mathcal{M}. \quad (1.16)$$

$H_S$  is a  $\mathcal{M} \times \mathcal{M}$  symmetric matrix. Therefore, one can always find a basis  $\{\mathbf{v}_1, \dots, \mathbf{v}_{\mathcal{M}}\}$  where  $H_S$  is diagonal. Its  $\mathcal{M}$  eigenvalues are  $\lambda_1 \geq \lambda_2 \geq \dots \geq \lambda_{\mathcal{M}}$ . Furthermore,  $D_S = \lambda_1 \cdot \lambda_2 \cdots \lambda_{\mathcal{M}}$  is the determinant of  $H_S$  also called the Hessian of  $S$ . Note that  $H_f$  the Hessian matrix of  $f$  is equal to  $H_S$  since  $f$  is  $S$  plus a linear function of  $X$ .

In one hand, when  $\lambda_1 < 0$  holds at  $X = X_0$ , then  $S(X)$  is said to be a concave function at  $X_0$  (it is a *local* property). In the other hand, when  $\lambda_{\mathcal{M}} > 0$  at  $X_0$  then  $S(X_0)$  is locally convex.

Now in the case of a multidimensional parameter space,  $f(X, x_0)$  is the result of the shearing of  $S$  by a plane of equation  $x_0 \cdot X$ . In the Gaussian approximation, the fluctuation of the full parameter-vector  $\sqrt{\langle X^2 \rangle - \langle X \rangle^2}$  is proportional to  $\left( (-1)^{\mathcal{M}+1} D_S \right)^{-1}$ . Again, this implies that  $(-1)^{\mathcal{M}+1} D_S$  is positive. One can even show that *all* the eigenvalues of  $H_S$  have to be negative, i.e.  $\lambda_1 < 0$  [GV00, FG01]. Or on other words,  $S$  must be concave at  $X_0$ . This generalizes the constraint of a positive heat capacity for a system with  $\mathcal{M} = 1$ .

### 1.2.3 Equivalence conditions

At the thermodynamical limit, CE and ME are said to be equivalent at  $X = X_0$  if the following conditions hold

1.  $\langle X \rangle_{CE} = X_0$ ,
2.  $\lim_{N \rightarrow \infty} \langle X^2 \rangle - \langle X \rangle^2 \sim N$ ,

where

$$\langle X \rangle_{CE} = - \frac{1}{\mathcal{Z}} \frac{\partial \mathcal{Z}}{\partial x} \Big|_{x_0 = \frac{\partial S}{\partial X} \Big|_{x_0}}, \quad (1.17)$$

is the mean value of  $X$  in CE, and

$$\langle X^2 \rangle_{CE} = \frac{1}{\mathcal{Z}} \frac{\partial^2 \mathcal{Z}}{\partial x^2} \Big|_{x_0 = \frac{\partial S}{\partial X} \Big|_{x_0}}. \quad (1.18)$$

Condition (2) ensures the specific heat capacity to be a *finite and positive* quantity.

At the limit  $N \rightarrow \infty$ , if ME and CE are equivalent then  $\frac{X}{N}$  does not fluctuate in CE. Its distribution function  $P\left(\frac{X}{N}, \frac{X_0}{N}\right)$  as a function of the specific “extensive” variables is a  $\delta$ -Dirac distribution, i.e.

$$P\left(\frac{X}{N}, \frac{X_0}{N}\right) = N\delta(X - X_0). \quad (1.19)$$

For finite systems, as  $\frac{X}{N}$  fluctuates one needs a set of “weaker” conditions where small fluctuations are allowed

$$0'. \quad \mathcal{Z}(x_0) = \int dX \exp(-x_0 \cdot X + S(X)) < +\infty,$$

$$1'. \quad X_0 - \Delta X_0 < \langle X \rangle_{CE} < X_0 + \Delta X_0,$$

$$2'. \quad \langle X^2 \rangle - \langle X \rangle^2 < \delta X_0,$$

where  $x_0 = \frac{\partial S}{\partial X}|_{X_0}$ .  $\delta X_0$  and  $\Delta X_0$  are two arbitrary positive constants. For small systems a zeroth condition must be added:  $\mathcal{Z}$  must be finite. This condition holds for all systems at the thermodynamical limit since their entropies are everywhere concave as van Hove’s theorem states it <sup>o</sup>. In part III, a model is presented for which condition (0’) does not hold for some values of  $X_0$  and a particular choice of intensive parameters (see section 6.4.4).

In order to fulfill these equivalence conditions at  $X_0$ ,  $f(X, X_0)$  must have a global maximum at  $X_0$ . Locally this means that  $f$  and therefore  $S$  must be concave at  $X_0$ . I.e. CE and ME can be equivalent for small systems at  $X_0$  only if  $\lambda_1(X_0) < 0$ . But if the plane  $x_0 \cdot X + K(X_0) = 0$  touches more than one time the entropy surface then at least condition (2’) is not satisfied, consequently CE is not equivalent to ME at  $X_0$ . Hence, the equivalence at  $X_0$  implies that  $\lambda_1(X_0) < 0$ , whereas the converse proposition is not always true.

### 1.3 Microcanonical or canonical ensemble?

As ME and CE are equivalent at the thermodynamical limit (except at phase transitions, see below in section 2.2), the choice of the ensemble used to describe the infinite system is only a matter of conveniency. The canonical description is commonly preferred because therein the computations are usually “reduced” to optimization problems. They are in most of the cases technically easier to handle and faster to solve than computing averages over the whole microcanonical phase spaces. Moreover, the notion of heat bath is well defined and the assumptions made in sec. 1.2.1 on page 7 in order to define CE are valid.

For small systems the situation is dramatically different. CE relies on the assumption that the interactions between the system  $A$  and its reservoir  $B$  can be neglected and that the conserved quantities are extensive. These assumptions generally do not hold for small systems, i.e. when the range of the forces is of the order of the range of the system. For a small system the interactions between  $A$  and  $B$  dramatically affect the whole system  $A$  [GRO97, SCH97, CP01, SSHT00, STH00].

Nevertheless, one can go on and simply *assume* a canonical distribution for the “extensive” variables. This in order to benefit from technical advantages of CE compared to ME. In this respect, the canonical ensemble can be seen as a trick (as already noticed by

<sup>o</sup>To be more precise, when  $N \rightarrow +\infty$  it is  $\mathcal{Z}^{1/N}$  which is a finite quantity.

Ehrenfest eighty years ago [EE12]). But, if one uses this trick, one would lose a lot of information about the physics of the system near and at phase transitions. This information is accessible to ME. Some information is lost because the equivalence conditions (1') or (2') do not hold near and at phase transitions (see section 2.2, see also [GV00] where half of the parametric space is in practice lost after the Laplace transform <sup>p</sup>). One could not observe for example multifragmentation of nuclei [CGD00, DGC<sup>+</sup>00, DBB<sup>+</sup>99, GRO90] or of metallic clusters [GMS97, SKM<sup>+</sup>97, GM97, MHGS97]. In a model presented in part III, all the phenomena of astrophysical interest are overlooked by CE.

As there is a hierarchy of system parameters,  $X \rightarrow x$  (see page 5) there is a hierarchy of ensembles  $ME \rightarrow CE$  with a loss of information from ME to CE [CH88, GM97].

In summary, ME is the proper ensemble to describe small systems and information is lost in the transformations  $ME \leftrightarrow CE$ .

For all these reasons *the microcanonical description of a small system should be preferred to the canonical one.*

## 1.4 Toy models

In chapter 2 the definitions of phases and phase transitions are illustrated by the following simple analytical entropy-models. The model considered as one-dimensional  $S(X) = S(E)$  is adapted from [HÜL94A]. The two dimensional model is the one of a gas in the van der Waals approximation. In sec. 1.4.2 some classical results for this model are recalled [LL94, DGLR89].

### 1.4.1 1-D toy model

Hüller introduced in [HÜL94A] several models of typical density of states (or entropy), in order to illustrate the smearing of information in CE. In the following chapter, one of these 1-dimensional entropy model is used to illustrate (a) the influence of the surfaces through the surface entropy  $S_{surf}$  and (b) the behavior of the caloric curve towards the thermodynamical limit. The entropy-model  $S_1$  is defined as

$$S_1(\epsilon) = S_\infty(\epsilon) + N^{2/3} S_{surf}(\epsilon), \quad (1.20)$$

where  $\epsilon$  is the specific energy  $\epsilon = E/N$ .  $s_\infty(\epsilon) = \frac{S_\infty(\epsilon)}{N}$ , the “infinite” system specific entropy (the volume part of  $S_1$ ) as a function of the specific energy  $\epsilon$  is given by

$$s_\infty(\epsilon) = \beta_t \epsilon - \begin{cases} 0 & \text{if } -d < \epsilon < d, \\ a_4 (|\epsilon| - d)^4 & \text{else,} \end{cases} \quad (1.21)$$

with the constants  $\beta_t = 1$ ,  $a_4 = 0.04$ , and  $d = 0.5$ . As required by van Hove’s theorem  $\frac{\partial^2 s_\infty}{\partial \epsilon^2} \leq 0$  for all  $\epsilon$  [vH49];  $\frac{\partial^2 s_\infty}{\partial \epsilon^2} = 0$  for a range of energies  $-d < \epsilon < d$ .

The surface effects are described by an entropy  $S_{surf}$  modeled in the following way

$$S_{surf}(\epsilon) = -a \cos(\pi\epsilon), \quad (1.22)$$

---

<sup>p</sup>Formally  $\mathcal{Z}$  contains the same information as  $S$ . But in practice, the inverse Laplace transform, needed to recover  $S$  from  $\mathcal{Z}$ , is a very unstable transformation when finite precision is used [CH88]. Moreover, in CE the quantities are mostly computed thanks to some optimization algorithms (e.g. maximization of free energy, or  $f$ , etc.). Hence, the information near minima ( $\lambda_1(X_0) > 0$ ) is overlooked by those methods.

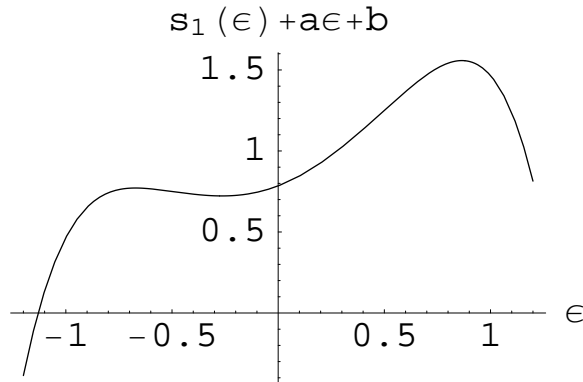


Figure 1.3: Specific entropy  $s_1(\epsilon)$ . A linear term in  $\epsilon$  is added to  $s_1(\epsilon)$  in order to emphasize the convex intruder ( $a = -0.5$ ,  $b = 1$  and  $N = 100$ ). For finite  $N$  the specific heat capacity is negative for  $\epsilon \in ]-0.5, 0.5[$  and positive elsewhere.

where  $a = 0.01$ .

For  $N$  finite,  $s_1$  has a convex intruder ( $\frac{\partial^2 s_\infty}{\partial \epsilon^2} > 0$ ) for a range of energies  $-d < \epsilon < d$ . See for an illustration fig. 1.3. As shown in the next chapter, this negative specific heat signals a first order phase transition [GRO97]. At the thermodynamical limit,  $s_1 = S_1/N$  must satisfy van Hove's theorem, so the influence of surface effects must decrease relatively to the volume ones. A reasonable assumption is that the scaling of the surface effects should be  $\sim N^{2/3}$  as already written in eq. (1.20) on the facing page. This scaling implies that  $\lim_{N \rightarrow \infty} s_1 = s_\infty$ , thus  $s_1$  satisfies van Hove's theorem.

#### 1.4.2 2-D toy model: the van der Waals approximation

The second model is the van der Waals gas [DGLR89, LL94]. It is a simple analytical model that presents first and second order phase transitions. Its *microcanonical* specific entropy ( $s = \frac{S}{N}$ ) as a function of the specific energy  $\epsilon$  and the specific volume  $v = \frac{V}{N}$  is (up to an additive constant that does not depend on  $\epsilon$  and  $v$ )

$$s(\epsilon, v) = \ln(v - b) + \frac{3}{2} \ln\left(\epsilon + \frac{a}{v}\right), \quad (1.23)$$

where  $a$  and  $b$  are two phenomenological constants. Their values depend on the fluid:  $a$  is linked to the interaction potential acting in the mean on one particle,  $b$  is an approximation for the avoided volume per particle <sup>9</sup>.

With a suitable choice of units, i.e.  $\epsilon \frac{b}{a} \rightarrow \epsilon$  and  $\frac{v}{b} \rightarrow v$ , eq. (1.23) becomes

$$s(\epsilon, v) = \ln(v - 1) + \frac{3}{2} \ln\left(\epsilon + \frac{1}{v}\right). \quad (1.24)$$

In these units  $\beta$  the inverse temperature is

$$\beta \doteq \frac{\partial s}{\partial \epsilon} = \frac{3}{2} \frac{1}{\epsilon + \frac{1}{v}}, \quad (1.25)$$

<sup>9</sup>For a discussion on the avoided volume see app. A.

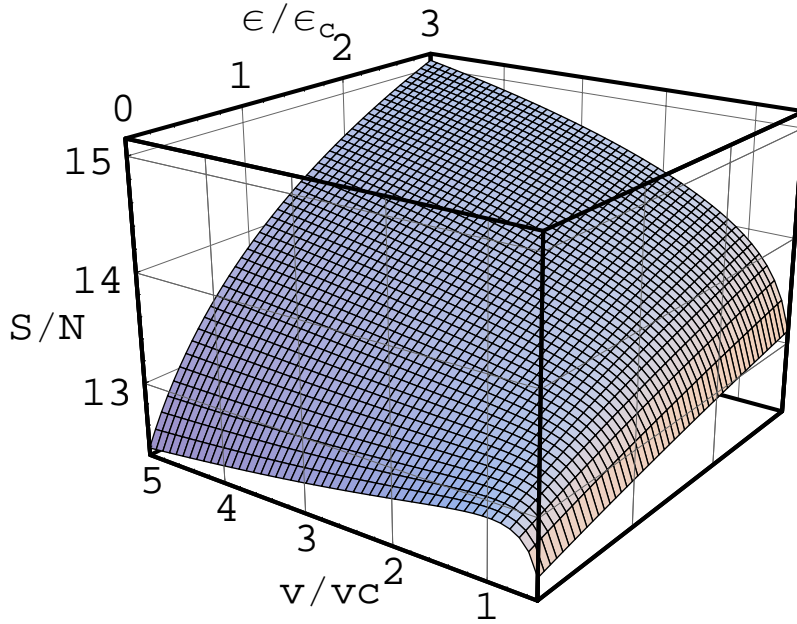


Figure 1.4: Specific entropy surface of the van der Waals model as a function of the specific energy  $\epsilon$  and volume  $v$ .  $\epsilon_c$  and  $v_c$  are the specific critical energy and volume.

and the pressure  $p$

$$\beta p \doteq \frac{\partial s}{\partial v} = \frac{1}{v-1} - \frac{3}{2} \frac{1}{v^2 \left(\epsilon + \frac{1}{v}\right)}. \quad (1.26)$$

This model has a critical point (second order phase transition) at  $\epsilon_c = \frac{1}{9}$ ,  $v_c = 3 \Rightarrow \beta_c = \frac{27}{8}$ ,  $p_c = \frac{1}{27}$ . At this critical point the following relations hold [DGLR89, LY52B]

$$\left. \frac{\partial p}{\partial v} \right|_{\beta=cst} = 0, \quad (1.27)$$

$$\left. \frac{\partial^2 p}{\partial v^2} \right|_{\beta=cst} = 0. \quad (1.28)$$

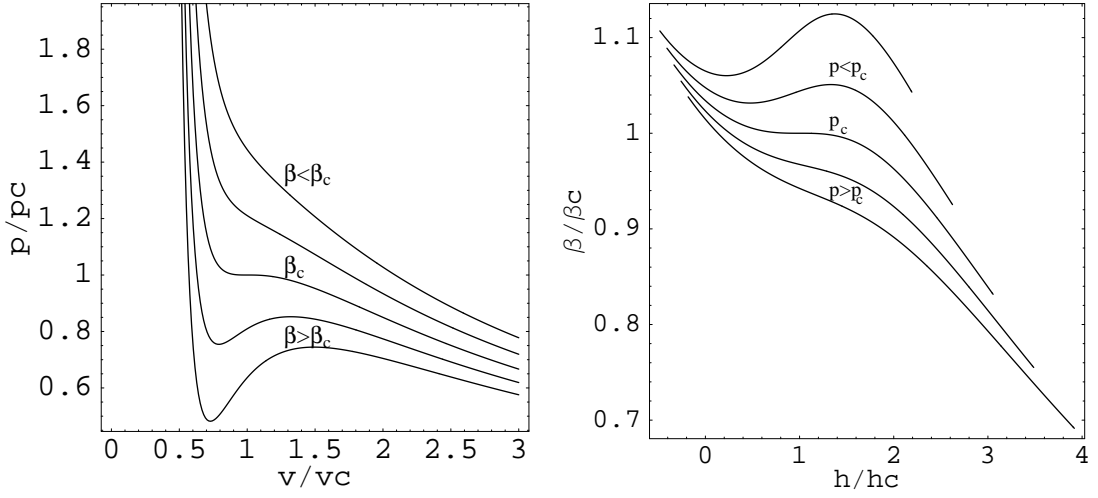
All quantities written in the following, for this model, are normalized by these critical values.

Fig. 1.4 shows the specific entropy  $s$  as a function of  $\epsilon$  and  $v$ .

In fig. 1.5(a) on the next page isotherms are plotted in the plane  $(p, v)$  for different temperatures. At large volumes, the compressibility  $\chi \doteq -\frac{\partial v}{\partial p}$  is large like in a gas. At small volumes,  $\chi$  is small like in a liquid. Below  $\beta_c$ , the isotherms have a loop, i.e. there is a region of negative  $\chi$ . In other words, the equation  $p(v) = p_0$  has one solution above  $\beta_c$  and three below  $\beta_c$ . This loop is classically interpreted as a signal of a first order transition with phase coexistence [DGLR89]. Along the critical isotherm ( $\beta = \beta_c$ ), the compressibility diverges at  $v = v_c$ . This divergence signals a second order phase transition.

In fig. 1.5(b) isobars are plotted in the plane  $(\beta, h)$ , where  $h = \epsilon + pv$  is the specific enthalpy. At low pressure and for a given isotherm,  $\beta$  is a multiple valued function of  $h$ . On the critical isobar ( $p = p_c$ ),  $\frac{\partial \beta}{\partial h}$  diverges at  $h_c$ .

The domain of physical validity of the van der Waals (vdW) approximation is smaller than the domain of definition of its entropy ( $v > -1$  and  $\epsilon > -\frac{1}{v}$ , see eq. (1.24)). E.g.



(a) Isotherms: pressure vs volume. From top to bottom increasing  $\beta$ .

(b) Isobars:  $\beta$  vs enthalpy. From top to down increasing pressure.

Figure 1.5: Isotherms and isobars of the van der Waals model.

in the phase transition region, where for a real liquid–gas phase transition the density is no longer uniform, in contrast with the uniform density assumption made in the vdW approximation. Another region where the physical validity of eq. (1.24) breaks down is where the pressure becomes negative, i.e.  $\frac{\partial s}{\partial v} < 0$  (see fig. 1.4 at  $\epsilon = 0$  and  $v \gtrsim 1$ , see also eq. (1.26)). Moreover,  $S$  does not have a proper thermodynamical limit since the region of negative compressibility remains even at the limit  $N \rightarrow \infty$ . However, for illustration in the following the underlying physical system is forgotten and  $s$  is taken as it is. It is simply used as an entropy-model.



## Chapter 2

# Thermostatistics of small systems

At the thermodynamical limit, a first (second) order phase transition at say  $x = x_0 = \frac{\partial S}{\partial X}|_{X_0}$  is signaled by a singularity in the second (third) derivative of the free energy  $F$  (canonical potential) with respect to the intensive variables  $x$  [LY52A, LY52B, GR69, GL69]. From the properties of the probability distribution of the “extensive” variables  $X$  in CE (whenever  $F$  is singular or not), one can infer a definition of phases and phase transitions based on the *local* curvature of the microcanonical entropy-surface (see for systems depending on  $\mathcal{M} = 1$  “extensive” parameter [GM87, GMS97, GRO90, GRO01], special cases of  $\mathcal{M} = 2$  [GEZ96, GV00, GRO01] and a straightforward generalization in [FG01]).

In this chapter, these definitions and their origins are recalled and illustrated with the analytical models presented in section 1.4 on page 12. Some consequences of these new definitions and their link to the standard ones are also discussed. Finally, alternative definitions are reviewed and commented in section 2.5.

### 2.1 Pure phases

#### 2.1.1 Definition

At the thermodynamical limit a system is in a pure phase at say  $x_0$  when  $F$  is an infinitely differentiable function of  $x$  at  $x_0$  [LY52A, CAL85, GL69]. In a pure phase ME and CE are equivalent. The distribution of  $\frac{X}{N}$  in CE is a delta peak centered at  $X_0$ , where  $X_0$  satisfies  $x_0 = \frac{\partial S}{\partial X}|_{X_0}$ . For a finite system, the precursor of this delta peak is a distribution with a *maximum* at  $X_0$  (see sec. 1.2.2). This means that, at  $X_0$ , the entropy is a *concave* function. I.e.  $\lambda_1$ , the largest eigenvalue of the Hessian matrix of  $S$ , is negative. Thus, for a one dimensional system, its heat capacity is positive,  $C_V \propto - \left( \frac{\partial^2 S}{\partial X^2} \right)^{-1} > 0$ .

**Definition 3.** *A microcanonical ensemble of states is in a pure phase at  $X = X_0$  if  $\lambda_1(X_0) < 0$ .*

#### 2.1.2 Example

In fig. 2.1 on the next page the sign of  $\lambda_1$ , the largest eigenvalue of the Hessian matrix of  $s$  the entropy of the van der Waals model <sup>a</sup> (presented in section 1.2.1) is plotted versus the

---

<sup>a</sup> $s(\epsilon, v) \doteq \ln(v-1) + \frac{3}{2} \ln(\epsilon + \frac{1}{v})$ .

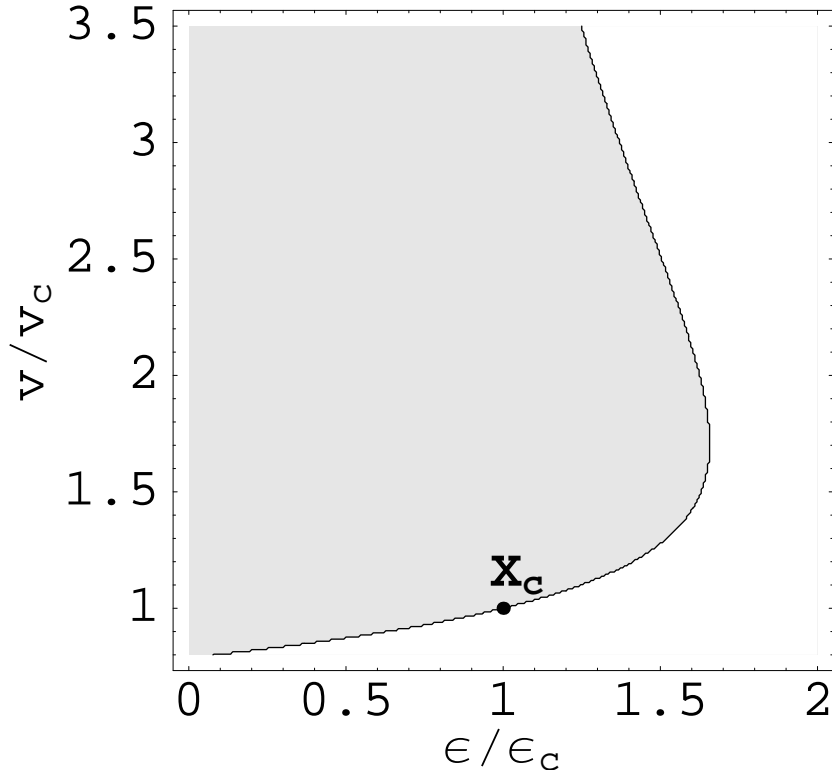


Figure 2.1: Sign of  $\lambda_1$ , the largest eigenvalue of the Hessian matrix of  $s$  for the van der Waals entropy-model. The white region at large volume corresponds to  $\lambda_1 < 0$  (pure phase). The gray region corresponds to  $\lambda_1 > 0$ .  $\lambda_1$  is equal to zero along the boarder-line between these two regions. The black dot locates the critical point  $X_c$  known form standard thermostatistics.

specific energy  $\epsilon$  and volume  $v$ . The white region at large energies corresponds to  $\lambda_1 < 0$  and therefore, according to def. 3, to a pure phase.

If one chooses a pressure  $p_0$  and a temperature  $T_0 = \beta_0^{-1}$  at say  $X_0 = (\epsilon_0, v_0)$ , i.e.  $\beta_0 = \frac{\partial s}{\partial \epsilon}|_{X_0}$  and  $\beta_0 p_0 = \frac{\partial s}{\partial v}|_{X_0}$  where  $\lambda_1(X_0) < 0$ , then  $f(X, X_0) = f(X, x_0 = (\beta_0, p_0)) = -x_0 \cdot X + s(X)$  has a local maximum at  $X_0$ . This is illustrated in fig. 2.2 on the facing page, where a density-contour plot of  $f$  is shown for  $(\epsilon_0, v_0) = (5, 5) \Rightarrow (\beta_0, p_0) = (\frac{5}{7}, \frac{17}{25}) \approx (0.71, 0.68)$ .  $f$  has a clear maximum at  $(5, 5)$ . It is even a *global* maximum. In this example, CE and ME are equivalent at  $X_0$  in the sense given in sec. 1.2.3.

## 2.2 First order phase transitions

### 2.2.1 Definitions

Pure phases are locally defined by a negative  $\lambda_1$ . What does happen to the probability distribution  $P(X, X_0)$  if  $\lambda_1(X_0) > 0$ ? First of all, for  $\mathcal{M} = 1$  (i.e.  $S(X) = S(E)$ ) this implies a *negative* specific heat capacity. There ME and CE cannot be equivalent. Furthermore, the probability distribution  $P(X, X_0) \propto \exp(f(X, X_0))$  has a *local minimum* at  $X_0$ .

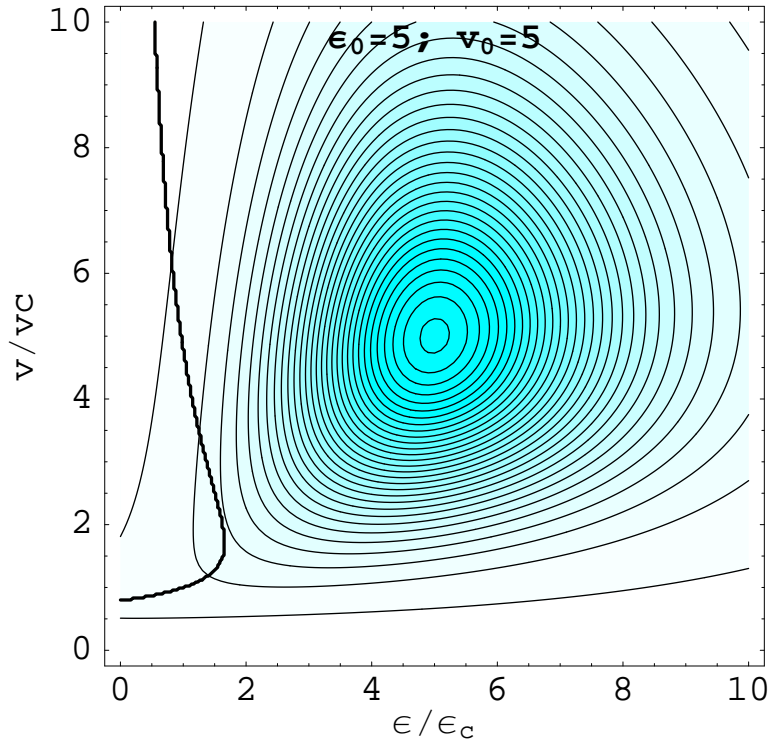


Figure 2.2: Contour-Density plot of  $f(X, X_0) \equiv f(X, x_0) = -x_0 \cdot X + s(X)$  for the van der Waals entropy-model at  $X_0 = (\epsilon_0, v_0) = (5, 5)$ , where  $x_0 = (\beta_0, \beta_0 p_0) = \frac{\partial s}{\partial X}|_{X_0} = (\frac{5}{7}, \frac{17}{35})$  and  $\lambda_1(X_0) < 0$ . There is a clear maximum at  $(\epsilon_0, v_0)$ . The gray level correspond to the value of  $f$ : the grayer the larger is  $f$ . The thick line corresponds to  $\lambda_1 = 0$  (see fig. 2.1 on the facing page); on the right side of this line  $\lambda_1 < 0$  and on the left one  $\lambda_1 > 0$ . The scale of  $f$  is non-linear.

This is illustrated in fig. 2.3(a) on the next page, where  $P(\epsilon, \epsilon_0)$  (unnormalized) is plotted for the entropy-model  $s_1^b$  for different value of  $\beta$ . The first one has been taken at  $\epsilon_0 = 0$  and the other at  $\epsilon_0 = 0.2$  which correspond to  $\beta = \beta_t = 1$  and  $\beta \approx 1.002$ , resp., and for  $N = 10^2$ . The two probability distributions have a minimum at their respective  $\epsilon_0$ . Moreover, in each distribution there are two maxima which have, by construction, the same temperature than their respective  $\epsilon_0$ , but their respective heat capacities are positive. I.e. the two peaks correspond to two pure phases. For  $\beta = 1$  the two peaks are of equal height, while for  $\beta = 1.002$  the peak at low energy is higher than the other one. In CE (at finite size and at  $\beta = \beta_t$ ), the two pure phases have the same probability of occurrence. Therefore, the fluctuations and consequently the specific heat capacity are large in CE (eq. (1.13) on page 8). Hence, the equivalence condition (2')<sup>c</sup> does not hold, although condition (1')<sup>d</sup> is fulfilled since  $\langle \epsilon \rangle_{CE} = \epsilon_0$  ( $f$  is an even function for  $\beta = \beta_t$ ). For  $\beta = 1.002$  the condition (1') clearly does not hold.

In fig. 2.3(b) the same distribution functions as in fig. 2.3(a) are plotted but this time for  $N = 10^3$ . The width of the peaks are smaller. For  $\beta = 1.002$  the smallest peak is of

<sup>b</sup> $s_1(\epsilon) \doteq \epsilon - 0.04(|\epsilon| - 0.5)^4 \theta(|\epsilon| - 0.5) - 0.01N^{-1/3} \cos(\pi\epsilon)$ , as defined in sec. 1.4.1.

<sup>c</sup>Small fluctuations of the “extensive” parameters in CE, see page 11.

<sup>d</sup> $\langle X \rangle_{CE} = X_0 = 0$ , see page 11.

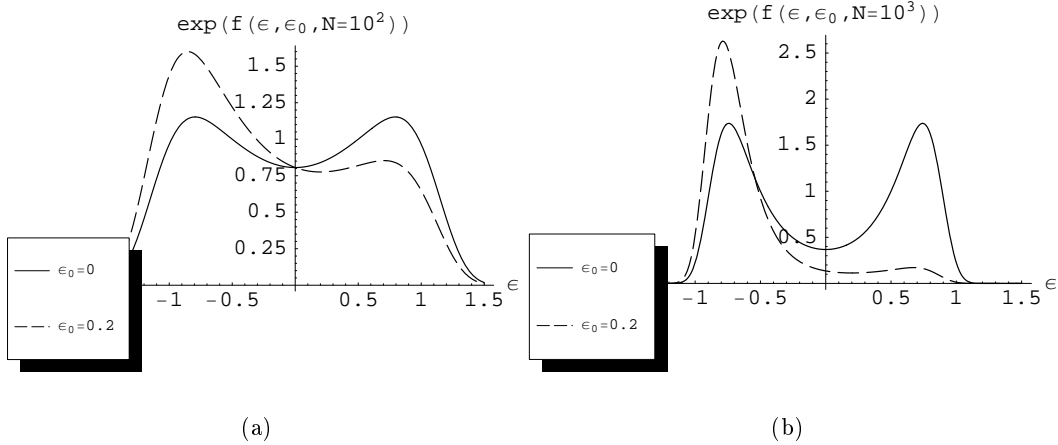


Figure 2.3: Unnormalized distribution functions  $P(\epsilon, \epsilon_0) \propto \exp(f(\epsilon, \epsilon_0)) = \exp\left(-\frac{\partial s_1}{\partial \epsilon}|_{\epsilon_0} \cdot \epsilon + s_1(\epsilon)\right)$  for the entropy model  $s_1$  (see eq. (1.20) or footnote (b) on the preceding page); for two values of  $N$  and of temperatures  $T_0^{-1} = \frac{\partial s_1}{\partial \epsilon}|_{\epsilon_0}$ . When  $\epsilon_0$  is chosen in the region of negative specific heat capacity, the probability distribution of  $\epsilon$  has a double peak structure.

no importance compared to the one at low energy. At the thermodynamical limit, this distribution function is simply a single Dirac distribution at  $\epsilon \approx -0.8$ , and not at  $\epsilon = \epsilon_0!$  Now, for  $\beta = 1$ , i.e.  $\epsilon_0 = 0$ , the two peaks remain. At the thermodynamical limit, the distribution function is composed of *two* delta Dirac<sup>e</sup>, one at  $\epsilon = -0.5$  and the other at  $\epsilon = 0.5$ . In CE, the fluctuations of the energy are larger for  $\beta = 1$  and smaller for  $\beta = 1.002$ . But nevertheless, the equivalence conditions (1') or (2') do not hold for any of the two  $\epsilon_0$ .

These two delta peaks are at the origin of the critical behavior of  $F$  at a first order phase transitions [GRO97]. Consider the system at the thermodynamical limit and its probability distribution for  $X$ , i.e.  $\lim_{N \rightarrow \infty} P\left(\frac{X}{N}, \frac{X_0}{N}\right)$ . At  $\beta = \beta_t - \delta\beta \lesssim \beta_t$ ,  $P$  has a single peak at  $\frac{X_0}{N} \equiv \epsilon_0 = \langle \epsilon \rangle_{CE} \lesssim -0.5$ . At  $\beta = \beta_t + \delta\beta \gtrsim \beta_t$ ,  $P$  has a single peak at  $\frac{X_0}{N} \equiv \epsilon_0 = \langle \epsilon \rangle_{CE} \gtrsim 0.5$  and at exactly  $\beta = \beta_t$ ,  $P$  has *two* peaks, one at  $\epsilon_1 = -0.5$  and the other at  $\epsilon_2 = 0.5$  (implying  $\langle \epsilon \rangle_{CE} = (\epsilon_1 + \epsilon_2)/2$ ). Consequently, in CE,  $\beta$  is a *discontinuous* function of  $\langle \epsilon \rangle$ . Therefore, the specific heat capacity  $C_V = \frac{\partial \langle \epsilon \rangle}{\partial \beta^{-1}}$  *diverges* at  $\beta = \beta_t$ . This divergence signals a first order phase transition in standard

<sup>e</sup>It may be not clear why  $P$  should be composed of two peaks at the thermodynamical limit and at the transition temperature. Indeed, at the limit  $N \rightarrow \infty$ ,  $s_1 \doteq s_\infty + N^{-1/3}s_{surf}$  is just  $s_\infty \doteq \epsilon - 0.04(|\epsilon| - 0.5)^4\theta(|\epsilon| - 0.5)$ .  $s_\infty$  is a linear function of  $\epsilon$  in the range  $[-0.5, 0.5]$ . Therefore  $P$  should be simply flat in this interval.

This argument is not correct since the limit  $N \rightarrow \infty$  has been taken too soon. Consider  $P(\epsilon, N) \propto \exp\left(N\left(-\epsilon\beta + s_\infty(\epsilon) + N^{-1/3}s_{surf}(\epsilon)\right)\right)$  for a finite  $N$ , at the transition temperature  $\beta = \beta_t$  and for  $\epsilon \in [-0.5, 0.5]$ . The points in the transition region are suppressed exponentially because  $N(s_\infty - s_1) = N^{2/3}S_{surf} < 0$ . When  $N \rightarrow \infty$ , although the *relative* weight of  $S_1$  compared to  $S_\infty$  vanishes, i.e.  $\lim_{N \rightarrow \infty} \frac{S_1}{S_\infty} = \lim_{N \rightarrow \infty} \frac{s_\infty + N^{-1/3}s_{surf}}{s_\infty} = 1$ , their *absolute* difference *diverges*  $\lim_{N \rightarrow \infty} S_\infty - S_1 = \lim_{N \rightarrow \infty} N^{2/3}s_{surf} = -\infty$ , leading to the double  $\delta$ -peak shape of  $P$  at the limit  $N \rightarrow \infty$ . This illustrates nicely the danger of taking the limit  $N \rightarrow \infty$  too soon.

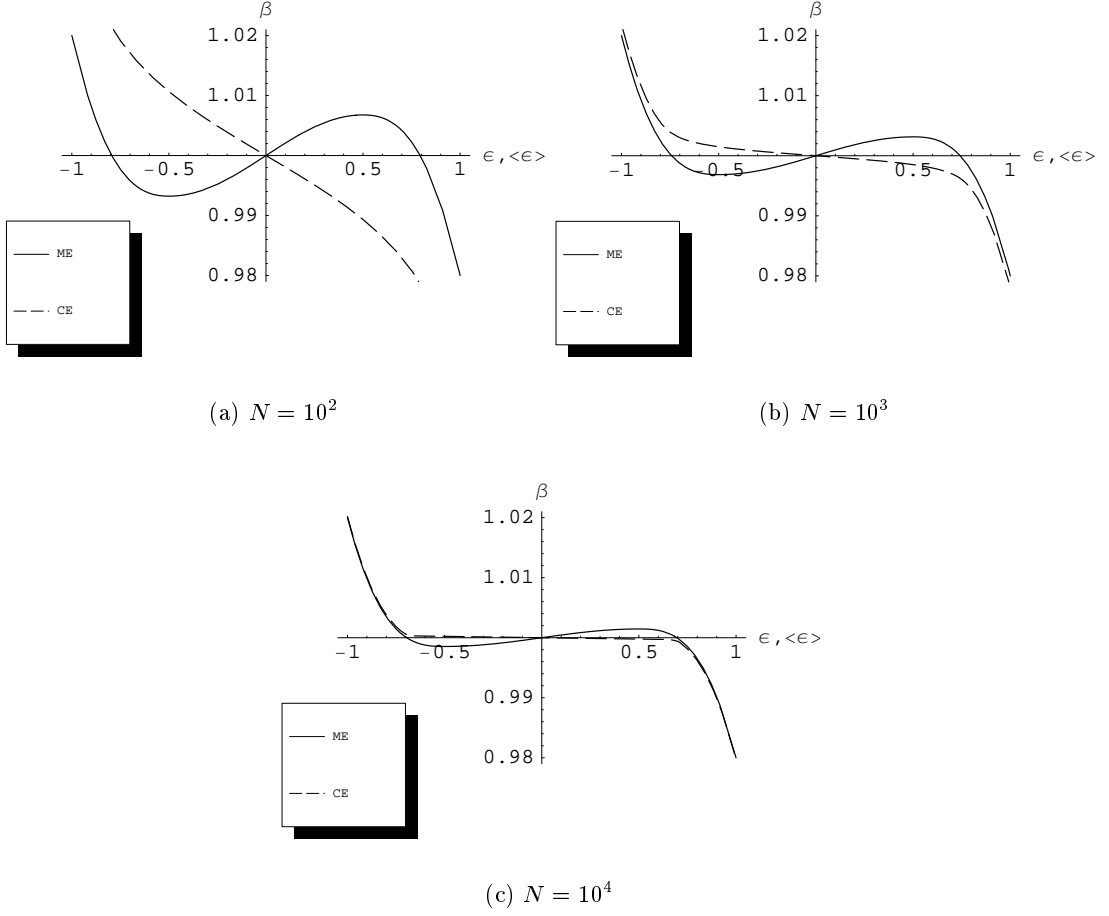


Figure 2.4: Inverse temperature as a function of  $\epsilon$  (ME; plain lines) and  $\langle\epsilon\rangle$  (CE; dashed lines) and  $N$  for the model  $s_1$  (see eq. (1.20) or footnote (b) on page 19).  $\beta_{ME}(\epsilon, N) \doteq \frac{\partial s_1}{\partial \epsilon} = -0.16(|\epsilon| - 0.5)^3 + 0.01\pi N^{-1/3} \sin(\pi\epsilon)$ . For finite  $N$ ,  $\frac{\partial \beta_{ME}}{\partial \epsilon} > 0$  for  $\epsilon \in ]-0.5, 0.5[$ , whereas  $\frac{\partial \beta_{CE}}{\partial \langle\epsilon\rangle} < 0$  for any  $\langle\epsilon\rangle$ . With increasing  $N$  the differences between both inverse temperatures vanish. However, in the limit  $N \rightarrow +\infty$ ,  $\beta_{CE}$  is not defined for  $\langle\epsilon\rangle \in ]-0.5, 0[ \cup ]0, 0.5[$  in contrast to  $\beta_{ME}$  which is defined for all  $\epsilon$ . The discontinuity of  $\langle\epsilon\rangle$  ( $\beta_{CE}$ ) leads to the conventional signal of a first order phase transition.

thermostatistics [RUE69, CAL85, LL94, LY52A].

In fig. 2.4 the inverse temperature curves for the same entropy-model  $s_1$  are plotted versus  $\epsilon$  (microcanonical  $\beta \equiv \beta_{ME}$ ) and  $\langle\epsilon\rangle$  (canonical  $\beta \equiv \beta_{CE}$ ) for different  $N$ . For all  $N$ ,  $\beta_{ME}$  and  $\beta_{CE}$  are clearly different in the energy range  $[-0.5, 0.5]$  where the microcanonical specific heat capacity is negative. Close to these regions even though  $\lambda_1 < 0$ , ME and CE are also not equivalent because of the presence of a second peak in their respective canonical distribution functions (see fig. 2.3). For small systems, a phase transition in ME implies the non-equivalence between the ensemble, while the non-equivalence does not lead to a phase transition (in ME). With increasing  $N$ , these non-equivalence regions with  $\lambda_1 < 0$  shrinks to the transition region if the surface effects vanishes. For increasing  $N$ , both the microcanonical and the canonical specific heat capacity increases at  $\beta = \beta_t$  to

eventually diverge at the limit  $N \rightarrow \infty$ . Again, this signals a first order phase transition.

The previous examples enlighten the fact that the singularity signaling a first order phases transition at the thermodynamical limit has its origins in an anomalous curvature of  $S$ , i.e.  $\lambda_1 > 0$ . The converse statement is not necessarily true, i.e. a negative curvature at a given finite  $N$  does not imply a phase transition at the limit  $N \rightarrow \infty$ , indeed nothing forbids the sign of  $\lambda_1$  to be also a function of  $N$  at fixed  $\frac{X_0}{N}$ .

**Definition 4.** *A microcanonical ensemble of states is in a first order phase transition at  $X = X_0$  if  $\lambda_1(X_0) > 0$ .*

The eigenvalue  $\mathbf{v}_1$  associated with  $\lambda_1$  gives the direction of the largest negative curvature. In simple models when one follows the trajectory given by  $\mathbf{v}_1$ <sup>f</sup>, one reaches the two extrema (pure phases) which have the same  $x_0$  than the one at  $X_0$ . Therefore,  $\mathbf{v}_1$  gives the direction of the *local order parameter* (see below and also [GRO01]).

**Definition 5.** *The direction of the local order parameter of a first order phase transition is given by  $\mathbf{v}_1$ .*

Note that, for a multidimensional  $X$ , there might be many positive eigenvalues (say from  $i = 1, \dots, k$ ), this means that there are several first order phase transitions. A basis for the order parameters is simply given by the set  $\{\mathbf{v}_1, \dots, \mathbf{v}_k\}$ .

There is an important point to add. From the fig. 2.3 on page 20 one sees that the information contained in the region where  $\lambda_1 > 0$  are overridden by the ones coming from the dominant peak (see also footnote (e) on page 20). Information contained in the convex part of  $S$  is smeared out in CE [HÜL94A]. Formally no information is lost since one can always perform a inverse Laplace transform (when of course the equivalence condition (0)<sup>g</sup> is fulfilled). But this inverse transform is in practice so unstable that this information is actually *lost* in CE [CH88].

So far, only models with simple topological entropy-surfaces have been studied. For these models a first order transition region always led to two local maxima in  $f$  connected by the curve of constant control parameter (as defined in footnote (f)). However, a priori, more complicated cases (i.e. with more than two maxima) are not excluded (see for a “three-peaks” system [GRO01]).

## 2.2.2 Example

In fig. 2.5 on the facing page,  $\exp \left\{ f(X, X_0) \right\} \propto P(X, X_0)$  is plotted for the van der Waals entropy-model.  $X_0 = (\epsilon_0, v_0) = (0.94, 1)$  has been chosen in the region where  $\lambda_1 > 0$ . At  $(\epsilon_0, v_0)$ ,  $f$  has a saddle point because the second eigenvector  $\lambda_2$  is negative. One sees also, just like for the one dimensional model in fig. 2.3, that  $f$  has two maxima in the pure phase region. One corresponds to the liquid phase (small  $\epsilon$  and  $v$ ) and the other to the gas phase. By construction, their temperature and pressure are the same than the ones at  $X_0$ .

The fig. 2.6 on page 24 is the same as fig. 2.5 plus the vector field  $\mathbf{v}_1$ , and the line of constant control parameter that goes through  $X_0 = (\epsilon_0, v_0)$  as defined in footnote (f). It

<sup>f</sup>It is the line solution of the following differential equation

$$\dot{X}(t) = \mathbf{v}_1(X(t)), \quad (2.1)$$

with  $X(t=0) = X_0$  and  $t \in ]-\infty, +\infty[$  is a parameter. This line can be labeled by a *control parameter*.

<sup>g</sup>Finite partition function, see page 11.

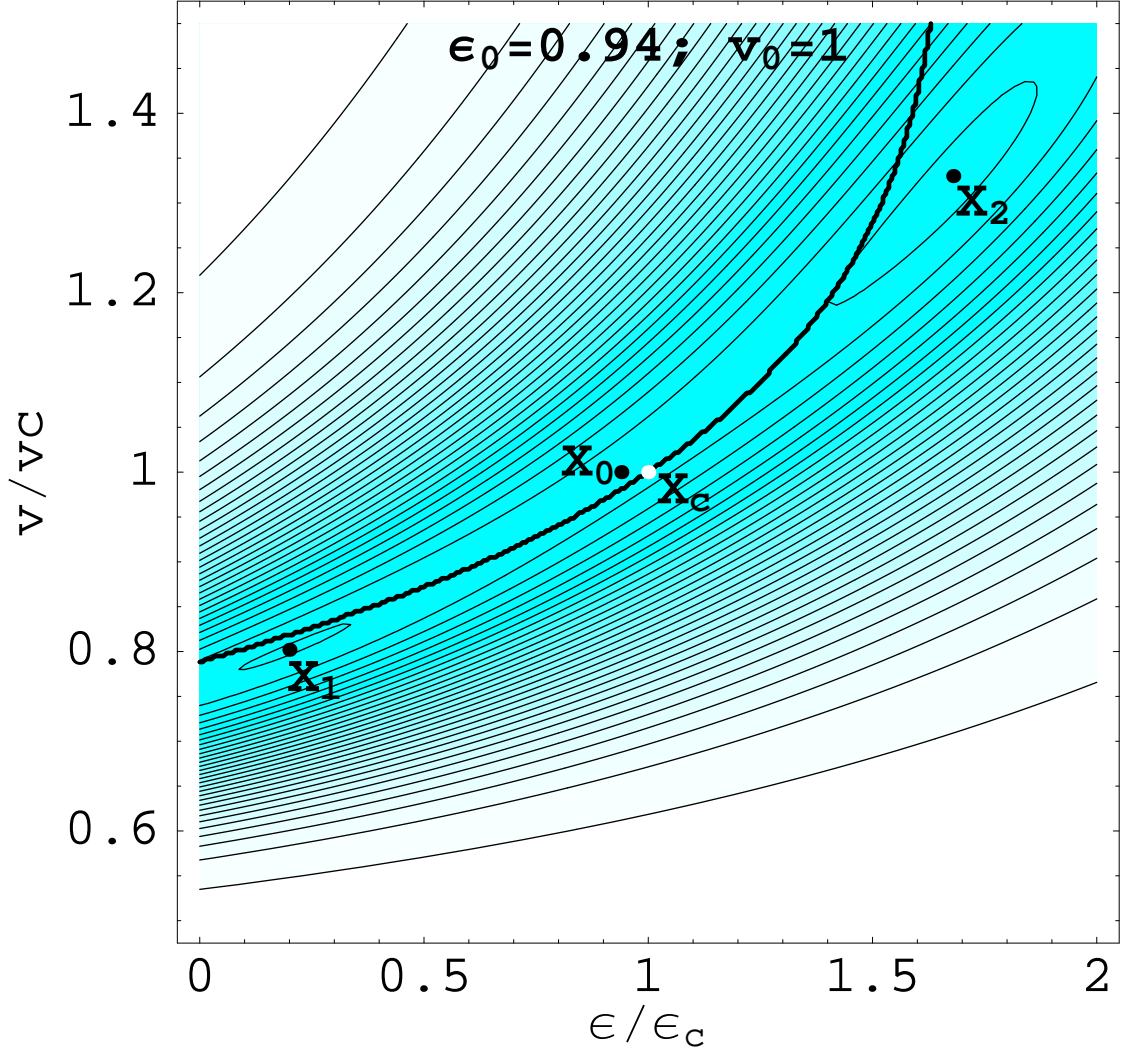


Figure 2.5: Contour-Density plot of  $f(X, X_0) = -x_0 \cdot X + s(X)$  for the van der Waals entropy-model at  $X_0 = (\epsilon_0, v_0) = (0.94, 1)$ , where  $x_0 = \frac{\partial s}{\partial X}|_{X_0}$ . The thick line corresponds to  $\lambda_1 = 0$ . Below (above) it,  $\lambda_1$  is negative (positive), hence  $\lambda_1(X_0) > 0$ .  $f$  has two local maxima one at  $X_1 \approx (1.68, 1.32)$  and another at  $X_2 \approx (0.2, 0.8)$  which correspond to two pure phases peak ( $\lambda_1(X_{1,2}) < 0$ ).  $f$  has a saddle point at  $X_0 = (\epsilon_0, v_0)$  ( $\lambda_1(X_0) > 0$  and  $\lambda_2(X_0) < 0$ ). By construction,  $\frac{\partial s}{\partial X}|_{X_1} = \frac{\partial s}{\partial X}|_{X_2} = \frac{\partial s}{\partial X}|_{X_0} = x_0$ . In CE the main contributions to the partition function  $\mathcal{Z}(x_0)$  comes from the two peaks  $X_1$  and  $X_2$ , and the information from  $X_0$  is in practice lost. The white dot locates the critical point  $X_c$ .

nicely illustrates the definitions of the order and control parameters. If one follows the curve tangent to  $\mathbf{v}_1$  starting from  $X_0$  (gray line in fig. 2.6), one eventually reaches the gas or liquid extrema (labeled by  $X_1$  and  $X_2$ ). Along this gray line  $f$  has an extremum<sup>h</sup> in the  $\mathbf{v}_2$  direction, in a symbolic formulation

$$\nabla f \cdot \mathbf{v}_1 = 0. \quad (2.2)$$

<sup>h</sup>Here it is an maximum since  $\lambda_2 < 0$ .

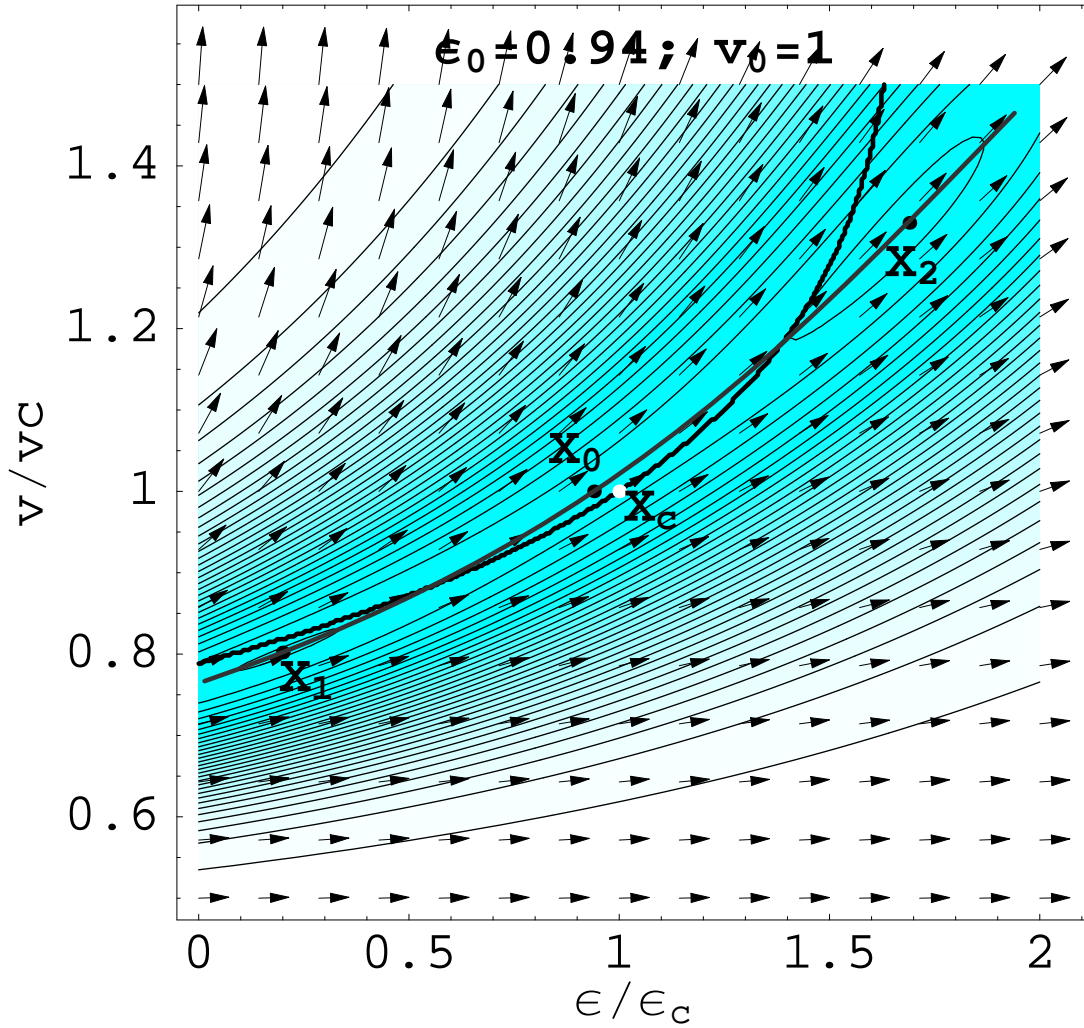


Figure 2.6: Contour-Density plot of  $f(X, X_0) = -x_0 \cdot X + s(X)$  for the vdW entropy-model at  $X_0 = (\epsilon_0, v_0) = (0.94, 1)$ , where  $x_0 = \frac{\partial S}{\partial X}|_{X_0}$ , plus the vector field  $\mathbf{v}_1$  and the line of constant control parameter (as defined in footnote (f) on page 22) that goes through  $X_0$  (gray line; see fig. 2.7). As one can see this line goes also through the two maxima  $X_1$  and  $X_2$ . At the maxima, by construction the values of the inverse temperature and pressure are equal to  $x_0$  (which are defined at  $X_0$ ). The thick line corresponds to  $\lambda_1 = 0$ , below (above) it  $\lambda_1$  is negative (positive). The critical point  $X_c$  is located by a white dot.

In fig. 2.7 on the next page, the parametric lines  $(\epsilon(t), \alpha_\beta(t))$  and  $(\epsilon(t), \alpha_p(t))$  along the constant control parameter line in fig. 2.6 are shown, where

$$\alpha_\beta(t) \doteq \frac{|\beta(t) - \beta(X_0)|}{\beta(X_0)}, \quad (2.3)$$

$$\alpha_p(t) \doteq \frac{|p(t) - p(X_0)|}{p(X_0)}, \quad (2.4)$$

and  $t$  is the “time” parameter as defined in footnote (f) on page 22. This figure shows that the gray line goes indeed through the two local maxima in the pure phase regions.

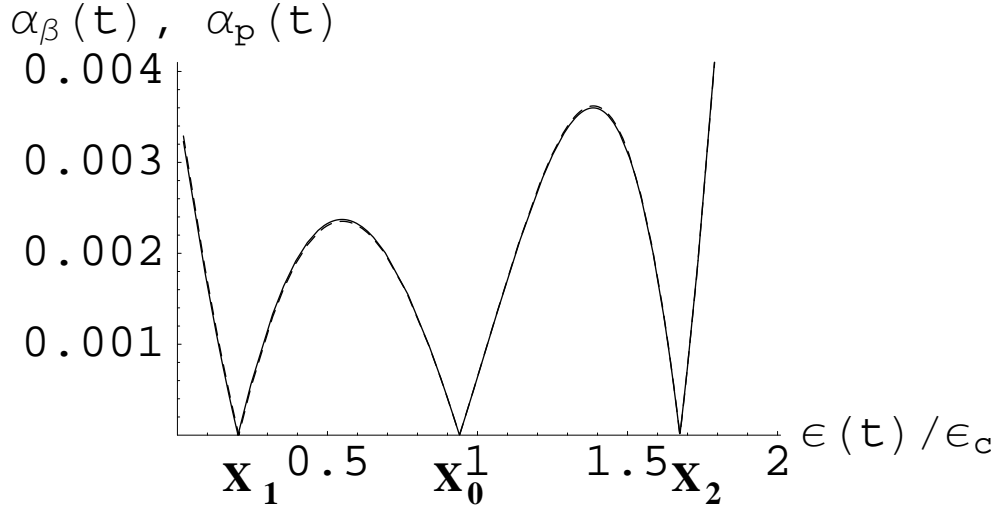


Figure 2.7: Parametric plots  $(\epsilon(t), \alpha_\beta(t))$  (dashed line) and  $(\epsilon(t), \alpha_p(t))$  (plain line) along the constant control parameter line (as defined in footnote (f) on page 22) with  $X_0 = (\epsilon_0, v_0) = (0.94, 1)$  (gray line in fig. 2.6).  $\alpha_\beta$  and  $\alpha_p$  are the relative difference between resp.  $\beta_0$  and  $p_0$  as a function of  $t$  where  $(\beta_0, \beta_0 p_0) = x_0 = \frac{\partial S}{\partial X}|_{X_0}$  (see eqs. (2.3) and (2.4)).  $\alpha_p(t) = \alpha_\beta(t) = 0$ , for  $t$  such that  $X(t)$  is equal to  $X_0, X_1$  or  $X_2$ .

The two equations  $\alpha_\beta(t) = 0$  and  $\alpha_p(t) = 0$  shares the same three solutions,  $t_0, t_1$  and  $t_2$  which correspond time to  $X(t_i) = X_i, i = 0, 1$  and  $2$ .

In fig. 2.8 on the following page, the vector field  $\mathbf{v}_1$  for the van der Waals model is plotted along with the sign of  $\lambda_1$  and with the contour plots of the inverse temperature  $\beta$  and of  $\beta p$ . I.e.  $\beta$  and  $\beta p$  are constants along their respective contour lines. The lines  $\beta p = cst$  are almost <sup>i</sup> tangent to  $\mathbf{v}_1$ . Hence,  $\beta p$  is at a good approximation a control parameter.

Although it is hardly to be seen on fig. 2.8, due to the scale and to the orientation of the axes, the lines of constant  $\beta$  and the one of constant  $\beta p$  cross each other one or three times (as checked in fig. 2.7). In the latter case one crossing is located in the  $\lambda_1 > 0$  region.

Another point worth to be noticed, is that at  $\lambda_1 = 0$ , the lines of constant  $\beta$  and constant  $\beta p$  are parallel to each other and also to  $\mathbf{v}_1$ , i.e.

$$\nabla \beta \wedge \nabla \beta p = 0, \quad (2.5a)$$

and

$$\nabla \beta \cdot \mathbf{v}_1 = 0. \quad (2.5b)$$

This is easy to understand since

$$\nabla \beta = \nabla \left( \frac{\partial s}{\partial \epsilon} \right) = \left( \begin{array}{c} \frac{\partial^2 s}{\partial \epsilon^2} \\ \frac{\partial^2 s}{\partial v \partial \epsilon} \end{array} \right) \quad (2.6a)$$

<sup>i</sup>The angle  $\theta$  between  $\mathbf{v}_1$  and  $\nabla \beta p$  is  $\pi/2$  along the line  $\lambda_1 = 0$ , elsewhere in the parametric range used on fig. 2.8 the absolute difference  $|\theta - \pi/2|$  is of the order of  $10^{-9}$ .

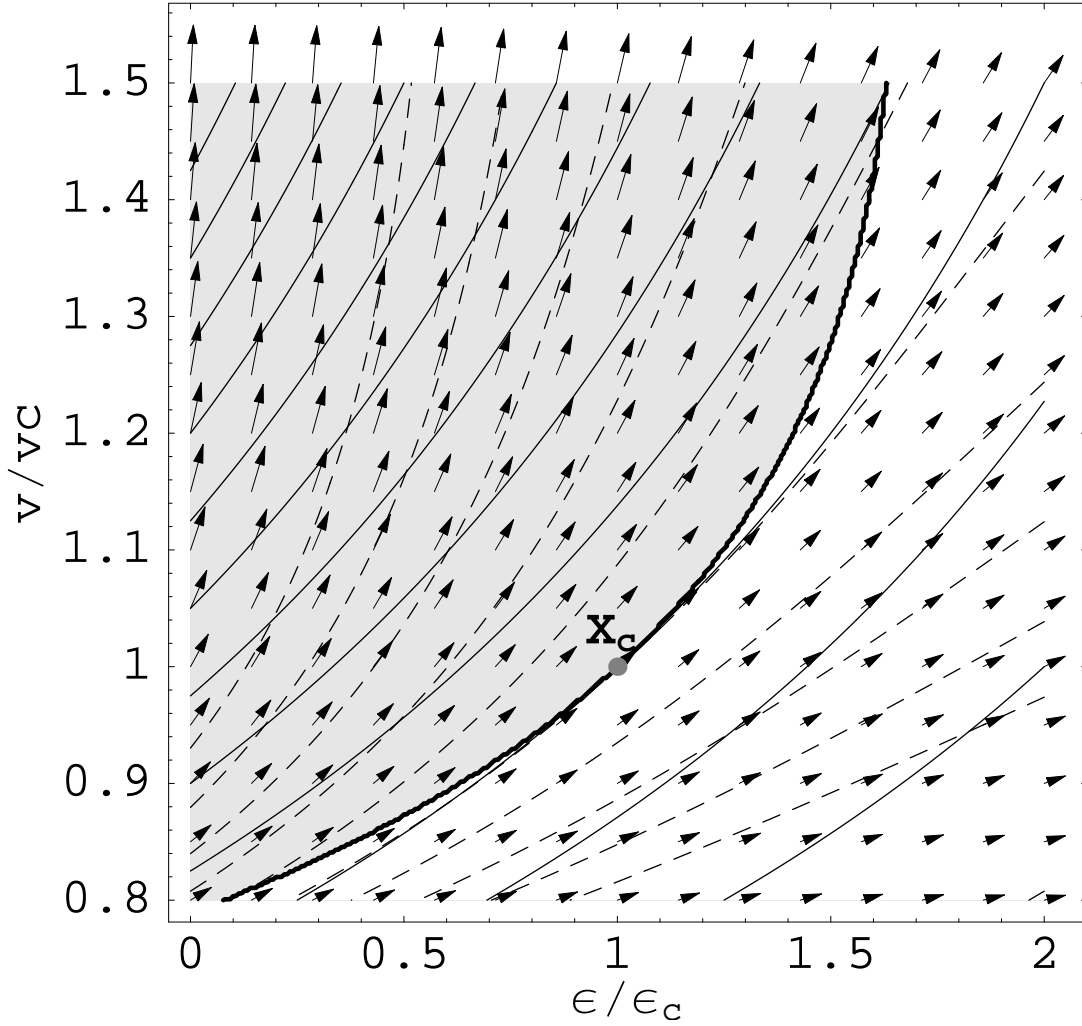


Figure 2.8: vdW entropy-model. Vector field  $\mathbf{v}_1$ ; Contour-plot  $\beta = cst$  and  $\beta p = cst$  solid and dashed lines, respectively. Sign of  $\lambda_1$ : gray shaded region  $\lambda_1 > 0$  (first order phase transition), white region  $\lambda_1 < 0$  (pure phase). The dot at  $(\epsilon, v) = (1, 1)$  locates the critical point of the first order phase transition of the vdW entropy-model. The vectors  $\mathbf{v}_1$  are almost tangent to the lines  $\beta p = cst$ , i.e. at a good approximation  $\beta p$  is the control parameter of this first order phase transition.

and

$$\nabla \beta p = \nabla \left( \frac{\partial S}{\partial v} \right) = \begin{pmatrix} \frac{\partial^2 S}{\partial \epsilon \partial v} \\ \frac{\partial^2 S}{\partial v^2} \end{pmatrix} \quad (2.6b)$$

which are the columns of  $H_S$ , the Hessian matrix of  $S$  in the coordinates  $(\epsilon, v)$ . Now, the fact that  $\lambda_1 = 0$  implies that these columns are linear combinations of the eigenvectors whose eigenvalues are not zero. Thus, the columns are linearly dependent. Therefore, and as the dimension of the parametric space is two,  $\nabla \beta \propto \nabla \beta p \propto \mathbf{v}_2 \perp \mathbf{v}_1$ . The latter relations lead to eqs. 2.5a. In other words, at  $\lambda_1 = 0$  the constant intensive parameters lines are all parallel to each other and to  $\mathbf{v}_1$ .

In fig. 2.8 one can also notice that the lines of constant intensive parameters are tangent to the line  $\lambda_1 = 0$  at the critical point  $X_c$ . This is discussed further in sec. 2.3.

The eqs. (2.5) can trivially be extended for  $\mathcal{M} > 2$ . The gradients of  $x = \{x_1, \dots, x_{\mathcal{M}}\}$  are linear combinations of the eigenvectors whose eigenvalues are non null. Therefore, if e.g.  $\lambda_1 = 0$  then  $\{\nabla x_1, \dots, \nabla x_{\mathcal{M}}\}$  is a set of linearly dependant vectors which are all orthogonal to  $\mathbf{v}_1$ .

### 2.2.3 Transition parameters

In classical thermodynamics one characterizes first order phase transitions by some couples of quantities, the transition parameters, e.g. transition temperature  $T_t \doteq \frac{1}{\beta_t}$ , latent heat  $q_{lat}$ , surface tension  $\gamma$ , etc.

These parameters are well defined for infinite systems. However, for small ones they hardly make sense. As one can see on figs. 2.4 on page 21, there is no temperature at which the transition take place, but on the contrary, the transition occurs (in ME sense) within a certain *range* of temperatures. Of course, at the thermodynamical limit, if it exists, this range shrinks to one point and the usual definition of the transition temperature is recovered. As the other transition parameters rely on the value of  $T_t$ , they are in their turn not unambiguously defined for small systems. For the surface tension  $\gamma$ , the difficulties are even greater since it is almost impossible to define surface areas for small systems. Indeed, in macroscopic systems the interphase is a two dimensional object only at a first approximation. The density of the liquid does not abruptly change from its liquid value to its vapor one; it decreases smoothly over a length of the order of the particle interaction range. Hence, for a small system, whose size is of the order of the interaction range, the definition surfaces are rarely unambiguous (an exception is e.g. spin systems [GEZ96]). E.g. for the liquid–gas transition of metallic clusters how to define a gas part, a liquid part, and a surface area between them when the system is composed of a few thousands of atoms?

Again all these parameters are defined in the limit  $N \rightarrow \infty$ . Nevertheless, it could be useful to have some “finite–size” definitions (though ambiguous and inaccurate) in order to make the bridge to their thermodynamical limit ones. I.e. definitions that converge to the usual ones at the limit  $N \rightarrow \infty$ . This can be useful to perform some finite–size scaling as done in sec. 3.4.

$\mathcal{M} = 1$

A convex intruder in the specific entropy curve  $s(\epsilon)$  is forbidden for infinite systems, because there the system gains entropy if it would divide itself into two pieces one with specific energy  $\epsilon = \epsilon_1$  and the other with  $\epsilon = \epsilon_3$  see fig. 2.9(a) on the next page. Both pieces together would have a larger entropy  $s_{hull}(\epsilon) = \alpha_1 s(\epsilon_1) + \alpha_3 s(\epsilon_3) \geq s(\epsilon = \alpha_1 \epsilon_1 + \alpha_3 \epsilon_3)$ , where  $\alpha_1 = \frac{\epsilon - \epsilon_3}{\epsilon_1 - \epsilon_3}$ ,  $\alpha_3 = \frac{\epsilon_1 - \epsilon}{\epsilon_1 - \epsilon_3}$  and  $\alpha_1 + \alpha_3 = 1$  are the relative sizes of the two parts<sup>j</sup> [CAL85, HÜL94B]. Then, the slope of  $s_{hull}$  gives the transition temperature  $\beta_t$ . An equivalent approach is to make the Maxwell construction (see fig. 2.9(b); there  $\beta_t = 1$ ). The latent heat  $q_{lat}$  is simply given by  $q_{lat} = \epsilon_3 - \epsilon_1$ , i.e. by the length of the Maxwell construction segment. By construction, in fig. 2.9(b) the shaded area on the left side below  $\beta_{tr}$  is equal to the one on the right side above  $\beta_t$  and also to  $s_{hull}(\epsilon_2) - s(\epsilon_2) \doteq \Delta s_{surf} \equiv \Delta s$  the surface entropy, see also fig. 2.9(a).

<sup>j</sup>It is implicitly assumed that the surface effects can be neglected [GRO01, GRO00B].

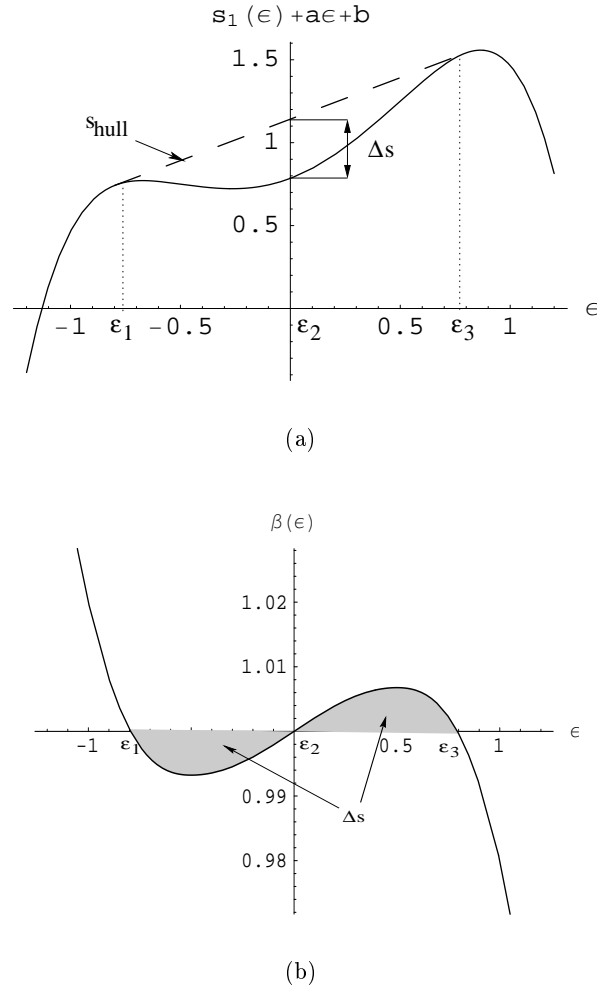


Figure 2.9: Determination of the transition parameters for the entropy-model  $s_1$  (as defined in sec. 1.4.1, eq. (1.20)),  $N = 100$ . At a first order phase transition, the specific entropy has a convex intruder (panel (a); for conveniency a linear function of  $\epsilon$  is added to  $s_1$ ,  $a = -0.5$ ,  $b = 1$ ). For short-range interaction systems, this intruder is forbidden by van Hove's theorem [vH49] in the limit  $N \rightarrow +\infty$ . Indeed, those systems would gain entropy by splitting up into two parts, one at specific energy  $\epsilon_1$  and the other at  $\epsilon_3$  (the resulting entropy is  $s_{hull}$  in panel (a)). For finite system,  $\frac{\partial s_{hull}}{\partial \epsilon} \doteq \beta_t$  defines the transition temperature  $T_t = \beta_t^{-1}$ . This temperature is also the one given by the Maxwell construction (panel (b)). The latent heat can be defined as  $\epsilon_3 - \epsilon_1$ , the length of the Maxwell segment, or alternatively, as  $0.5 - (-0.5) = 1$ , the length of the negative specific heat capacity region (see text). At  $\epsilon_2$ ,  $\Delta s = s_{hull} - s_1$ , the entropy-loss induced by the surface correlations is by construction equal to the areas between the Maxwell line and the lobes of the  $\beta$  curve (gray shaded areas in panel (b)).

The intra-phase surface  $\gamma$  tension is related to  $\Delta s_{surf}$  by

$$\gamma = \nabla s_{surf} T_t \frac{N}{\mathcal{A}}, \quad (2.7)$$

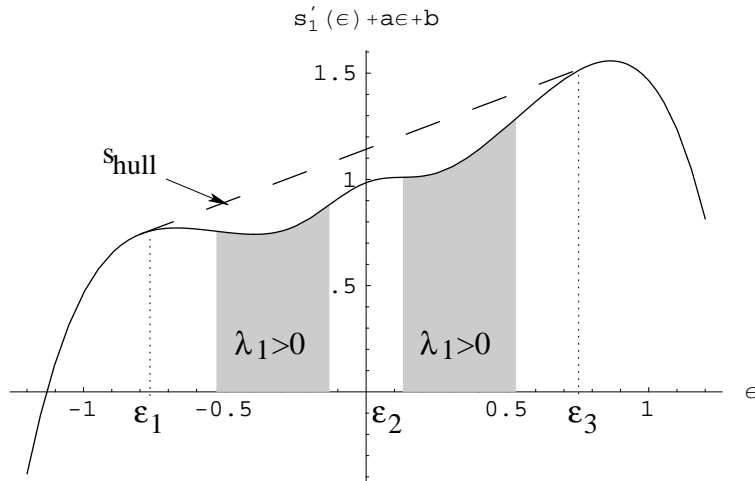


Figure 2.10: Specific entropy  $s'_1(\epsilon) = s_1(\epsilon) + \frac{1}{5} \exp(-20\epsilon^2)$  ( $a = -0.5$ ,  $b = 1$ ); for  $|\epsilon| \gtrsim 0.5$   $s'_1(\epsilon) \approx s_1(\epsilon)$ . If one uses the convex hull  $s_{hull}$  ( $\sim$  Maxwell line) to define first order phase transitions ( $\sim$  canonical definition), one would conclude that there is *one* first order phase transition between  $\epsilon_1$  and  $\epsilon_3$  (just like for  $s_1$ , see fig. 2.9(a)). However, in the microcanonical sense there are *two* phase transition regions for  $|\epsilon| \in ]0.13, 0.53[$  ( $\lambda_1(\epsilon) > 0$ ). This is an illustration of the deeper insight that gives ME compared to CE into small systems phase transitions. Moreover, it shows also how ambiguous can be the definition of transition parameters based on the Maxwell construction.

where  $\mathcal{A}$  is the surface area.

As an approximation, one can use these definitions for small systems with  $\mathcal{M} = 1$ . However, as already mentioned they are ambiguous and should be used with caution. As an example, one can realize that these definitions consider everything below the Maxwell line as being a mixture of two pure phases (the ones at the end points of this line). But a priori, there is no reason that forbids the presence of another pure phase below this line, i.e. a region characterized by  $\lambda_1 > 0$  but whose entropy is smaller than  $s_{hull}$  (see for an illustration fig. 2.10). In this sense, the surface entropy and the other usual macroscopic transition parameters are *global* properties of  $s$ , because at one point  $X = X_0$ ,  $\Delta s$  depends on the values taken by  $s$  on the *whole* parameter space.

An alternative definition for the latent heat is the length of the energy region over which the specific heat capacity is negative (in fig. 2.9 on the preceding page,  $q_{lat} = 0.5 - (-0.5) = 1 < \epsilon_3 - \epsilon_1$ ). At the thermodynamical limit, the two definitions for  $q_{lat}$  are equivalent.

$\mathcal{M} > 1$

For these systems there is so far no equivalent of the Maxwell construction. The simplest solution is to reduce the problem to a one dimensional one by considering only the lines at constant control parameter (gray line in fig. 2.6). This allows to have  $s$  as a function of a unique parameter order and to use the machinery developed for  $\mathcal{M} = 1$ .

Again, the parameters obtained are ambiguous and global. One should use them only to make the bridge to their infinite system values.

## 2.3 Second order phase transitions

### 2.3.1 Definition

At a second order phase transition the surface tension between the phases vanishes. Two (or more) phases coexist without any entropy loss. E.g. for  $\mathcal{M} = 1$  when the two peaks in  $P(E)$  at  $\beta_t$  are infinitely close from each other leading to macroscopic fluctuation of  $\epsilon$  in CE. But, in contrast with a first order phase transition,  $\langle \epsilon \rangle$  is still a continuous function of  $\beta$  at a critical point. In one dimension, these transitions are characterized by  $\frac{\partial \beta}{\partial \epsilon} = \frac{\partial^2 s}{\partial \epsilon^2} = 0$  and  $\frac{\partial^2 \beta}{\partial \epsilon^2} = \frac{\partial^3 s}{\partial \epsilon^3} = 0$ . Taking as an example the van der Waals entropy-model, one can see in fig. 2.11 how the two peaks merges when one approaches the critical point from the first order phase transition region. In a multidimensional parameter-space the above mentioned criteria for 1-D systems can be extended as: first  $\lambda_1 = 0$  and second  $\boldsymbol{\alpha} \cdot \nabla \lambda_1 = 0$ , where  $\nabla \lambda_1$  is the gradient of  $\lambda_1$  and  $\boldsymbol{\alpha}$  is a yet unknown vector that gives simply the direction along which  $\lambda_1$  is flat up to the first order approximation ( $\sim$ vanishing third derivative of  $S$ ). From the infinite systems and from the fact that often second order transitions are end-points of first order ones it can be inferred that this derivatives vanishes along the order parameter [LL94], i.e.  $\mathbf{v}_1$ . Hence, the second criteria is  $\mathbf{v}_1 \cdot \nabla \lambda_1 = 0$  [GV99, GRO01].

**Definition 6.** *A microcanonical ensemble of states is in a second order phase transition at  $X = X_0$  if  $\lambda_1(X_0) = 0$  and  $\mathbf{v}_1(X_0) \cdot \nabla \lambda_1(X_0) = 0$ .*

The first eigenvalue  $\lambda_1$  may not be the only one to fulfill the condition given in def. 6, i.e.  $\lambda_i(X_0) = 0$  and  $\mathbf{v}_i(X_0) \cdot \nabla \lambda_i(X_0) = 0$  for  $i = 1, \dots, k \leq \mathcal{M}$ , in this case  $X_0$  is called a *multicritical* point.

For a system depending on two “extensive” parameters ( $\mathcal{M} = 2$ ), it is shown in sec. 2.2.2 that, where  $\lambda_1 = 0$ , the lines of constant intensive parameters are parallel to each other and to  $\mathbf{v}_1$ . The second criterium in def. 6 implies that the line of constant intensive parameters are parallel to the line  $\lambda_1 = 0$  (as already notices in the previous section).

This equivalent condition for second order phase transition can also be straightforwardly generalized for  $\mathcal{M} > 2$ . At a critical point the lines of constant intensive parameters are orthogonal to  $\mathbf{v}_1$  where  $\lambda_1 = 0$ .

### 2.3.2 Example

Fig. 2.11(a)–(c) show how for the vdW entropy-model the two pure phases peaks merge when  $X_0 \rightarrow X_c$  where  $\lambda_1(X_0) > 0$ . Fig. 2.11(c) illustrates the fact the derivative of  $\lambda_1$  along  $\mathbf{v}_1$  vanishes.  $f(X, X_c) = -\frac{\partial s}{\partial X}|_{X_c} + s(X)$  is a flat function (at least up to the third order) along  $\mathbf{v}_1$  at  $X_c$ , i.e. the contours close to the value  $f(X_c)$  are at first approximation, ellipses whose larger axes are roughly parallel to  $\mathbf{v}_1(X_c)$  and with large ratios of the major axes length to the minor’s one.

In fig. 2.12 on page 32 the two criteria given in def. 6 are plotted for the van der Waals model. The thin line corresponds to  $\lambda_1 = 0$  and the thick one to  $\mathbf{v}_1 \cdot \nabla \lambda_1 = 0$ . These two lines cross each other at the already known critical point  $X_c = (\epsilon = \epsilon_c, v = v_c)$ . There is no other point in the parameter space  $(\epsilon, v)$  satisfying the conditions for a critical point given in def. 6.

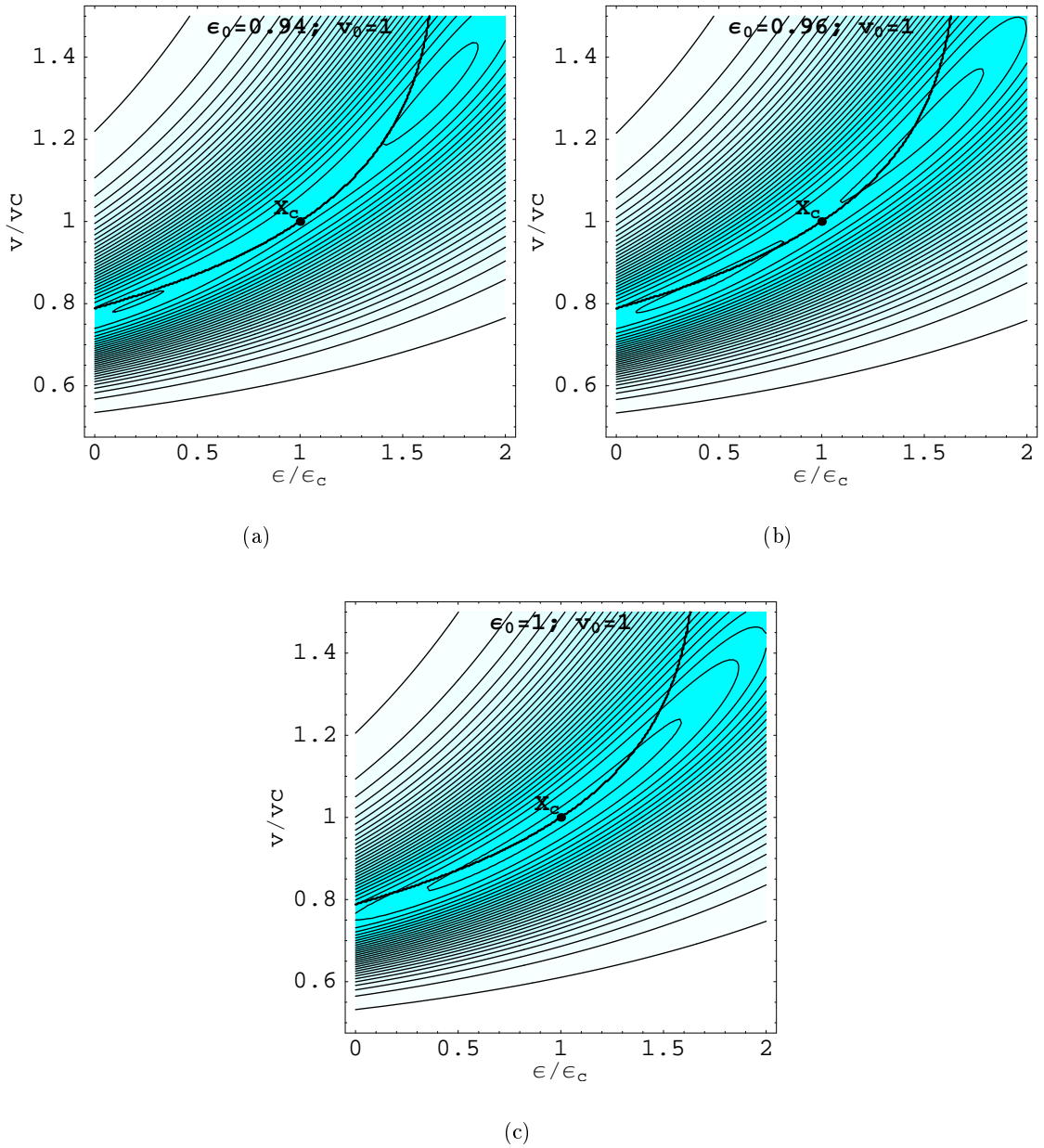


Figure 2.11: Contour density plot of  $f(\epsilon_0, v_0 = 1) = -x_0 \cdot X + s(X)$  for the vdW entropy-model, where  $x_0 = \frac{\partial S}{\partial X}|_{(\epsilon_0, v_0=1)}$  and for different values of  $\epsilon_0$ , when  $\epsilon_0 \rightarrow 1^-$ . The thick line locates  $\lambda_1 = 0$ . Below (above) this line  $\lambda_1$  is negative (positive). For  $v_0 = 1$  and  $\epsilon_0 < 1$ ,  $\lambda_1$  is positive.  $\lambda_1 > 0$  defines a first order phase transition region. There  $f$  ( $\sim$  minus the canonical free-energy) has two maxima in the pure phase regions (panels (a) and (b)). At the limit  $\epsilon_0 \rightarrow 1$ , these two maxima merge giving raise to a second order phase transition (see text).

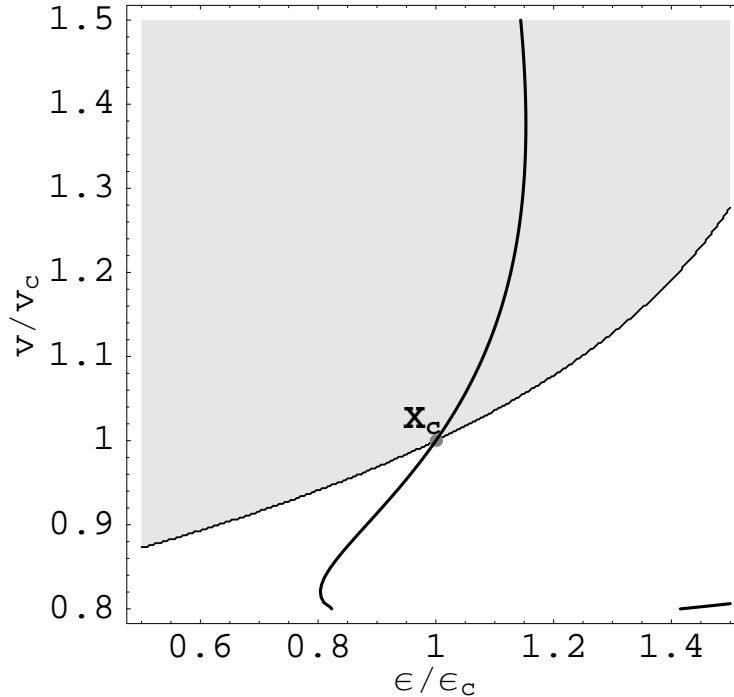


Figure 2.12: Criteria in def. 6 for second order phase transition applied to the vdW entropy-model. The thin and the thick lines correspond to  $\lambda_1 = 0$  and  $\mathbf{v}_1 \cdot \nabla \lambda_1 = 0$ , respectively. These two lines cross each other at the already known critical point at  $X_c = (\epsilon/\epsilon_c, v/v_c) = (1, 1)$  (gray dot). In the gray (white) region  $\lambda_1 > 0$  ( $< 0$ ).

## 2.4 Single event as a signal for phase transition?

Consider as an example, the study of the liquid–gas phase transition of metallic clusters (this transition is studied in part II). At very low energy all atoms are bounded in one big cluster (liquid phase). At higher energies the system enters the phase transition at an energy, say  $E = E_e$ , and starts to evaporate some monomers. Now, from a microcanonical experiment, where the energy  $E_1$  is fixed but *unknown*, an event is randomly singled out. Its mass distribution  $\mu_1$  is simply a big cluster and one monomer. The question is whether this event, characterized by  $\mu_1$ , signals the beginning (with increasing energy) of the phase transition. In other words, does  $\mu_1$  imply  $E_1 = E_e$ ?

As defined in the previous sections, phases and phase transitions are linked to the local properties of the microcanonical entropy surface. In its turn, the entropy is a property of an *ensemble* of states via Boltzmann’s principle. Therefore, phases and phase transitions are properties of an *ensemble* of states and not of a *single* event.

Again, in other words, in a small system, a single event *cannot* be the signal of a phase transition. At most, one can single out from the ensemble an event that would characterize it by means of some most probable or average values of observables. E.g. at  $E = E_e$  events with  $\mu = \mu_1$  are the most probable ones. The inverse proposition is not necessarily true since the values of the observables can fluctuate (pretty much like the energy fluctuates in CE for small systems). For example, an ensemble may contain events with  $\mu_1$  though the energy of this ensemble is very different from  $E_e$ . Of course, in

general, the probability for a single event to have  $\mu = \mu_1$  decreases as  $|E - E_e|$  increases. At the thermodynamical limit this probability becomes so small that the measurement of an event with  $\mu = \mu_1$  at  $E_1 \neq E_e$  may be regarded as practically impossible (to paraphrase Maxwell's own words [MAX]). Hence, at this limit the one-to-one mapping is recovered  $\mu = \mu_1 \Leftrightarrow E = E_e$ .

## 2.5 Alternative theories

In this section two alternative frameworks for the thermostatics of small (or more generally non-extensive) systems are briefly reviewed. They are also compared with the theory presented in the previous sections. The first one tackles the problem of the lack of usual signals of phase transitions (Yang-Lee divergences) in CE by seeking their roots in the finite size partition function  $\mathcal{Z}$ . The other is based on an extension (generalization) of Boltzmann's principle by redefining the entropy  $S$ . Most of the introduction materials are taken directly from the respective literatures ([BMH00] for section 2.5.1 and [TSA99] for section 2.5.2).

### 2.5.1 Distribution of zeros

#### Classification of phase transitions

At the thermodynamical limit Lee and Yang [LY52A], Grossmann & al. [GL69] and Fisher [FIS65] showed that a classification of the phase transitions is made possible by studying the properties of the distribution of zeros (DOZ) of the partition function  $\mathcal{Z}(\mathcal{B})$  on the complex temperature plane ( $\mathcal{B} = \beta + i\tau$ ). The DOZ is on one (or many) dense line(s). This line crosses the real axis at the transition temperature and the angle made by this line with the real axis gives the order of the phase transition.

For finite size systems the DOZ is discrete and there is no zero on the real axis. The partition sum can be written as a function of its zeros  $\mathcal{B}_k = \mathcal{B}_{-k}^* = \beta_k + i\tau_k$  ( $k \in \mathbb{N}$ )

$$\begin{aligned} \mathcal{Z}(\mathcal{B}) &= \mathcal{Z}_{lim}(\beta) \mathcal{Z}_{int}(0) \exp(\mathcal{B} \partial_{\mathcal{B}} \mathcal{Z}_{int}(0)) \\ &\times \prod_{k \in \mathbb{N}} \left(1 - \frac{\mathcal{B}}{\mathcal{B}_k}\right) \left(1 - \frac{\mathcal{B}}{\mathcal{B}_k^*}\right) \exp\left(\frac{\mathcal{B}}{\mathcal{B}_k} + \frac{\mathcal{B}}{\mathcal{B}_k^*}\right) \end{aligned} \quad (2.8)$$

$$= \mathcal{Z}_{lim}(\beta) \prod_{k \in \mathbb{N}} \left(\frac{\tau_k^2 + (\beta_k - \mathcal{B})^2}{\beta_k^2 + \tau_k^2}\right) \exp\left(\frac{2\mathcal{B}\beta_k}{\beta_k^2 + \tau_k^2}\right) \quad (2.9)$$

where  $\mathcal{Z}_{lim}(\mathcal{B})$  describes the limiting behavior of  $\mathcal{Z}(\mathcal{B})$  for  $\mathcal{B} \rightarrow 0$  imposing

$$\lim_{\mathcal{B} \rightarrow 0} \mathcal{Z}_{int}(\mathcal{B}) = 1. \quad (2.10)$$

The free energy  $F(\mathcal{B}) = -\frac{1}{\mathcal{B}} \ln \mathcal{Z}(\mathcal{B})$ , has a derivative at every point in the complex temperature plane except at the zeros of  $\mathcal{Z}(\mathcal{B})$ . The calculation of the specific heat capacity  $C_V(\mathcal{B})$  by standard derivation yields

$$C_V(\mathcal{B}) = C_{V\,lim}(\mathcal{B}) - \mathcal{B}^2 \sum_{k \in \mathbb{N}} \left(\frac{1}{(\mathcal{B}_k - \mathcal{B})^2} + \frac{1}{(\mathcal{B}_k^* - \mathcal{B})^2}\right). \quad (2.11)$$

Zeros of  $\mathcal{Z}(\mathcal{B})$  are poles of  $F(\mathcal{B})$  and  $C_V(\mathcal{B})$ . As can be seen from eq. (2.11) the major contributions to the specific heat capacity come from zeros close to the real axis,

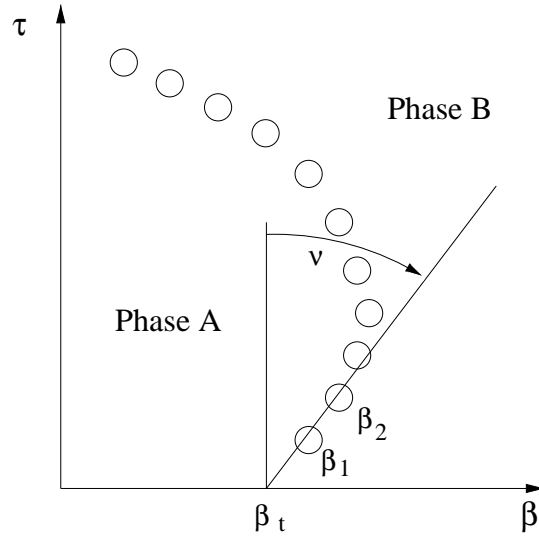


Figure 2.13: Schematic plot of the distribution of zeros on the complex temperature plane illustrating the definition of the classification parameters (taken from [MBHS00]). The circles give the positions of the zeros.

and a zero approaching the real axis infinitely close causes a divergence in the specific heat capacity.

Borrmann et al. [BMH00, MBHS00, MB01] and Janke & Kenna [JK00] proposed a discretized version of Grossmann's classification scheme.

First let us assume that the DOZ lies approximately on a straight line near the real axis. The crossing angle of this line with the imaginary axis (see fig. 2.13) is then  $\nu = \tan \gamma$  with  $\gamma = (\beta_2 - \beta_1) / (\tau_2 - \tau_1)$ . The crossing point of this line with the real axis is given by  $\beta_t = \beta_1 - \gamma\tau_1$ . The discrete line density  $\phi$  as a function of  $\tau_k$  is defined as the average of the inverse distances between  $\mathcal{B}_k$  and its neighboring zeros

$$\phi(\tau_k) = \frac{1}{2} \left( \frac{1}{|\mathcal{B}_k - \mathcal{B}_{k-1}|} + \frac{1}{|\mathcal{B}_{k+1} - \mathcal{B}_k|} \right), \quad k = 2, 3, \dots \quad (2.12)$$

$\phi(\tau)$  in the region of small  $\tau$  is approximated by a simple power law  $\phi(\tau) \sim \tau^\alpha$ . A rough estimate of  $\alpha$  considering only the first two zeros gives

$$\alpha = \frac{\ln \phi(\tau_3) - \ln \phi(\tau_2)}{\ln \tau_3 - \ln \tau_2}. \quad (2.13)$$

When  $\alpha = 0$  and  $\gamma = 0$  the specific  $C_V$  exhibits a  $\delta$ -peak which corresponds to a first order phase transition. For  $0 < \alpha < 1$  and  $\gamma = 0$  or  $\gamma \neq 0$  the transition is of second order.

### Comments

All the previous discussion on the DOZ is made explicitly in the *canonical ensemble*. It is implicitly assumed that  $\mathcal{Z} < \infty$  (condition (0'), i.e.  $\mathcal{Z}$  converges) and that the distribution of the energy is well described by the canonical distribution. These points (in particular the latter one) are criticized for small systems in section 1.3 on page 11.

See also [SSHT00, STH00] and part III where the studied system does not always fulfill condition (0').

The classification scheme based on the DOZ relies on the formally true fact that there is no information loss from ME to CE after the Laplace transform of  $\exp S$ . But in practice, the location of the zeros should be very sensitive to numerical precision leading to a loss of information [CH88]. The question whether and how information extracted from the DOZ is sensitive to these uncertainties deserve further studies. Moreover, the dimension of the parametric space to be explored as been multiplied by two. This complicates the classification for  $\mathcal{M} > 1$ . Furthermore, the richness of a system is reflected in the DOZ, see fig. 4(b) of [BMH00] where the classification is already difficult for small  $N \sim 30$ . An important question is how this complexity reflected in the DOZ affects the classification scheme and its usefulness. Finally, if the partition function cannot be estimated directly from analytical works, one has to Laplace transform the canonical probability distribution for different temperatures. This distribution is in its turn generally estimated by some numerical integration, e.g. Monte–Carlo integration. Here an important point is that one *cannot* use the usual optimization procedures to compute the probability distribution since there are only sensitive to extrema of  $P(X)$  leading to a tremendous loss of information. This information is needed to have an accurate DOZ. All in all, one must estimate  $P(X)$  over a broad  $X$ -range. But  $P(X)$  is nothing but the entropy  $S$  up to a linear constant which can be trivially removed. So, estimating  $P$  is also estimating  $S$  which contains already all the information about phases and phase transitions as shown in this chapter. Thus, in this respect, a classification based the local topology of  $S$  is more *direct* than the one using the DOZ.

## 2.5.2 Tsallis entropy

### Schematic overview

It is probably true that Boltzmann's principle has its own domain of physical validity (much like classical mechanics is valid if at least the velocities involved are smaller than the speed of light). As an attempt to extent this yet hypothetical restricted domain Tsallis conjectured the following generalization of Boltzmann's principle [TSA88]

$$S_q = k \frac{1 - \sum_{i=1}^W p_i^q}{q - 1}, \quad (2.14)$$

where  $\sum_{i=1}^W p_i = 1$ ,  $q \in \mathbb{R}$  and  $k^k$  is a positive constant and  $W$  is the total number of microscopic possibilities of the system. This expression recovers the usual Boltzmann–Gibbs entropy namely  $-k_B \sum_{i=1}^W p_i \ln p_i$  in the limit  $q \rightarrow 1$ . The entropic index  $q$  characterizes the degree of nonextensivity reflected in the following pseudo–additivity entropy rule

$$S_q(A + B) / k = S_q(A) / k + S_q(B) / k + (1 - q) (S_q(A) / k) (S_q(B) / k), \quad (2.15)$$

where  $A$  and  $B$  are two independent systems. Since  $S_q \geq 0$ ,  $q < 1$ ,  $q = 1$  and  $q > 1$  respectively correspond to superadditivity (superextensivity), additivity (extensivity) and subadditivity (subextensivity). The  $q$  expectation value  $\langle \mathcal{O} \rangle_q$  of an observable  $\mathcal{O}$  is

$$\langle \mathcal{O} \rangle_q = \frac{\sum_{i=1}^W p_i^q \mathcal{O}_i}{\sum_{i=1}^W p_i^q}. \quad (2.16)$$

---

<sup>k</sup> $k$  may also be a function of  $q$  provided that  $k \rightarrow k_B$  for  $q \rightarrow 1$  where  $k_B$  is Boltzmann's constant [MNPP00, AMPP00].

Tsallis proved also in [TSA95] that the heat capacity

$$C_q \doteq T \frac{\partial S_q}{\partial T} = \frac{\partial U_q}{\partial T}, \quad (2.17)$$

is positive, i.e.

$$\frac{1}{q} C_q \geq 0, \quad (2.18)$$

$$q \frac{\partial^2 S_q}{\partial U_q^2} \leq 0. \quad (2.19)$$

### Comments

One of the main criticism found in the literature against Tsallis' entropy is the lack of physical interpretation for  $q$ . Its value is usually adjusted *a posteriori* in order to fit experimental data. For some authors,  $q$  is related to and determined by the microscopic dynamics [BLR, LBRT00], or to be more precise,  $q$  is linked to the system sensitivity to the initial conditions (see e.g. [AT98]). For others,  $q$  describes effects due to the finiteness of the heat bath. I.e. the heat bath heat capacity is not infinity as it is usual assumed to build the canonical distribution function, but instead  $C_v \propto (q - 1)^{-1}$  [ALM01]. The latter point illustrates how Tsallis' entropy (at least how it is used in literature) is closely related to the canonical ensemble. Even Tsallis is keen on keeping the Legendre structure of his theory, *imposing* therefore a positive heat capacity as shown in [TSA99, TSA95].

For the followers of Tsallis' entropy, the domains where Boltzmann's principle is no longer valid are e.g. long-range systems and those with (multi-)fractal boundary conditions [TSA99]. At least for long-range interaction systems, it is the *usual canonical description that appeared to be un-valid*, whereas up to now they could be well described within the *microcanonical ensemble* avoiding the need of an extension of Boltzmann principle (see part III, see also [GRO01, PAD90] and references quoted therein).

## 2.6 Conclusions

By studying the topology of the microcanonical entropy defined via Boltzmann's principle one can define phases and phase transitions for any physical system without invoking the thermodynamical limit.

The microcanonical ensemble is the proper ensemble for "small" systems. It gives a deeper insight onto the physical properties of "small" systems than *any* other "canonical" ensemble.

Up to now, the thermostatistics of small systems, as presented in this chapter, has been very successful [GRO01, GMS97, GRO90, DGC<sup>+</sup>00]. However, there are still open questions. E.g. is there a second law for "small" systems and how to express it without invoking the thermodynamical limit [GRO00A]? What are the links between the critical exponent in CE to the local topology of the microcanonical entropy-surface?

In the following, original studies of the equilibrium properties of two systems far from the thermodynamical limit are presented. In part II, the liquid-gas phase transition of small sodium clusters is explored as a function of the system size and also of the microcanonical pressure. On the other hand of the physical length scale, the equilibrium properties of a self-gravitating system at fixed total energy and angular momentum are studied in part III.

## Part II

# Liquid–gas transition of metallic clusters



# Chapter 3

## Low pressure and scaling properties

### 3.1 Introduction

The theory presented in part I addresses the thermostatics of “small” systems. This thermostatics has already been applied to many models covering a wide range of physical domains. Historically, one of its firsts applications, were linked to the study of “liquid–gas” phase transitions of hot nuclei and metallic clusters composed of a few hundreds of particles or atoms, see e.g. [GRO90, GH95, GM97]. For those systems there is no heat–bath, and they exhibit properties that are absent in the limit  $N \rightarrow \infty$ .

In this part, the study of the equilibrium properties of the transition from (liquid) sodium <sup>a</sup> clusters composed of 50 up to 5000 atoms to gases of atoms as functions of the microcanonical pressure and of the total excitation energy is presented. This work continues the one done by Gross et al., e.g. [GMS97, MHGS97, SKM<sup>+</sup>97, GM97].

In previous applications of the microcanonical thermodynamics for small systems the numerical works were based on MMMC, the Microcanonical-Metropolis-Monte-Carlo sampling. It is a method that samples the accessible *microcanonical* phase space of  $N$ -body systems [ZGXZ87], rather than performing dynamical computations, e.g. [BBG97]. In MMMC, contrary to dynamical calculations, there is no need to follow every single degree of freedom (see below). One of the key feature of MMMC is that it explores the partitioning phase–space without any *a priori* assumption about the mass distribution (in contrast with e.g. an evaporation model). Practical applications of MMMC already gave good qualitative and quantitative results and shed new lights onto the problems of coulomb explosions of metallic clusters [SKM<sup>+</sup>97, SCH97] and on their liquid–gas phase transition. The main outcome of these works is, in complete analogy with the nuclear application of MMMC <sup>b</sup>, the prediction of a first order phase transition and of a multifragmentation regime within a certain range of energies [GM97]. The nuclear model and the cluster model have both a multifragmentation regime although the physical reasons that lead to this regime are different. In the cluster case, the multifragmentation is mainly induced by the electronic shell effects (see below). Whereas, in the nuclear case, the coulomb repulsion of the uniformly distributed charges plays a major role. The multifragmentation regime, the mass

---

<sup>a</sup>Sodium has been chosen since it is experimentally well explored, and a lot of material data are available, e.g. [FL95].

<sup>b</sup>In the following, the cluster and nuclear *models* which use the MMMC *method* are also noted by MMMC.

distribution is characterized by the presence of many intermediate mass fragments (see below). This regime vanishes in the limit  $N \rightarrow +\infty$ .

One of the first aim of the work presented in this thesis was to study the liquid–gas phase transition of small metallic clusters at high pressure up to eventually the critical point as defined in chap. 2 (if it exists at all) and to study whether and how precursors of critical behaviors show up (e.g. mass distribution described by a power law, infinite correlation lengths <sup>c</sup>, etc). Another goal was to explore in details this phase transition at low pressures.

In order to achieve this program the old code implementing the MMC method on the cluster model <sup>d</sup> was rewritten from scratch for several reasons, e.g.

- MMC77 uses an approximation in order to estimate  $NCC$ , a quantity linked to the avoided volume (see below and app. A), which is far from being valid and useful at high pressures.
- The algorithm to sample the mass partition fulfills the detailed balance only “on average” in MMC77 [GM87, ZGXZ87, GRO97]. At low pressure, this approximation is in most of the cases sufficient. But, since huge fluctuations in the mass distribution can be expected near the critical point, it is safer to implement a correct sampling that fulfills “locally” the detailed balance equation (see app. B.2.1).
- Finally, some new improvement to the model had to be incorporated in the code, especially regarding the model of the internal entropy of the clusters.

The rest of this chapter is organized as follow. In section 3.2 the cluster model is introduced. Then, the MMC method is briefly presented in sec. 3.3. More technical “details” are left for the appendices A and B. In section 3.4 the numerical results on the liquid–gas transition of small clusters of sodium at atmospheric pressure are presented and discussed <sup>e</sup>. First, for a system composed of two hundreds atoms in sec. 3.4.1. Then, the scaling behavior of the mass distributions and of the transition parameters are discussed in sec. 3.4.2. Results on the liquid–gas transitions of sodium clusters based on MMC77 have already been published in e.g. [GMS97, MHGS97, SKM<sup>+</sup>97, GM97]. In sect. 3.4 some of these results (noted hereafter [GM] or [GM97]) are compared with the ones of the present thesis. The results are collected and summarized in section 3.5.

## 3.2 Model

The MMC cluster model has been described in many papers and reviews [GRO97, SCH97]. Hence hereafter, only the basic assumptions are recalled with a particular stress on the differences between the “old” and the “new” model <sup>f</sup>.

The aim of MMC is to sample the phase space accessible to a model for metallic clusters <sup>g</sup> and to get information about the derivatives of its entropy and about its mass distribution. It is a *microcanonical* model, thus the “extensive” parameters of the model as defined in part I are conserved.

---

<sup>c</sup>Of course in finite size systems the correlation lengths can only be very large, and the mass distributions are described by power laws over a finite range of masses.

<sup>d</sup>Hereafter, the previous and the new codes are noted MMC77 and MMC95, respectively.

<sup>e</sup>High pressures studies are presented in chap. 4.

<sup>f</sup>Throughout this section atomic units are used, i.e.  $\hbar = m_e = e = 4\pi\epsilon_0 = 1$

<sup>g</sup>In the present work only *uncharged* sodium clusters are considered.

## System

The system is composed by a spherical container whose volume is fixed and equal to  $V = \frac{4\pi}{3}R^3$  and of  $A$  atoms of sodium. These atoms can be bounded and form clusters. Inside this container, the clusters are positioned (they must fit within  $V$ ). Neither the number of clusters  $N_f$  nor the mass distributions are restricted, provided again, that they satisfy the microcanonical constraints and fit within the container.

The container breaks the translational symmetry. Therefore, the total linear momentum  $\mathbf{P}$  is not conserved. In order to avoid a dependence of the results on the box-shape, the total angular momentum  $\mathbf{L}$  is also considered as free to fluctuate<sup>h</sup>. The conserved quantities are the total number of atoms  $A$ , the volume  $V$  and the total energy  $E$ .

## Clusters

The clusters are modeled in the following way:

1. All clusters are assumed to be *spherical hard spheres*<sup>i</sup>. Their individual volume  $v_i$  is  $v_i = \frac{4\pi}{3}N_i r_w^3 = \frac{4\pi}{3}R_i^3$  where  $r_w$  is the Wigner–Seitz radius,  $N_i$  the number of atoms of the cluster  $i$  and  $R_i$  its radius. Hence, all clusters have the same density.
2. The mass  $m_i$  of a cluster of size  $N_i$  is given by  $m_i = m_0 N_i$  where  $m_0$  is the mass of a monomer (atom)<sup>j,k</sup>. The total mass of the system  $M$  is given by  $M = A m_0$ .
3. The binding energy of a cluster  $E_{b_i}$  is a function of its mass<sup>l</sup>  $N_i$ . For clusters of mass within the range  $[2, 21]$  the binding energies are taken from experimental data [KSR<sup>+</sup>88]. For  $N_i > 21$ , the classical metallic–drop model is used. For the ground–state binding energy this model gives

$$E_{b_i} = -a_v N_i + a_s N_i^{2/3}, \quad (3.1)$$

where  $a_v$  and  $a_s$  are two positive coefficients related to the volume and to the surface energy, see fig. 3.1 on the following page.

4. The eigen–rotation of a cluster with  $N_i > 2$  is treated classically. For dimers and trimers their geometrical structures are taken explicitly. As a dimer is a linear molecule, only two angles are required in order to determine its orientation in space (three angles are needed for  $N_i > 2$ ). Its principal moment of inertia are  $I_1 = I_2 = \frac{1}{2}m_0 d^2$ ,  $I_3 = 0$ , where  $d$  is the dimer bond length. For a trimer, the principal moment

<sup>h</sup>In the previous MMC model, there was no real container, but a freeze–out volume within which the system was assumed to be equilibrated before escaping this volume. This was closely related to the experiments, since in experimental cluster physics the systems are open [Gro97]. Consequently  $\mathbf{P}$  and  $\mathbf{L}$  were conserved quantities. Here, a real volume is needed to make the concept of pressure sensible.

<sup>i</sup>In the previous model, the monomers were allowed to overlap with other clusters (other monomers included). This was a way to simulate highly excited clusters. I.e. clusters whose internal excitation energies are well above maximal allowed specific internal excitation energy  $\epsilon_{max}^*$  (see below). For practical reasons, this is not included in the present model. This decision is supported a posteriori by the fact that, in all the performed simulations, the internal excitation energy of the clusters were seldomly close to  $\epsilon_{max}^*$  (see below).

<sup>j</sup>As the mass of a cluster is proportional to its number of atoms and for simplicity,  $N_i$  is in the following a short hand for the number of atoms but also for the mass of cluster  $i$ .

<sup>k</sup>To avoid cumbersome notations, the monomers are also called “clusters”.

<sup>l</sup>For a monomer  $E_{b_i} = 0$ .

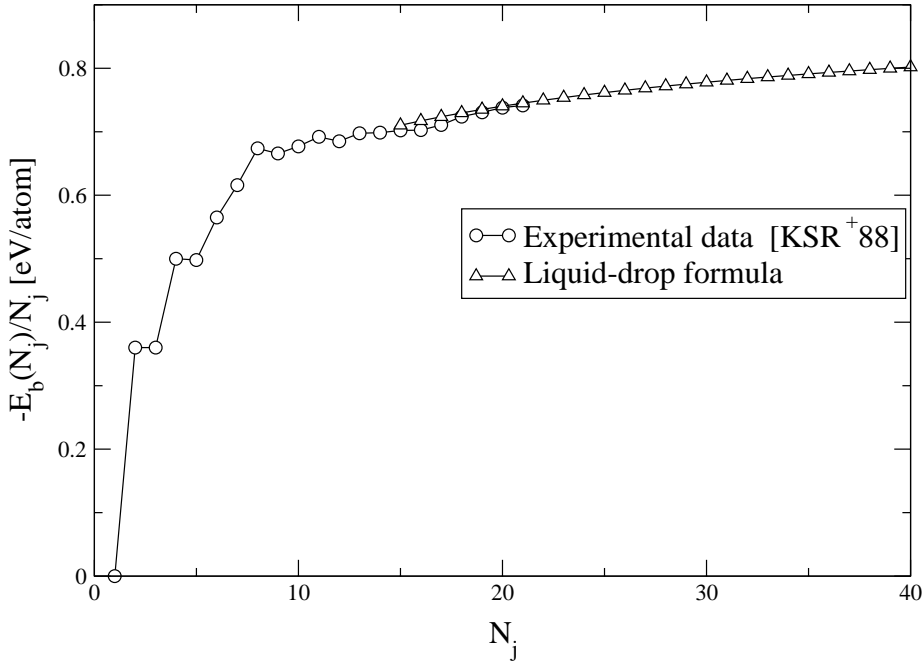


Figure 3.1: Specific binding energy as a function of the cluster size: experimental data [KSR<sup>+</sup>88] and liquid-drop formula with  $a_v = 1.039$  eV [BCC<sup>+</sup>90, BCC<sup>+</sup>95] and  $a_s = 0.8109$  eV. Note that the value of  $a_s$  is experimentally known with a large uncertainty (see [GM97] and refs. quoted therein). Here,  $a_s$  is adjusted to obtain the best fit with the experimental data. Note also the local maxima of  $E_b/N_j$  at  $N_j = 2, 4, 8$  and  $12$  due to the electronic shell effects.

of inertia are determined assuming a triangular geometry. The clusters with  $N_i > 4$  are regarded as classical homogeneous spherical body. Their principal moment of inertia are given by  $I_1 = I_2 = I_3 = \frac{2}{5} N_i m_0 R_i^2$ .

The monomers have a spin degeneracy of 2.

5. Clusters ( $N_i > 1$ ) have internal degrees of freedom (dof). The internal excitation energy of cluster  $i$  is noted by  $E_i^*$ . For the dimers and the trimers, it is assumed that the internal dofs are well described by quantum Einstein models. Moreover, the internal excitation energy for dimers and trimers are upper bounded by their respective dissociation energies  $D_d$  and  $D_t$ .
  - (a) A dimer has one internal dof which is associated with one quantum harmonic oscillator having a frequency  $\omega_d$ . The discrete energy levels are given by  $E_i^* = (k_1 + \frac{1}{2}) \hbar \omega_d$  where  $k_1 \in \mathbb{N}$ . These levels are not degenerate, so in this model, a dimer carries no internal entropy.
  - (b) A trimer is a non-linear molecule with three internal dofs which are associated with three independent distinguishable quantum harmonic oscillators having all the same frequency  $\omega_t$ . The energy levels  $E_i^*$  are given by  $E_i^* = (k_1 + k_2 + k_3 + \frac{3}{2}) \hbar \omega_t$ , where  $k_1, k_2, k_3 \in \mathbb{N}$ . The degeneracy number  $n_t$  of an

energy level is given by  $n_t(E_i^*) = \frac{1}{2} \left( \frac{E_i^*}{\hbar\omega_t} \right)^2 - \frac{1}{8}$ . The internal entropy of a trimer is simply

$$S_t(E_i^*) = \ln n_t(E_i^*). \quad (3.2)$$

- (c) In the previous model, clusters with  $N_i > 3$  did not have an individual excitation energy but, on contrary, an overall  $E^*$  was assigned to all those clusters. I.e. they were considered as one unique big fragment. Or in other words, all their internal dofs had the same specific excitation energy. Moreover, as there is no available data on the entropy for *all cluster sizes*, the functional form of the entropy of this “overall” cluster was taken from the bulk.

In the new version, all clusters have their own internal excitation energy  $E_i^*$ . This energy takes its values within the range  $[0, N_i^* \epsilon_{max}^*]$  where  $\epsilon_{max}^* \approx 0.35 \frac{\text{eV}}{N^*}$  is the maximum specific internal energy<sup>m</sup> and  $N_i^* = N_i - 2 = \frac{3N-6}{3} = \frac{\text{internal dofs}}{3}$ . Here, it is assumed that 3 degrees of freedom represent together one bulk atom [GRO97]. Furthermore, in order to include some surface effects to the expression of the internal entropy  $S_{int}$  and to have a smooth specific entropy  $s_{int} = S_{int}/N^*$  as a function of  $\epsilon_i^* = E_i^*/N^*$  and  $N^*$  from  $N^* = 3$  to  $N^* \rightarrow \infty$  the following model is assumed

$$S_{int}(\epsilon^*, N^*) \doteq N_s^* s_t(\epsilon^*) + N_v^* s_\infty(\epsilon^*), \quad (3.3)$$

where  $s_t$  and  $s_\infty$  are the trimer and the bulk specific entropies.  $N_s^*$  and  $N_v^*$  are the number of surface and volume “atoms”, respectively.

$s_t$  is given by eq. (3.2).  $s_\infty$  is computed from the experimental specific heat capacity at constant pressure  $c_p(T)$  [FL95] (for further and detailed explanations see e.g. [GRO97]). In fig. 3.2 the specific heat capacity at constant pressure  $c_p(T)$  is plotted at atmospheric pressure and the specific entropy and the temperature versus  $\epsilon$  are shown on fig. 3.3. It is worth to notice that the bulk remains in the liquid phase up to a specific energy of  $\epsilon_{max}^* \approx 0.35$  eV/atom.

The number  $N_s^*$  of surface atoms are estimated in the following way (see fig. 3.4 on page 45). Consider a cluster of diameter  $R_i$ . Its surface fragments are approximatively inside an external layer of thickness  $\approx 2r_w$  (the diameter of a monomer). The volume of this layer is  $V_s$  and the number of surface atoms is  $\sim \frac{V_s}{v_0}$  where  $v_0$  is the monomer volume (eigen-volume), i.e.  $v_0 = \frac{4\pi}{3}r_w^3$ , it follows

$$N_v^* = \max\left(0, N^* - 6N^{*2/3} + 12N^{*1/3} - 8\right), \quad (3.4a)$$

$$N_s^* = N^* - N_v^*. \quad (3.4b)$$

Fig. 3.5 on page 45 shows the specific entropy  $s$  at  $\epsilon^* = 0.35\text{eV}/N^* = \epsilon_{max}^*$  along with the proportion of volume atoms  $N_v^*/N^* = 1 - N_s^*/N^*$  as functions of  $N^*$ . There is no volume fragment for clusters of size  $N = N^* + 2 < 14$ ; the number of surface fragments and therefore the relative weight of the surface entropy in the total cluster entropy is very important even for clusters composed of ten thousands atoms<sup>n,o</sup>.

<sup>m</sup>In fact, the exact value of  $\epsilon_{max}^*$  is not very constraining, as the results of the MMMC95 simulations depend only marginally on  $\epsilon_{max}^*$ . The excitation energy of a given cluster is seldomly close to the limit  $N_i^* \epsilon_{max}^*$ , at least for the range of system total mass studied (see below).

<sup>n</sup>The largest system considered in this work is composed of 5000 atoms.

<sup>o</sup> $s_\infty(\epsilon^* = 0.35) \approx 11.7$ .

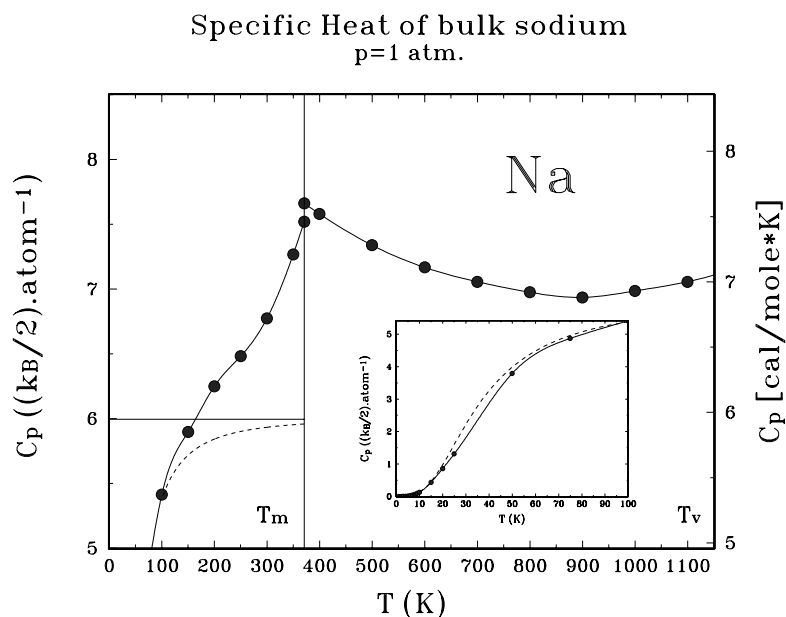


Figure 3.2: Specific heat capacity at constant (atmospheric) pressure of bulk sodium  $C_p$  [BOR63, HOAK63]. The dashed line represents the specific heat capacity calculated within the Debye model.

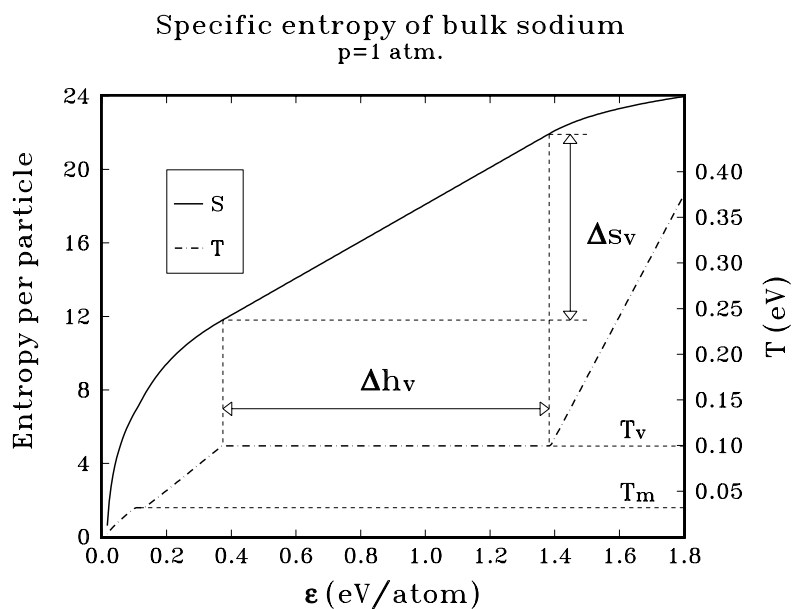


Figure 3.3: Specific entropy and temperature of bulk sodium at atmospheric pressure.  $\Delta h_v$  is the latent heat at constant pressure;  $T_m$  and  $T_v$  are resp. the melting and the vaporization temperatures.

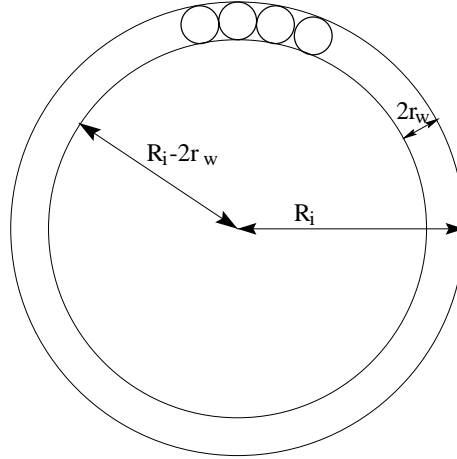


Figure 3.4: Schematic cluster model for the number of surface and volume degrees of freedom.  $R_i$  is the actual clusters radius and  $r_w$  is the Wigner-Seitz radius (radius of a monomer). The surface atoms are located on spherical shell of inner (outer) radius equal to  $R_i - 2r_w$  ( $R_i$ ).

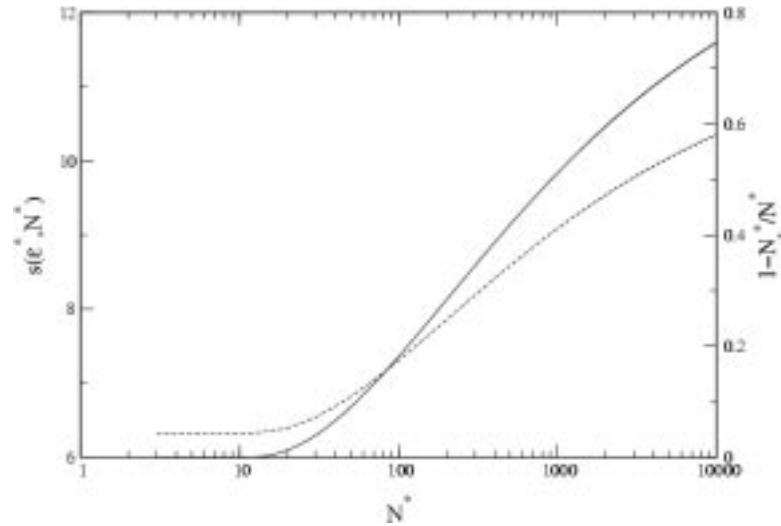


Figure 3.5: Entropy  $s(\epsilon^* = 0.35 \text{ eV/atom}, N^*)$  (dashed line; defined by eq. (3.3) on page 43) and proportion of volume “fragments”  $N_v^*/N^* = 1 - N_s^*/N^*$  (plain line; defined by eq. (3.4b) on page 43) versus  $N^*$ . Within the present model the surface effects are very important for clusters as heavy as  $A = 10^4$ .

6. The polarization effects between the metallic clusters are neglected.

The simulation parameters used throughout part II are listed in table 3.1.

### Total energy

The conserved total energy  $E$  is

$$E = E^* + E_k + E_r - E_b, \quad (3.5)$$

$r_w$ (Å)	2.310
$a_s$ (eV)	0.8109
$a_v$ (eV)	1.039
$\omega_d$ (eV)	0.01490
$\omega_t$ (eV)	0.01048
$d$ (Å <sup>2</sup> )	2.67
$I_2/m_0$ (Å <sup>2</sup> )	4.74
$I_{3,1}/m_0$ (Å <sup>2</sup> )	4.84
$I_{3,2}/m_0$ (Å <sup>2</sup> )	5.66
$I_{3,3}/m_0$ (Å <sup>2</sup> )	10.49
$D_d$ (eV)	0.72
$D_t$ (eV)	0.36

Table 3.1: Experimental and theoretical values of the different parameters used in the calculations.  $r_w$  is the Wigner–Seitz radius at one atmosphere [FL95];  $a_v$  is the volume cohesion energy and  $a_s$  its surface part (the value of  $a_s$  is adjusted in order to have a smooth binding energy per degrees of freedom for  $15 \lesssim N \lesssim 31$ , see fig. 3.1 on page 42) [BCC<sup>+</sup>90, BCC<sup>+</sup>95].;  $d$  is the dimer bond length [FID<sup>+</sup>83]; the principal moment of inertia for the dimer  $I_2$  and for the trimer  $I_3$ .

where  $E_b = \sum_i E_{b_i}$  and  $E^* = \sum_i E_i^*$  are the total binding and internal energies (see items (3) and (5) on page 41).  $E_k = \sum_i \frac{\mathbf{p}_i^2}{2m_i} + \sum_i \sum_{\nu=1}^{f_{ri}} \frac{l_{\nu i}^2}{2I_{\nu i}}$  is the sum of the total kinetic and total rotational energy, where  $\mathbf{l}_i$  and  $I_{\nu i}$ ,  $i = 1, \dots, f_{ri}$  are the angular momentum the principal moment of inertia, respectively and  $f_{ri}$  is the number of rotational dof (see item (4) on page 41).  $E_k$  is also called “remaining energy”.

### 3.3 Simulation method

#### Microcanonical weight

MMC is based on a Metropolis Monte–Carlo method [MRR<sup>+</sup>53]. It builds a (Markovian) chain of states in the phase space accessible to the system. As in the microcanonical ensemble all microstates are accessible with the same probability the weight that should be used during the Metropolis test is the same for all microstates  $\{\mathbf{q}, \mathbf{p}\}$  (see app. B.2). However some of the coordinates (dofs) are irrelevant in the sense that they are unobservable (e.g. internal degrees of freedom) and/or the observables of interest do not depend explicitly on those coordinates.

Therefore instead of working with the full generalized set of coordinates it is more reasonable to integrate, if possible, over the irrelevant (unobserved) coordinates. For the present model, the results of this integration gives the following new set of coordinates

$$\mathbf{x} \doteq \{\mu = \{N_i\}_{i=1}^{N_f}, \{E_i^*\}\}, \quad (3.6)$$

where  $\mu$  is a short hand for the mass distribution, and  $\{E_i^*\}$  is the set of internal excitation energies (there are  $N_f - N_m$  elements in this set, where  $N_m$  is the number of monomers in  $\mu$ ). The set over which  $\mathbf{x}$  is defined is noted by  $W'$ .

Now in this set of coordinates the microcanonical density of states  $\omega(\mathbf{x})$  is no longer uniform but equal to

$$\omega(\mathbf{x}) d\mathbf{x} = \int_{\Omega} d\mathbf{q} d\mathbf{p} \delta(X(\{\mathbf{q}, \mathbf{p}\}) - X_0) \delta(\mathbf{x}(\{\mathbf{q}, \mathbf{p}\}) - \mathbf{x}), \quad (3.7)$$

where  $X_0 = \{E, N, V\}$  is the set of “extensive” conserved quantities.

The detailed derivation of the microcanonical weight for the fragmentation phase space of atomic clusters can be found in refs. [GROB, GH95].

$\omega(\mathbf{x})$  can be divided in the following way

$$\omega \equiv \omega_{sym} \omega_{pl} \omega_r \omega_{NCC} \omega_{int}, \quad (3.8)$$

where

$\omega_{sym}$  is the quantum symmetrization weight factor

$$\omega_{sym}(\mu) \doteq \frac{1}{\prod_{i=1}^A \xi_{\mu}(i)!}, \quad (3.9)$$

where  $\xi_{\mu}(i)$  is the number of clusters of size  $i$  in  $\mu$ . In MMMC77 an approximation of eq. (3.9) is used. In app. B.2.1 the method used in MMMC95 is presented. It is an exact method. Even though  $\omega_{sym}$  is not explicitly computed it is exactly taken into account in the Metropolis sampling (for an independent and generalized discussion, including charges and continuous variables, see Raduta [RR97]).

$\omega_{pl}$  is the result of the integration over the linear and angular momenta

$$\omega_{pl} \propto C(\mu) E_r^{\tilde{N}}, \quad (3.10)$$

where  $E_r = E - E_b - E^* = E_k$  is the remaining energy.  $C(\mu)$  is only a function of the mass distribution  $\mu$ , it is proportional to the product of the clusters masses and of the clusters principal moment of inertia;  $\tilde{N}$  is the number of translational–rotational dofs divided by two minus one, e.g. for a gas of monomers  $\tilde{N} = \frac{3A}{2} - 1$ .

At fixed remaining energy  $E_r$ ,  $\omega_{pl}$  drives the mass distribution towards an increasing number of translational–rotational dofs, i.e. increasing number of fragments.

$\omega_r$  is the weight due to the angular part of the clusters eigen rotation. It depends on the number of rotational dofs.

Results of simulations show that this weight plays no significant role at low pressure (neither qualitatively nor quantitatively), at least for reasonable values of the input parameters, i.e. essentially the value taken by the inertial momenta.

$\omega_{int}$  is the factor due to the internal dofs of the clusters. It is the product of the internal degeneracy  $\omega_{int,i}$  of each clusters (provided that  $N_i > 2$ )

$$\omega_{int,i}(E_i^*) \doteq \exp S_{int}(N_i^*, E_i^*), \quad (3.11)$$

where  $S_{int}(N_i^*, E_i^*)$  is given by eq. (3.3) on page 43.

As the specific surface entropy at fixed specific internal excitation energy is smaller than the specific volume entropy,  $\omega_{int}$  tries to form big clusters in opposition with  $\omega_{pl}$ .

$\omega_{NCC}$  is due to the integration over the clusters center of mass  $\{\mathbf{r}_1, \dots, \mathbf{r}_{N_f}\}$ , i.e. the number of spatial configurations allowed in the container (no overlap with the boundary or between the clusters is allowed)

$$\omega_{NCC} \doteq \int_V \dots \int_V d\mathbf{r}_1 \dots d\mathbf{r}_{N_f} \Theta(\mathbf{r}_1, \dots, \mathbf{r}_{N_f}) \eta(\mathbf{r}_1, \dots, \mathbf{r}_{N_f}) \quad (3.12a)$$

$$\doteq \frac{V^{N_f}}{NCC}, \quad (3.12b)$$

where  $\Theta$  forbids the overlapping of a cluster with the boundary

$$\Theta(\mathbf{r}_1, \dots, \mathbf{r}_{N_f}) \doteq \begin{cases} 0 & \exists i \text{ such that } |\mathbf{r}_i| > R - R_i, \\ 1 & \text{else.} \end{cases} \quad (3.13)$$

$\eta$  forbids the overlapping between two clusters

$$\eta(\mathbf{r}_1, \dots, \mathbf{r}_{N_f}) \doteq \begin{cases} 0 & \exists i, j \text{ such that } |\mathbf{r}_i - \mathbf{r}_j| < R_i + R_j, \\ 1 & \text{else.} \end{cases} \quad (3.14)$$

$NCC$  is the inverse probability to find a set of positions for the clusters center of mass so that all clusters fit into the container. For very large volumes  $NCC$  is close to one. For  $N_f > 2$  exact analytical evaluation of  $NCC$  is up to now practically impossible. In app. A.1.2 an approximation of  $NCC$  is worked out using the equation of state (EOS) of hard-spheres gas [MCSL71]. For  $A \approx 500$ , this approximation turns out to be relatively good for pressures up to  $\sim 100$  atmospheres<sup>p</sup> (see chap. 4). For higher pressures, estimates of  $NCC$  based on EOS which are in their turn only based on two body correlations are useless and  $NCC$  has to be evaluated via a Monte-Carlo scheme. The one used in the present work is briefly described in app. A.2.

At low pressures  $\omega_{NCC} \approx V^{N_f}$ . Hence, this weight drives the system mass in the same direction as  $\omega_{pl}$ , i.e. towards increasing number of fragments.

The caloric curves presented in sec. 3.4 are mostly the results of a competition between the internal dofs and the translational+positioning ones (the former try to bound the atoms in clusters, whereas the latter prefer as many fragments as possible). Moreover, as discussed in sec. 3.4 two key ingredients for the multifragmentation regime are the shell structure of the clusters reflected in the binding energies and the quantum symmetrization weight  $\omega_{sym}$ .

## Observables

The physical quantities of interest are the averages  $\langle F \rangle$  of observables  $F$  over the micro-canonical ensemble

$$\langle F \rangle \doteq \frac{\int_W F(\{\mathbf{q}, \mathbf{p}\}) d\mathbf{q} d\mathbf{p}}{\int_W d\mathbf{q} d\mathbf{p}} \quad (3.15)$$

$$= \frac{\int_{W'} F(\mathbf{x}) \omega(\mathbf{x}) d\mathbf{x}}{\int_{W'} \omega(\mathbf{x}) d\mathbf{x}} \quad (3.16)$$

---

<sup>p</sup>For a given microcanonical pressure, the approximation becomes better with increasing  $A$ , because the relative weights of  $NCC$  and its derivatives are less and less important as the system grows  $A \rightarrow \infty$ ,  $p = cst$ , see below.

The Metropolis sampling replaces the integral in eq. (3.16) on the preceding page by a discrete sum

$$\langle F \rangle = \frac{1}{N} \sum_{j=1}^N F(\mathbf{x}_j). \quad (3.17)$$

The energy and volume dependencies of  $\omega(\mathbf{x})$  appear explicitly only in  $\omega_{pl}$  and  $\omega_{NCC}$ . Thus the system entropy can be written in the following condensed way

$$S = \ln \int_{W'} d\mathbf{x} \omega(\mathbf{x}) \quad (3.18)$$

$$= \ln \int_{W'} d\mathbf{x} C(\mathbf{x}) \frac{V^{N_f}}{NCC} E_k^{\tilde{N}}, \quad (3.19)$$

where  $V$ ,  $N_f$ ,  $NCC$ ,  $E_k$  and  $\tilde{N}$  depend implicitly on  $\mathbf{x}$ ,  $C(\mathbf{x})$  does not depend explicitly on  $E$  or on  $V$ . The inverse temperature (at constant volume)  $\beta \equiv \beta_V$  is defined as

$$\beta \doteq \frac{\partial S}{\partial E} \quad (3.20)$$

$$\begin{aligned} &= \frac{\int d\mathbf{x} C(\mathbf{x}) \tilde{N} \frac{V^{N_f}}{NCC} E_k^{\tilde{N}-1}}{\int d\mathbf{x} C(\mathbf{x}) \frac{V^{N_f}}{NCC} E_k^{\tilde{N}}} \\ &\equiv \left\langle \frac{\tilde{N}}{E_k} \right\rangle. \end{aligned} \quad (3.21)$$

The microcanonical pressure  $p$  is

$$p \doteq \frac{1}{\beta} \frac{\partial S}{\partial V} \quad (3.22)$$

$$\begin{aligned} &= \frac{1}{\beta} \frac{1}{\int d\mathbf{x} \omega(\mathbf{x})} \left[ \int d\mathbf{x} C(\mathbf{x}) N_f \frac{V^{N_f-1}}{NCC} E_k^{\tilde{N}} - \int d\mathbf{x} C(\mathbf{x}) \frac{1}{NCC} \frac{\partial NCC}{\partial V} \frac{V^{N_f}}{NCC} E_k^{\tilde{N}} \right] \\ &\equiv \frac{1}{\beta} \left[ \left\langle \frac{N_f}{V} \right\rangle - \left\langle \frac{\partial \ln NCC}{\partial V} \right\rangle \right] \end{aligned} \quad (3.23)$$

$$\doteq p_{kin} + p_{NCC}. \quad (3.24)$$

where  $p_{kin} \doteq \frac{1}{\beta} \left\langle \frac{N_f}{V} \right\rangle$  and  $p_{NCC} \doteq -\frac{1}{\beta} \left\langle \frac{\partial \ln NCC}{\partial V} \right\rangle > 0$  are resp. the kinetic and the ‘‘avoided volume’’ or  $NCC$  parts of the total pressure  $p$ .

Most of the results presented in the next section are shown at constant *microcanonical* pressure. The reasons are that all macroscopic parameters for the liquid–gas transition of sodium are experimentally measured at constant pressure. Furthermore, near the critical point, the pressure is a control parameter for the first and second order phase transitions (see sec. 2.2). Nevertheless, the computations are *not* performed at constant pressure leaving the volume free to fluctuate. But, on the contrary, the volume is *fixed* for each run and slowly adapted from one run to the other in order to reach the desired pressure. This procedure allows one to follow an isobar in the energy–volume plane just like the ones computed for the van der Waals model in sec. 2.2 (see e.g. fig. 1.5(b) on page 15). The uniqueness of this isobar, i.e. that there is only *one*  $v$  solution of  $p(\epsilon, v) = p_0$  at fixed  $\epsilon$ , is a priori not guaranteed. Indeed, at small energies and volumes the isobars split up into three branches, see fig. 3.6 on the next page. For a given total specific excitation energy smaller

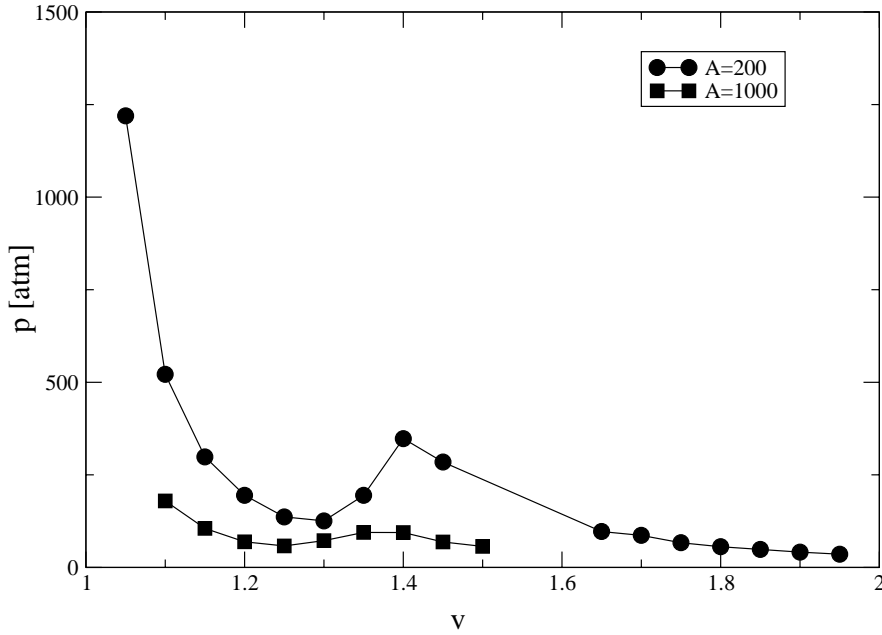


Figure 3.6: Pressure vs normalized volume  $v$  at fixed excitation energy  $\epsilon \approx 0.2$  eV/atom and for different total masses. At fixed low energy, the equation  $p(v) = v_0$  can have three solutions. The mass distribution for the branch with the lowest volume is composed of only one big cluster. As the system volume increases this cluster starts to evaporate some monomers (beginning of the negative compressibility region). The evaporation of the first monomers are responsible of this negative compressibility region via  $p_{NCC}$ , the avoided volume term in the total microcanonical pressure  $p$  (see eq. (3.24)).

than  $\epsilon_{max}^*$  it is always possible to get the desired pressure by quenching the big cluster in a very small volume (at very low energy this is the only way to reach the appropriate pressure). This branch has very high temperatures, e.g. at  $h \approx 0.2$ ,  $T_V \approx 1200$  K. But the volume of the phase space of this solution is small compared to the one with many fragments at large system volume (if this branch is open). There is a third branch between the two above mentioned branches. It is characterized by a positive  $\frac{\partial p}{\partial v}|_{\epsilon}$ . In the following, solutions from the branch with the largest volume are plotted. It is the only branch that goes from the gas to the liquid solution when  $\epsilon \rightarrow 0$  by slow variations of  $\epsilon$  and  $v$ . This effect vanishes in the limit  $N \rightarrow \infty$ , because the difference of the system volumes of these two solutions shrinks. A more satisfactory solution would have been to study the temperature-surface over the *whole* parameter space, i.e. as a function of the “extensive” parameters  $\epsilon$  and  $v$ .

## 3.4 Results

### 3.4.1 $N_{a200}$ , 1 atm.

On fig. 3.7 on the facing page the results from MMMC95 for  $A = 200$  at atmospheric pressure are summarized.

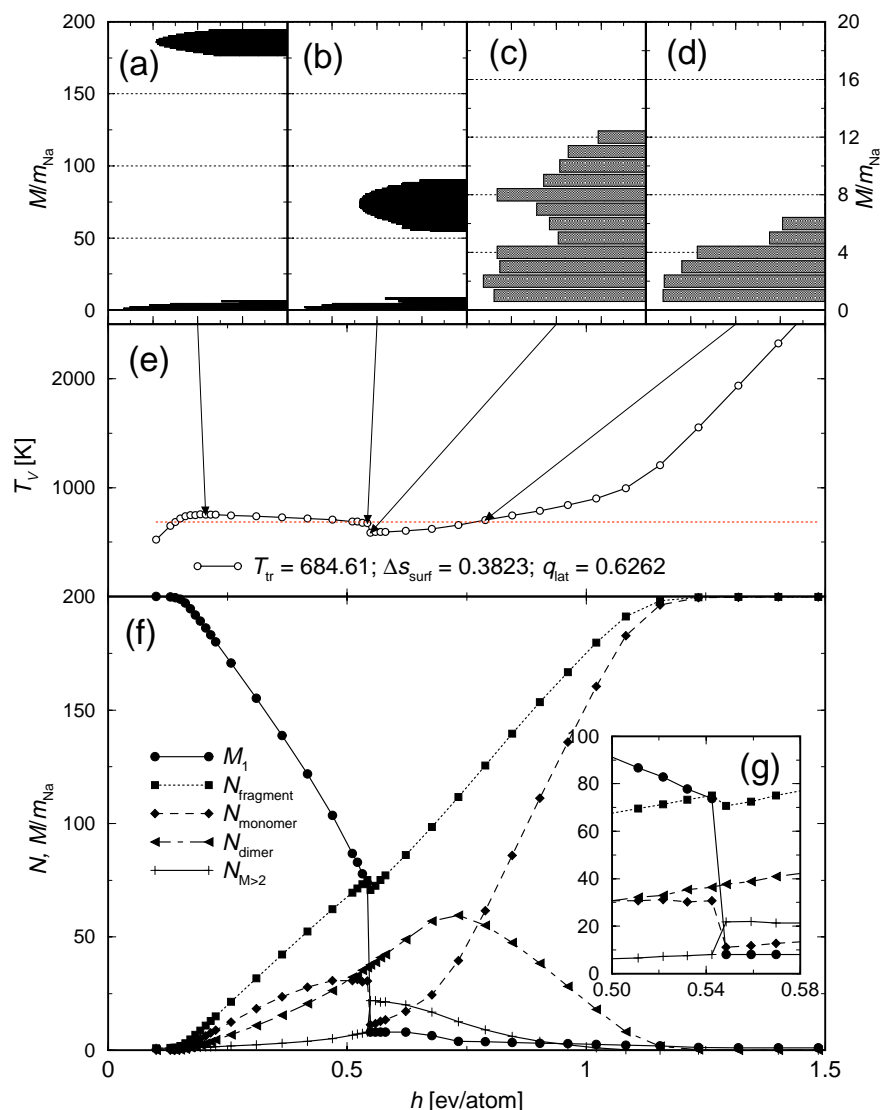


Figure 3.7: Summary of the results for  $N_a 200$  at 1 atm. Panels (a) to (d), (f) and (g) give information about the mean mass distribution as a function of the specific enthalpy  $h = \epsilon + pv$ . In panels (a) to (d) the mean mass distribution (unnormalized logarithmic scale) is plotted for four different values of  $h$  (these are given by the arrows in panel (e)). In panel (f) are plotted:  $M_1$ ,  $N_{fragment}$ ,  $N_{monomer}$ ,  $N_{dimer}$  and  $N_{M>2}$  which are respectively the mean mass of the largest fragment, the mean number of fragments, of monomers, of dimers and of fragments bigger than 2. The inset (g) is a zoom in panel (f) toward  $h = 0.54$  eV/atom. The microcanonical temperature  $T_V$  (plain line) is plotted in panel (e) along with the Maxwell line (dotted line). In the range  $0.15 \lesssim h \lesssim 0.55$  the specific heat capacity is *negative*; it is the signal of a first order phase transition. Some of its parameters, extracted from the Maxwell construction, are given in (e). Around  $h = 0.55$  there is a drastic change in the mass distribution; a multifragmentation regime shows up with a large number of medium-size fragments (8-mers, 4-mers, see (c), (f) and (g)).

### Caloric curve

On fig. 3.7(e) the isobar  $p = 1$  atm is plotted (plain line) in the  $(h, T_V)$  plane, where  $h = \epsilon + pv$  is the specific enthalpy and  $T_V$  the microcanonical temperature<sup>9</sup>.

There are several distinct enthalpy regions. For  $h \lesssim 0.15$  eV/atom  $T_V$  increases monotonically; at  $h \approx 0.15$  eV/atom  $T_V$  starts to be a *decreasing* function of  $h$ , i.e.  $C_V < 0$  which signals a first order phase transition.  $T_V$  decreases quasi-linearly up to  $h \approx 0.55$  eV/atom. There it drops down within a small  $h$ -range (very low heat capacity). After that,  $T_V(h)$  recovers a “normal” behavior (positive heat capacity) with three distinct parts, one for enthalpies within  $\approx [0.55, 0.75]$ , another<sup>s</sup> for  $h \in [0.75, 1.15]$  and the last for  $h > 1.15$ .

According to sec. 2.2.3 on page 27 one can define transition parameters via the Maxwell construction (dotted line in fig. 3.7(e)). The transition temperature is  $T_t \equiv T_{tr} \approx 685$  K, the latent heat  $q_{lat} \approx 0.382$  eV/atom and the specific surface entropy  $\Delta s_{surf} \approx 0.626$  atom<sup>-1</sup> (the bulk values are  $T_t = 1156$  K,  $q_{lat} = 0.923$  eV/atom and the specific surface entropy  $\Delta s_{surf}$  vanishes [FL95]). The behavior of the transition parameters as function of the systems total mass is discussed in sec. 3.4.2.

### Mass distribution

Several observables giving information about the mean mass distribution as a function of  $h$  are plotted in fig. 3.7 on the page before. In figs. 3.7(a)–(d) the logarithm of  $\langle N_j \rangle$  the mean number of fragments of size  $N_j$  is plotted (arbitrary scale), at different enthalpies (given by the arrows on fig. 3.7(e)).

In fig. 3.7(f) are plotted:  $M_1 \equiv \langle M_1 \rangle$ ,  $N_{fragment} \equiv \langle N_f \rangle$ ,  $N_{monomer} \equiv \langle N_m \rangle$ ,  $N_{dimer} \equiv \langle N_d \rangle$  and  $N_{M>2} \equiv \langle N_{M>2} \rangle$  which are respectively the mean mass of the largest fragment, number of fragments, number of monomers, number of dimers and number of fragments bigger than 2,  $\langle N_f \rangle = \langle N_m \rangle + \langle N_d \rangle + \langle N_{M>2} \rangle$ .

At low enthalpy,  $h \lesssim 0.15$ , all the atoms are in one big cluster ( $\sim$  liquid phase). Starting from  $h \approx 0.15 < 0.35 = \epsilon_{max}^*$  up to  $h \approx 0.55$  the big cluster size shrinks and light fragments (essentially monomers and dimers) are produced.  $\langle N_f \rangle$  is a linear function of  $h$ . Here, as the specific heat capacity is negative, there is a first order phase transition, with co-existence of a “liquid” ( $\sim$  big cluster) embeded in a “gas” ( $\sim$  light fragments). It is an evaporation regime.

Around  $h = 0.55$  the mass distribution is completely reorganized within a short  $h$ -range (see inset fig. 3.7(g)). From a mass distribution composed by one big “liquid” cluster and a gas of monomers and dimers it changes to a multifragmentation regime with a broad mass distribution of relatively small clusters,  $N_j \lesssim 12$  (figs. 3.7(b), (c) and (g)). The dominant fragment sizes are in decreasing order: dimers (2-mers), monomers (1-mers), quadrimers (4-mers), octomers (8-mers). The relative large number of clusters of those

<sup>9</sup>The  $pv$ -shift is not very important at atmospheric pressure, i.e.  $h_2 - h_1 \approx \epsilon_2 - \epsilon_1$  for two neighboring points on the curve in fig. 3.7(e). One can check that in fig. 3.7(e); there the energy difference  $\Delta\epsilon$  between two points (small circles) is  $\Delta\epsilon = 0.05$  eV/atom, which is also the difference expressed in  $h$ ,  $\Delta h \approx 0.05$  eV/atom (apart around  $\epsilon = 0.55$  and  $\epsilon = 0.25$  where smaller energy steps are used).

<sup>1</sup>Each point in the energy–volume plane (represented by a point in fig. 3.7) is the results of the averaging over  $2 \cdot 10^6$  events except for  $\epsilon \approx 0.25$  and  $\epsilon \approx 0.55$  where higher statistics (up to  $20 \cdot 10^6$  events) are used in order to ensure stable results. The statistical errors due to the Monte–Carlo averaging for the temperature and the mass distribution curves are below 1 %. The convergence of the results has been check by starting from several initial conditions and also by studying intermediate averages in very long run.

<sup>s</sup>Due to the temperature scale in fig. 3.7(e), it is difficult to distinguish the two first parts; they can be better seen in fig. 3.17 on page 64.

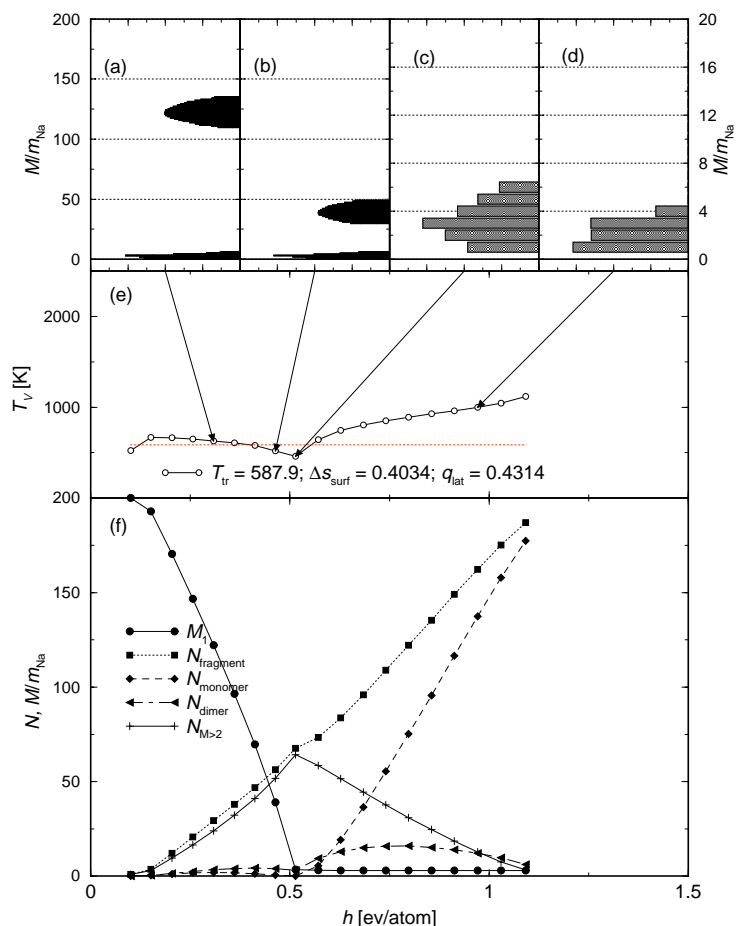


Figure 3.8: Summary of the results for  $N_{a200}$  at 1 atm; same as fig. 3.7 but the ground-state binding energy of a cluster is given by the metal-drop formula for *all* cluster sizes. Contrary to the results with experimental binding energies for small clusters, the dominant clusters are here the trimers. All other cluster sizes (apart of the liquid cluster and of the monomers at high enthalpies) have almost disappeared from the mass distribution. The trimers are chosen because they are smallest fragments with internal entropy. There is no multifragmentation in the sense of a rapid drop of the temperature. The transition is done in two evaporation steps. First from the big cluster to trimers. Second from the trimers to the monomers (with very few number of dimers). Only the first one is a phase transition (at least in the energy direction).

sizes is explained by the relative maxima at  $N_j = 2, 4$  and  $8$  in the specific binding energy as a function of  $N_j$ , see fig. 3.1 on page 42.

Indeed if the metal-drop formula is used to describe the ground-state binding energy for *all* cluster sizes, then the 8-mers and the 4-mers are no longer dominant during the “multifragmentation” regime but the 3-mers, see fig. 3.8. The 3-mers are selected because they are the smallest clusters with internal entropy.

The symmetrization weight plays also a key role as already noticed by Gross and its collaborators [GM87, GRO90]. Without this weight the mass distribution is simple:

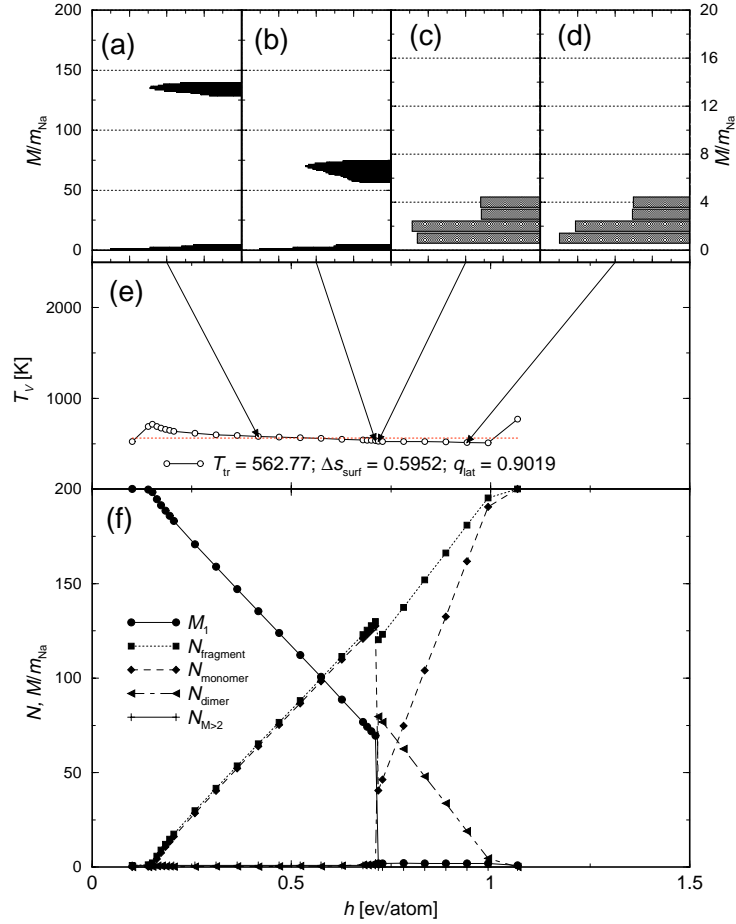


Figure 3.9: Summary of the results for  $N_{a200}$  at 1 atm; same as fig. 3.7 but without the quantum symmetrization weight. Its absence induces more simple mass distributions. The number of clusters of size bigger than 2 is very small. The jump down of the temperature at the “multifragmentation” is here quasi-inexistent (of the order of only several degrees). In the “multifragmentation” region the mass distribution is only composed of dimers and monomers.

there is no light fragment heavier than 2; hence, the “multifragmentation” regime is only composed of dimers and monomers.  $w_{sym}$  spreads the mass distribution of the small fragments (gas part), see fig. 3.9.

The multifragmentation channel is preferred because of the weights linked to the translational-rotational and positioning dofs, i.e.  $\omega_{pl}$  and  $\omega_{NCC}$ . As already written they support an increasing number of fragments. But as around  $h = -0.5$  there is not energy to vaporize the whole cluster, intermediate masses are chosen. The ones which correspond to relative maxima in the specific binding energy curve (see fig. 3.1) are favoured. The multifragmentation channel opens as soon as there is enough excitation energy in the system. However the multifragmentation regime starts later on. This delay is due to the competition of the above mentioned weights with the one linked to the internal degrees of freedom of the big liquid cluster,  $\omega_{int}$ . Hence, as the cluster specific entropy increases (at

fixed specific internal energy), due to the fading of surface effects with increasing cluster size, one can already predict that the multifragmentation transition is more and more delayed (shifted to higher  $h$ ) with increasing  $A$ .

During this fast transition (from an evaporation regime to a multifragmentation one) the number of monomers decreases from 30 to 10. From  $h = 0.55$  the number of fragments bigger than 2 and the mass of the biggest one steadily decrease, while the number of monomers continuously increases up to eventually a complete gas of monomers for  $h \gtrsim 1.15$ . However between  $h \in [0.55, 0.75]$  the dimers are the dominant fragments, the mean number of dimers even increases within this range (see fig. 3.7(e)).

### Surface tension $\gamma$

As already written in sec. 2.2.3 the depth of the convex intruder in the specific entropy  $\Delta s_{surf}$  can be linked to the surface tension  $\gamma$  by

$$\gamma = T_t \frac{A \Delta s_{surf}}{\mathcal{A}}, \quad (3.25)$$

where  $\mathcal{A}$  is the interphase surface area,  $T_t$  the transition temperature defined by the Maxwell line and  $A$  the system total number of atoms.

Gross and Madjet have presented in [GM97] the first successful microscopic calculation of the surface tension  $\gamma$  in liquid sodium (and other metals) at atmospheric pressure. The principal obstacle towards an estimate of  $\gamma$  is the definition and estimate of  $\mathcal{A}$  (see discussion in sec. 2.2.3 in part I). In [GM97] the authors proposed the total surface area of the fragments of total mass bigger than 1 as a measure of  $\mathcal{A}$ . This area is proportional to  $N_{\text{eff}}$ , the effective number of surface atoms

$$N_{\text{eff}} = \sum_{j=2}^A j^{2/3} \xi_{\mu}(j), \quad (3.26)$$

where  $\xi(j)$  is the mean number of clusters of size  $j$  in the mass distribution  $\mu$ . The interphase surface area is given by

$$\mathcal{A} = 4\pi r_w^2 N_{\text{eff}}, \quad (3.27)$$

where  $r_w$  is the Wigner–Seitz radius.

In [GM97]  $N_{\text{eff}}$  is approximatively constant in the evaporation region for  $A = 200$  and  $A = 3000$  (see fig.1 in [GM97]), then it increases abruptly at the beginning of the multifragmentation. Finally it decreases and eventually vanishes in the gas phase. In [GM97] the value of  $N_{\text{eff}}$  used in eq. (3.27) to estimate the surface tension (or to be more precise the surface tension parameter divided by the transition temperature  $\frac{\sigma}{T_t} = 4\pi r_w^2 \frac{\gamma}{T_t} = \Delta s_{surf} \frac{A}{N_{\text{eff}}}$ ) is the average of  $N_{\text{eff}}$  over the evaporation region.

In the new simulations  $N_{\text{eff}}$  is not constant at all for either  $A = 200$  or  $A = 1000$  (see figs 3.10 and 3.11 on the next page) or for any other studied system size. For  $A = 200$ ,  $N_{\text{eff}}$  is an increasing function in the evaporation region and *also* in the multifragmentation one for  $h < 0.75$ . This is due to the huge ongoing production of 2-mers up to  $h = 0.75$  (see fig. 3.7 on page 51). This can be verified in fig. 3.10 where  $N_{\text{eff}}$  has been plotted for another definition, i.e. the same as the one given by eq. (3.26), but the sum goes from 4 to  $A$  (instead of 2 to  $A$ ). The qualitative behavior of this new  $N_{\text{eff}}$  is similar to the one of  $N_{\text{eff}}$

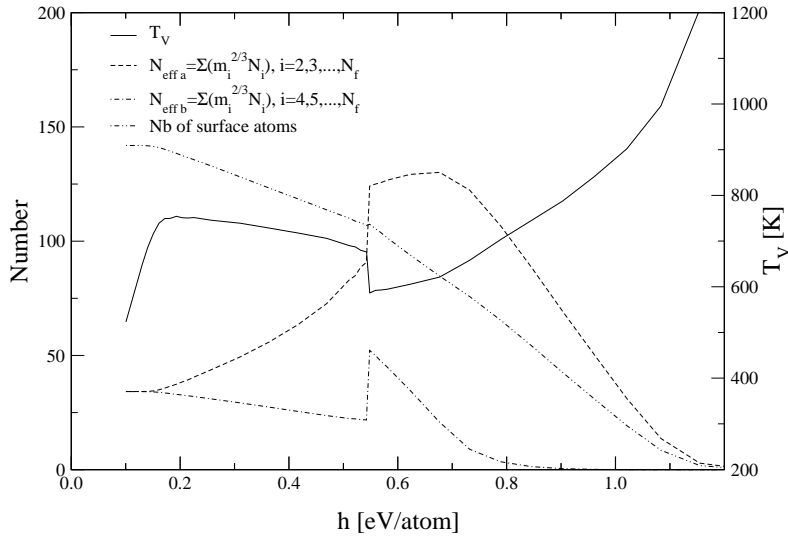


Figure 3.10: Effective number of surface atoms  $N_{\text{eff}}$  based on different definitions ( $A = 200$ ) and microcanonical temperature  $T_V$  (solid line). The definitions for  $N_{\text{eff}}$  are (a)  $N_{\text{eff } a} = \sum_{i=2}^{N_f} i^{2/3} \xi(i)$  (dashed line), (b)  $N_{\text{eff } b} = \sum_{i=4}^{N_f} i^{2/3} \xi(i)$  (point-dashed line) and (c) the number of surface atoms  $N_{\text{eff } c} = N_s^*$  as defined by eqs. 3.4a and 3.4b on page 43 (point-point-dashed line).  $N_{\text{eff } b} - N_{\text{eff } a}$  gives simply the 2-mers contribution since  $\langle N_d \rangle \gg \langle N_t \rangle$  (see fig. 3.7).  $N_{\text{eff } a}$  increases up to  $h = 0.75$ , i.e. even in the multifragmentation regime (this is a consequence of the 2-mers production see fig. 3.7) while  $N_{\text{eff } b}$  steadily decreases apart at  $h \approx 0.55$  where it suddenly jumps because of the production of many 8-mers and 4-mers.

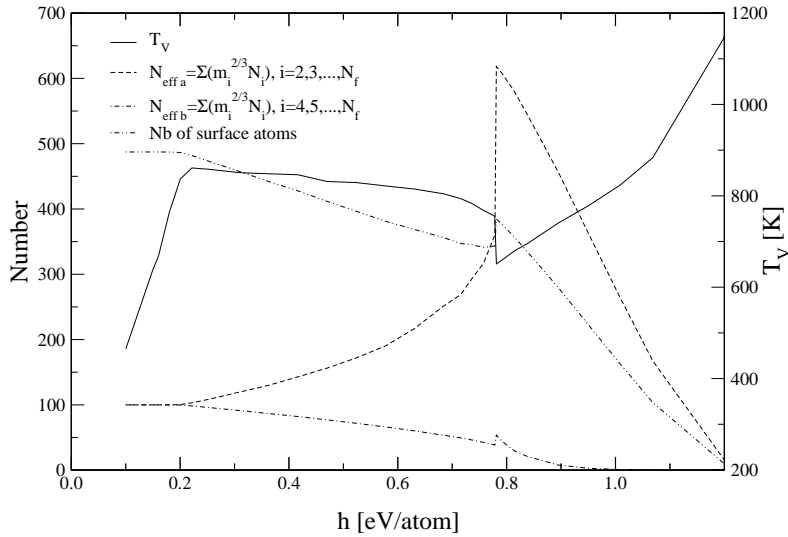


Figure 3.11: Same as fig. 3.10 but for  $A = 1000$ .  $N_{\text{eff } a}$  does no longer increase in the multifragmentation regime. The contribution of the 2-mers to  $N_{\text{eff } a}$ , i.e.  $N_{\text{eff } b} - N_{\text{eff } a}$  is even more important than for  $A = 200$ .

presented in [GM97], hence by analogy and also by considering that the 2-mers and the 3-mers can be regarded as members of the vapor, it is the average over the evaporation region of the new  $N_{\text{eff}}$  that is used in the rest of this section to estimate the interphase surface area. And the results are for  $A = 200$

$$\begin{aligned} N_{\text{eff}} &= 29.3 \\ \frac{\sigma}{T_t} &= 2.61. \end{aligned}$$

The bulk values are  $N_{\text{eff}} = \infty$  and  $\frac{\sigma}{T_t} = 7.41$  [GM97].

Clearly these results suffer from the ambiguity of the definition of the surface area, and as any other “reasonable” definition the one used here is rather arbitrary (see discussion in sec. 2.2.3). Hence the error bars on  $\frac{\sigma}{T_t}$  are big. Nevertheless one can see that microscopic computations give at least the order of magnitude of the transition parameters. For increasing system size these estimates become better, see sec. 3.4.2 where the scaling properties of the transition parameters (including  $\frac{\sigma}{T_t}$ ) are discussed.

### Comparison with [GM97]

As already noticed there are some differences between the results for the liquid–gas phase transition of small sodium clusters presented here and the one by Gross and Madjet published in [GM97]. In the following the origins of some of these differences are discussed and explained.

In fig. 3.12 a summary of the results obtained from MMMC77 for  $N_a 200$  is shown [GM97, GROA].

First, note that the temperature plotted is not  $T_V(h)$  but the microcanonical temperature at *fixed pressure*  $T_p(\epsilon) \doteq \beta_p^{-1}(\epsilon)$ , where

$$\beta_p \doteq \left. \frac{\partial S}{\partial E} \right|_p \quad (3.28)$$

$$= \beta_V \left[ 1 - p \frac{\left. \frac{\partial p}{\partial E} \right|_V}{\left. \frac{\partial p}{\partial V} \right|_E} \right], \quad (3.29)$$

where  $p$  is the microcanonical pressure (see app. D). For small pressure  $\beta_p > \beta_V \Leftrightarrow T_p < T_V$ . As the  $pv$ -shift is not very important at atmospheric pressure (see footnote q on page 52) one can use alternatively  $\epsilon$  or  $h$  as a parameter (although  $h$  is the correct one according to standard thermodynamics). But the choice of  $T_p$  as an observable changes clearly the value of the transition parameters. In practice as it is shown below, in the transition region, the caloric curves  $T_p$  are simply shifted vertically compared to  $T_V$  curves, i.e.  $T_p \approx T_V - K$ , where  $K$  is a positive constant ( $K$  is of the order of 150 Kelvin for  $A = 200$ ).

The results in fig. 3.12 are qualitatively comparable with the ones shown in fig. 3.7 on page 51. The main qualitative difference is the absence in MMMC95 of the “second” transition from dimers to monomers at  $\epsilon^* \approx 1.1$  eV/atom in fig. 3.12. This transition has two origins. The first one is a missing move in the algorithm of MMMC77. To be more precise MMMC77 proposes the move

$$2 \rightarrow 1 + 1, \quad (3.30)$$

“splitting of a dimer” but not its inverse ( $1 + 1 \rightarrow 2$ ). This missing move breaks “locally” the detailed balance condition (see app. B). At  $\epsilon^* \approx 1.1$  there are mainly dimers and

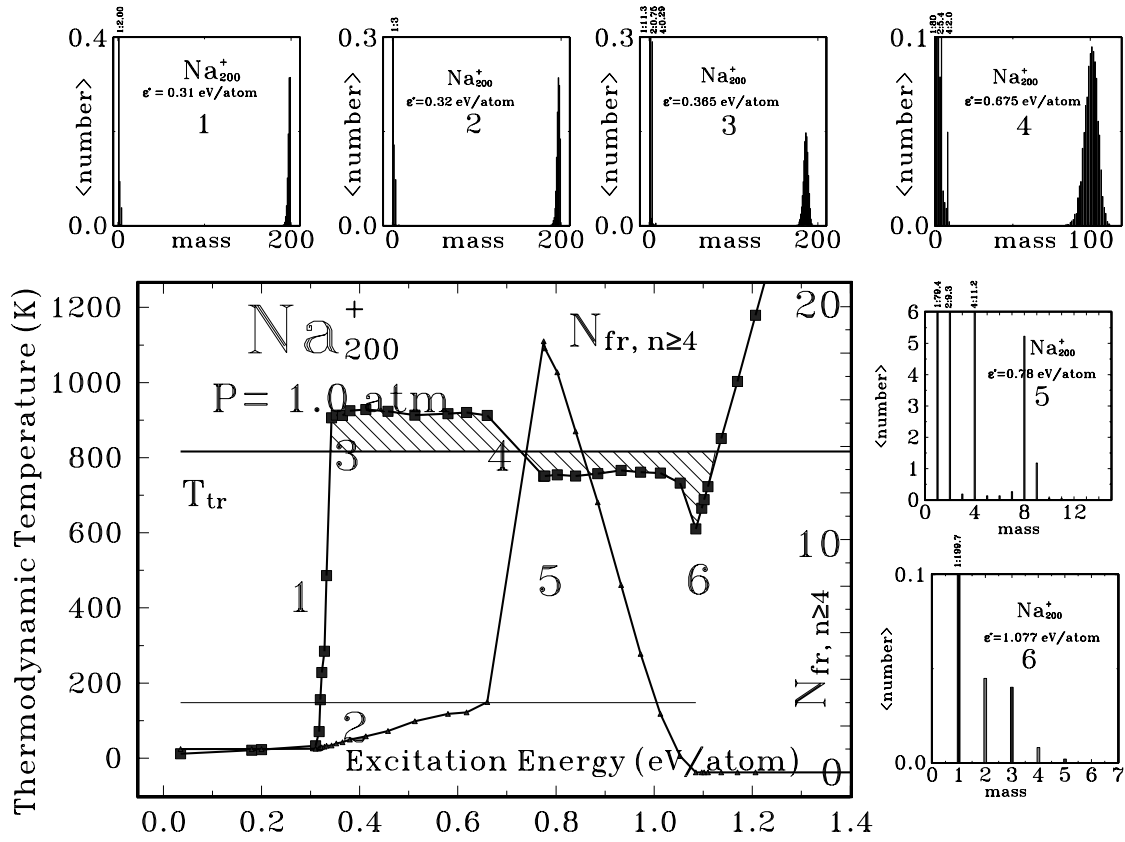


Figure 3.12:  $\text{Na}_{200}$  at 1 atm from [GM97, GROA]. Microcanonical temperature at *constant pressure* (square) as a function of the excitation energy  $\epsilon^*$ , number of fragments of mass bigger than 3 (triangle) and Maxwell line. The small figures show the mass distribution of fragments at six different  $\epsilon^*$  which are indicated in the main figure by their number. The small vertical numbers on the top of the mass distribution give the real number of fragments, e.g. 2 : 9.3 means there are on the average 9.3 dimers at  $\epsilon^* = 0.78$  eV/atom.

monomers, so if the move  $2 \rightarrow 1 + 1$  is accepted, the simplest (“shortest”) way to go back is the following chain of successive moves

$$\begin{aligned} 1 + 2 &\rightarrow 3, \\ 1 + 3 &\rightarrow 4, \\ 4 &\rightarrow 2 + 2. \end{aligned}$$

But as it is suggested by the small number of trimers and 4-mers, the probability of occurrence of this chain of events is very small. Hence at  $\epsilon^* \approx 1.1$  once a dimer is split up into two monomers the monomers remain as they are for the rest of the MMMC77 run. Thus MMMC77 produces more monomer than it should. This abnormal increase of the number of particles cools down the system.

The second explanation for the lack of second transition is the choice of  $T_p$  as observable as it is shown below.

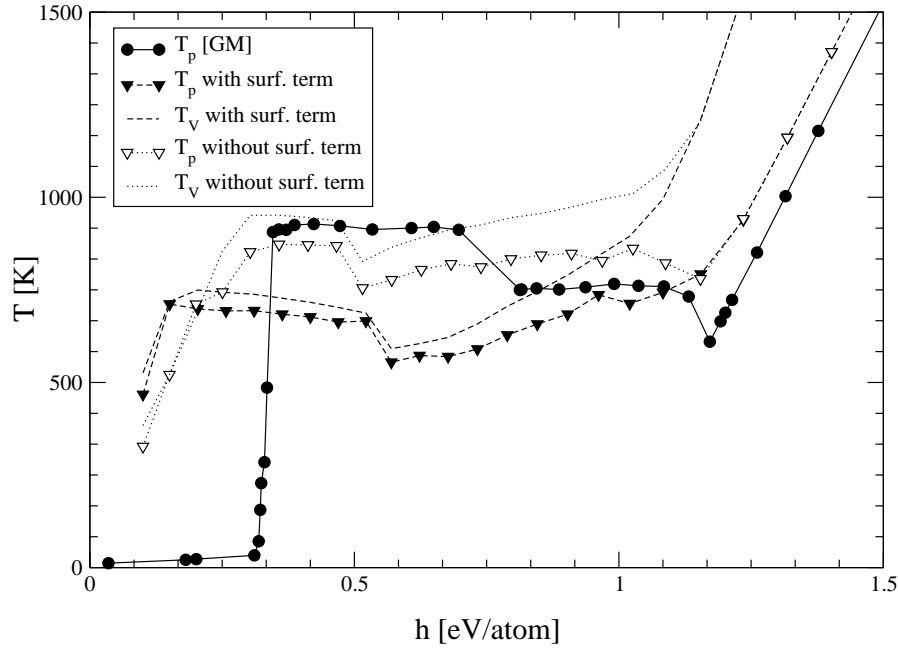


Figure 3.13:  $N_{a200}$ . Temperature at fixed pressure  $T_p$  from [GM] $\equiv$ [GM97] (solid line, circles), from the present work (triangles) and temperatures at fixed volume  $T_V$  (no symbol) as functions of the specific enthalpy  $h$ . The two latter temperatures are plotted for MMMC with surface entropy term for the cluster internal entropy (dashed line) and without this surface term (dotted line). Note that the statistical errors on  $T_p$  are larger than the one on  $T_V$  since  $T_p$  relies on the estimate of second order derivatives of  $S$  (see app. D). These errors are of the order of 10 %  $\rightarrow \pm 80$  K toward  $h = 1.1$  eV/atom. The “second” phase transition in  $T_p$  [GM] can only merely be seen in  $T_p$  without surface term and is completely absent in the other curves from MMMC95.

To enable qualitative comparisons, different temperature curves from several models are plotted in fig. 3.13. First the solid line with circles reproduces the  $T_p$  curve from fig. 3.12, but now  $T_p$  is a function of  $h$ . The other curves represent temperatures from MMMC95. The ones with symbols are microcanonical temperatures at constant volume  $T_V$  and the curves without symbols are microcanonical temperatures at constant pressure  $T_p$ . The dashed lines reproduce the results from fig. 3.7 on page 51. One of the major difference between the two MMMC models is the presence of a surface entropy term for clusters entropy in MMMC95 (see sec. 3.2 and eq. (3.3) on page 43). So in order to emphasize the role of this surface term the temperature curves ( $T_V$  and  $T_p$ ) from MMMC95 but *without* surface terms<sup>†</sup> are also plotted in fig. 3.13 (dotted lines). One can find a summary of the results for the model without surface term in fig. 3.14 on the next page.

Compared to MMMC77, in MMMC95 the evaporation starts earlier<sup>‡</sup>. This is because of the internal entropy model, since in the new version the specific entropy is smaller than in

<sup>†</sup>This is simply achieved by setting  $N_v^*$  the number of volume “atoms” to  $N^* = N - 2$  the cluster total number of “atoms” in eqs.(3.3) and (3.4) on page 43.

<sup>‡</sup>It occurs well below the imposed limit in the internal excitation energy at  $\epsilon^* = \epsilon_{max}^* = 0.35$  eV/atom, see item 3 on page 41. This is in contrast with MMMC77 where the transition starts at  $\epsilon_{max}^*$  for any system size  $A$  (see figs. 3 and 4 in [GM97]).

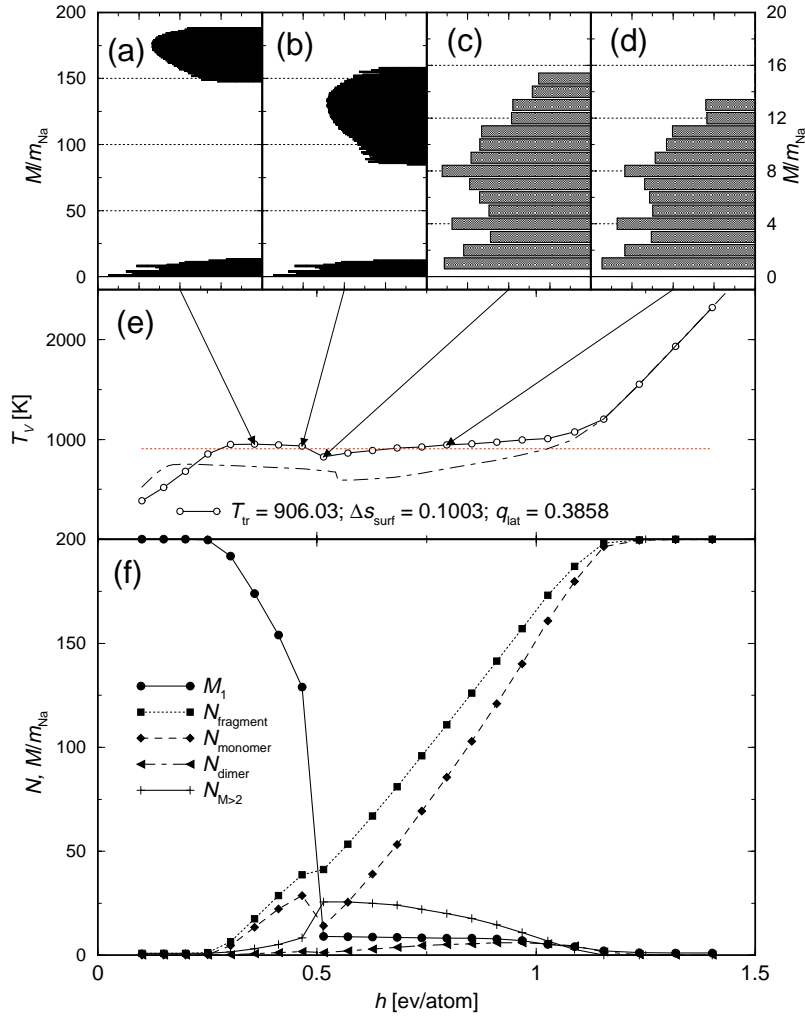


Figure 3.14: Same as fig. 3.7 on page 51,  $A = 200$  but this time the internal entropy of clusters bigger than 3 contains no surface term, i.e. all the internal entropies are described by the bulk one. In panel (e) the temperature from fig. 3.7(e) is reproduced (dot-dashed line) in order to compare the two temperature curves. As expected the evaporation starts later  $h \approx 0.25$  eV/atom, and the multifragmentation appears earlier, at  $h \approx 0.45$ , since the small fragments have a much bigger specific entropy (at fixed specific energy). The mass distribution of small fragments is also different from the one in fig. 3.7. The dimers do no longer play a key role and are replaced by 4-mers and 8-mers. This is a direct consequence of their larger internal specific entropy. The overall temperature curve is above the one in fig. 3.7 since the number of fragments is here smaller than the one with surface term (e.g. at  $h = 0.5$  there are 40 clusters, see (f), whereas in fig. 3.7(f) one can find 75 fragments). The transition parameters are written in panel (f). Note the small specific surface entropy and latent heat compared to the ones of the model with surface entropy term, see e.g. fig. 3.7(e).

the older (this explanation is supported by the  $T_V$  curve of MMMC95 without surface term).

Hence as the specific entropy of a fragment is smaller the big cluster starts to evaporate monomers much earlier ( $h \approx 0.35$  in MMMC77 compared to  $h \approx 0.15$  in MMMC95). This leads to a larger number of translational-rotational dofs which in its turn cools the system down. One can check this argument in fig. 3.14.

The multifragmentation occurs also at smaller  $h$  in MMMC95, but this time the difference of specific internal entropy cannot be invoked since as one can see on fig. 3.13 and 3.14 a higher specific entropy implies an even earlier start of the multifragmentation. Here an explanation for this fact is that contrary to MMMC77, in MMMC95 each cluster has its own internal energy (item 3 on page 41), thus at fixed overall internal energy the system has more dofs in MMMC95 than in MMMC77 due to the partitioning of the excitation energy among the clusters.

In the gas phase the temperature curves are shifted to lower  $h$  in MMMC95 compared to MMMC77 ( $\Delta h \approx 0.1$  eV/atom). This comes from the fact that the ground state binding energy in MMMC95 is higher than in MMMC77 ( $\sim -180$  eV compared to  $\sim -199$  eV), due to a slight changes in the input parameter values of the metal-drop model for the binding energies (i.e.  $a_v$  and  $a_s$ ).

### 3.4.2 Scaling properties

In fig. 3.15 a summary of the results for  $A = 1000$  at atmospheric pressure is plotted. The overall qualitative behavior is similar than for  $A = 200$ . The main quantitative differences are

- Essentially because of the increase of the cluster specific internal entropy at fixed  $\epsilon^*$  with cluster size, the evaporation starts later,  $h \sim 0.2$ . Hence the overall evaporation region takes place at higher temperatures.
- The multifragmentation is also shifted to higher enthalpies. The reasons are first, again the increase of the specific internal entropy, second the lower sensitivity of the system to the symmetrization weight factor (compared with  $\omega_{NCC} \sim V^{N_f}$  and  $\omega_{pl} \sim E_r^{\tilde{N}}$ ) and finally the relatively smallest gain in energy due to binding energy of small clusters. The two latter arguments induce a decrease in the number of clusters bigger than one in the gas part of the mass distribution. This favors an larger number of the number of monomers which now dominate the mass distribution over almost all the enthalpy range (except of course at very low energy and in a tiny region around  $h = 0.8$ , see fig. 3.15(g)).
- The relative fluctuations of the size of the big liquid cluster are smaller than for  $A = 200$  (compare figs. 3.7(a)–(b) and figs. 3.15(a)–(b)).

As a consequence of the above second point, the length of the evaporation region gets longer relatively to the one of the multifragmentation regime (for  $A = 200$  the ratio of the former  $h$ -length to the later is  $\sim 0.6$  see fig. 3.7 whereas for  $A = 1000$  this ratio is about 1.4).

The relative weight of  $p_{NCC}$  the “avoided volume” pressure in the total pressure  $p = p_{kin} + p_{NCC}$  where  $p_{kin}$  is the usual kinetic pressure (see sec. 3.3 and eq. (3.24) on page 49) is plotted on fig. 3.16. At atmospheric pressure the contribution from  $p_{NCC}$  can be neglected except at very low enthalpies; there a small volume is needed because almost all the excitation energy is absorbed by the internal dofs of the liquid cluster. With increasing

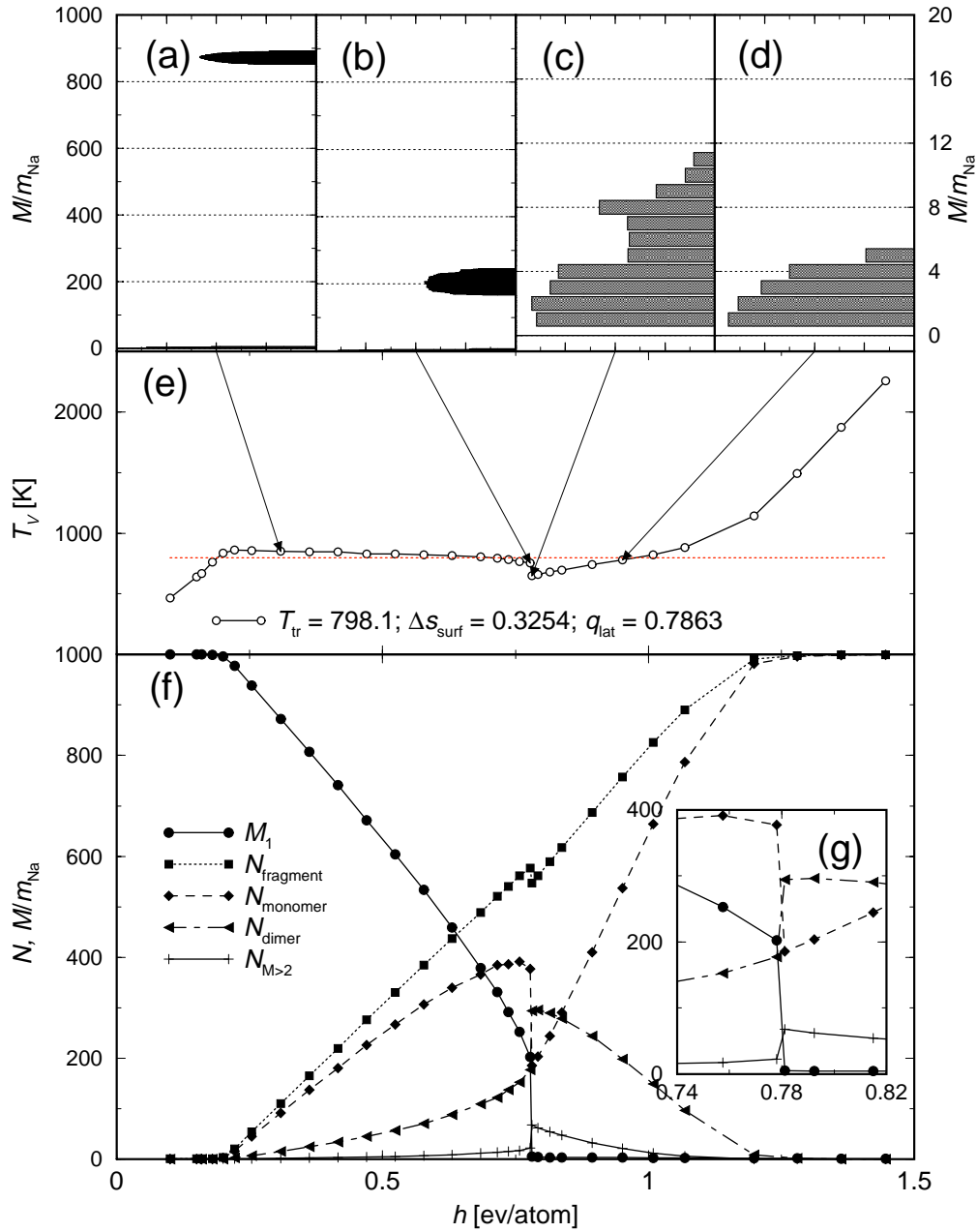


Figure 3.15: Summary of the results for  $N_a = 1000$  at 1 atm (see fig. 3.7 on page 51). Compared with  $N_a = 200$  the evaporation and the multifragmentation start later. The specific length of multifragmentation region shrinks relatively to the one of the evaporation regime. In the latter regime the number of monomers is now clearly larger than the number of dimers. Those dimers are now dominant only within a small enthalpy range ( $h \approx 0.8$ , see panel (g)). During the overall liquid–gas transition the number of clusters bigger than one in the gas part of the mass distribution decreases. Compared to fig. 3.7 where  $A = 200$  these results show a clear trend towards the bulk liquid–gas transition.

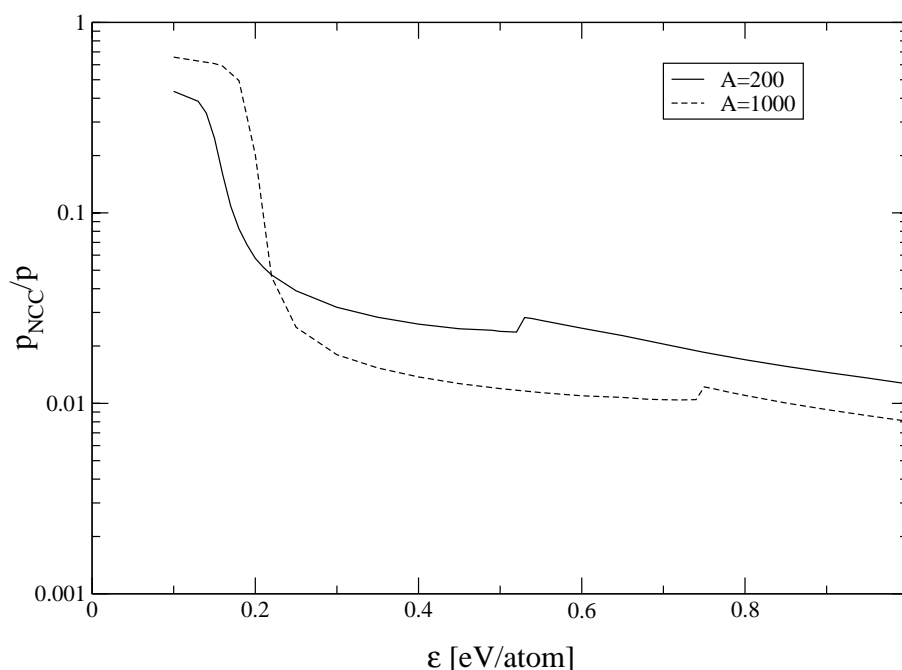


Figure 3.16: Relative weight of  $p_{NCC}$  in the total pressure versus  $\epsilon$  for  $A = 200$  (plain line) and  $A = 1000$  (dashed line).  $p_{NCC}$  is the pressure term coming from the avoided volume. At low pressures  $p_{NCC}$  can be neglected apart at very low enthalpies where there is only one cluster.  $p_{NCC}$  gets more negligible as  $A$  increases.

system size  $p_{NCC}$  is more and more negligible as soon as there are more than one fragment in the system; there, at the thermodynamical limit  $p_{NCC} = 0$ .

In fig. 3.17 the microcanonical temperature (at fixed volume) are plotted as a function of the specific enthalpy and for several system total sizes (from  $A = 50$  up to  $A = 5000$ ). One can see a tendency towards the bulk limit even though for  $A = 5000$  the curve is still far away from this limit<sup>v</sup>. The specific length of the multifragmentation region gets short with increasing  $A$  and eventually vanishes at the thermodynamical limit.

The transition parameters as functions of the system total size  $A$  are given in table 3.2 and shown in fig. 3.18 on page 66. They all clearly tend towards their bulk values (as already suggested by the temperatures curves in fig. 3.17). However the specific surface entropy is an increasing of  $A$  for  $A \lesssim 500$ . Hence for  $A \lesssim 500$  the system is far from having reach a “scaling behavior” where the specific surface effects would simply vanish as  $A^{-1/3}$ .

To emphasize the influence of the internal entropy surface term in the cluster entropy model (eq. (3.3)), the transitions parameters for the model *without* this surface term are given in table 3.3. As in table 3.2 they also show a clear trend towards their values at the thermodynamical limit. The notable difference with the results presented in table 3.2 is the very low values of the surface entropy depth  $\Delta s_{surf}$  and hence of  $\sigma/T_t$ . This is due mainly to the very early occurrence of the multifragmentation and the relatively short

<sup>v</sup>Remember that the proportion of surface “atoms” for  $N^* = 5000$  is still around 35 %, see fig. 3.5 on page 45.

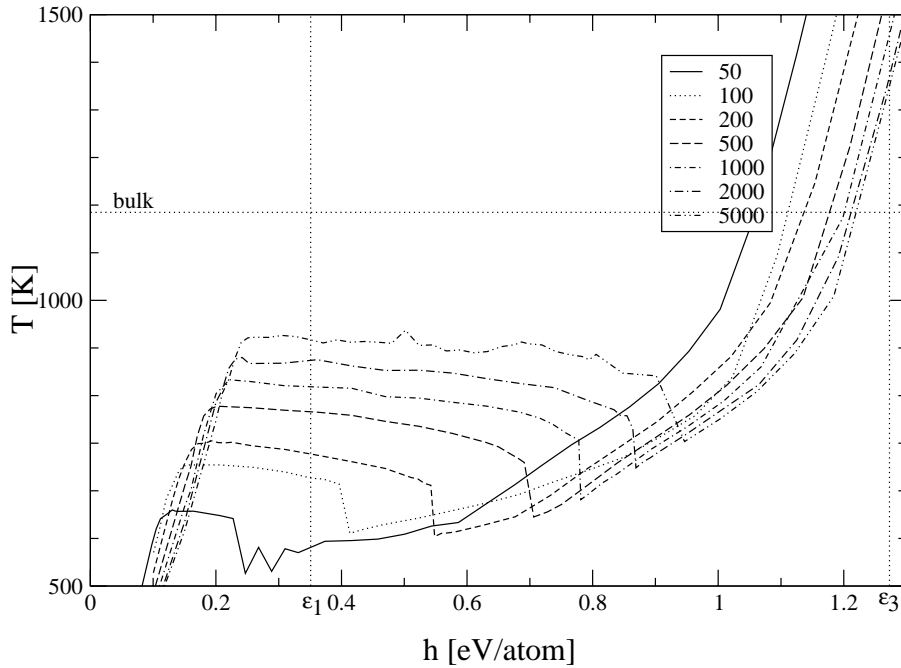


Figure 3.17: Caloric curves versus  $h$  for several system total masses, from  $A = 50$  up to  $A = 5000$ . The bulk transition temperature ( $T_{t\ bulk} = 1156$  K) is indicated by the horizontal dotted line.  $\epsilon_1 \approx h_1$  ( $\epsilon_3 \approx h_3$ ) is the specific energy at which the bulk liquid–gas phase transition starts (ends). For  $A \lesssim 1000$  the statistical error on the temperature estimate is for each point below 1 %. Above  $A \approx 1000$  this error grows rapidly with  $A$ : at  $A = 5000$  it is about 5 %. Thus the “structures” at the beginning of the multifragmentation for  $A = 50$  are not due to statistical fluctuations. Each sudden drops of the temperature in the multifragmentation region corresponds to the fragmentation of a 8–mers.

evaporation region and also to the slightly different mass distributions<sup>w</sup> which induces higher temperature in the multifragmentation regime.

### 3.5 Summary

Although the cluster model and the numerical code have changed the overall qualitative pictures of the liquid–gas phase transition of sodium clusters at atmospheric pressures, as given in [GM97], is confirmed (apart the “second” phase transition at high enthalpies). From very low enthalpies up to very high ones there are: first a big liquid cluster, then an evaporation regime (the big cluster evaporates very light fragment). This evaporation is eventually followed by a complete reorganization of the mass distribution (multifragmentation) over a small enthalpy range. Then, there is again an evaporation regime or multifragmentation regime (from intermediate cluster masses to monomers). Finally, at high enthalpies the system is a gas of monomers.

According to the definitions of phases and phase transition given in chapter 2, only the

<sup>w</sup>without surface terms there are in the mean less fragments; the monomers are bounded in bigger clusters, e.g. 8–, 4– and 2–mers, see figs. 3.7 and 3.14

$A$	50	100	200	500	1000	2000	5000	<b>bulk</b>
$T_t$	584.5	659.9	684.6	752.7	799.1	842.4	891.5	<b>1156</b>
$q_{lat}$	0.370	0.557	0.626	0.723	0.786	0.843	0.871	<b>0.923</b>
$s_{boil}$	7.34	9.80	10.62	11.14	11.43	11.62	11.34	<b>9.267</b>
$\Delta s_{surf}$	0.165	0.278	0.383	0.358	0.327	0.287	0.291	
$N_{\text{eff}}$	13.3	20.5	29.3	48.6	74.7	105	219	$\infty$
$\sigma/T_t$	0.09	1.35	2.61	3.65	4.38	5.47	6.63	<b>7.41</b>

Table 3.2: Scaling of the transition parameters deduced from the Maxwell construction (cluster internal entropy with surface term).  $T_t$ ,  $q_{lat}$ ,  $s_{boil}$ ,  $\Delta s_{surf}$ ,  $N_{\text{eff}}$  and  $\sigma/T_t$  are the transition temperature, the latent heat, the entropy gain of an evaporated atom  $s_{boil} = \frac{q_{lat}}{T_t}$ , the entropy surface, the effective number of interphase atoms and the ratio of the surface tension parameter  $\sigma$  to the transition temperature  $T_t$ , respectively. The experimental bulk values are given in the last column.

$A$	50	100	200	500	1000	2000	<b>bulk</b>
$T_t$	750	843	911	960	985	1010	<b>1156</b>
$q_{lat}$	0.154	0.252	0.401	0.638	0.673	0.750	<b>0.923</b>
$s_{boil}$	2.38	3.46	5.11	7.71	7.93	8.61	<b>9.267</b>
$\Delta s_{surf}$	0.0836	0.103	0.103	0.0846	0.0790	0.0840	
$N_{\text{eff}}$	16.8	25.6	39.3	77	124	209	$\infty$
$\sigma/T_t$	0.249	0.40	0.524	0.549	0.637	0.803	<b>7.41</b>

Table 3.3: Scaling of the transition parameters given by the Maxwell construction (cluster internal entropy without surface term), see table 3.2.

first evaporation and the multifragmentation are phase transitions, at least in the energy direction. For a complete picture, it is necessary to study the entropy and its derivatives in the energy-volume plane. It is not excluded that the multifragmentation regime (i.e. evaporation of intermediate cluster sizes), corresponds to a phase transition in the *volume* direction.

The influence of different parameters has been studied in this chapter.

Only the quantitative behavior is affected by “reasonable” choices for the clusters internal entropy. In order to choose among these models for the internal entropies, experimental inputs are needed.

The main factors which lead the system to the multifragmentation regime are the symmetrization weight factor and the electronic shell effects. Thus, the confidence on the prediction of the presence of this regime (for systems at equilibrium) is good, because these factors are well established physical facts (theoretically and experimentally). However, at this moment, the cluster experiments are too rough in order to make any comparison with the present model, see e.g. [SKVIH98].

In this chapter it is shown how and why the multifragmentation vanishes at the thermodynamical limit. Hence, the microcanonical thermodynamics allows one to have access to physical phenomena that do not exist at this limit. The multifragmentation regime is only hardly accessible to a canonical computation. Indeed, its associated temperature is

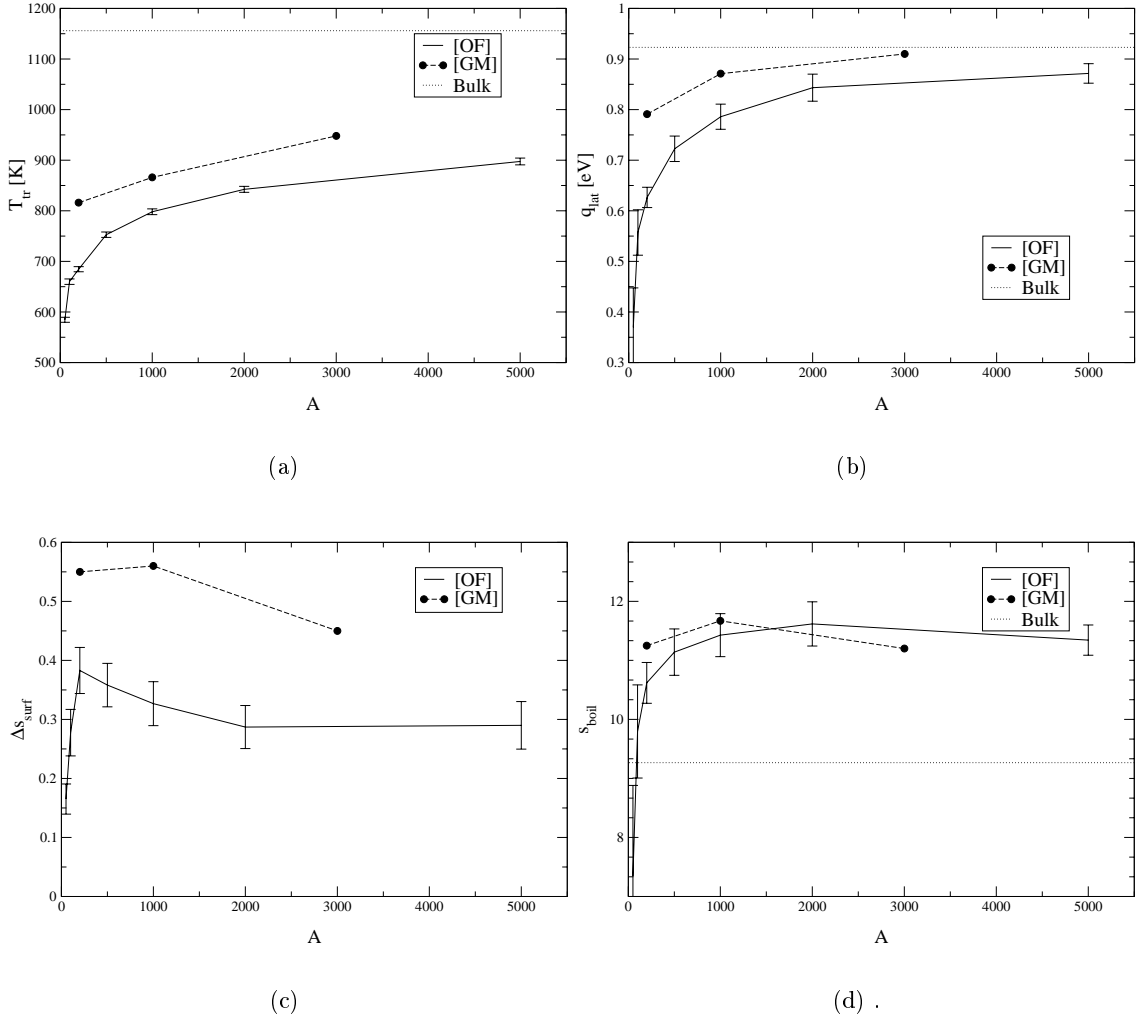


Figure 3.18: Scaling of some transition parameters. (a) Transition temperature  $T_t \equiv T_t$ . (b) Latent heat  $q_{lat}$ . (c) Specific surface entropy  $\Delta s_{surf}$ . (d) Entropy gain of an evaporated atom  $s_{boil} \doteq \frac{q_{lat}}{T_t}$ . On each panel the results from [GM]  $\equiv$  [GM97] (dashed line) and from the present work [OF] (plain line) are plotted along with the resp. bulk value (dotted line). The error bars for [OF] are estimated granted the fact that the fluctuations of the temperature are of the order of 1 % (this is not the case for  $A = 5000$ , for this system size the error bars are here underestimated by a factor  $\sim 2$ , see fig. 3.17 on page 64).

in the transition region (defined by the Maxwell construction). Therefore, these points do not correspond to global maxima of the Laplace transform, or, to use, the usual “canonical” vocabulary, they do not correspond to minima of the free energy.

Microcanonical thermostatics offers an efficient way to estimate the surface entropy without imposing any a priori geometry to the surfaces. But the definition of the surface itself area is ambiguous for the present cluster model. Hence, the numerical values for the values of the surface tension parameters presented in this chapter have big error bars. Nevertheless, for systems composed of only a few hundreds of particles, the order of

magnitude of the bulk value is already reached.



# Chapter 4

## Towards the critical point

### 4.1 Introduction

The liquid–gas phase transition of small clusters of sodium at atmospheric pressure is discussed in chap. 3. For the bulk matter this first order phase transition has a critical point at a pressure of  $p_{c\infty} = 253$  atm and a temperature of  $T_{c\infty} = 2503.7$  K [FL95]. There the density is  $\rho_{c\infty} = 219$  kg · m<sup>-3</sup> [FL95] which corresponds to a packing fraction of  $\kappa_{c\infty} = \frac{v_0}{v_c} \approx 0.3$  (where  $v_0$  is the Wigner-Seitz volume of an atom of sodium, assuming that it is a sphere of radius 2.3 Å and  $v_c$  is the critical specific system volume). Hence, one can naturally ask whether systems with a few hundreds of atoms also present a critical point in the sense given in sec. 2.3 on page 30 in chapter 2. I.e. by means of properties of the local curvature of the microcanonical entropy surface. The latter is a function of the energy and of the system volume. If there is a second order phase transition, one can further ask about the physical properties of an ensemble of systems at this transition (pressure, density, mean mass distribution, etc.) and how they can be related to their bulk values (scaling properties).

In this chapter several attempts to reach the critical point of the liquid–gas phase transition of finite size clusters are presented. First, within the cluster MMC model introduced in the previous chapter with different technics to estimate  $NCC$  ( $\sim$  the avoided volume to the clusters). Second, as the previous MMC model approach fails due to computational difficulties (see below), a new model, inspired from lattice gas models, is presented. This new model shows for the time the critical point of the liquid–gas transition of such finite size physical models.

### 4.2 mmmc results

#### *NCC* from EOS

In chapter 3, the caloric curves are obtained from MMC using the hard spheres equation of states (EOS) approximation to estimate  $NCC$  (see app. A.1.2). At atmospheric pressures, there is a first order phase transition. The Maxwell line gives the transition parameters. The specific enthalpies at the two end points of the Maxwell construction are noted by  $h_1$  (liquid side) and  $h_3$  (gas side). The specific latent heat of the transition is defined as  $h_3 - h_1$  (see sec. 2.2.3). In the bulk, at the critical point, these two points merge, i.e. the latent heat vanishes.

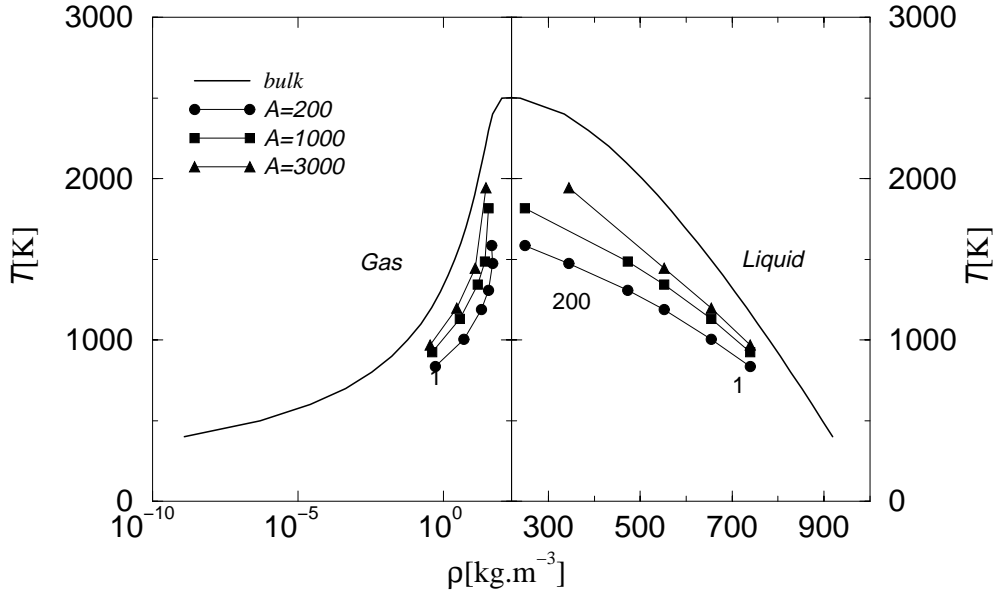


Figure 4.1: Temperature versus density  $\rho$  at  $h_1$  (liquid side) and  $h_3$  (gas side) given by the Maxwell construction for different system sizes and pressures ( $p = 1, 10, 50, 100, 200, 300$  atm, the latter is well above the bulk critical pressure  $p_{c\infty} = 253$  atm), compared to the bulk liquid and gas densities along the saturation curve (solid line, no symbol) [FL95]. The computations are done within MMMC95 with  $NCC$  derived from the hard spheres equation of state (see app. A.1.2). For small pressures there is a clear tendency towards the bulk curves. None of the finite size curves are closed for  $p = 300$  atm, this is perhaps an indication that the critical for small systems is located at larger pressures than the bulk one.

As a first attempt to reach the critical point of finite size sodium clusters (if it exists), one can use the same procedure as in the previous chapter and compute caloric curves at constant pressure for higher values of  $p$ . Then, one can check whether a critical point shows up, i.e. whether  $h_3 - h_1 \rightarrow 0$ .

In fig. 4.1 the transition temperatures are plotted versus the liquid and the gas density at  $h_1$  (liquid) and  $h_3$  (gas) for different pressures (from 1 atm up to 300 atm) and for several system total masses  $A = 200, 1000$  and  $3000$ . The curves show a clear tendency towards the bulk saturation density curve with increasing  $A$ . However there is no critical point, i.e. no curve is closed even for a pressure as large as 300 atm (for  $A = 200$  and  $A = 1000$ ). The latter pressure is well above the bulk critical one. One can even see that the gas density for  $A = 200$  decreases for  $p > 200$  atm.

At these high pressures a closer study of the simulation outputs shows that

- (a) almost all the pressure comes from the avoided volume pressure term  $p_{NCC}$  (up to 80 %),
- (b) the system volume  $V$  is actually *too small* to contain all the clusters of a typical mass distribution.

The latter point is due to the approximation used to estimate  $NCC$ , the avoided volume.

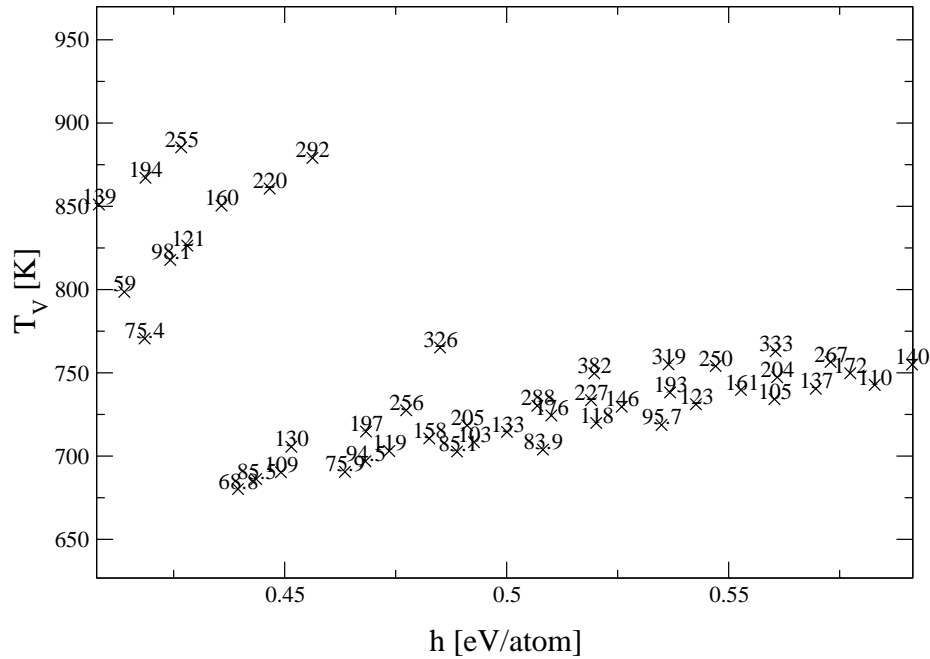


Figure 4.2: Temperature (cross) and pressure (number) as functions of the specific enthalpy  $h$  for various values of  $(E, V)$  near the multifragmentation transition. The system total mass is  $A = 100$ .  $NCC$  is estimated by means of the Monte–Carlo algorithm presented in app. A.2. Clearly for  $p \approx 350$  atm there is still an enthalpy region where  $\frac{\partial T^{-1}}{\partial h}|_{p=cst}$  is positive (at  $h \approx 0.52$  there is a point  $(T_V, p) \approx (750, 382)$  whereas there is at  $h \approx 0.46$  a point for which  $(T_V, p) \approx (870, 292)$ , therefore the isobar  $p = 382$  have an higher temperature at  $h = 0.47$  than at  $h = 0.52$ ). Hence, the critical point of this model, if it exists, is located at a pressure larger than 350 atm, which is well above the bulk value.

As already mentioned this approximation is based on the hard spheres EOS, which is in its turn based on two body correlations. In this approximation, the critical packing fraction is  $\kappa_c = 1$ . This packing fraction, where  $NCC$  diverges, is unrealistic (for the closest packing of equal size hard spheres  $\kappa_c \approx 0.74$ ). Hence, for pressures larger than one hundred atmospheres, in the transition region, the system is no longer in the range of volumes where higher correlations can be neglected. There, the EOS approximation is not valid and MMMC95 do not sample the correct mass distributions. In other words, by using the EOS approximation some mass distributions have a *finite*  $NCC$  although they actually do not fit within the system volume which should imply an *infinite*  $NCC$ .

### $NCC$ from Monte–Carlo

As there is no other suitable approximations of  $NCC$  available for the MMMC model, one has to use Monte–Carlo sampling schemes in order to estimate  $NCC$  (see app. A.2).

In fig. 4.2 the temperature along with the pressure as functions of the enthalpy are plotted for several points in the parameter space  $(E, V)$  toward the multifragmentation transition. The system total mass is  $A = 100$ . One can immediately conclude that there is *no critical point* for such model for pressures below 382 atm, i.e. if there is a critical point for this cluster model then it is located at a pressure much larger than the bulk one

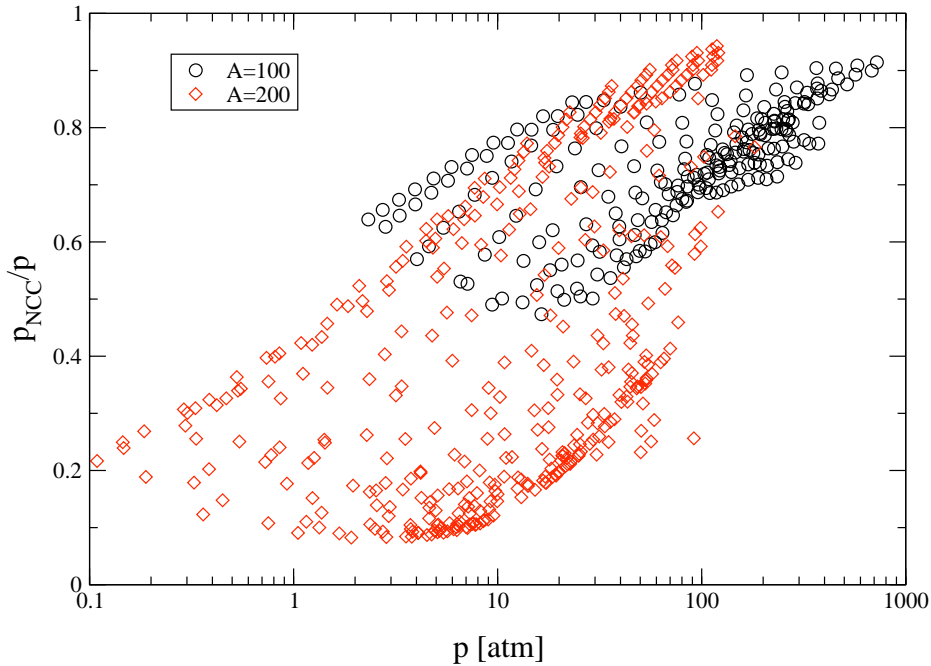


Figure 4.3: Scatter plot of the relative proportion of  $p_{NCC} = \beta^{-1} \langle \frac{\partial \ln NCC}{\partial V} \rangle$ , the avoided volume pressure (see sec. 3.3), in the total pressure  $p = p_{kin} + p_{NCC}$  as a function of  $p$  for  $A = 100$  (circles) and  $A = 200$  (diamonds). Each point in the figure corresponds to one point in the energy–volume plane. As the total pressure increases, the main contribution to  $p$  comes from  $p_{NCC}$ .

(see figure caption).

For such high pressures,  $p_{NCC}$  the avoided volume pressure is the dominant term in the total pressure  $p = p_{kin} + p_{NCC}$  for enthalpies below and in the transition region. At higher enthalpy the kinetic term provides again the main contribution. To illustrate that, a scatter plot of  $p_{NCC}/p$  versus  $p$  is shown in fig. 4.3 for several points in the  $(E, V)$  plane near and below the multifragmentation transition. The system total masses are  $A = 100$  (circles) and  $A = 200$  (diamonds). For pressures larger than 100 atm,  $p_{NCC}$  is at least responsible of 60 % of the total pressure in the transition region. This shows how it is crucial to have accurate estimates of  $NCC$  and of its derivatives.

These results confirm the ones obtain in the previous section. They suggest that the critical point of finite size clusters is located at higher pressure than the bulk one, e.g.  $p_{c A=100} > 380$  atm. To check this hypothesis, one should follow isobars at larger pressures. Unfortunately, this is an impossibly difficult task within MMMC. The typical computation time for one single point in the  $(E, V)$  plane for pressures around 150 atm and near the multifragmentation for  $A = 200$  is one day on an ALPHA-workstation. This time grows *exponentially* with decreasing volume. More than 99 % of the run time is spend in the numerical estimate of  $NCC$  and its derivatives. Thus, a complete study of the transition region at higher pressures is at this moment out of reach.

One may suggest to study smaller systems because less computational efforts should be needed in order to estimate  $NCC$  if the number of fragments is reduced. It is indeed the case. However, on the other hand, the critical point seems to be located at even

higher pressures and hence closer to the critical packing fraction where  $NCC$  diverges<sup>a</sup>. There, it is very difficult to obtain good estimate of  $NCC$  and even more of its derivative with respect to the volume (needed to compute  $p_{NCC}$ , the main component of the total pressure).

### 4.3 Lattice model (cl)

At this moment the critical point is out of reach to MMMC95. As written above, this is due to the very long time needed to estimate  $NCC$ , which is defined as a multiple integral of the centers of mass of the clusters over the system volume (see eq. (A.1a)). One could argue that a solution is to give up this integration, i.e. leaving the weight  $\omega_{NCC}$  and position explicitly the centers of mass event by event along the Markovian chain. However, in order to have a correct detailed balance, one has to estimate the a priori probability (see app. B.2) to find a set of positions for the centers of mass so that all clusters fit within the volume. This probability is nothing else but the inverse of  $NCC$ .

To overcome this main difficulty, a new model is developed. It is inspired from lattice gas models. This new model is called hereafter Clusters on Lattice (CL). In CL the *atoms* are first positioned on a lattice. Hence, the a priori probability to position all the atoms on the grid is the same for all events. The price to pay is that the pressure is no longer an observable as in the cluster MMMC model. The reason is that in CL there is no longer any explicit dependence on the system volume in the microcanonical weight (in MMMC this dependence is carried by  $\omega_{NCC}$  see eqs. (3.19) and (3.23) on page 49).

CL uses the MMMC method. It is a microcanonical model. The total energy, mass and volume  $V = \frac{4\pi}{3}R^3$  are conserved.

#### 4.3.1 Model

As CL and the cluster MMMC model are very similar, only the differences between them are stressed in the following section.

#### Clusters

In MMMC the basic elements are the clusters which are assumed to be spherical hard spheres. In CL the atoms are *first* positioned on a lattice. Two neighboring atoms create a link between them. Linked atoms form together *clusters* (for an illustration see fig. 4.4). Hence, a cluster of a given size can have different shapes characterized by e.g. different principal moment of inertia or total number of links  $l$ . For a given mass  $N$  a cluster can have up to  $l_{\max}$  links ( $l_{\max}$  depends on the cluster size).

Once the clusters are created, there are almost treated as in the cluster MMMC model.

The underlying lattice used in the present work is a fcc lattice (face-centered cubic) [AM76]. This lattice does not pretend to simulate the real geometrical properties of sodium clusters [CS00]. It is only a way to get rid of  $NCC$  and to add some shape dofs. The distance between two sites is adjusted so that the volume of the lattice primitive cell is equal to the Wigner–Seitz volume of an atom  $v_w = \frac{4\pi}{3}r_w^3$ . The coordinate number  $k$  of fcc is 12, i.e. one site has 12 closest neighboring sites.

<sup>a</sup>This is confirmed by the results presented in the next section.

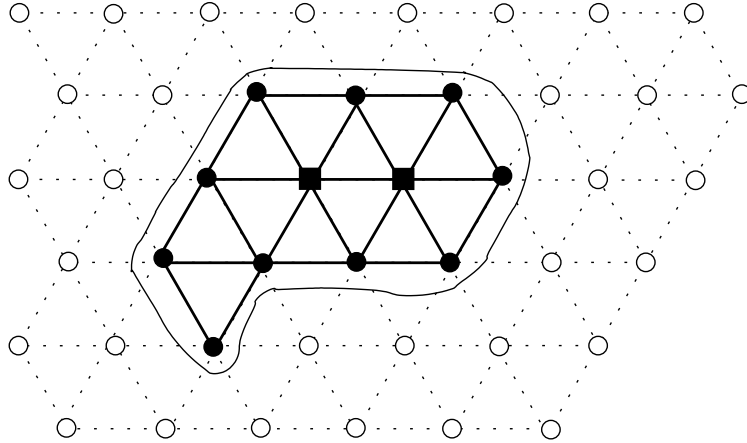


Figure 4.4: Schematic two dimensional illustration of a cluster in CL. An empty lattice site is represented by a circle. A site occupied by an atom is represented either by filled circles or squares. Between two neighboring atoms a link is created (thick segment). An atom whose all neighboring sites are occupied is a volume atom (filled square). In this figure a cluster of size  $N = 12$  is represented. It has two volume atoms and 22 links.

In order to have explicit spatial dimensions<sup>b</sup>, the center of mass of a cluster is assumed to be located within the volume of a primitive cell  $\Delta v = v_w$ .

### Binding energy

In CL the binding energy of a cluster is a function of  $N$  and of  $l$ , its number of links. This implies a shape dependence of the binding energy.

In the limit  $N \rightarrow +\infty$  the binding energy is given by

$$E_b(N, l) \approx N\epsilon_\infty \quad (4.1)$$

$$= \frac{2l}{k}\epsilon_\infty, \quad (4.2)$$

where  $\epsilon_\infty \equiv -a_v = -1.039$  eV/atom is minus the bulk specific binding energy. In the limit  $N \rightarrow \infty$ , each atom has  $k$  neighbors, and there are  $l = N\frac{k}{2}$  links. The binding energy of a finite size cluster is given by

$$E_b(N, l) = -\frac{2l}{k}a_v + K(N), \quad (4.3)$$

where  $K(N)$  is a constant. For  $N > 21$ ,  $K(N)$  is chosen in order to adjust the binding energy of the cluster with the largest number of links (at fixed  $N$ ) to the metal-drop formula, see eq. (3.1). For  $N < 21$ , the binding energy of the cluster with the largest number of links (at fixed  $N$ ) is adjusted to the experimental data. Hence, the electronic shell effects, which are crucial for the presence of the multifragmentation regime (as shown in sec. 3.4.1), are implemented in CL. In the limit  $N \rightarrow \infty$ ,  $K(N)$  vanishes.

<sup>b</sup>This is needed in order to make the microcanonical weight  $\omega(\mathbf{x})d\mathbf{x}$  dimensionless, see sec. 4.3.2.

### Internal entropy

For the specific internal entropy  $s_{int}(\epsilon^*, N^*, l)$  of a cluster bigger than 3, the same equations as for the cluster MMMC model is used, i.e.

$$N^* s_{int}(\epsilon^*, N^*, l) \doteq N_s^* s_t(\epsilon^*) + N_v^* s_\infty(\epsilon^*), \quad (4.4)$$

where  $s_t$  is the trimer entropy given by eq. (3.2) on page 43.  $s_\infty$  is the bulk specific entropy obtain from the bulk heat capacity curve (see sec. 3.2 and [GRO97]).

### Volume and surface “atoms”

The number of volume atoms  $N_v^*$  of a given cluster used in eq. (4.4) to compute its internal entropy is the number of atoms whose all neighboring sites are occupied (squares in fig. 4.4 on the preceding page).

The number of surface “atoms” is simply given by

$$N_s^* = N - 2 - N_v^*. \quad (4.5)$$

In CL a cluster of mass 200 can have up to 76 volume atoms, whereas in MMMC this number is only 56. Hence the specific entropy of the big clusters is larger in CL than in MMMC, whereas for small clusters  $N < 12$  the respective internal entropies are the same in both models.

### 4.3.2 Simulation method

The discussion on the simulation method use for CL is also very similar to the one of MMMC95 (sec. 3.3). The outline of the beginning of this section follows the one of sec. 3.3. To avoid unnecessary repetitions, this section is very brief. For more details the reader should refer to sec. 3.3.

### Microcanonical weight

The coordinates of an event are

$$\mathbf{x} \doteq \{\mu = \{N_i, l_i\}_{i=1}^{N_f}, \{E_i^*\}\}, \quad (4.6)$$

where  $\mu$  is a short hand for the mass distribution. The  $i^{\text{th}}$  cluster is characterized by its mass  $N_i$ , number of links  $l_i$  and internal excitation energy  $E_i^*$ . The positions of the atoms on the grid and  $\mu$  are two equivalent coordinates.

The microcanonical weight  $\omega(\mathbf{x})$  is divided in the following way

$$\omega \equiv \omega_{sym} \omega_{pl} \omega_r \omega_{int} \omega_{\Delta v}, \quad (4.7)$$

where  $\omega_{sym}$  is the quantum symmetrization weight factor, see eq. (3.9).  $\omega_{pl}$  is the result of the integration over the linear and angular momenta, see eq. (3.10).  $\omega_r$  is the weight due to the angular part of the clusters eigen rotation, see page 47.  $\omega_{int}$  is the factor due to the internal dofs of the clusters, see eqs. (3.11) and (4.4).  $\omega_{\Delta v}$  ensures a dimensionless probability weight

$$\omega_{v_w} = v_w^{N_f}, \quad (4.8)$$

where  $\Delta v$  is equal to the Wigner–Seitz volume of an atom, i.e.  $\Delta v \equiv v_w = \frac{4\pi}{3}r_w^3$ . Contrary to eq. (3.12a), there is no  $\omega_{NCC}$  in eq. (4.8).

$\omega_{pl}$  and  $\omega_r$  depend on the clusters shape via the principal moment of inertia of the clusters. Once the clusters are defined, there are considered in  $\omega_{pl}$  and  $\omega_r$  as free to move spatially, i.e. the underlying lattice is forgotten.

### Observables

The inverse temperature  $\beta$  is an observable as in MMMC95. However, as there is no explicit dependence on the system total volume in CL, see eq. (4.7), therefore, the pressure is not an observable.

Nevertheless, some information about the pressure and its derivatives with respect to the volume<sup>c</sup> and to the energy are needed in order to define phases and phase transitions, see chap. 2. To overcome this difficulty, one can proceed in the following way.

Consider first a caloric curve at fixed volume.  $\beta$  is nothing else but the derivative of the entropy with respect to the energy at fixed volume. Hence one can integrate at fixed volume the  $\beta$  curve and obtain the entropy  $S(E, V)$  at fixed volume. This entropy curve is known only up to a constant.

Now, one can proceed in the same way for different system volumes. Each of these entropy curves is known up to an additive constant. One has to find a way to link them in the volume direction.

At very low energy, the system is composed by only one big cluster. Almost all the excitation energy is in the internal dofs of this cluster. Therefore at very low energy the system entropy  $S(E, V)$  can be approximatively written as

$$S(E, V) \approx \log \left( \frac{4\pi}{3} (R - r)^3 \right) + C(E), \quad (4.9)$$

where  $C(E)$  is a function of  $E$ .  $\frac{4\pi}{3} (R - r)^3$  is the eigen- $NCC$  of the big cluster of radius  $r$  within the system volume of radius  $R$  (see eq. (A.4) in app. A.1.1). In eq. (4.9) it is implicitly assumed that the big cluster has a spherical shape. This is verified at very low energy, since large clusters with spherical shapes have the lowest binding energy (largest number of internal links).

Hence the difference of entropy  $S(E, V_2) - S(E, V_1)$  between two points in the  $(E, V)$  plane at low and fixed  $E$  is simply

$$S(E, V_2) - S(E, V_1) = 3 \log \left( \frac{R_2 - r}{R_1 - r} \right). \quad (4.10)$$

Eq. (4.10) gives the relative shifts between all the entropy curves at constant volume.

Finally, a spline interpolation method is used in order to have a continuous coverage of the energy-volume parameter space.

### Algorithm

The basic idea is very simple. From one event  $\mathbf{x} = \{\mu, \{E_i^*\}\}$ , a new spatial configuration (i.e. new mass distribution  $\mu'$ ) is generated by moving randomly one atom. To get

---

<sup>c</sup>The accessible volume to the atoms is discrete since they are positioned on a grid. The actual system volume is proportional to the number of cells. In the following, a continuous approximation for the system volume is adopted.

the needed information about  $\mu'$  (masses, number of links, of volume fragments, inertial tensor), the algorithm from Hoshen and Kopelman [HK76] and a straightforward extension [HBM97] is used (see also [BAB98]). This algorithm has been introduced to study the distribution of clusters in percolation systems. Once the new mass distribution is generated, when needed, the excitation energies of the clusters affected by this move are resampled following the algorithm given in app. B.2.2.

Special care has been taken to fulfill the detailed balance condition. The typical number of events used for averaging is  $5 \cdot 10^6$ . More events (up to  $1 \cdot 10^8$ ) are needed at low energies and large volumes, and also in the multifragmentation region for small volumes. For five millions of event the typical CPU-time is of the order of 5 minutes.

### 4.3.3 Results

In this section numerical results are shown. They are first compared with MMMC95 results. At large volumes the caloric curves have a region of negative specific heat capacity. It is the signal of a first order phase transition (see sec. 2.2). Finally the critical end point of this phase transition is shown. This is the first time that the critical point of small clusters liquid-gas transition is found.

#### Comparison with mmmc95

In fig. 4.5 caloric curves at constant system volume as functions of the excitation energy  $\epsilon^*$  are shown. One of these curves is a result from MMMC95 (circles,  $T_{95}$ ), the other from CL (squares,  $T_{CL}$ ). The overall qualitative behaviors are similar. For both curves there is a region of negative specific which signals a first order phase transition. However the temperature from CL is almost everywhere larger than the one from MMMC95.

In order to explain these quantitative differences, the information about the corresponding mass distributions as functions of  $\epsilon^*$  are plotted in fig. 4.6. An important fact is that there is also, in this model, a multifragmentation regime.

From the figure 4.6 one can conclude that the larger temperature in CL is due to its smallest number of fragments compared with MMMC95.

At very low energies ( $\epsilon^* \lesssim 0.15$ ),  $T_{CL} < T_{95}$  although there is in both simulation only one big cluster. This can be partially explained by the largest specific entropy energy in CL<sup>d</sup>. There is another reason. In CL, near the ground state the big cluster maximizes its number of internal links in order to gain some excitation energy by loosing binding energy (see eq. (4.3) on page 74). But, as soon as there is enough energy the shape of the big cluster changes in order to maximize  $N_v^*$  the number of volume atoms. This is done by adopting a spheroid shape. But this cluster shape has a larger binding energy. All in all, at  $\epsilon^* \approx 0.1$  the big liquid cluster has a larger binding energy and a larger internal specific entropy in CL than MMMC95. This implies a smaller overall temperature in CL.

As the energy increases the big clusters have more degrees of freedom in CL. The clusters can have different shapes. These shape dofs delay the evaporation of light fragments. This is the main reason, along with their larger number of volume atoms, why  $T_{CL} > T_{95}$ . This explain also the delayed multifragmentation in CL. There the big clusters can stand the “weight-competition” at larger energy with a mass distribution composed by several intermediate fragment sizes.

<sup>d</sup>This phenomenom is also to be seen in MMMC95 when there is no entropy surface term, see sec. 3.4.1. and fig. 3.14 on page 60.

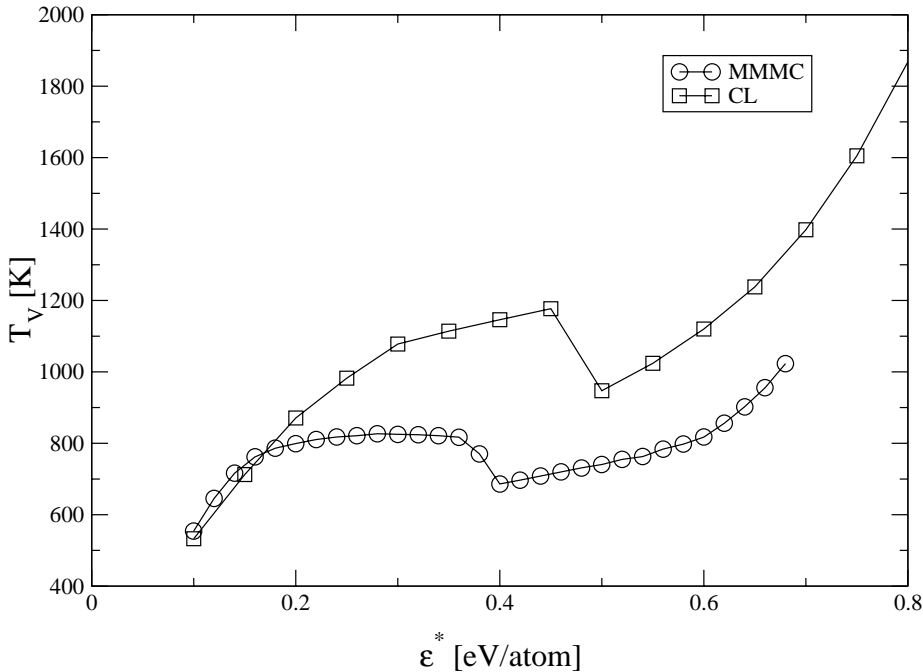


Figure 4.5: Temperatures from MMMC and CL at *constant volume* as functions of the specific excitation energy  $\epsilon^*$ . For both models the system total mass is  $A = 100$  and the system volume is  $V \approx 11V_0 = 11 \left( \frac{4\pi}{3} A r_w^3 \right)$  where  $r_w$  is the Wigner-Seitz radius. The qualitative behaviors of both models are identical. However, the temperature of CL is well above the one of MMMC95 in the transition region. This quantitative differences is related to the differences of the respective mass distributions (see text and fig. 4.6).

Finally, one must stress that CL and MMMC are two models that are qualitatively equivalent but quantitatively different. By tuning the input one can reduce the differences between these models. However, only experimental data (which are at this moment unavailable) can say which model, if any, present the correct behavior.

### Critical point

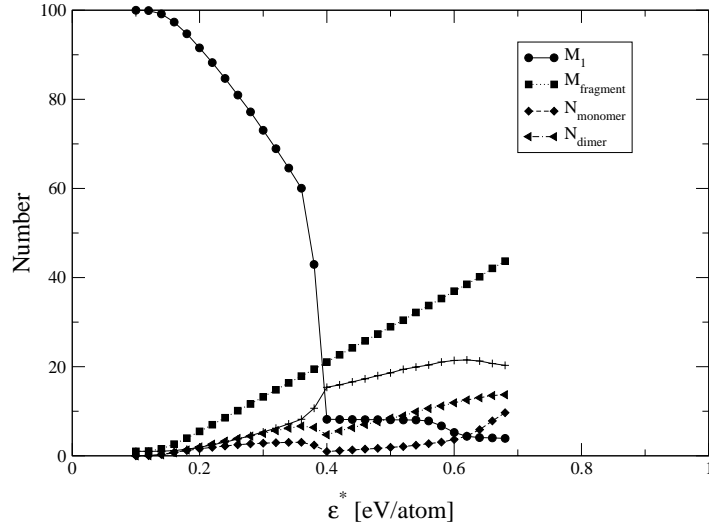
In fig. 4.7 inverse temperature curves as functions of the energy  $\epsilon^*$  are plotted, each one at constant volume. For systems with a volume smaller than  $V_{c'} \approx 3.48 \cdot 10^4 \text{ \AA}^3$  the heat capacity is positive over the whole energy range. Note that  $V_{c'}$  does not obligatory correspond to the critical point volume  $V_c$ .

At the critical point the following relations hold (see sec. 2.3.1)

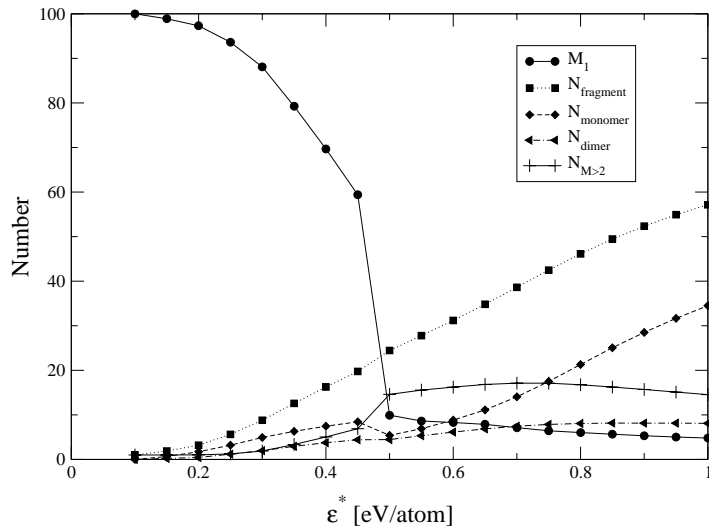
$$\lambda_1 = 0, \quad (4.11a)$$

$$\mathbf{v}_1 \cdot \nabla \lambda_1 = 0, \quad (4.11b)$$

where  $\lambda_1$  is the largest eigenvalue of the Hessian matrix of  $S$  and  $\mathbf{v}_1$  its associated eigenvector. As discussed in sec. 2.3.2, for a two dimensional parameter system the conditions (4.11) can be simplified to “the lines of constant extensive parameters are tangent to the line  $\lambda_1 = 0$ ”.



(a) MMMC95



(b) CL

Figure 4.6: Comparisons of mass distributions of CL and MMMC95 at constant system volume as functions of the excitation energy  $\epsilon^*$ . The system total mass is  $A = 100$ , its volume  $V$  is eleven time the compound cluster volume  $V_0 = \frac{4\pi}{3}100r_w^3$ , where  $r_w \approx 2.3 \text{ \AA}$  is the Wigner–Seitz radius.  $M_1$ ,  $N_{fragment}$ ,  $N_{monomer}$ ,  $N_{dimer}$  and  $N_{M>2}$  are respectively the mean mass of the largest fragment, the mean number of fragments, of monomers, of dimers and of fragments bigger than 2. The qualitative behavior of all the observables are very similar. In particular, in CL there also is a multifragmentation (fast reorganization of the mass distribution) and a multifragmentation regime (evaporation of intermediate cluster sizes).

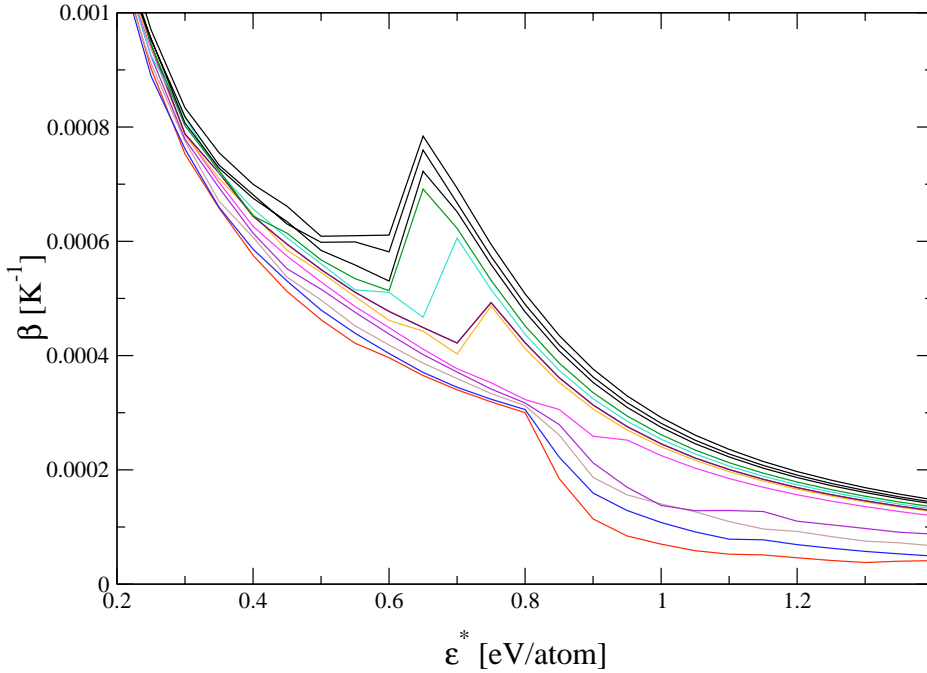


Figure 4.7: Inverse temperature curves at constant volume as functions of the excitation energy  $\epsilon^*$  and for several system volumes. The system total mass is  $A = 200$  and the packing fraction goes from  $\kappa = 1.7 \cdot 10^{-4}$  (highest curve) to  $\kappa = 0.54$  (lowest curve). For large volume (small  $\kappa$ ) a region of negative heat capacity is clearly to be seen. For  $\kappa > \kappa_{c'} \approx 0.3$  the back bending vanishes and there is no phase transition in the energy direction. The fluctuations that can be seen at large volumes and at energies below and close to the multifragmentation are not due to statistical errors. They are the consequences of sudden changes of the shape of the big (liquid) cluster. These changes occur when the big cluster loses a “volume” fragment. There it tries to maximize its number of links by adopting a spherical shape. As it loses atoms, it keeps  $N_v^*$  fixed by adopting more and more spheroid shape (see text).

From the caloric curves plotted in fig. 4.7 one can infer the entropy and its derivatives in the energy-volume plane as explained in sec. 4.3.2.

In fig. 4.8 the sign of  $\lambda_1$  along with contour plots of the pressure and the temperature are shown for three system total masses ( $A = 100, 200$  and  $400$ ) as functions of the specific excitation energy  $\epsilon$  and of the density given in  $\text{kg} \cdot \text{m}^{-3}$ .

For all masses, the first order phase transition has a critical end point. This is the first time that critical points are obtained for this type of model. However, their exact locations cannot be deduce from the actual numerical data due to a lack of numerical precision and of the noises generated by the integrations and the spline interpolation used to obtain the entropy surface.

In table 4.1 the critical point parameters,  $\rho_c$ ,  $T_c$  and  $p_c$  (the critical density, temperature and mass, resp.) are given for three system sizes  $A = 100, 200$  and  $300$ . These parameters are estimated by averaging there respective values within the circles locating the critical points (see figs. 4.8). The errors bars are simply the highest and the lowest values of these parameters within the circles.

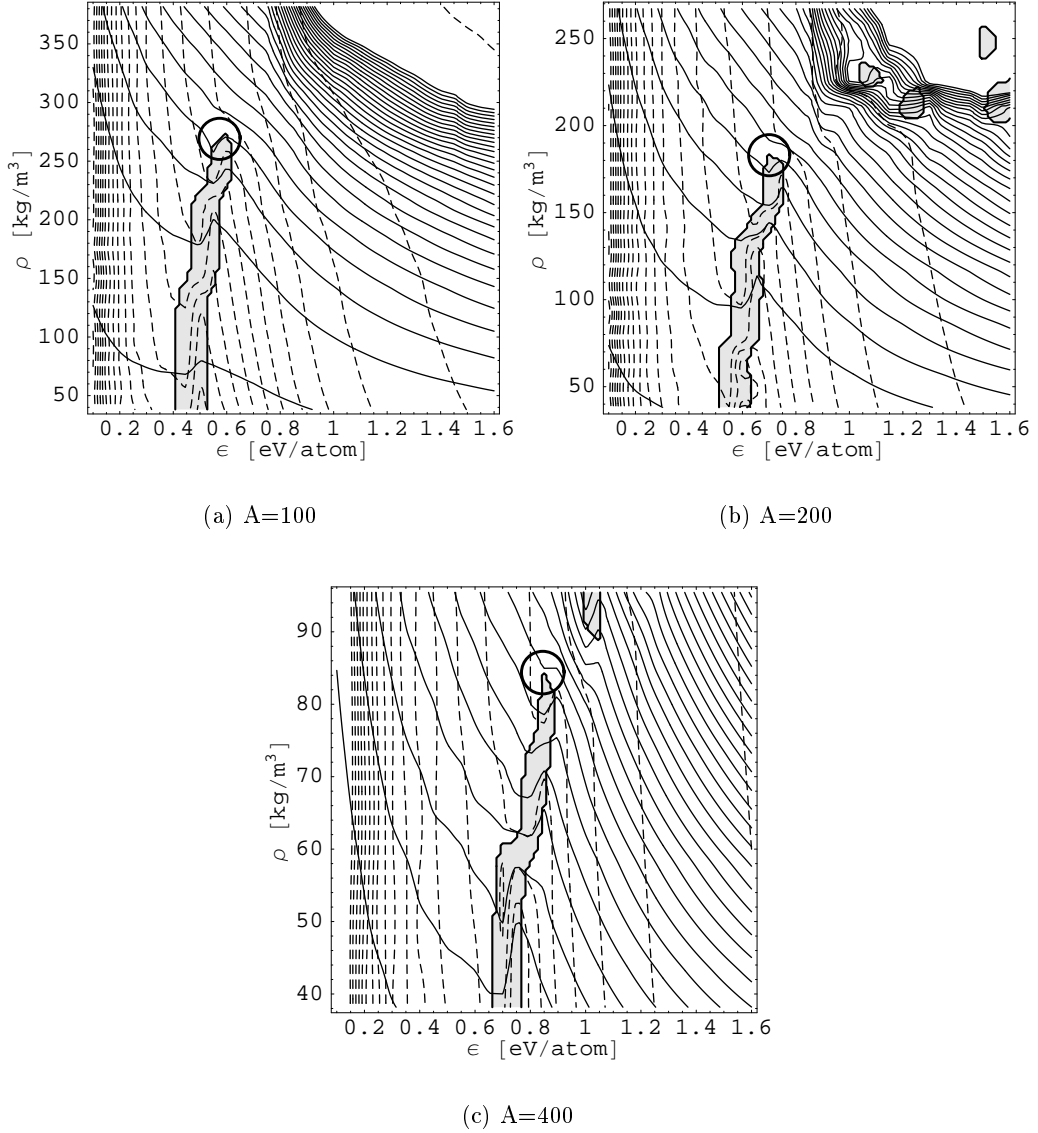


Figure 4.8: Sign of  $\lambda_1$ , the largest eigenvalue of the Hessian of the entropy.  $\lambda_1$  is positive (negative) in the gray (white) region,  $\lambda_1 = 0$  along the thick line. Contour plots of the pressure  $p$  and the temperature  $T$ , solid and dashed line respectively. All these observables are plotted in the energy-density plane and for several system total masses ( $A = 100, 200$  and  $400$ ).  $\lambda_1 < 0$  implies a pure phase whereas  $\lambda_1 > 0$  locates first order phase transition. In the pure phase regions the density at constant pressure and at constant temperature have a “normal” behavior, i.e.  $\frac{\partial \rho}{\partial \epsilon}|_{p=cst} < 0$ . In the first order transition  $\frac{\partial \rho}{\partial \epsilon}|_{p=cst} > 0$ . The critical point of this first order phase transition is located where the line of constant pressure (or equivalently of constant temperature) is tangent to the line  $\lambda_1 = 0$ . The critical points are approximately located by the thick circles. The regions of positive  $\lambda_1$  at high density and large energy are due to numerical uncertainties in the caloric curve (see fig. 4.7).

	$\rho_c$ [ $\text{kg} \cdot \text{m}^{-3}$ ]	$T_c$ [K]	$p_c$ [ $10^3$ atm]
100	$270 \pm 17$	$2070 \pm 200$	$296 \pm 60$
200	$183 \pm 10$	$2570 \pm 170$	$96 \pm 10$
400	$85 \pm 3$	$2950 \pm 230$	$18.7 \pm 2.9$
$\infty$	219	2503	0.253

Table 4.1: Critical parameters as functions of the system total mass.  $\rho_c$ ,  $T_c$  and  $p_c$  are the critical density, temperature and pressure, respectively. The experimental sodium bulk values are given in the last line [FL95]. The numerical values are estimated from the data shown in fig. 4.8. The errors bars gives the range of values taken by the observables within the circles in fig. 4.8.

Although a simple scaling would not converge to the sodium bulk critical values, they are at least in the correct order of magnitude (apart from the pressure, but one can see that it decreases rapidly with increasing  $A$ ). These results also confirm the ones from MMC95 at high pressures. The critical pressure and density *decrease* whereas the critical temperature *increases* with increasing system total mass.

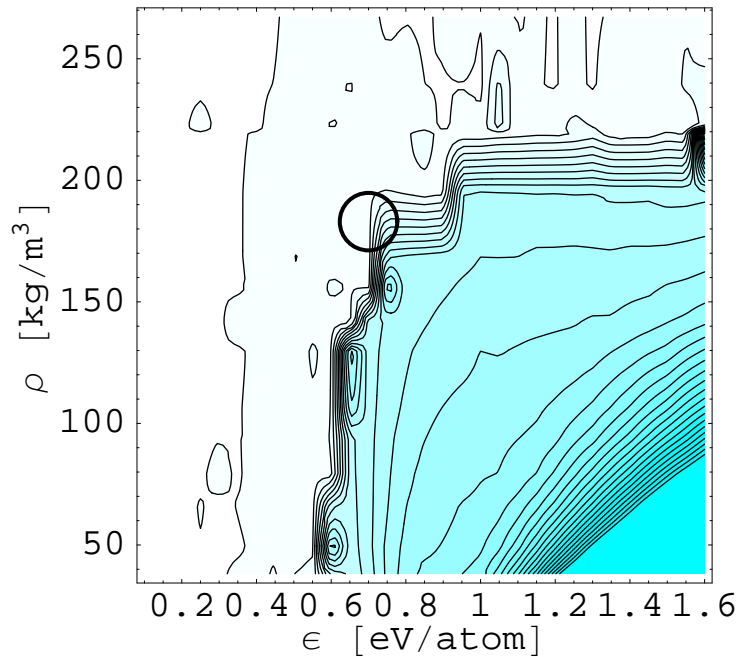


Figure 4.9: Contour-Density plot of the relative fluctuations of  $\alpha = \frac{I_{\min}}{I_{\max}}$ , the ratio of the smallest principal moment of inertia to the largest one of the biggest cluster in CL toward the critical point in the specific energy-density plane.  $A = 200$ . The grayer the larger are the fluctuations. The values of  $\sigma_\alpha/\alpha$  is  $\sim 0.1$  at the lower right hand of the figure. The second order phase transition is approximately located by the circle. Within the available numerical precision  $\alpha$  do not exhibit any particular behavior near the critical point. The relative fluctuation increases after the multifragmentation because the principal moment of inertia of small clusters are more sensitive to a shape-changes.

Higher critical density means a more important role of the avoided volume  $NCC$  in MMMC95.

The study of this model at high pressures is so far from being complete. Particularly regarding the mass distribution near and at the critical point.

First studies of the mass distribution (and its fluctuations) near and at the critical point do not exhibit any remarkable properties.

As an example, in fig. 4.9 the relative fluctuations of  $\alpha = \frac{I_{\min}}{I_{\max}}$ , the ratio of the smallest principal moment of inertia to the largest one of the *largest* cluster. This observable probes the shape fluctuations of the biggest cluster. It has been suggested [VOT] that the lack of critical point in MMMC95 is due to the lack of shape dofs in the cluster MMMC model. As one can see in fig. 4.9, nothing special happens near or at the critical point. In particular, the biggest cluster shape does not have large relative fluctuations at the critical point. This result has to be taken with caution. Maybe the absence of large fluctuations are only due to a lack of numerical precision. Further studies, with finer grids are needed.

## 4.4 Conclusions

In this chapter the liquid-gas transition of small sodium clusters at high pressures is studied.

For small systems the cluster avoided volume ( $NCC$ ) plays a very important role. In the transition region, its derivative with respect to the system volume gives the main contribution to the total microcanonical pressure. Moreover, the very high values of  $NCC$  (see app. A.2) prevent one to study the critical point of the liquid-gas transition of the cluster MMMC model (if it exists at all). These very high values are numerically extremely difficult to evaluate.

A new model inspired from lattice gas models is introduced (CL). By putting the atoms on a fixed grid it avoids the use of  $NCC$ . This grids gives new degrees of freedom to the clusters compared to the MMMC cluster model; namely shape-dofs. Moreover, compared to clusters in MMMC, the clusters in CL have a larger number of “volume” atoms for intermediate cluster sizes.

In CL there is no  $NCC$ . The price to pay is that the pressure is no longer an observable. The pressure can to be inferred from a set of caloric curves after some integrations and interpolations and by assuming a certain volume dependency of the entropy  $S$  at very low energies. All these procedures add a fairly large amount of uncertainty in the numerical evaluation of the derivatives of  $S$  with respect to the system volume.

Nevertheless a study of the liquid-gas transition is possible in this model.

At large volumes ( $\sim$  low pressures) the caloric curves for CL are very similar to the one of MMMC95. In particular, there is again a multifragmentation. In CL the overall temperature is larger due to (a) a larger number of volume “atoms” implying a larger specific internal entropy at fixed internal energy and cluster size, (b) the new shape degrees of freedom.

As already written, from a set of caloric curves one can infer the entropy surface  $S$  in the energy-volume plane. By studying the topological properties of  $S$  one can define phases and phase transitions as discussed in chap. 2.

At small volumes (large densities,  $\sim$  large pressures), the study of the topology of  $S$  shows that the liquid-gas first order phase transition has a critical end point (second order phase transition).

The critical parameters can also be evaluated. Their values are of the order of the bulk ones (except for the critical pressure which is much larger). Qualitatively their values confirm what could be deduced from the MMMC95 computations. Namely that the critical point is located at lower density and temperature and at higher pressure for finite size systems compared to the bulk critical parameters

However, a simple scaling ansatz shows that these values do not converge to the bulk ones. This is due to all the simplifications made on the physics of the clusters in order to reach this critical point. For example, no highly excited clusters are allowed in CL, although their presence can not be excluded near the critical point (and as shown by preliminary studies). Work is in progress in this direction. As a second example, in CL, the inter-atomic distances are fixed. At very high pressures the atoms can certainly not be simply considered as hard spheres. This effect plays certainly an important role.

Some preliminary results regarding the mass distribution near and at the critical point do not show any particular behavior. Yet, it is unclear if this is simply due to a lack of numerical precision. This will be checked in a near future by performing new simulations with finer grids in the energy-volume plane.

## Part III

### Gravitational systems — Conservation of the angular momentum $L$ on long-range interaction systems —



# Chapter 5

## Introduction

The thermostatical properties of systems of  $N$  classical particles under long-range attractive potentials have been extensively studied since the seminal work of Antonov [ANT62], [PAD90, LYN67, LW68, HT71, TH170, SAS85]. One of their more specific and interesting properties is that they are unstable for all  $N$  [RUE63, PAD90] and therefore not thermodynamically extensive, i.e. they exhibit negative specific heat capacity regions even when the system is composed by a very large number of particles [LW68].

It is natural to ask whether the total angular momentum  $L$ , which is an integral of motion for systems of relevance in the astrophysical context, plays a non-trivial role on the equilibrium properties of these systems. Indeed,  $L$  is considered as an important parameter in order to understand the physics of systems like galaxies [LGM99, LDOP00, BT87]; globular clusters [LL96A, LL96B, HK77, KM00, LB00]; molecular clouds in multi-fragmentation regime [COM98, DVSC] which might eventually lead to stellar formation [BAT98, KFMT98, KB97, BB96, WASBW96, WHI96, CT90].

Previous works have already studied the effect of  $L$  in the mean field limit with a simplified potential [LAL99] or imposing a spherical symmetry [KM00]; or at  $L = 0$  [HK77].

In this part an attempt to overcome some of these approximations is presented <sup>a</sup>. No symmetry is imposed a priori and a “realistic” gravitational potential is used.

Thermodynamical equilibrium does not exist for Newtonian self-gravitating systems, due both to evaporation of stars (the systems are not self-bounded) and short distance singularity in the interaction potential. However there exists intermediate stages where these two effects might be neglected and a quasi-equilibrium state might be reached [HK77, CP01] (dynamical issues like ergodicity, mixing or “approach to equilibrium” [SAS85, YM97, RN93] are not considered in this chapter). In order to make the existence of equilibrium configurations possible one has, first, to bound the system in an artificial box and, second, to add a short distance cutoff to the potential. The latter point can be seen as an attempt to take into account the appearance of new physics at very short distances (about the influence of this short cut see e.g. [ROM97, SLVH97, FL00]). Another way to avoid the difficulties due to the short distance singularity is to describe the function of distribution of the “stars” within a Fermi–Dirac statistic [LYN67, CHA98].

The box breaks the translational symmetry of the system, therefore, strictly speaking the total linear momentum  $\mathbf{P}$  and angular momentum with respect to the system center of mass  $\mathbf{L}$  are not conserved. Nevertheless, it is assumed that the equilibration time is smaller than the characteristic time after which the box plays a significant role [HK77,

---

<sup>a</sup>Most of the material presented in this part can be found in [FG01].

LAL99, CP01]. Therefore  $\mathbf{P}$  and  $\mathbf{L}$  are considered as (quasi-)conserved quantities (see discussion in sec. 1.1.2). The center of the box is put at the center of mass  $R_{CM}$  which is also set to be the center of the coordinates, thus  $P = 0$ .

As already mentioned, self-gravitating systems are non-extensive, i.e. “small” in the sense given in the general introduction of this thesis. A statistical description based on their intensive parameters should be taken with caution since the different statistical ensembles are only equivalent at the thermodynamical limit far from first order transitions as defined in the first part of this thesis. Hence, following the discussions in part I the equilibrium properties of these self-gravitating systems are worked out within the microcanonical ensemble (ME).

In order to perform the computation in a reasonable time and as a first step an only two dimensional system is considered. Thus, the total angular momentum is a pseudo-vector characterized by one number; it is noted from now on by  $L$ .

The next chapter is organized as follow. First the analytical expressions for entropy and its derivatives are recalled (sec. 6.1), then the two first moments of the distribution of the linear momentum of a given particle at a fixed position (sec. 6.2) are derived and commented, and finally a numerical method based on an importance sampling algorithm in order to estimate suitable observables is presented (sec. 6.3). Numerical results are presented in section 6.4. First thermostatical properties are shown and discussed. Then the link between the average mass distribution and the thermostatical properties is made in sec. 6.4.2. In sec. 6.4.3 the definition of phase introduced in chap. 2 is used to construct the phase diagram of the self-gravitating system as a function of its energy  $E$  and angular momentum  $L$ . The ensemble introduced by Klinko and Miller in [KM00] is discussed. In this paper this ensemble is used to treat another model of rotating and self-gravitating system. This ensemble is a function of the (intensive) variables conjugate of  $E$  and  $L^2$ . For the present model it is shown how the predictions using this ensemble are inaccurate and misleading (sec. 6.4.4); the more “standard” CE where the intensive variables are the conjugate of  $E$  and  $L$ , i.e. the inverse temperature  $\beta$  and the angular velocity  $\omega$  is also discussed in sec. 6.4.4. Results are summarized and discussed in section 6.5.

# Chapter 6

## Microcanonical properties

### 6.1 Microcanonical definitions

Consider a system of  $N$  classical particles on a disk of radius  $R$  whose interaction is described by a Plummer softened potential [PLU11, YEP97]

$$\varphi_{ij} = -\frac{Gm_i m_j}{\sqrt{s^2 + (\mathbf{q}_i - \mathbf{q}_j)^2}}, \quad (6.1)$$

where  $m_i$  and  $\mathbf{q}_i = \{q_i^1, q_i^2\}$  are the mass and position of particle  $i$  respectively,  $s$  is the softening length and  $G$  is the gravitational constant. The fixed total energy  $E$  is described by the Hamiltonian

$$\mathcal{H} = \sum_i \frac{\mathbf{p}_i^2}{2m_i} + \varphi(\mathbf{q}), \quad (6.2)$$

where  $\mathbf{p}_i = \{p_i^1, p_i^2\}$  is the linear momentum of particle  $i$ ,  $\varphi = \sum_{i < j} \varphi_{ij}$ .  $\mathbf{q}$  is a  $2N$ -dimensional vector whose coordinates are  $\{\mathbf{q}_1, \dots, \mathbf{q}_N\}$ , representing the spatial configuration.  $\mathbf{q}$  is an element of the spatial configuration space  $V_c$ ,  $\mathbf{q} \in V_c \subset \mathbb{R}^{2N}$ .

The entropy  $S$  is given through Boltzmann's principle

$$S(E, L, N) \doteq \ln W(E, L, N), \quad (6.3)$$

where  $W(E, L, N)$  is the volume of the accessible phase-space at  $E$ ,  $L$  and  $N$  fixed (under the assumptions given in chap. 5 on page 87)

$$\begin{aligned} W(E, L, N) &= \frac{1}{N!} \int \prod_{i=1}^N \left( \frac{d\mathbf{p}_i d\mathbf{q}_i}{(2\pi\hbar)^2} \right) \delta(E - \mathcal{H}) \delta^{(2)} \left( \sum_i \mathbf{p}_i \right) \\ &\quad \times \delta \left( L - \sum_i \mathbf{q}_i \times \mathbf{p}_i \right) \delta^{(2)} \left( \sum_i \mathbf{q}_i \right), \end{aligned} \quad (6.4)$$

where  $\mathbf{q}_i \times \mathbf{p}_i = q_i^1 p_i^2 - q_i^2 p_i^1$ . After integration over the momenta eq. (6.4) becomes [LAL99, CL98]

$$W(E, L, N) = \mathcal{C} \int_{V_c} d\mathbf{q} \frac{1}{\sqrt{I}} E_r^{N-5/2} \delta^{(2)} \left( \sum_i \mathbf{q}_i \right), \quad (6.5)$$

where  $\mathcal{C} = \frac{(2\pi)^{(N-9/2)} \prod_i m_i}{(2\pi\hbar)^{2N} N! (\sum_i m_i) \Gamma(N-3/2)}$  is a constant,  $I = \sum_i m_i \mathbf{q}_i^2$  is the inertial momentum and  $E_r = E - \frac{L^2}{2I} - \varphi$  the remaining energy <sup>a</sup>. From the point of view of the remaining energy, if  $L \neq 0$  one can already notice that the equilibrium properties are the result of a competition between two terms: the rotational energy  $\frac{L^2}{2I}$  and the potential energy  $\varphi$ . The former tries to drive the particles away from the center of mass in order to increase  $I$  whereas the latter tries to group the particles together in order to decrease  $\varphi$ , but since the center of mass is fixed this will lead to a concentration of particles near the center and consequently will decrease  $I$ .

The microcanonical temperature  $T$  is defined by

$$\frac{1}{T} \doteq \beta \doteq \frac{\partial S}{\partial E} = \left\langle \frac{N-5/2}{E_r} \right\rangle, \quad (6.6)$$

where  $\langle \cdot \rangle$  is the microcanonical average

$$\langle \mathcal{O} \rangle = \frac{\mathcal{C}}{W} \int_{V_c} d\mathbf{q} \frac{\mathcal{O}(\mathbf{q})}{\sqrt{I}} E_r^{N-5/2} \delta^{(2)} \left( \sum_i \mathbf{q}_i \right). \quad (6.7)$$

The angular velocity  $\omega$  is defined as minus the conjugate force of  $L$  times  $T$  [DGLR89]

$$\omega \doteq -\frac{1}{\beta} \frac{\partial S}{\partial L} = \frac{\langle \frac{L}{T} E_r^{-1} \rangle}{\langle E_r^{-1} \rangle}. \quad (6.8)$$

$\gamma\beta$  is defined as the conjugate of  $L^2$

$$\gamma\beta \doteq \frac{\partial S}{\partial L^2} = -\left\langle \frac{1}{2I} \frac{N-5/2}{E_r} \right\rangle, \quad (6.9)$$

$$\omega = -2L\gamma. \quad (6.10)$$

## 6.2 Momentum average and dispersion

In this section the average and the dispersion of the linear momentum of a particle is derived, its mean angular velocity is also computed and related to the one of the system as defined in eq. (6.8).

The derivation of  $\langle \mathbf{p}_k \rangle_{\mathbf{q}_k}$  the average momentum of particle  $k$  at fixed position  $\mathbf{q}_k$  (while the other particles are free) is similar to that of  $W$ . Details of the derivation can be found in Appendix C on page 133, and the result is

$$\langle \mathbf{p}_k \rangle_{\mathbf{q}_k} = L \langle I^{-1} \rangle_{\mathbf{q}_k} m_k \sum_{\alpha, \gamma=1}^2 \epsilon_{\alpha\gamma} q_k^\gamma \hat{\mathbf{e}}_\alpha, \quad (6.11)$$

where  $\epsilon$  is the antisymmetric tensor of rank 2 and  $\hat{\mathbf{e}}_\alpha$  the unit vector of coordinate  $\alpha$ . Equation (6.11) shows that  $\langle \mathbf{p}_k \rangle_{\mathbf{q}_k}$  is a vector perpendicular to  $\mathbf{q}_k$  whose module is a function of  $\|\mathbf{q}_k\|$ . In other words the orbit of a particle is in the mean circular (this result is expected since the system is rotationally symmetric). One can compute  $\langle \omega_k \rangle_{\mathbf{q}_k}$  the

<sup>a</sup>the number  $\frac{5}{2}$  in eq. (6.5) is due to the different delta functions in eq. (6.4) that are integrated out:  $\frac{1}{2}$  for the conservation of  $L$ ,  $2 \cdot \frac{1}{2} = 1$  for  $\mathbf{P}$  and one for the total energy  $E$ .

mean angular velocity of  $k$  at distance  $\|\mathbf{q}_k\|$  by first considering  $\langle L_k \rangle_{\mathbf{q}_k}$  the mean angular momentum of  $k$  at distance  $\|\mathbf{q}_k\|$

$$\begin{aligned}\langle L_k \rangle_{\mathbf{q}_k} &\doteq \mathbf{q}_k \times \langle \mathbf{p}_k \rangle_{\mathbf{q}_k} \\ &= L \langle I^{-1} \rangle_{\mathbf{q}_k} I_k,\end{aligned}\tag{6.12}$$

where  $I_k = m_k \mathbf{q}_k^2$ . The angular mean velocity of a particle on a circular orbit is classically linked to  $\langle L_k \rangle_{\mathbf{q}_k}$  by

$$\langle L_k \rangle_{\mathbf{q}_k} = \langle \omega_k \rangle_{\mathbf{q}_k} I_k.\tag{6.13}$$

Using eqs. (6.12) and (6.13) leads to the following expression for  $\langle \omega_k \rangle_{\mathbf{q}_k}$

$$\langle \omega_k \rangle_{\mathbf{q}_k} = L \langle I^{-1} \rangle_{\mathbf{q}_k}.\tag{6.14}$$

The dependence of  $\langle \omega \rangle_{\mathbf{q}_k}$  on  $\|\mathbf{q}_k\|$  is of the order  $1/N$ <sup>b</sup>, therefore for large  $N$ ,  $\langle \omega \rangle_{\mathbf{q}_k}$  becomes (see eq. (6.8) on the preceding page)

$$\langle \omega_k \rangle_{\mathbf{q}_k} \sim L \langle I^{-1} \rangle \approx \langle \omega \rangle.\tag{6.15}$$

For large  $N$  the mean angular velocity is the same for all the particles at any distance from the center, in other words the system in the mean rotates like a solid body. Moreover  $\langle \omega_k \rangle_{\mathbf{q}_k}$  corresponds to the thermostistical angular velocity  $\omega$  defined by eq. (6.8) on the facing page. These are also a classical results for extensive systems at low  $L$  [DGLR89, LL94]. Note also that these results do not depend explicitly on the interaction potential  $\varphi$ .

The momentum dispersion  $\sigma_{\mathbf{p}_k}$  can also be derived. Using eq. (6.11) and eq. (C.16) on page 135, one gets for large  $N$

$$\begin{aligned}\sigma_{\mathbf{p}_k}^2 &\equiv \langle \mathbf{p}_k^2 \rangle_{\mathbf{q}_k} - \langle \mathbf{p}_k \rangle_{\mathbf{q}_k}^2 \\ &\sim 2 \frac{m_k}{\beta} + I_k L^2 m_k (\langle I^{-2} \rangle - \langle I^{-1} \rangle^2)\end{aligned}\tag{6.16}$$

The second term of eq. (6.16) is proportional to the square of the dispersion of  $I^{-1}$  and to  $\mathbf{q}_k^2$  ( $I_k = m_k \mathbf{q}_k^2$ ). When this term vanishes relatively to the first one, e.g. when the fluctuations of  $I^{-1}$  are small, or at high energy (low  $\beta$ ) and low  $L$ , the usual dispersion of the Maxwell–Boltzmann distribution is recovered. This term also gives a correction to the usual equipartition theorem; for large  $N$

$$\begin{aligned}\langle E_k \rangle &\equiv \frac{\sigma_{\mathbf{p}_k}^2}{2m_k} \\ &\sim T + \frac{I_k L^2}{2} (\langle I^{-2} \rangle - \langle I^{-1} \rangle^2),\end{aligned}\tag{6.17}$$

where  $\langle E_k \rangle$  is the average internal kinetic energy (without the contribution from the collective hydrodynamic rotational movement) of particle  $k$ . Again this correction is position–dependent via  $I_k$ . In the regimes where the fluctuations of the mass distribution cannot be neglected in eqs. (6.16) and (6.17) (e.g. at phase transitions) an estimate of the temperature based on the velocity dispersion would suggest that the temperature is smaller in the core than at the edge. At high energies and in the limit  $N \rightarrow \infty$  the fluctuations of  $I^{-1}$  should vanish faster than  $L$  ( $\sim N$ ) grows in order to recover the equipartition of energy. However this scaling behavior is not known in the whole parameter space. These fluctuations might play a non–trivial role in phase transition regions even for large  $N$ .

---

<sup>b</sup> $\langle I^{-1} \rangle_{\mathbf{q}_k} = \langle I^{-1} \rangle + \mathcal{O}(N^{-1})$

### 6.3 Numerical method

From now all the particles have the same mass, i.e.  $m_i = m, \forall i = 1, \dots, N$  and the following dimensionless variables are used

$$E \rightarrow \epsilon = \frac{ER}{Gm^2 N^2}, \quad (6.18a)$$

$$L \rightarrow l^2 = \Omega = \frac{L^2}{2Gm^3 RN^2}, \quad (6.18b)$$

$$s \rightarrow \sigma = \frac{s}{R}, \quad (6.18c)$$

$$\mathbf{q} \rightarrow \mathbf{r} = \frac{\mathbf{q}}{R}, \quad (6.18d)$$

$$V_c \rightarrow v_c, \quad (6.18e)$$

$$\varphi \rightarrow \phi = \frac{R}{Gm^2 N^2} \varphi = -\frac{1}{N^2} \sum_{i < j} \frac{1}{\sqrt{\sigma^2 + (\mathbf{r}_i - \mathbf{r}_j)^2}}, \quad (6.18f)$$

$$I \rightarrow I = \sum_i r_i^2. \quad (6.18g)$$

The weight is now

$$W(\epsilon, \Omega) = \mathcal{C}' \int_{v_c} d\mathbf{r} \frac{1}{\sqrt{I}} \epsilon_r^{N-5/2} \delta^{(2)}\left(\sum_i \mathbf{r}_i\right), \quad (6.19)$$

where  $\epsilon_r = \epsilon - \frac{\Omega}{I} - \phi$  is the dimensionless remaining energy and  $\mathcal{C}'$  a constant. Later on this constant is omitted since it plays classically no significant role (it only shifts the entropy by  $\log \mathcal{C}'$ ). The derivatives of entropy ( $\beta, \omega, \dots$ ) are now dimensionless quantities.

One usually estimates (6.19) by means of some Monte Carlo algorithm, updating the positions  $\mathbf{r}$  by some small amount  $\delta \mathbf{r}$  in order to get a good pass acceptance and using the configuration weight  $W(\mathbf{r}) \doteq \frac{1}{\sqrt{I}} \epsilon_r^{N-5/2}$  in the Metropolis pass. Unfortunately this strategy does not really work (within a reasonable CPU-time), because the  $2N$ -dim configuration weight-landscape at fixed  $\epsilon$  and  $\Omega$  presents troughs and high peaks [TA99], so exploring the total configuration-space (or at least a subset containing the highest peaks) would take a very long, in practice infinite, time. This weight-landscape looks like the energy-landscape found in spin-glass systems [MPRTZ00].

The strategy adopted here is partly described in the following. First eq. (6.19) can be rewritten as

$$W(\epsilon, \Omega) = \int dI d\phi Bg(I, \phi) \frac{1}{\sqrt{I}} \epsilon_r^{N-5/2}, \quad (6.20)$$

where

$$Bg(I, \phi) = \int_{v_c} d\mathbf{r} \delta(I'(\mathbf{r}) - I) \delta(\phi'(\mathbf{r}) - \phi) \left(\sum_i \mathbf{r}_i\right). \quad (6.21)$$

$Bg(I, \phi)$  is the density of spatial configurations at given  $I$  and  $\phi$ . Given  $Bg$  one can compute  $W, S$  and its derivatives for *any*  $\epsilon$  and  $\Omega$ , e.g.

$$\begin{aligned} \gamma &= \frac{1}{\beta} \frac{\partial S}{\partial \Omega} \\ &= -\frac{N-5/2}{\beta} \frac{\int dI d\phi Bg(I, \phi) I^{-3/2} \epsilon_r^{N-7/2}}{W(\epsilon, \Omega)}. \end{aligned} \quad (6.22)$$

The expectation value  $\langle \mathcal{O} \rangle$  of an observable  $\mathcal{O}(\mathbf{r})$  can be estimated if  $Bg$  and  $\langle \mathcal{O} \rangle_{I,\phi}$  are known

$$\begin{aligned} \langle \mathcal{O} \rangle &\equiv \frac{\int_{v_c} d\mathbf{r} \mathcal{O}(\mathbf{r}) I^{-1/2} \epsilon_r^{N-5/2} \delta^{(2)}(\sum_i \mathbf{r}_i)}{\int_{v_c} d\mathbf{r} I^{-1/2} \epsilon_r^{N-5/2} \delta^{(2)}(\sum_i \mathbf{r}_i)} \\ &= \frac{\int dI d\phi \langle \mathcal{O} \rangle_{I,\phi} Bg(I, \phi) I^{-1/2} \epsilon_r^{N-5/2}}{W(\epsilon, \Omega)}, \end{aligned} \quad (6.23)$$

where

$$\langle \mathcal{O} \rangle_{I,\phi} = \frac{\int_v d\mathbf{r} \mathcal{O}(\mathbf{r}) \delta(I' - I) \delta(\phi' - \phi) \delta^{(2)}(\sum_i \mathbf{r}_i)}{Bg(I, \phi)}. \quad (6.24)$$

Now, the task is to compute  $Bg(I, \phi)$  and  $\langle \mathcal{O} \rangle_{I,\phi}$ . *A priori*  $Bg(I, \phi)$  is highly peaked around the values of  $I$  and  $\phi$  that describe the gas (disordered) phase and should drop rapidly down to the edges. Nevertheless a good estimate of  $Bg(I, \phi)$  is needed for almost all values taken by  $(I, \phi)$  even when  $Bg(I, \phi)$  is very small comparing to its maximum. For example at small total energy  $\epsilon$  only the part of  $Bg(I, \phi)$  for which  $\epsilon_r = \epsilon - \frac{\Omega^2}{I} - \phi > 0$  contributes to the integral (6.20) on the preceding page.

In order to get a good estimate of  $Bg$  an iterative scheme inspired by multicanonical algorithms has been used [LEE93, BH93, FS89, SMI96]. For further details see app. B.3.

In the present thesis results for  $\sigma = 0.05$  and  $N = 20$  are presented <sup>c</sup>. No qualitative changes are expected with larger number of particles (preliminary studies for  $N$  up to 100 support all the following results).

## 6.4 Results

### 6.4.1 Entropy and its derivatives

Figure 6.1 on the following page shows the entropy surface  $S$  as a function of  $\epsilon$  and  $\Omega$ . The ground state energy  $\epsilon_g(\Omega)$  (thick line in Fig. 6.1) increases with  $\Omega$ ;  $\epsilon_g$  classically corresponds to  $\epsilon_r = 0$  implying  $S = -\infty$ . For all  $\Omega$ ,  $\epsilon_g(\Omega)$  is a concave function of  $\Omega$ , i.e.  $\frac{\partial^2 \epsilon_g}{\partial \Omega^2} \leq 0$ ; at high  $\Omega$  ( $\Omega \gtrsim 12$ ) it is almost linear  $\frac{\partial^2 \epsilon_g}{\partial \Omega^2} \rightarrow 0^-$ . In sec. 6.4.4 dramatic consequences for the canonical ensemble introduced by Klinko and Miller [KM00] resulting from this quasi-linear behavior are discussed.

At fixed  $\Omega$ ,  $S(\epsilon)$  is not concave for all  $\epsilon$  but shows for some energy interval a convex intruder which signals a first order phase transition with negative specific heat capacity ( $\frac{\partial \beta}{\partial \epsilon} > 0$ ). This can be better viewed by plotting  $\beta(\epsilon, \Omega) = \frac{\partial S}{\partial \epsilon}$  (Fig. 6.2 on page 95). Here the counter part of the entropy-intruder is a region of multiple valued  $\epsilon(\beta)$ . This is the case for  $\beta$  between 15 and 20.

The latent heat at fixed  $\Omega$ ,  $q_\epsilon(\Omega)$  decreases for  $0 \leq \Omega \lesssim 12$  and is a constant for  $\Omega > 12$ . There is no critical value of  $\Omega$ ,  $\Omega_c$  above which  $S(\epsilon)$  is concave for all  $\epsilon$ , i.e. there is a first order phase transition in the energy direction for all values of  $\Omega$ . In another model for self-gravitating systems such a  $\Omega_c$  was reported [LAL99], but not in the one presented in [KM00].

On Fig. 6.3 on page 96 the microcanonical angular velocity  $\omega$  as a function of  $\Omega$  and  $\epsilon$  is plotted. As a direct consequence of eq. (6.8) on page 90,  $\omega$  tends to zero with  $\Omega$ , and at

<sup>c</sup>See in app. B.3 a discussion about the technical reasons that limit the value of  $N$ .

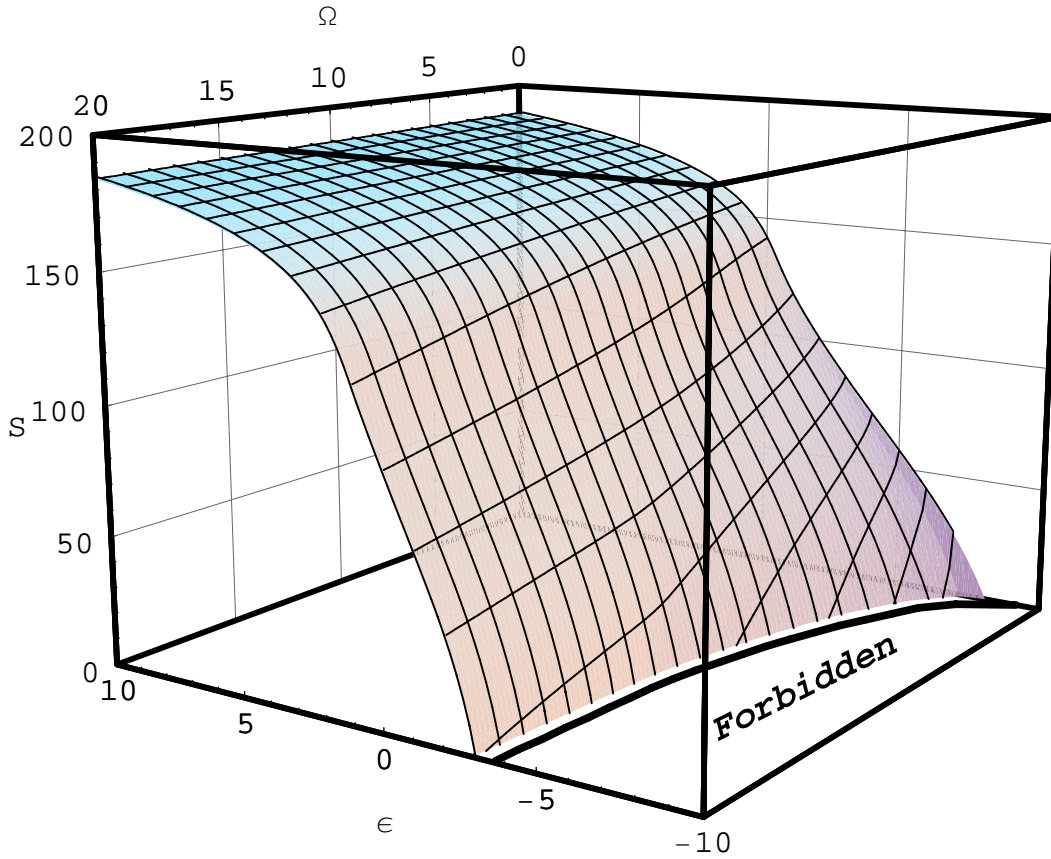


Figure 6.1: Entropy surface  $S(\epsilon, \Omega = l^2)$ , the mesh lines are at constant  $\epsilon$  or constant  $\Omega$ . The thick line is the projection of the  $T = 0$  ( $S \rightarrow -\infty$ ) isotherm. A convex intruder at constant  $\Omega$  and for a certain energy range (e.g.  $-2 < \epsilon < 0$  for  $\Omega = 20$ ) can be seen for all  $\Omega$ .  $S$  is not defined in the *forbidden* region; there the remaining energy  $\epsilon_r$  is negative for any spatial configuration.

high energies  $\omega$  is proportional to  $\sqrt{\Omega} = l$  ( $\propto L$ ). For low energies and  $\Omega < 12$ ,  $\omega$  exhibits some structures with peaks and troughs. In another words at fixed  $\epsilon$ ,  $\omega$  is not necessarily an increasing function of  $\Omega$ . At high  $\Omega$  ( $\Omega > 12$ ) and near the ground states  $\omega$  is almost a constant. All these structures can be understood in terms of mass distributions which influence  $\omega$  through  $I$  (see sec. 6.4.2).

### 6.4.2 Mass distribution

In order to understand the origin of the structures seen in the different microcanonical quantities ( $S$ ,  $\beta$ ,  $\omega$ , ...) one has to have a closer look at the spatial configurations, i.e. at the mass distributions. One of the observable studied in this work is the mass density  $\rho$  (see eq. (6.23) and (6.24) on the preceding page). As the system is rotationally invariant,  $\rho$  can only be a function of  $r$ , the distance from the center of coordinates.

On Fig. 6.4 on page 97  $\rho$  is plotted for different energies and for  $\Omega = 0$  and  $\Omega = 4$ . For  $\Omega = 0$  (Fig. 6.4(a)) the classical case (when  $E$  is the only fixed “extensive” parameter) is recovered. At high energy the system is in a homogeneous gas phase (flat  $\rho$ ), when

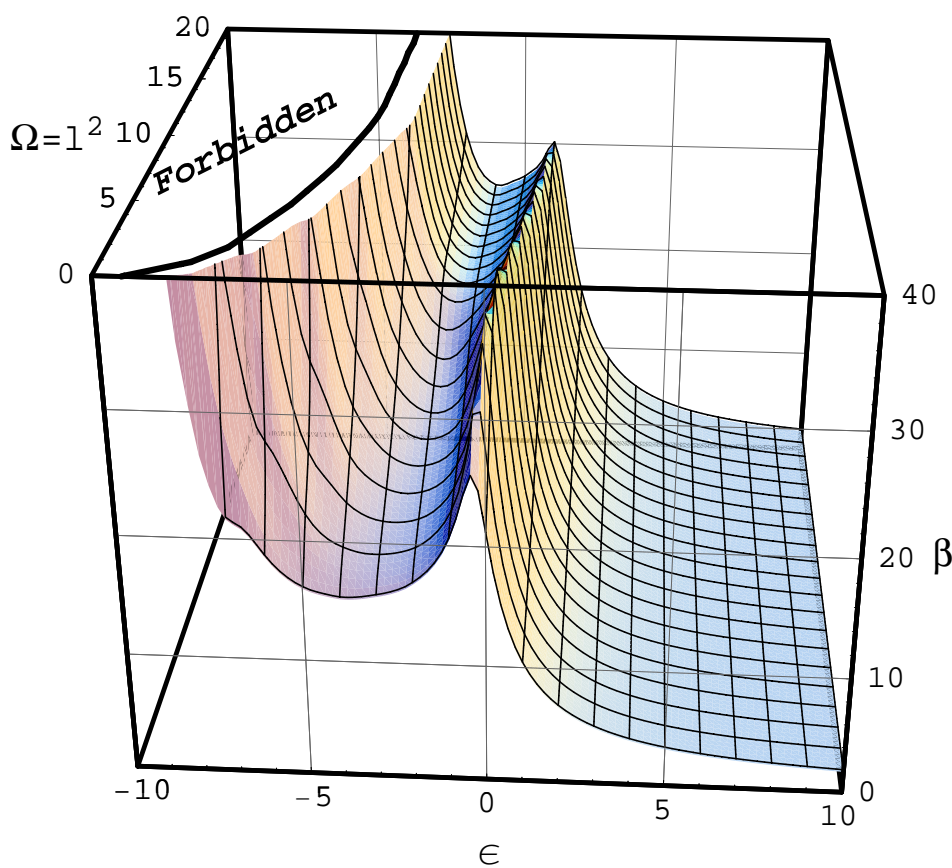


Figure 6.2: Inverse temperature  $\beta(\epsilon, \Omega = l^2)$  surface. The mesh lines are at constant  $\epsilon$  or constant  $\Omega$ . The intruder in  $S$  at fixed  $\Omega$  corresponds here to a multiple energy value for a given  $\beta$  and  $\Omega$ , e.g.  $\beta(\epsilon, \Omega = 0) = 20$  has three solutions  $\epsilon_1 \approx 0$ ,  $\epsilon_2 \approx -1$  and  $\epsilon_3 \approx -6$ . The thick line is the projection of the  $\beta = \infty$  isotherm;  $\beta$  is not defined in the *forbidden* region.

the energy decreases the system undergoes a phase transition and eventually ends up in a collapse phase where a majority of particles are in a cluster near the center of coordinates ( $\rho$  peaked at  $r = 0$ ). For  $\Omega \neq 0$  (Fig. 6.4(b)) the situation is very different. At high energy the homogeneous gas phase is still present. But at low energy the system cannot collapse entirely at the center of mass. This is due to the rotational energy term ( $\epsilon_{rot} = \frac{\Omega}{I}$ ) in the remaining energy, see eq. (6.19) on page 92. If the system contracts at the center then the inertial momentum  $I$  will tend to zero and therefore  $\epsilon_{rot}$  will diverge leading to a negative remaining energy  $\epsilon_r$ . So depending on the value of  $\Omega$  the main cluster will eject a certain amount of particles in order to increase  $I$ . Near the ground state these “free” particles will eventually collapse to form a second cluster in order to decrease the potential energy  $\phi$ . Due to the conservation of the center of mass, the position of the biggest cluster will be shifted from the center by a certain amount (see Fig. 6.4(b) at  $\epsilon = -5$ ). At low  $\Omega$  one particle will be ejected. With increasing  $\Omega$  the number of ejected particles raises and this process stops when two equal-size clusters are formed. This explains the discreteness of the peaks in  $\omega$  (Fig. 6.3 on the next page); the increase of the ground state energy  $\epsilon_g(\Omega)$ , because the potential energy of a single cluster of size  $N$  is smaller than the one of two

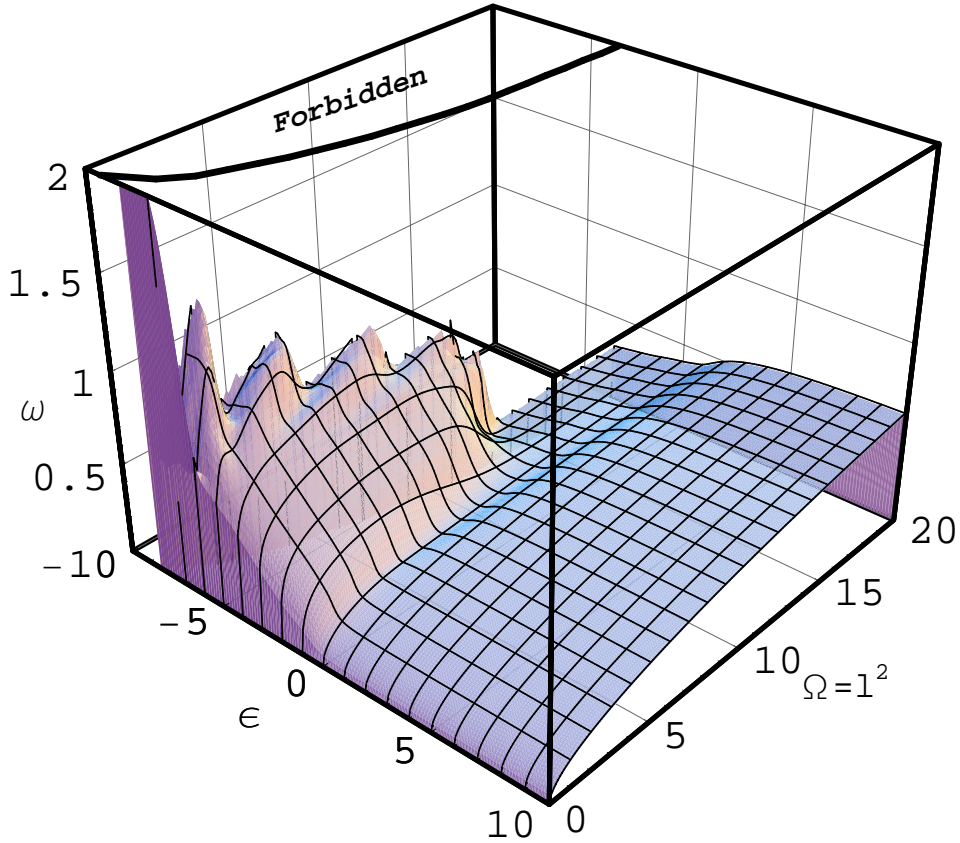


Figure 6.3: Microcanonical angular velocity  $\omega(\epsilon, \Omega = l^2)$  surface. The mesh lines are at constant  $\epsilon$  or constant  $\Omega$ .  $\omega$  is not defined in the *forbidden* region. At high energy  $\omega \propto \sqrt{\Omega} = l$ ; Near the ground states  $\omega$  shows a richer non-monotonic behavior with peaks and troughs for small  $\Omega$  and has a nearly constant value for large  $\Omega$  (see text).

well separated clusters. At high  $\Omega \gtrsim 12$  the system undergoes a phase transition from a gas phase to a collapse phase with two equal size clusters close to the boundary. From one value of  $\Omega = \Omega_1 > 12$  to another one  $\Omega_2 > \Omega_1$  the whole entropy curve at fixed angular momentum is simply shifted along the energy axis, i.e.  $S(\epsilon, \Omega_1) \approx S(\epsilon + \frac{\Omega_2 - \Omega_1}{N}, \Omega_2)$ . So the ground state energy  $\epsilon_g(\Omega)$  at high  $\Omega$  is almost on a line of equation  $\epsilon_g + \frac{\Omega}{N} + \phi_g \approx 0$ , where  $\frac{\Omega}{N}$  and  $\phi_g$  are the rotational energy and the potential energy of 2 clusters of size  $N/2$  at radius  $r = 1$  respectively. This monotonic behavior has already been mentioned for all the thermodynamical variables e.g.  $S$ ,  $\beta$ ,  $\omega$ , see Figs. 6.1 to 6.3 on pages 94–96.

One could object that, as  $\rho$  is only a function of  $r$  it cannot be used to infer the angular distribution of the particles, i.e. there is not enough information to say if a peak in  $\rho$  at  $r_0 \neq 0$  corresponds to one or many clusters or to a uniform distribution of the particles lying on a circle of radius  $r_0$  (ring). However at least at very low energy a many clusters (more than two) configuration is very unlikely and will not contribute to the average values for reasons linked to the configurational weight  $W(\mathbf{r}) = \frac{1}{\sqrt{I}} \epsilon_r^{N-5/2}$ . For simplicity let us assume that there is only one strong peak in  $\rho$  at  $r = r_0 \neq 0$ . Since the center of mass is fixed this cannot be the signature of a 1-cluster system. At least 2-clusters lying on a circle of radius  $r_0$  are needed. All the  $n$ -clusters systems compatible with the assumed

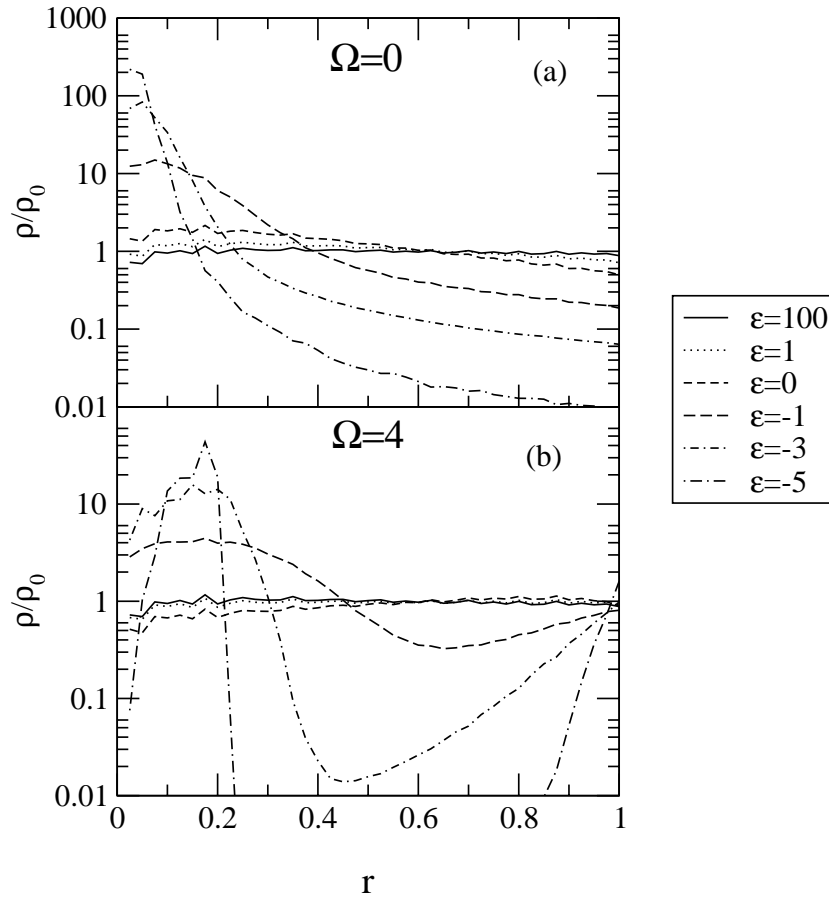


Figure 6.4: Density as a function of the distance from the center  $r$  for different values of energy  $\epsilon$  and angular velocity  $\Omega$  (arbitrary units). At high energy and for all  $\Omega$  the density is flat; the system is in the homogeneous gas phase. Near the ground state the density shows one peak for  $\Omega = 0$  (a) and two peaks for  $\Omega > 0$  (b), which correspond respectively to a one cluster and to a two clusters phase surrounded by some gas (see text).

radial density have the same rotational energy  $\frac{\Omega}{I} = \frac{\Omega}{Nr_0^2}$ , but their corresponding potential energy  $\phi_n$  are different. For example, with  $\sigma = 0.05$ ,  $r_0 = 0.5$  and  $N = 24$  the ratio of potential energy is  $\frac{\phi_2}{\phi_3} \simeq 1.7$ . So at low energy, the remaining energy  $\epsilon_r$  corresponding to a 2-clusters system will be much larger than the 3-clusters' one, leading to a *huge* difference<sup>d</sup> in the weight  $W(\mathbf{r})$ . So at low energy and for  $\Omega \neq 0$  the 2-clusters case is dominant. At higher energies, the term  $Bg(I, \phi)$  in eq. (6.19) on page 92 can compensate the difference in the weight  $W(\mathbf{r})$  and allow many clusters configurations and eventually at high energy a complete random configuration on the ring of radius  $r_0$  will dominate the average mass distribution.

This argument can be checked by studying other observables, for example the normalized distance distribution  $P(d)$ , i.e. the density of probability that the distance between two given particles is  $d$ . To probe the information given by  $P(d)$ , it has been estimated for four simple mass distributions: (a) 2-clusters, (b) 3-clusters, (c) ring, (d) uniform random

<sup>d</sup>The energy  $\epsilon_r$  is put to a power of  $\sim N$ , see eq. (6.19).

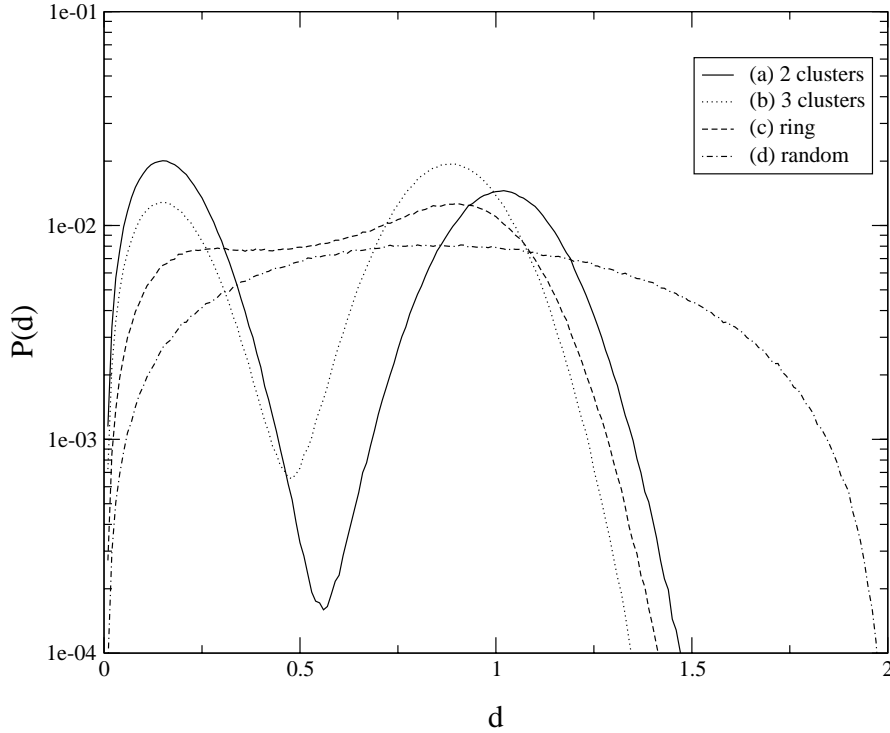


Figure 6.5: Average of  $P(d)$  the distance distribution for different simulated spatial configurations. See text.

distribution. For (a), (b) and (c) the particles were put on a circle of radius  $r_0 = 0.5$ , and then randomly shifted several times (in order to give a spatial extension to these idealized initial configurations). Finally the  $\frac{N(N-1)}{2}$  distances are recorded for all realizations and averaged. Figure 6.5 shows the average of  $P(d)$  over 1000 realizations. Note that the density distribution  $\rho(r)$  is by construction exactly the same for the three first cases, i.e. strongly peaked at  $r_0$  with a width of about 0.5. The latter value depends on the shift one applies on the initial idealized spatial configurations.

As one can see on Fig. 6.5 that although the density distribution is the same for (a), (b) and (c),  $P(d)$  gives some new insight on the mass distribution:

- (a) There are two peaks, one at small  $d$  which corresponds to a clusterisation and another one at  $r \simeq 1 = 2 * r_0$ ; this is exactly the distance between the two clusters (more precisely between their center of mass). The areas under the small and large  $d$  peaks are equal. Indeed the number of short distance pairs is about  $\frac{N^2}{4}$  which is also the number of pairs with  $d \simeq 1$ . The widths of the first and second peaks are (as expected)  $\sim 0.5$  and  $\sim 1 = 2 * 0.5$ , respectively.
- (b) There are again two peaks one at small  $d$  and another at  $d \simeq 0.8 < 1$  and their respective widths are similar to the case (a). The large  $d$  is compatible with the length of one side of the equilateral triangle on top of which the idealized 3-clusters mass distribution has been built. This time the area under the large  $d$  peak is larger than the one under the short  $d$  peak, since the number of short distance pairs is about  $\frac{N^2}{6}$  whereas the number of pairs with  $d \simeq 0.8$  is  $\frac{N^2}{3}$ .

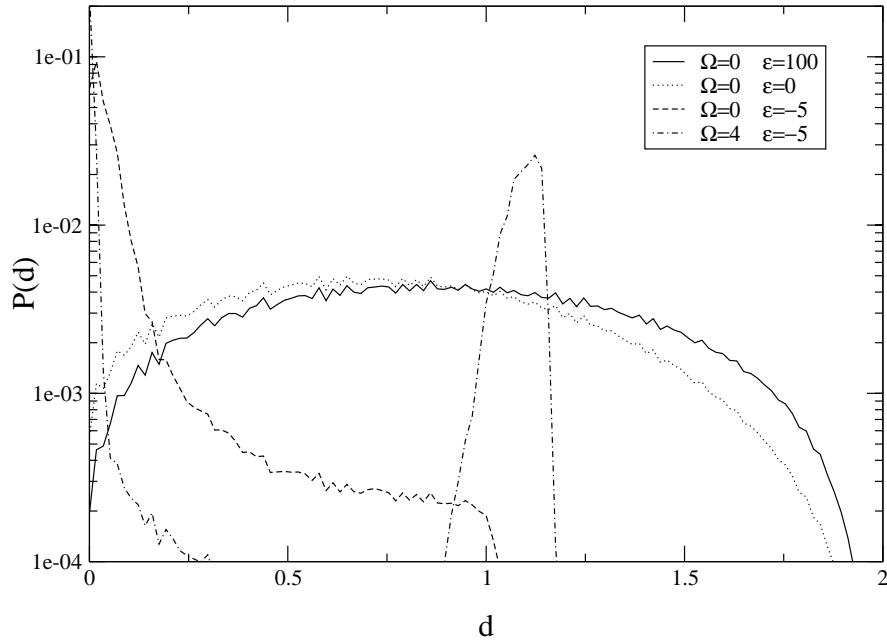


Figure 6.6: Distance distribution  $P(d)$  for different values of  $(\epsilon, \Omega)$ . At high energy  $P(d)$  corresponds to a random distribution (see Fig. 6.5 on the facing page). For  $\Omega = 0$  and at low energy,  $P(d)$  has one peak at  $d \approx 0$ ; almost all particles are very close from each other, and there is a single cluster collapse phase. For  $\Omega \neq 0$  there are two peaks at low energy: one at very small  $d$  which is a sign of clusterisation and another peak at large  $d$  which signals multiple clusterisations; in fact there are two clusters (see text).

- (c) For the ring case a trace of the two peaks still exists but they are not well separated because a lot of intermediate distances are compatible with this model.
- (d) When the particles are uniformly distributed  $P(d)$  has a binomial-like shape.

$P(d)$  has also been estimated for the present gravitational system, as shown on Fig 6.6. At high energy,  $P(d)$  corresponds to the randomly distributed case (see Fig. 6.5 on the facing page). At low energy with  $\Omega = 0$ ,  $P(d)$  has only one peak at  $d = 0$ , this corresponds clearly to a single cluster case surrounded by some gas. For  $\Omega \neq 0$  and at low energy (in Fig. 6.6  $\epsilon = -5$  and  $\Omega = 4$ ), there are two well separated peaks, one at small  $d_0 = 0$  and the other at  $d_1 \simeq 1.1$ . The peaks imply the presence of at least two clusters. However, the fact that the widths of the peaks are small excludes a large number of clusters and even more the ring case (see Fig. 6.5). Now one can combine this information with the one obtained from the study of the radial density  $\rho(r)$  (see Fig. 6.4 on page 97). For  $\epsilon = -5$  and  $\Omega = 4$ ,  $\rho$  has two peaks at  $r_1 \simeq 0.15$  and  $r_2 \simeq 1$ . All in all, this means that there are, in the mean, two clusters rotating around the center of mass. The distance between these clusters is  $r_1 + r_2 \simeq 1.15 \simeq d_1$ . Their mass ratio is  $\frac{m_2}{m_1} = \frac{r_1}{r_2} \simeq 0.15$ . Since the total mass is  $m_1 + m_2 = 20$ , hence  $m_1 \simeq 17$  and  $m_2 \simeq 3$ .

The distance distribution can be of great help to identify the mass distributions at low energies. However at the transition regions since there is a superposition of different types of mass distributions the knowledge  $\rho$  and  $P(d)$  is not sufficient and therefore of no help if one wants to study for example the “fractality” of the mass distribution as it has been

done in other self-gravitating systems [DVS00, SIM<sup>+</sup>00], and further work is needed to get a more detailed picture.

At very low energy, near the ground state at least one of the clusters (the smallest) is very close to the boundary. There the assumption of a small evaporation rate made in chap. 5 on page 87 does not hold.

### 6.4.3 Phase diagram

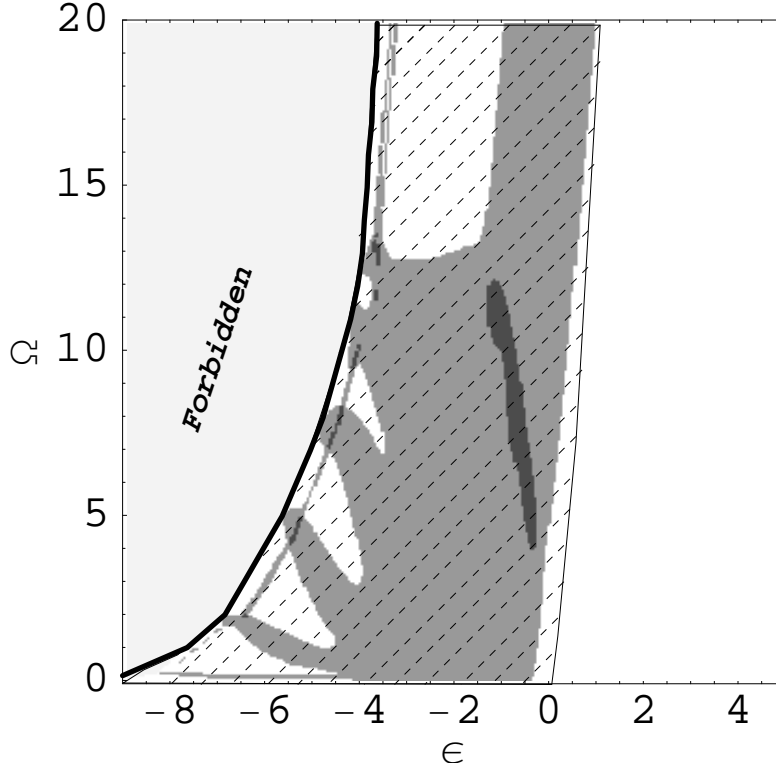


Figure 6.7: Sign of the largest eigenvalues of  $H_S$  the Hessian matrix of  $S$  as defined in chapter 2. The white regions correspond to  $\lambda_1 < 0$ . These are pure phase regions. The gray region corresponds to  $\lambda_1 > 0$  and  $\lambda_2 < 0$  and the dark gray ones also to  $\lambda_1 > 0$  but  $\lambda_2 > 0$ .  $\lambda_2$  is the second eigenvalue of  $H_S$ .  $\lambda_1 > 0$  defines first order phase transition regions (see text). Points in  $G$  (the region filled with dashed lines) correspond to *local* maxima (minima) of  $f(X, X_0) = -x_0 \cdot X + S(X)$  (see eq. (1.12) on page 7) if  $\lambda_1(X_0) < 0$  ( $\lambda_1(X_0) > 0$ ). Points outside  $G$  correspond to *global* maxima of  $f(X, X_0)$ . There is a one-to-one mapping between the microcanonical ensemble and the GBE only outside the  $G$  region (see text).  $S$  is not defined in the *forbidden* region, here in light gray. Note that (a) the points at  $\Omega = 0$  and low energies  $\epsilon < -7$  are not included in  $G$ , (b) the high energy limit of  $G$  is known only approximately.

In Fig. 6.7, the sign of  $\lambda_1$  as a function of  $\epsilon$  and  $\Omega$  is plotted.  $\lambda_1$  is the largest eigenvalue of the Hessian matrix of  $S$  (see sec. 1.2.2 on page 8)

$$H_s = \left\| \begin{array}{cc} \frac{\partial^2 S}{\partial r^2} & \frac{\partial^2 S}{\partial \epsilon \partial l} \\ \frac{\partial^2 S}{\partial l \partial \epsilon} & \frac{\partial^2 S}{\partial l^2} \end{array} \right\|. \quad (6.25)$$

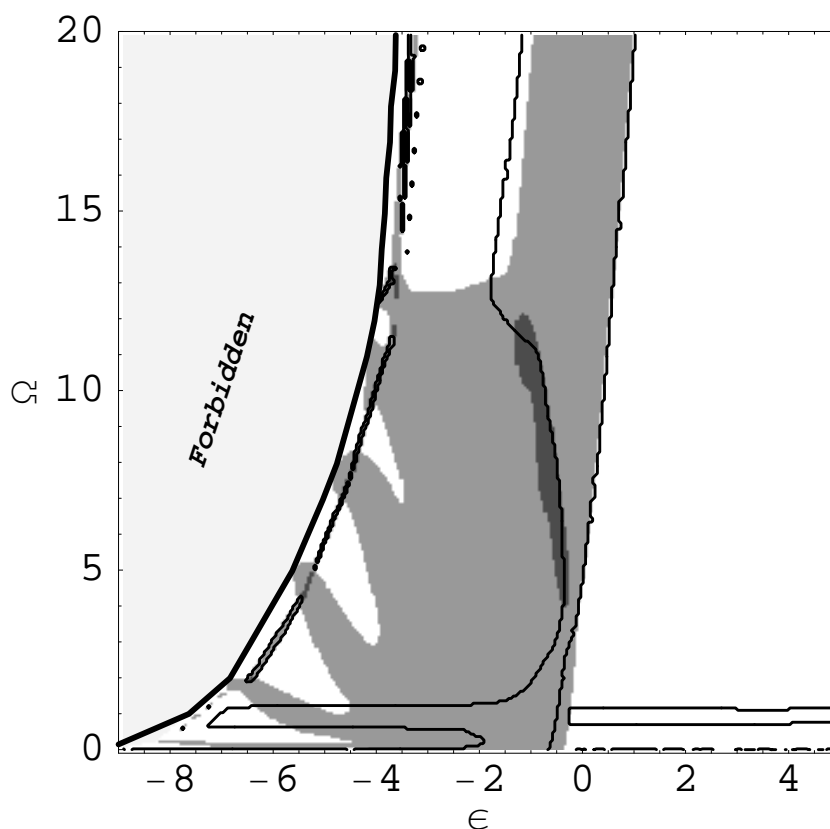


Figure 6.8: Locus of second order phase transitions (see text).

This plot can be taken as the phase diagram of the self-gravitating system at fixed  $\epsilon$  and  $l$ . The white regions correspond to pure phases ( $\lambda_1 < 0$ ). At high energy there is a homogeneous gas phase and at low energy there are several pure collapse phases with one ( $l = \sqrt{\Omega} = 0$ ) or two ( $l \neq 0$ ) clusters. The different 2-clusters phases are characterized by the relative size of their clusters (see sec. 6.4.2). These regions are separated by first order phase transition regions where  $\lambda_1 > 0$  (gray in Fig. 6.7). There is even one region (dark gray) where the entropy  $S$  is a *convex* function of  $\epsilon$  and  $l$ ; i.e. all the eigenvalues of  $H_S$  are positive ( $\lambda_1 > 0$  and  $\lambda_2 > 0$ ). This region is rather stable with respect to the number of particles (at least for  $N \lesssim 100$ ). Its specific surface slightly increases with the number of particles  $N$ .

The orientation of  $\mathbf{v}_1$  the eigenvector associated with  $\lambda_1$  (defined as the largest eigenvalue of  $H_S$ ) is not yet known in details for all  $(\epsilon, l)$ . However it can already be stated that at “high” energy  $\mathbf{v}_1$  is almost parallel to the energy axe (phase transition in the  $\epsilon$  direction) and should be parallel to the ground state at very low energy. The overall structure of the collapse phases matches the one of the angular velocity  $\omega$  (see Fig. 6.3 on page 96): roughly, the peaks in  $\omega$  correspond to pure phases while the valleys between these peaks belong to the first order phase transition region.

As already mentioned, unlike in the model presented by Laliena in [LAL99] there is no critical angular momentum  $L_c$  above which the first order phase transition vanishes giving rise to a second order phase transition at  $L_c$ . Nevertheless this does not exclude second order phase transition (critical point) at all. They are defined in the microcanonical

ensemble by: (i)  $\lambda_1 = 0$ ; (ii)  $\nabla\lambda_1 \cdot \mathbf{v}_1 = 0$  (see sec. 2.3 on page 30). On Fig. 6.8 on the page before (just like on Fig. 6.7 on page 100) regions where  $\lambda_1 < 0$  ( $> 0$ ) are in white (gray). The condition (i) is simply achieved at the boarder between the gray and the white regions. The thick lines on Fig. 6.8 correspond to condition (ii). Second order phase transitions are located at the crossing points of the thick lines and the boarders. One immediately sees that there are several critical points. However there are not all of (astro-)physical interest since most of them are close to the ground states line or at very high angular momentum where the small evaporation rate assumption is not valid. Nevertheless there are two points one at  $(\epsilon, \Omega) \approx (-0.5, 1)$  and another one at  $(\epsilon, \Omega) \approx (0, 4)$  where this assumption is valid and therefore they deserve further investigations and especially regarding their corresponding mass distributions.

#### 6.4.4 Loss of information in CE

In a recent paper Klinko and Miller have studied another model for rotating self-gravitating systems [KM00]. They introduced the canonical analogous of the  $X = \{\epsilon, \Omega = l^2\}$  ensemble namely the  $x = \{\beta, \gamma\}$  ensemble (GBE), see eq. (6.6) and (6.9) on page 90.

If one inspects the entropy surface  $S(X)$  (see Fig. 6.1 on page 94) it is clear that conditions (1')<sup>e</sup> or (2')<sup>f</sup> are not satisfied for all the points in the region filled with dashed lines ( $G$ ) in Fig. 6.7 on page 100. This is due to the concavity of the energy ground state  $\epsilon_g(\Omega)$ .  $G$  includes all the two-clusters collapsed phases, the first and second order phase transitions (except for  $\omega = \gamma = l = 0$ ). All the information contained in  $G$  is smeared out through the Laplace transform linking ME and GBE (eq. (1.12) on page 7) and, in practice, lost.

The fact that GBE misses all the two-clusters collapse phases would already be enough to disqualify it as being a good approximation (mathematical trick) of the ME. But, furthermore, if one studies more carefully  $f(X, X_0) = f(X, x_0 = \frac{\partial S}{\partial X}|_{X_0}) = -x_0 \cdot X + S(X)$ ,  $X_0 \in G$ ; one will notice that (a) there is one local maximum at  $\Omega = 0$  and (b) there is no maximum for high  $\Omega$ : in the direction of increasing  $\Omega$  at low energy,  $f(X, x_0)$  is a never ending increasing function, i.e.  $f(X, x_0)$  has *no global maximum* for  $X \in G$  (see Fig. 6.9 on the next page). Therefore the integral in eq. (1.12) on page 7 *diverges* for all  $x_0, X_0 \in G$ . In other words the GBE, for the present model, is *not defined* for high  $\beta$  and  $\gamma \neq 0$  ( $\omega \neq 0$ ). Although this result can sound very surprise, it is a direct consequence of the quasi-linear behavior of the ground state of  $S$  as a function of  $\Omega \sim L^2$ , hence a similar result can be found for the van der Waals gas presented in chapter 1. The domain of definition of the entropy of this model ( $\neq$  domain of physical validity) is convex, and there is a region where although the conjugates of the entropy are clearly defined in the microcanonical ensemble<sup>g</sup>, the partition sum *diverges* for these values of the intensive parameters.

One could argue that GBE is not the correct canonical ensemble (CE) for this system. I.e. one should rather fix the conjugate of  $\epsilon$  and  $l$ , the inverse temperature  $\beta$  and the angular velocity  $\omega$ , respectively.

In order to simplify the discussion, the microcanonical entropy  $S$  is plotted in fig. 6.10 (see also fig. 6.1 on page 94) as a function of the energy and the angular momentum  $l$ .

<sup>e</sup> $\langle X \rangle_{\text{CE}} = X_0$ , see sec. 1.2.3 on page 10.

<sup>f</sup>Small fluctuations of  $X$  in GBE, see sec. 1.2.3 on page 10.

<sup>g</sup>The conjugates are clearly defined from a mathematical point of view, physically it is not the case since there the pressure is *negative*.

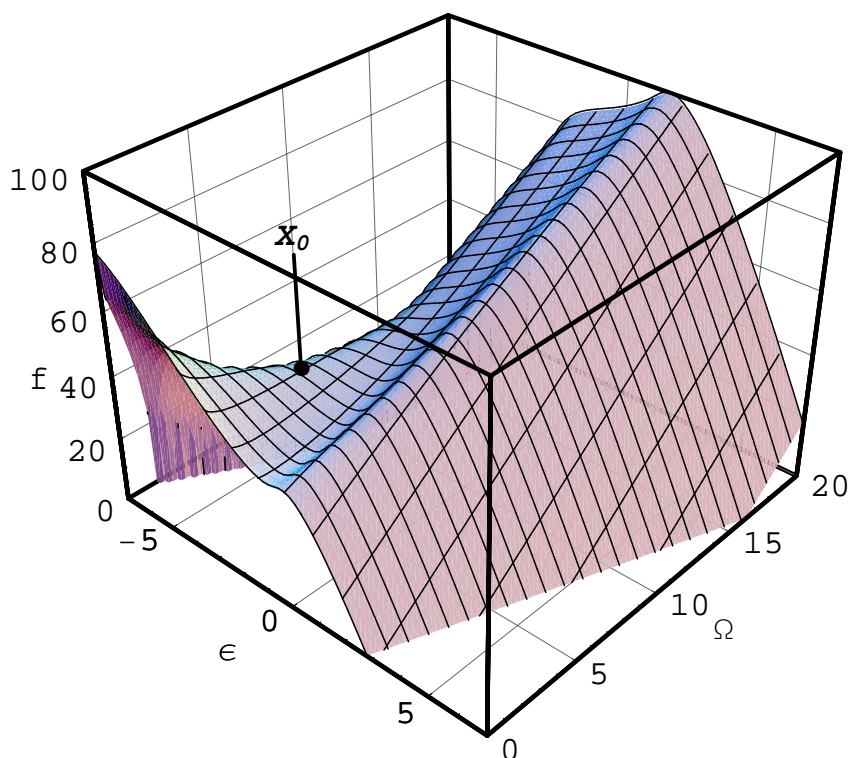


Figure 6.9:  $f(\epsilon, \Omega, \beta_0, \gamma_0) = -\epsilon\beta_0 - \Omega\beta_0\gamma_0 + S(\epsilon, \Omega) - K$  as a function of  $\epsilon$  and  $\Omega$ , where  $K$  is an arbitrary constant;  $\beta_0 = \beta(\epsilon_0, \Omega_0)$ ;  $\Omega_0 = \Omega(\epsilon_0, \Omega_0)$ ;  $X_0 = (\epsilon_0, \Omega_0) = (-3, 5) \Rightarrow (\Omega_0, \gamma_0) \approx (27.9, -0.196)$ . The mesh lines are at constant  $\epsilon$  or constant  $\Omega$ . As expected  $f$  has a saddle point at  $X_0 \approx (\beta_0, \gamma_0)$  since  $\lambda_1(X_0) > 0$  and  $\lambda_2(X_0) < 0$  (see text and Fig. 6.7 on page 100).  $f$  has a global maximum at  $\Omega = 0$  and  $\epsilon \approx -7$ , but one sees that it is an monotonically increasing function for increasing  $\Omega$  and  $\epsilon(\Omega) \approx \epsilon_g(\Omega) + 2$ . Therefore the integral in eq. (1.12) on page 7 *diverges* and the  $(\beta, \gamma\beta)$  ensemble is *not defined* for  $(\beta_0, \gamma_0)$ .

One can clearly distinguish two parts. One for  $0 \leq l \lesssim 4$  and the other with  $l \gtrsim 4$ . The ground states at  $l < 4$  correspond to the two asymmetric clusters cases (except at  $l = 0$ ) whereas for  $l > 4$  two equal size clusters compose the ground states. At large  $l$ , the ground states line is convex as a function of  $l$ , i.e.  $\frac{\partial^2 \epsilon_g}{\partial l^2} > 0$ . Hence, the origin of the divergences in GBE is removed in CE. However, one can directly conclude from fig. 6.10 that no point  $X_0 = (\epsilon_0, l_0)$  in the region where  $\epsilon \lesssim 0$  and  $l \lesssim 5$  corresponds to a global maximum of the function  $f(\epsilon, l, \beta_0, \omega_0) = -\epsilon\beta_0 - l\beta_0\omega_0 + S(\epsilon, l)$  (for an example see fig. 6.11). This implies that all the asymmetric pure phases are overlooked by CE. It can be shown that this is also the case for the two critical regions at relatively high energies.

All the examples of this section show how dramatic can be the information loss if one studies an isolated system in ensembles where the intensive variables are fixed.

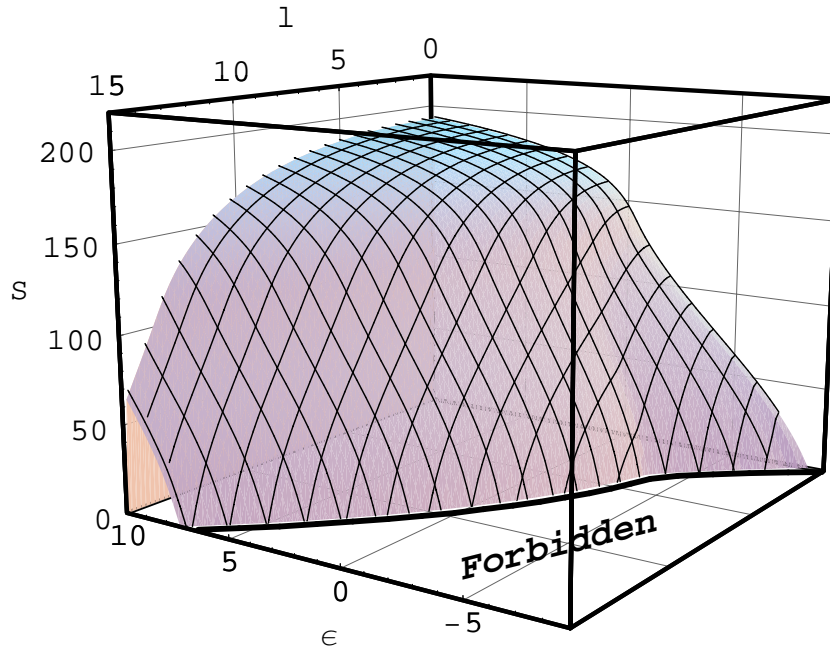


Figure 6.10: Entropy surface as function of  $l = \sqrt{\Omega}$  and  $\epsilon$ . The mesh line are at constant  $l$  or  $\epsilon$ . The thick line is the projection of the ground states.  $S$  is not defined in the *forbidden* region.

## 6.5 Discussion and conclusions

In this chapter the results of the study of the equilibrium properties of a self-gravitating system is presented. The “extensive” dynamical quantities are the total energy  $E$  and the angular momentum  $L$ . This is the first study where no assumption is made about the spatial properties of the mass distribution.

It is shown that the conservation of the angular momentum plays a non-trivial role. One can find that these systems have a surprisingly rich phase diagram with a large first order phase transition region and also non trivial second order phase transitions.

All the phase diagram is not of physical relevance since near the ground states line the small evaporation rates assumption breaks down. Nevertheless, there are two critical regions at relatively high energies which could be of astrophysical importance. Further studies are needed to

- localize more precisely these critical regions,
- check their presence for systems with large number of particles,
- study their corresponding mass distribution.

There is no heat bath for astrophysical system. But if one uses the canonical ensemble as a mathematical trick one would loose all the information about

- the asymmetric cluster phases,
- the first order transition region,

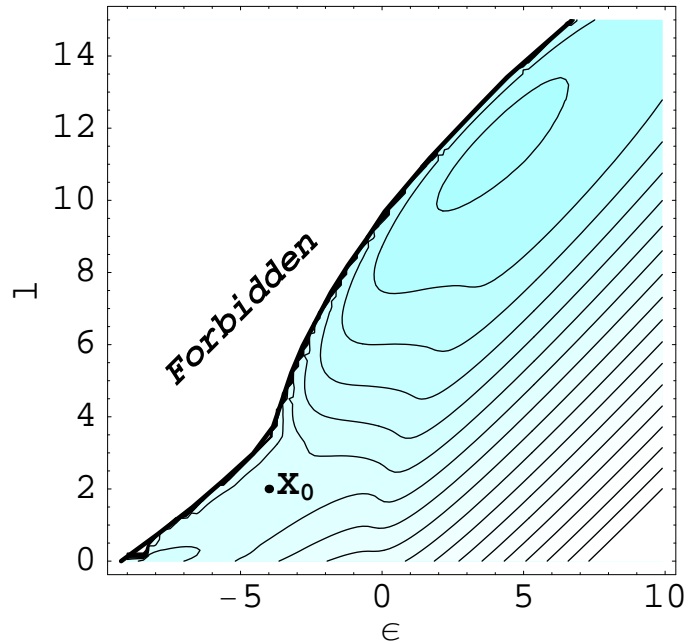


Figure 6.11: Contour-density plot of  $f(\epsilon, l, \beta_0, \omega_0) = -\epsilon\beta_0 - l\beta_0\omega_0 + S(\epsilon, l) - K$  as a function of  $\epsilon$  and  $l$ , where  $K$  is an arbitrary constant;  $\beta_0 = \beta(\epsilon_0, l_0)$ ;  $\omega_0 = \omega(\epsilon_0, l_0)$ .  $X_0 = (\epsilon_0, l_0) = (-4, 2)$ . As expected  $f$  has a saddle point at  $X_0 = (\beta_0, l_0)$  since  $\lambda_1(X_0) > 0$  and  $\lambda_2(X_0) < 0$  (see text and Fig. 6.7 on page 100). The main contribution to the partition sum for these values of the intensive variables comes from points located toward  $(\epsilon, l) \approx (5, 12)$ . Hence, in CE at  $(\beta_0, \omega_0)$ , The mass distribution is composed by two equal-size clusters rotating with large mean energies and angular momentum. This is in sharp contrast to the physical situations at  $X_0$ .  $f$  is not defined in the *forbidden* region.

- the critical point.

Furthermore, for a particular choice of intensive variables the partition sum *diverges* for some (microcanonically defined) values of these intensives variables.

Of course, it just an *equilibrium statistical* model that is presented. It may help to understand the physics of globular clusters or collapsing molecular clouds, but the results should be interpreted with caution especially in the case of star formation. A lot of “ingredients” are missing in order to have a complete picture of the formation of multiple stars systems and planetary systems, for instance the magnetic field [HMCB00, GSLL00], or the presence of vortices [CHA00].

The study of such self-gravitating system is in its infancy [LL96A, LAL99]. There are a lot of research directions.

The main weakness of the results presented in this chapter is the very limited number of particles that could be considered. Though, in many cases, in astrophysical context all the qualitative equilibrium behaviors could be given with small number of particles (see e.g. Padmanabhan and its two particles models in [PAD90]). However, if one wants to study the equilibrium properties of galaxies, one cannot be completely satisfied with results obtained from 20 particles models. Work is in progress to increase the number of particles and also to study the system in 3-dimensional space.



# General conclusions

This thesis has been devoted to the study of phase transitions in “small” systems. A system where the range of the forces is at least of the order of the system size is considered to be “small”.

These “small” systems cannot be considered as being at the thermodynamical limit, and are moreover non-extensive. Hence, the usual thermostatistics does not offer a satisfactory framework to study their equilibrium properties. As an example, in thermostatistics, phase transitions are defined by means of singularities of the canonical potential. These singularities cannot occur in finite-size systems, and extensivity is essential to define a proper canonical ensemble.

However, as recalled and many times illustrated in this thesis, one can define phases and phase transitions in the microcanonical ensemble by means of the topological properties of the entropy surface. The microcanonical ensemble is the proper ensemble to describe “small” systems. It is defined by means of the dynamical properties of the considered system. Extensivity and infinite number of particles are not required in order to define the microcanonical ensemble.

In this thesis new results from applications of the microcanonical thermostatistics to several “small” systems have been presented.

First, the liquid-gas phase transition of metal clusters has been studied for low and large microcanonical pressures.

At atmospheric pressure and for a certain range of enthalpy, the caloric curve is characterized by a *negative* heat capacity. In “small” systems, this signals a first order phase transition. This phase transition is divided into two parts (with increasing enthalpy). First, the big liquid cluster evaporates light fragments (monomers and dimers) over a relatively large enthalpy-range. Then, this time in a very narrow enthalpy region, the temperature drops down rapidly. There the mass distribution is reorganized completely. Before this fast transition, the mass distribution is composed by one big liquid cluster, embedded in a gas of light fragments. After this transition, there are no longer any very big liquid cluster, but on the contrary, there are several medium sized fragments (dimers, 4-mers and 8-mers). This particular mass selection is explained by the local maxima of their respective binding energy as a function of the cluster size. These irregularities are due to the electronic shell effects. After this fast transition, the caloric curve recovers a “normal” slope as a function of  $h$ , i.e. a *positive* heat capacity. Then, the fragments decay to monomers. In the present thesis, this region of the caloric curve has been called multifragmentation regime. At very high enthalpies, there are only monomers.

The multifragmentation is not accessible to a canonical description because it does not correspond to absolute minima of the free energy.

At the thermodynamical limit the multifragmentation regime vanishes, and the transition from a liquid to a gas occurs uniquely via evaporation.

At high pressures, the avoided volume to the clusters,  $NCC$ , plays a very important role by

- (a) selecting the mass distribution with small  $NCC$ ,
- (b) giving the main contribution to the pressure via its derivative with respect to the volume of the system.

In a new model of metallic clusters, the critical point (second order phase transition) of the liquid–gas transition has been reached for the first time. Although, in this simplified model the critical parameters do not scale to their bulk values, the results confirm the preliminary ones obtained from the previous cluster model. E.g. the critical point of finite size cluster is located at higher pressure and density and at lower temperature than the bulk critical point.

In order to improve the quantitative estimates of the critical parameters, one should include some properties of the clusters that have been removed from the model in order to make possible these firsts numerical computations (e.g. highly excited clusters).

The other “small” system studied within the microcanonical thermostatics is a model self-gravitating  $N$ -bodies. Due to the non saturation of the Newtonian gravitational potential, self-gravitating systems are “small”. This model is studied as a function of the total energy  $E$  and of the total angular momentum  $L$ .

On average, all the particles of the system rotates around the center of mass of the system with the same angular velocity. The dispersion of the linear momenta is a function of the distance to the center of mass  $d$ . This dispersion increases from the center to the boundary.

By using the definitions of phases and phase transitions of “small” systems, one could construct the phase diagram of the considered self-gravitation system. At high energies, the system is in a pure gas phase (uniform mass distribution). For  $L = 0$  and at low energy, the system is in a pure collapsed phase with a large concentration of particles at the center of mass (one cluster). For  $L \neq 0$  and near the ground states, there are several pure phases. Their respective mass distributions are composed of *two* clusters. At small  $L$  the respective masses of the clusters are very different. At large  $L$  and near the ground state, the pure phase is made of two equal-size clusters located very close to the system boundary. All the pure phases are separated by a first order phase transition region. There are even several second order phase transitions. Although, they are not all of physical relevance, two of them, located at relatively high energies, might be of astrophysical importance. They deserve further studies.

All the pure phases with non-symmetric cluster masses, the first order and all second order phase transitions are overlooked if one fixes the intensive variables. It is even shown, that for a particular choice of the intensive parameters the partition sum *diverges* for some microcanonical values of these parameters.

Hence, throughout this thesis many examples of the deep insight provided by the microcanonical thermostatics of “small” systems on the equilibrium properties of those systems have been given. They show that, contrary to the Schrödinger’s pessimistic prediction [SCH46], the microcanonical entropy defined via Boltzmann’s principle is not just only useful to study gases.

# Appendix A

## Avoided volume

The volume part  $\omega_{NCC}$  of the total microcanonical weight (see eq. (3.12a) on page 48) describes the accessible volume to  $N_f$  non-overlapping fragments positioned within a spherical container of volume  $V$ . For low pressures ( $\sim$  large volumes) analytical forms (exact and approximation) of  $\omega_{NCC}$  can be worked out (see sec. A.1). At very high densities, near the critical packing fraction (see below) a free-volume theory can be formulated (see e.g. [AW62] and refs. quoted therein). Unfortunately for intermediate pressures these approximations are not valid and there is no available ansatz suitable for MMC even for simple models of hard spheres, see e.g. [LUD01]. This issue is yet an unsolved, mathematical problem, that generates a lot of literatures in mathematics [WIL98, CS89, ARH98] but also for concrete applications in crystallography [WIL91, BS97], in chemical physics (via the equation of state, see sec. A.1.2), nuclear physics [BBI<sup>+</sup>95, RRS88, RAD01], molecular biology (see e.g. [KSS01]), etc.

### A.1 Analytical expressions — EOS ansatz

#### A.1.1 Exact expressions

For clarity, let us first recall the definition of  $NCC$

$$NCC \doteq \frac{\int_V \dots \int_V d\mathbf{r}_1 \dots d\mathbf{r}_{N_f}}{\int_V \dots \int_V d\mathbf{r}_1 \dots d\mathbf{r}_{N_f} \Theta(\mathbf{r}_1, \dots, \mathbf{r}_{N_f}) \eta(\mathbf{r}_1, \dots, \mathbf{r}_{N_f})} \quad (\text{A.1a})$$

$$= \frac{V^{N_f}}{\int_V \dots \int_V d\mathbf{r}_1 \dots d\mathbf{r}_{N_f} \Theta(\mathbf{r}_1, \dots, \mathbf{r}_{N_f}) \eta(\mathbf{r}_1, \dots, \mathbf{r}_{N_f})}, \quad (\text{A.1b})$$

where  $\Theta$  forbids the overlapping of a cluster with the system boundary

$$\Theta(\mathbf{r}_1, \dots, \mathbf{r}_{N_f}) \doteq \begin{cases} 0 & \text{if at least one cluster overlaps with the boundary,} \\ 1 & \text{else;} \end{cases} \quad (\text{A.2})$$

$\eta$  forbids the overlapping between two clusters

$$\eta(\mathbf{r}_1, \dots, \mathbf{r}_{N_f}) \doteq \begin{cases} 0 & \text{if at least two clusters overlap,} \\ 1 & \text{else;} \end{cases} \quad (\text{A.3})$$

$NCC$  is the inverse probability to find a set of positions so that the clusters fit into the system volume.

For a single particle of radius  $r_1$  in a container of volume  $V = \frac{4\pi}{3}R^3$ , the inverse probability to find a position that fits in  $V$  is

$$NCC = \frac{V}{\frac{4\pi}{3}(R-r_1)^3} = \left(1 - \frac{r_1}{R}\right)^{-3}, \quad (\text{A.4})$$

where  $\frac{4\pi}{3}(R-r_1)^3$  is the accessible volume to (the center of mass of) the particle, it is called the “eigen-accessible volume”. Let us define the packing fraction  $\kappa \doteq \frac{V_0}{V}$ , where  $V_0$  is the sum of the fragment volumes (here  $V_0$  is simply  $\frac{4\pi}{3}r_1^3$ ).  $NCC$  diverges at  $R = r_1$ , i.e. the critical packing fraction  $\kappa_c$  is equal to 1.

The one-particle  $NCC$  given by eq. (A.4) is called in the following “eigen- $NCC$ ”.

When there are two spheres of radius  $r_1$  and  $r_2$  the divergence of  $\kappa$  is located at  $R = r_1 + r_2$

$$1/2 \leq \kappa_c = \frac{r_1^2 + r_2^2}{(r_1 + r_2)^2} \leq 1.$$

$NCC$  can also be computed analytically for the two spheres case. First consider that the cluster number 1 is fixed far from the boundary. The accessible volume to the second cluster is its eigen accessible volume  $\frac{4\pi}{3}(R-r_2)^3$  minus the avoided volume due to cluster 1,  $\frac{4\pi}{3}(r_1+r_2)^3$ . An integration over all the positions allowed for 1 yields to a first estimate of  $V_{acc}$ , the total accessible volume

$$V_{acc} = \left[\frac{4\pi}{3}(R-r_1)^3\right] \left[\frac{4\pi}{3}(R-r_2)^3 - \frac{4\pi}{3}(r_1+r_2)^3\right]. \quad (\text{A.5})$$

However when 1 is close to the boundary the forbidden volume for 2 produced by the wall and by 1 overlap partially (dotted region in fig. A.1 on the facing page). This common part is therefore counted twice in eq. (A.5). The volume of this common part is equal to the spherical segment one of a sphere of radius  $r_1 + r_2$  and height  $r_1 r_2 \sin \gamma$  (outer spheres in fig. A.1) minus the spherical segment volume of a sphere of radius  $R - r_2$  and height  $R - r_2 - r - r_1 r_2 \sin \gamma$ . At fixed  $r$  the volume which is counted twice is

$$V_{for}(r) = \frac{\pi}{3}(r_1+r_2)^3(1-\cos\gamma)^2(2+\cos\gamma) - \frac{\pi}{3}(R-r_2-r-(r_1+r_2)\cos\gamma)^2(2(R-r_2)+r+(r_1+r_2)\cos\gamma), \quad (\text{A.6})$$

where

$$\cos\gamma = -\frac{1}{2} \frac{r^2 + (r_1+r_2)^2 - (R-r_2)^2}{r(r_1+r_2)}. \quad (\text{A.7})$$

An integration of  $4\pi r^2 V_{for}(r) dr$  between the radiuses  $r = R - r_1 - 2r_2$  and  $r = R - r_1$  yields

$$V_{for} = \frac{16\pi^2}{9} r_2^3 (3r_1^2 r_2 - 3R r_2^2 + 3R^2 r_2 + 3r_1 r_2^2 + 6R^2 r_1 - 6r_1^2 R - 9r_1 r_2 R + r_2^3). \quad (\text{A.8})$$

The total accessible volume is the sum of the right hand sides of eqs. (A.5) and (A.8). Finally,  $NCC$  is the inverse of this sum times  $V^2$

$$NCC = \frac{R^6}{(R^3 + 3r_1 r_2 R - r_1^3 - r_2^3)(R - r_1 - r_2)^3}. \quad (\text{A.9})$$

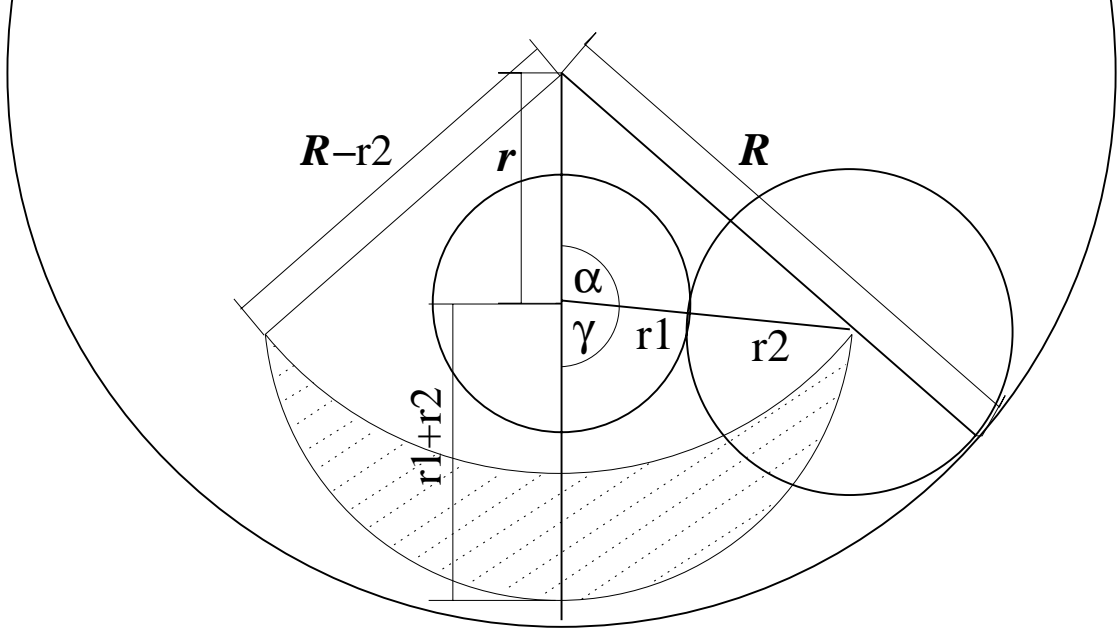


Figure A.1: Illustration of the avoided volume for two particles near the boundary. The forbidden region (dotted region) is counted twice in eq. (A.5) on the preceding page. In this two dimensional representation the surface counted twice is a crescent. Its area is equal to the outer disk segment area (radius of  $r_1 + r_2$ , angle  $2\gamma$ ) minus the inner one area (radius  $r + r_1 + r_2$ , angle  $\arccos \left[ \frac{(R-r_2)^2 + r^2 - (r_1+r_2)^2}{2r(R-r_2)} \right]$ ).

Using eq. (A.9), one can build a “two body” estimate of  $NCC$  for a system of  $N_f$  hard spheres

$$NCC_2 \doteq \left( \prod_{i < j}^{N_f} NCC(i, j) \right)^{\frac{1}{N_f - 1}}. \quad (\text{A.10})$$

where  $NCC(i, j)$  is given by eq. (A.9). The exponent  $\frac{1}{N_f - 1}$  takes into account the fact that the avoided volume of a given particle has been counted  $N_f - 1$  times in eq. (A.10). The  $NCC$  given by eq. (A.10) is a sort of geometric average. On the plus side,  $NCC_2$  has a critical packing fraction which varies which the mass distribution  $\mu$  and is smaller than one. On the minus side, from an algorithmic point of view, the updating scheme of  $NCC_2$  when two fragment sizes are changed is of the order of  $\mathcal{O}(N)$ .

### A.1.2 Approximations

The results presented in the previous subsection are the only exact ones used in MMMC. For  $N > 3$  approximations are needed.

There exist a large literature on *infinite* ( $N \rightarrow \infty$ ,  $N/V = cst$ ) *unbounded* diluted ( $\sim$  small pressures) gas of hard spheres (see e.g. [RFL59, SSM87, PCA]). Some results from these works are used in the following to estimate  $NCC$  for *finite bounded* systems.

The part in  $NCC$  due to the interactions with the wall vanishes in the infinite limit, so in the following only the part in  $NCC$  due to the interactions between spheres is worked

out. In order to add some boundary effect, as a first approximation,  $NCC$  is divided by  $\frac{R^{3N}}{\prod_{i=1}^N (R-r_i)^3}$ . The latter term is the product of the clusters eigen- $NCC$  (see eq. (A.4)).

For an infinite gas of hard spheres one defines  $Z$  as [PAT72]

$$Z \doteq \frac{p}{T}, \quad (\text{A.11a})$$

$$\equiv \left. \frac{\partial S}{\partial V} \right|_E. \quad (\text{A.11b})$$

$Z = \frac{p}{T}$  is the equation of state of the gas ( $\frac{ZN}{V}$  is the compressibility factor). The volume dependent part of the entropy of a hard sphere gas is

$$S = \ln \Omega = \ln \int_V \cdots \int_V \eta(\mathbf{r}_1, \cdots, \mathbf{r}_{N_f}) d\mathbf{r}_1 \cdots d\mathbf{r}_{N_f} \quad (\text{A.12})$$

where  $\eta$  is equal to zero when two clusters overlap, and to one otherwise, see eq. (A.3) on page 109. Of course  $\Omega$  depends on the mass (size) distribution  $\mu = \{N_1, N_2, \dots, N_{N_f}\}$  of particles.  $NCC$  as already defined is

$$NCC(\mu, V) = \frac{V^{N_f}}{\Omega(\mu, V)}. \quad (\text{A.13})$$

In the perfect gas approximation the spheres do not interact therefore  $\Omega$  is simply  $V^{N_f}$  ( $NCC = 1$ ), and the equations (A.11) and (A.13) lead to the following well-known equation of state

$$\frac{N_f}{V} = \frac{p}{T}. \quad (\text{A.14})$$

For a gas of equal size hard spheres (of radius  $r$ ) there exists another well-known simple approximation, the van der Waals approximation [DGLR89, LL94]. Since the minimal distance between two particles is  $2r$ , the forbidden volume due to these two spheres is approximatively  $\frac{4\pi}{3}(2r)^3$ . The total number of pairs is  $\approx \frac{N_f^2}{2}$ , hence the total avoided volume per particle is

$$V_{\text{avoid}} \approx \frac{1}{N_f} \frac{N_f^2}{2} \frac{4\pi}{3} (2r)^3 = 4V_0, \quad (\text{A.15})$$

where  $V_0 = N_f \frac{4\pi}{3} r^3$ . Consequently

$$\Omega \approx (V - 4V_0)^{N_f}, \quad (\text{A.16})$$

and eq. (A.11) yields

$$Z = \frac{N_f}{V - 4V_0}. \quad (\text{A.17})$$

In the last two examples,  $Z$  were computed from  $NCC$  (or  $\Omega$ ). Conversely, one can use  $Z$  to determine  $NCC$ . Indeed  $NCC$  can be linked to  $Z$  in the following way

$$NCC(\mu, V) = \frac{V^{N_f}}{\exp(S(\mu, V))} \quad \text{by (A.12) and (A.13),} \quad (\text{A.18})$$

$$= \frac{V^{N_f}}{\exp\left(C(\mu, V_0) + \int_{V_0}^V Z(\mu, V) dV\right)} \quad \text{by (A.11),} \quad (\text{A.19})$$

where  $C(\mu, V_0)$  is the constant of integration. At  $V = V_0$  the following relation holds

$$C(\mu, V_0) = N_f \ln V_0 - \ln NCC(\mu, V_0). \quad (\text{A.20})$$

At fixed mass distribution and in the limit  $V_0 \rightarrow \infty$ , the forbidden volume is constant while the accessible one diverges, i.e.  $\lim_{V_0 \rightarrow \infty} NCC = 1$ ; therefore

$$\lim_{V_0 \rightarrow \infty} \frac{C(\mu, V_0)}{N_f \ln V_0} = 1. \quad (\text{A.21})$$

Since in the following, all the quantities are worked out at *fixed* mass distribution  $\mu$  and for sake of simplicity the  $\mu$ -dependence is not explicitly written.

An usual approach to estimate  $Z$  is to develop it in powers of the density  $\rho = \frac{N_f}{V}$

$$Z = \rho + B_2 \rho^2 + B_3 \rho^3 + \dots \quad (\text{A.22})$$

where  $B_i$  is called the  $i^{\text{th}}$  virial coefficient [DGLR89]. Again there exists a large literature addressing the computation of these coefficients (see e.g. [EAG98] and refs. quoted therein).

Another approach is based on the virial equation, e.g. for a mixture of hard spheres

$$Z = \frac{p}{T} = \frac{N_f}{V} - \frac{2\pi N_f^2}{3TV^2} \sum_{ij} x_i x_j \int_0^\infty \frac{\partial u_{ij}(r)}{\partial r} g_{ij}(r) r^3 dr \quad (\text{A.23})$$

where  $x_i = \frac{N_i}{N_f}$  is the relative density of the species  $i$ ;  $u_{ij}(r)$  is the interaction potential between two particles from species  $i$  and  $j$  whose center of mass are separated by distance  $r$ ;  $g_{ij}(r)$  is the pair correlation function between species  $i$  and  $j$ . For a given  $g_{ij}$  one can integrate (at least numerically) the equation of state [THI63, WER63, RFL59].

For MMMC95, the Mansoori–Carnahan–Starling–Leland [MCSL71] formula for  $Z$  is used

$$Z = \frac{6}{\pi} \left\{ \frac{\xi_0}{(1 - \xi_3)} + \frac{3\xi_1 \xi_2}{(1 - \xi_3)^2} + \frac{3\xi_2^3}{(1 - \xi_3)^3} - \frac{\xi_3 \xi_2^3}{(1 - \xi_3)^3} \right\} \quad (\text{A.24})$$

where  $\xi_k = \frac{\pi}{6} \sum_i \rho_i d_i^k$ ,  $d_i = 2r_i$  and  $\rho_i = \frac{N_i}{V}$  is the density of species  $i$ .

In order to compute  $NCC$  one has to calculate  $\int Z(V) dV$ , see eq. (A.19) on the facing page. Because of the  $V$  dependence of  $Z$ , terms of the following form have to be integrated

$$W(p, q, \alpha_1, \alpha_2) = \frac{\frac{\alpha_1}{V^p}}{\left(1 - \frac{\alpha_2}{V}\right)^q} = \frac{\alpha_1 V^{q-p}}{(V - \alpha_2)^q}. \quad (\text{A.25})$$

First the substitution  $Y = V - \alpha_2$  is made and the integration of  $W$  becomes

$$\int W dV = \int \frac{\alpha_1 (Y + \alpha_2)^{q-p}}{Y^q} dY. \quad (\text{A.26})$$

The following cases are of interest

- for  $q - p = 0$  (see the first three terms of eq. (A.24))

$$\begin{aligned} \int W dV &= \int \frac{\alpha_1}{Y^q} dY \\ &= \begin{cases} \alpha_1 \ln Y & \text{when } q = 1, \\ \frac{\alpha_1}{1-q} Y^{1-q} & \text{else,} \end{cases} \end{aligned} \quad (\text{A.27})$$

- for  $q - p = -1$  and  $q = 3$  (see the last term of eq. (A.24) on the preceding page)

$$\begin{aligned} \int W dV &= \int \frac{\alpha_1}{(Y + \alpha_2) Y^3} dY \\ &= -\frac{\alpha_1 \ln(Y + \alpha_2)}{\alpha_2^3} + \frac{\alpha_1 \ln Y}{\alpha_2^3} + \frac{\alpha_1}{\alpha_2^2 Y} - \frac{\alpha_1}{2\alpha_2 Y^2} \end{aligned} \quad (\text{A.28})$$

$$= \frac{\alpha_1 [\ln Y - \ln(Y + \alpha_2)]}{\alpha_2^3} + \frac{\alpha_1}{\alpha_2 Y} \left( \frac{1}{\alpha_2} - \frac{1}{2Y} \right). \quad (\text{A.29})$$

Now one can define

$$\gamma_k = \xi_k V = \frac{\pi}{6} \sum_{i=1} N_i^A (2r_i)^k, \quad (\text{A.30})$$

where  $i$  is an index for the species. Combining the results yields

$$\begin{aligned} \hat{S}(V) \equiv \int Z dV &= \frac{6}{\pi} \left\{ \gamma_0 \ln(V - \gamma_3) - \frac{3\gamma_1\gamma_2}{(V - \gamma_3)} - \frac{3\gamma_2^3}{2(V - \gamma_3)^2} \right. \\ &\quad \left. + \frac{\gamma_2^3 [\ln V - \ln(V - \gamma_3)]}{\gamma_3^2} + \frac{\gamma_2^3}{(V - \gamma_3)} \left[ \frac{1}{2(V - \gamma_3)} - \frac{1}{\gamma_3} \right] \right\} \\ &= \frac{6}{\pi} \left\{ \gamma_0 \ln(V - \gamma_3) + \frac{\gamma_2^3 [\ln V - \ln(V - \gamma_3)]}{\gamma_3^2} \right. \\ &\quad \left. - \frac{\gamma_2}{(V - \gamma_3)} \left( 3\gamma_1 + \frac{V}{(V - \gamma_3)} \frac{\gamma_2^2}{\gamma_3} \right) \right\} \\ &\equiv \frac{6}{\pi} \gamma_0 \ln(V - \gamma_3) + \hat{S}_1(V). \end{aligned} \quad (\text{A.31})$$

From the definition of  $\hat{S}_1(V)$  one immediately deduces

$$\lim_{V \rightarrow \infty} \hat{S}_1(V) = 0, \quad (\text{A.32})$$

which is consistent with  $\lim_{V_0 \rightarrow \infty} \hat{S}(V_0) = N_f \ln V_0 = \lim_{V_0 \rightarrow \infty} \frac{6}{\pi} \gamma_0 \ln(V_0 - \gamma_3)$ .

The denominator of eq. (A.19) on page 112 can be written as

$$\begin{aligned} \exp \left( C(V_0) + \int_{V_0}^V Z(V_1) dV_1 \right) &= \frac{V_0^{N_f}}{NCC(V_0)} \frac{\exp(\hat{S}(V))}{\exp(\hat{S}(V_0))} \\ &= \frac{V_0^{N_f}}{NCC(V_0)} \frac{(V - \gamma_3)^{\frac{6}{\pi} \gamma_0} \exp(\hat{S}_1(V))}{(V_0 - \gamma_3)^{\frac{6}{\pi} \gamma_0} \exp(\hat{S}_1(V_0))} \end{aligned} \quad (\text{A.33})$$

Using eqs. (A.32) and (A.21) and the fact that  $\gamma_0 = \frac{\pi}{6} N_f$ , the limit of the denominator of eq. (A.19) when  $V_0 \rightarrow \infty$  is

$$\lim_{V_0 \rightarrow \infty} \exp \left( C(V_0) + \int_{V_0}^V Z(V_1) dV_1 \right) = (V - \gamma_3)_f^N \exp(\hat{S}_1(V)). \quad (\text{A.34})$$

Finally  $NCC$  is

$$NCC(V, \mu) = \left( \frac{V}{V - \gamma_3} \right)^{N_f - \frac{6}{\pi} \frac{\gamma_2^3}{\gamma_3}} \exp \left[ \frac{6}{\pi} \frac{\gamma_2}{V - \gamma_3} \left( 3\gamma_1 + \frac{V}{V - \gamma_3} \frac{\gamma_2^2}{\gamma_3} \right) \right]. \quad (\text{A.35})$$

The first and the second derivatives of  $\ln NCC$  with respect to the volume are also needed, e.g. to compute the microcanonical pressure (see sec. 3.3)

$$\frac{\partial \ln NCC}{\partial V} = \frac{6}{\pi N_f} \frac{1}{V - \gamma_3} \left[ \frac{1}{V} \left( \frac{\gamma_2^3}{\gamma_3} - \gamma_0 \gamma_3 \right) - \frac{\gamma_2}{V - \gamma_3} \left( 3\gamma_1 + \gamma_2^2 \left( \frac{1}{\gamma_3} + \frac{2}{V - \gamma_3} \right) \right) \right]. \quad (\text{A.36})$$

$$\frac{\partial^2 \ln NCC}{\partial V^2} = \frac{6}{\pi N_f} \frac{1}{V - \gamma_3} \left[ -\frac{1}{V} \left( \frac{1}{V} + \frac{1}{V - \gamma_3} \right) \left( \frac{\gamma_2^3}{\gamma_3} - \gamma_0 \gamma_3 \right) + 2 \frac{\gamma_2}{(V - \gamma_3)^2} \left( 3\gamma_1 + \gamma_2^2 \left( \frac{1}{\gamma_3} + \frac{3}{V - \gamma_3} \right) \right) \right]. \quad (\text{A.37})$$

The volume  $V_c$  at which  $NCC$  diverges is  $V_c = \gamma_3$ , which corresponds to a critical packing fraction of 1.

From an algorithmic point of view using eqs. (A.35) to (A.37) is very convenient. They depend only on the  $\gamma_k$  for which the updating scheme after each Monte–Carlo step is straightforward and fast in contrast to the claim of Raduta [RAD01].

On fig. A.2 on the next page are plotted different estimates of  $NCC$  using the EOS eq. (A.35) on the facing page ( $NCC_{EOS}$ ) and the Monte–Carlo sampling presented in the next section  $NCC_{MC}$  as a function of the packing fraction  $\kappa = \frac{V_0}{V}$ . The total masses are  $A = 200$  and  $A = 1000$ . For each  $A$  two characteristic mass distributions were taken from MMMC runs; one from the liquid side ( $N_{f A=200} = 48$ ,  $N_{f A=1000} = 194$ ) and the other from the gas side (near the multifragmentation region;  $N_{f A=200} = 194$ ,  $N_{f A=1000} = 545$ ). The agreement between the two estimates is good and they are equivalent in the limit  $\kappa \rightarrow 0$  ( $V \rightarrow \infty$ ). This agreement is largely enough for low pressure runs. Moreover what does matter in a Metropolis sampling is the relative differences between the weights of two consecutive states of the Markovian chain. So, even though the ratio  $NCC_{MC}/NCC_{EOS}$  might be rather big, one can assume that for a proposed move  $c \rightarrow c'$  (see app. B.2)  $NCC_{EOS}(c)/NCC_{EOS}(c') \approx NCC_{MC}(c)/NCC_{MC}(c')$  (of course this relation does not hold near the critical packing fraction). For intermediate pressures the pressure term due to the avoided volume  $p_{NCC}$  cannot be neglected. It is a function of the derivative of  $\ln NCC$  with respect to  $V$ . One can see in figs. A.2 that the slope of  $\ln NCC$  is quite accurately reproduced by  $NCC_{EOS}$ .

$NCC_{EOS}$  underestimate  $NCC$  since the equation of state is based only on two body correlations.

## A.2 Numerical estimates

For large packing fraction the estimate given by eq. (A.35) on the preceding page is not enough accurate. Although there exist (semi-)analytical estimates of  $Z$  for large  $\kappa$  (generally close to  $\kappa_c$ ) there are usually worked out for very particular mass distributions (mono-modal, bi-modal, and, if at all, with Gaussian dispersions around the maxima), see e.g. [EAG98]. This is in sharp contrast with the need of computing the avoided volume of thousands of *different* mass distributions in one single MMMC run. Moreover these distributions are not always as simple as the one studied in the above mentioned literature. Hence the only way to estimate  $NCC$  is to use Monte–Carlo schemes.

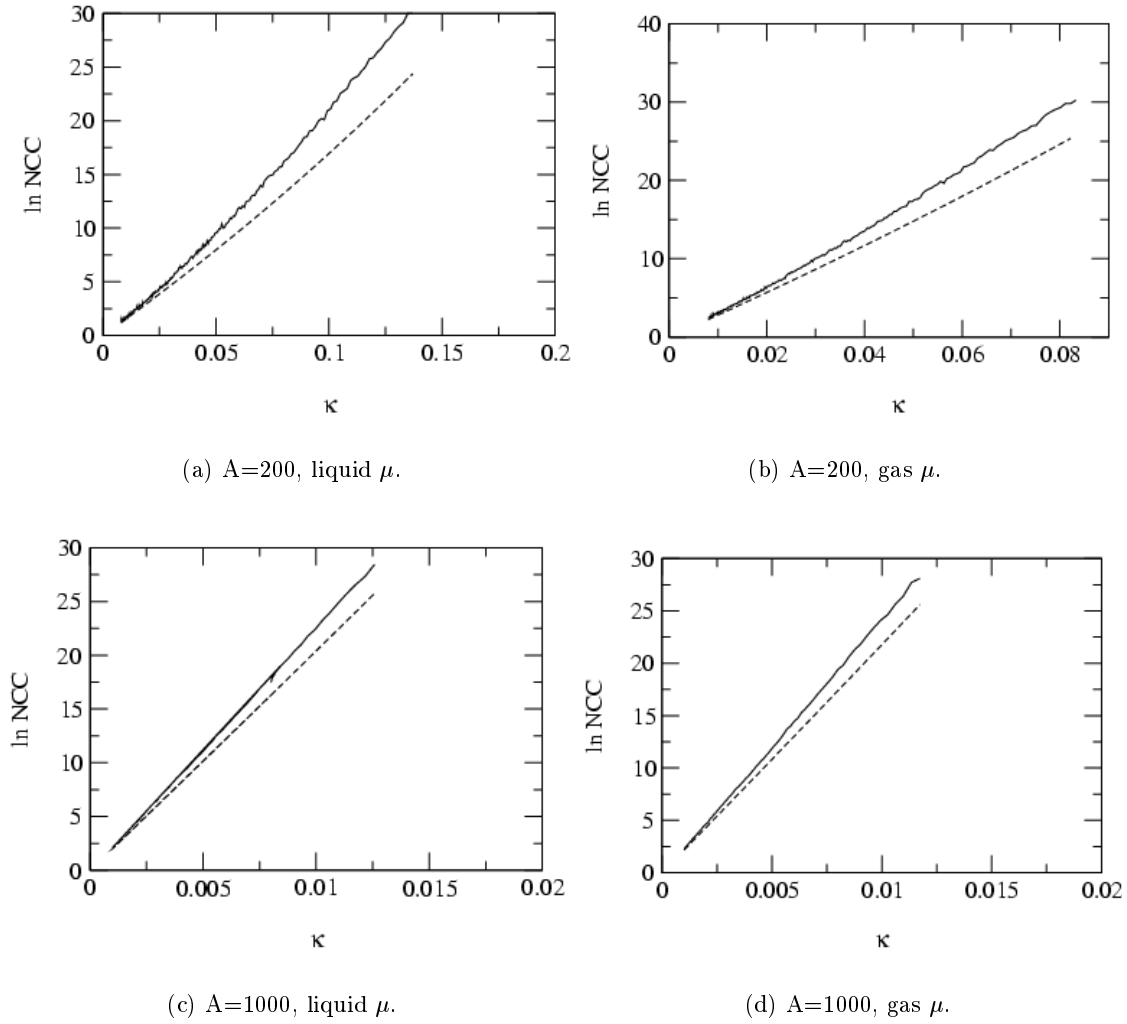


Figure A.2: Comparison between  $NCC$  given by eq. (A.35) on page 114 (dashed lines) and its “exact value” (Monte-Carlo estimates; solid lines) as a function of the packing fraction  $\kappa$  for different total masses  $A$  and mass distributions  $\mu$  (see text).

### A.2.1 Simple Monte–Carlo scheme

A straightforward estimate of the ratio eq. (A.1a) on page 109 consists of placing randomly each clusters and check for overlapping. A positioning (event) is considered as successful if all the  $N_f$  spheres have been placed successfully. Defining  $N_s$  as the number of successful events and  $N_t$  as total number of trial events, then an estimate of  $NCC$  is given by

$$NCC^{-1} = \frac{N_s}{N_t}. \quad (\text{A.38})$$

But since, on one hand,  $NCC$  can be very large (see e.g. figs. A.2 where  $NCC \sim 10^{10}$ ), and, on the other hand, a rather good estimate is needed in order to compute accurately the derivative of  $NCC$  with respect to  $V$ <sup>a</sup>, and since the relative statistical error in evaluating

<sup>a</sup>  $\frac{\partial NCC}{\partial V}$  and  $\frac{\partial^2 NCC}{\partial V^2}$  are needed to estimate the pressure and the inverse microcanonical temperature

$NCC^{-1}$  is of the order of  $1/\sqrt{N_t}$ , the simplest Monte–Carlo scheme is impractical [RAD01] (see figs. A.2 on the facing page).

### A.2.2 Advanced Monte–Carlo scheme

For the simplest Monte–Carlo scheme a failed positioning of cluster  $k$  implies a complete resampling of all the  $k - 1^{\text{th}}$  first “successful” positions. Indeed if one keeps the  $k - 1^{\text{th}}$  first positions and resamples only the  $k^{\text{th}}$  one many times one would introduce biases because of the correlations between the different events and therefore an estimate of  $NCC$  according to eq. (A.38) on the preceding page would be inaccurate.

Rodgers and Baddley in [RB91] introduced a technic to correct  $NCC$  from these correlations. An algorithm based on this technic by avoiding a lot of resampling is faster than the simplest one by almost two orders of magnitude. For example on figs. A.3 are plotted the CPU–time (in seconds) needed to compute  $NCC$  for different packing fractions and mass distributions (these are the same  $\mu s$  as in figs. A.2(a) and A.2(b) on the facing page for  $A = 200$ )

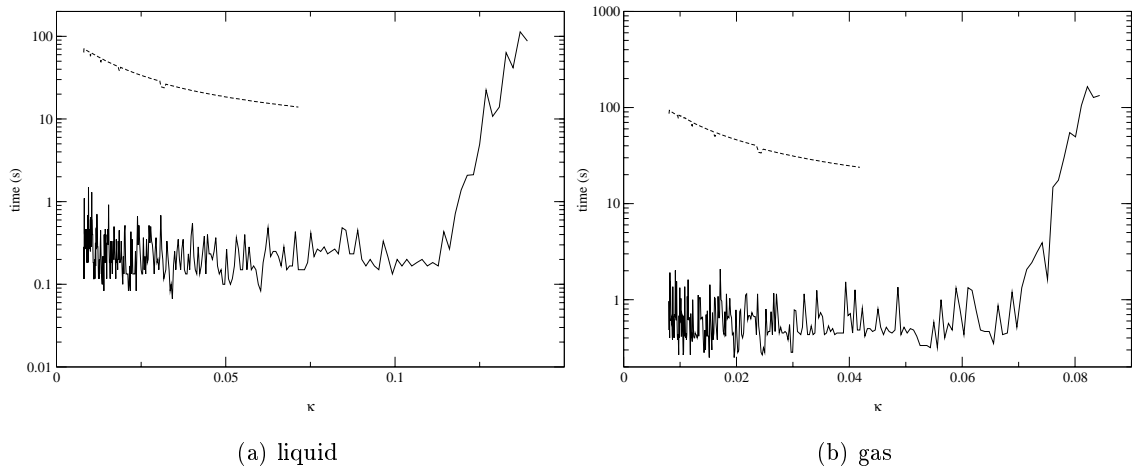


Figure A.3: Comparison of the CPU–time needed to compute  $NCC$ , for different mass distributions ( $A = 200$ , see text) as a function of the packing fraction  $\kappa$ . The dashed lines correspond to the simple Monte–Carlo algorithm (at fixed number of attempts), and the plain lines to the one using the technic presented in [RB91] (at fixed precision).

The results are presented at constant number of trial for the simplest algorithm and at constant precision for the advanced algorithm. The time for the former decreases with decreasing volume because the sampling of the positions for one given trial stops earlier<sup>b</sup> as the volume decreases. At constant precision the CPU–time would have been an increasing function of  $\kappa$ .

at constant pressure  $\beta_p$ , see secs. 3.3 and 3.4, and app. D.

<sup>b</sup>For one given trial, the center of mass are sampled sequentially. The smaller the volume the higher is the probability for this chain to be stopped early.

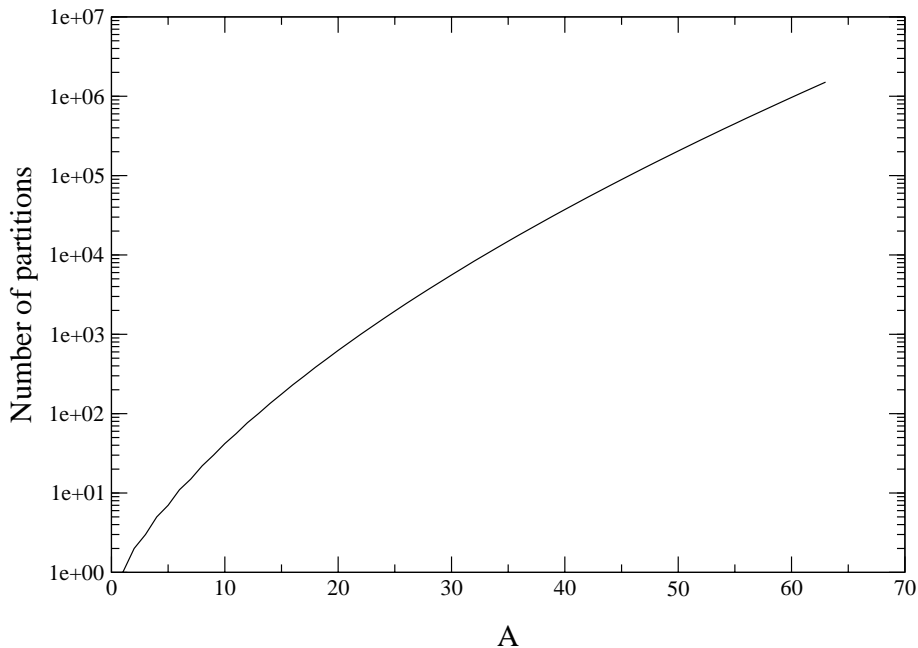


Figure A.4: Number of possible mass distributions as a function of the total mass  $A$ .

### A.2.3 Further improvements

Using the results from [RB91] leads already to a drastic gain in CPU-time. However a typical run at high pressure still takes too much CPU-time. During a typical MMC run (one point in the  $(E, V)$ -plane)  $\sim 2 \cdot 10^6$  events are generated. For each events  $NCC(\mu, V)$ ,  $NCC(\mu, V - \Delta V)$  and  $NCC(\mu, V + \Delta V)$  are estimated. By considering that much less precision is needed than the one asked to the data plotted in figs. A.3 on the page before (assuming that the statistical errors would be smoothed out due to the averaging) one ends up with run times of the order of  $2 \cdot 10^6 \times 3 \times 0.05$  seconds  $\approx 3$  days!

In the following some improvements to the advanced algorithm used in MMC95 are briefly reviewed.

- Several millions of events (mass distributions) are generated during one MMC run. Nevertheless there are not all different, on the contrary the value of  $\mu$  (the mass distribution) usually fluctuates around some mean mass distribution. Therefore after equilibration MMC has to compute  $NCC$ s which have already be computed and that many times. The solution is straightforward: the  $NCC$ s are stored and reused whenever needed. The concrete implementation of this simple idea is less straightforward. Indeed a mass distribution is a set of integers each standing for a cluster mass. Moreover the typical number of mass distributions to be stored is huge, see e.g. fig. A.4 where the number of partitions for  $A = 60$  is already  $\approx 10^6$ . Hence a straightforward storage would need a huge amount of RAM space for  $A = 200$ .

For simplicity the integers are sorted by decreasing order. There exists no simple direct *and* efficient way to sort these sets. However the storage of sets of sorted

integers is a well-known problem in computing science. It can be solved by using the B-tree technic [BM72, BY89]. Briefly, consider the sets of mass distributions (here  $A = 16$ ) in table A.1. These mass distributions can be represented in a tree-

(a)	8	3	3	2	
(b)	8	3	2	2	1
(c)	8	3	3	1	1
(d)	8	4	4		

Table A.1: Set of mass distributions #1.

form as in fig. A.5. All the sets in tab. A.1 shares the same biggest mass, i.e. the

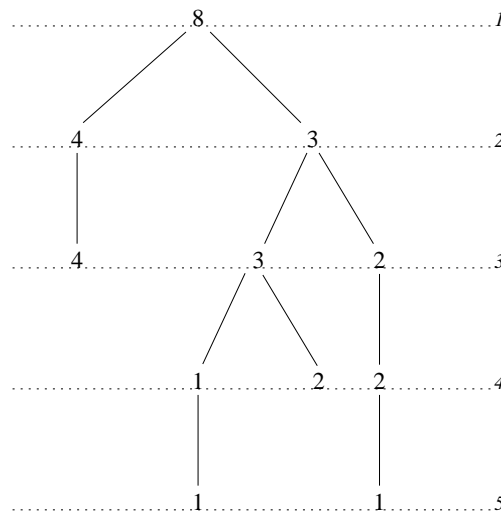


Figure A.5: Representation of the mass distributions of tab. A.1 on a tree. The numbers on the left side represent the height of the knots, i.e. the rank of the integer in the mass distribution.

same root in fig. A.5. The depth of a knot represents the rank of the attached integer in the mass distribution. The  $NCC$ s are stored at the level of the leaves (tips of the branches). There are as many leaves as mass distributions.

The advantage of the B-tree storage is clear. The knots might be shared by many mass distributions saving a lot of RAM. The implementation of this kind of storage by preventing from re-evaluating again and again  $NCC$ s of the most probable mass distributions saves a large amount of CPU-time (again of an order of magnitude). One can go a little bit further and instead of performing independent runs in the  $(E, V)$ -plane, one can use the  $NCC$ s at say  $(E_1, V_1)$  to perform a run at  $E_1 + \Delta E, V_1$ , since  $NCC$  does not depend on the system energy.

- Consider the two mass distributions in table A.2 on the following page; they have the same number of fragments and only their second and sixth clusters are different. Far from the critical packing fraction, it is reasonable to assume that  $NCC(a) \approx NCC(b)$  <sup>c</sup>. In other word  $NCC$  is a “smooth” function of the mass distribution  $\mu$ .

<sup>c</sup>This assumption has been verified many times in simulations.

(a)	100	4	3	3	3	2	1
(b)	100	3	3	3	3	3	1

Table A.2: Set of mass distributions #2.

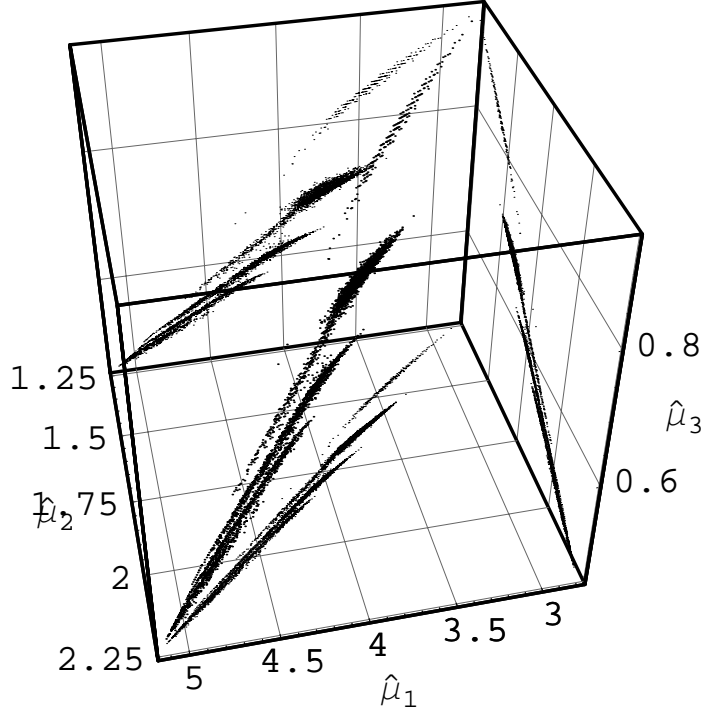


Figure A.6: Mass distributions on the  $(\hat{\mu}_1, \hat{\mu}_2, \hat{\mu}_4)$  space at fixed  $\hat{\mu}_0$ , and the projections of the points on the planes  $(\hat{\mu}_1, \hat{\mu}_2)$ ,  $(\hat{\mu}_1, \hat{\mu}_4)$  and  $(\hat{\mu}_2, \hat{\mu}_4)$ . The total mass is  $A = 200$  and the number of fragment is  $N_f = \hat{\mu}_0 = 12$ . This figure does not contain all the possible mass distributions satisfying  $\hat{\mu}_0$ .

One can use this result to interpolate some  $NCC$ s between already known values. The set of integers  $\mu$  does not provide a good basis for this interpolation, so one has to use some continuous parameterization that reduces the number of coordinates. The parameterization chosen in the present work is based on the set

$$\hat{\mu} = \{\hat{\mu}_0, \hat{\mu}_1, \hat{\mu}_2, \hat{\mu}_4\}, \quad (\text{A.39})$$

where  $\hat{\mu}_k \doteq \frac{1}{A^{k/3}} \sum_{i=1}^{N_f} N_i^{k/3}$ .  $\hat{\mu}_0$  is simply the number of fragments  $N_f$ ;  $\hat{\mu}_3$  is not used because it is a constant of  $\mu$ , indeed

$$\hat{\mu}_3 \doteq \frac{1}{A} \sum_{i=1}^{N_f} N_i = 1. \quad (\text{A.40})$$

In fig. A.6 each point corresponds to one given  $\mu$  in the new coordinates  $\hat{\mu}$ . The total mass and the number of fragments (clusters) are resp.  $A = 200$  and  $N_f = 12 = \hat{\mu}_0$ . Large values of  $\hat{\mu}_1$ ,  $\hat{\mu}_2$  and  $\hat{\mu}_4$  correspond to a monodisperse mass distribution (twelve

clusters of mass  $\approx \frac{200}{12}$ ), and small values to  $\mu$  with one big clusters and eleven monomers.

As one can see in fig. A.6 that the positions of the points are strongly correlated. The coordinates (A.39) on the preceding page are largely sufficient for interpolation ( $NCC$  itself is a smooth function of  $\hat{\mu}$ ). The storage of the  $\hat{\mu}$  is technically cumbersome (because the coordinates are not discrete and the density of points is not constant), but again it can be solved using some B-tree algorithms.



# Appendix B

## Technical “details”

### B.1 Introduction

The main method used for numerical applications in this thesis is based on the Metropolis sampling [MRR<sup>+</sup>53]: one builds a Markovian chain, i.e. from a state  $c$  a new state  $c'$  is sampled. This new state is accepted with a probability transition  $P(c \rightarrow c')$  given by

$$P(c \rightarrow c') = \min\left(1, \frac{\omega(c')}{\omega(c)}\right), \quad (\text{B.1})$$

where  $\omega(c)$  is the statistical weight of  $c$ . This probability transition satisfies the detailed balance equation which is the cornerstone of the Metropolis sampling

$$p(c \rightarrow c') \omega(c) = p(c' \rightarrow c) \omega(c'). \quad (\text{B.2})$$

The mean value of an observable  $F$  is given by

$$\langle F \rangle = \frac{1}{N} \sum_{j=1}^N F(c_j). \quad (\text{B.3})$$

Eq. (B.1) is the simplest form for  $P(c \rightarrow c')$ ; for practical reasons (either lack or a priori information) eq. (B.1) or eq. (B.3) can or have to be modified (see below).

### B.2 Monte–Carlo sampling

#### A priori probability

There is an implicit assumption made from eq. (B.2) to eq. (B.1); namely the *a priori probability*  $\mathcal{A}(c \rightarrow c')$  to sample  $c'$  “from”  $c$  satisfies [KRA98]

$$\mathcal{A}(c \rightarrow c') = \mathcal{A}(c' \rightarrow c). \quad (\text{B.4})$$

Eq. (B.4) is not necessarily always satisfied. Hence it is sometimes technically difficult to ensure that the move  $c \rightarrow c'$  is chosen with the same a priori probability than  $c' \rightarrow c$ . One can also force the Markovian chain to go in a given direction in the parametric space by using some a priori knowledge.

Now the detailed balance equation has to be reevaluated and explicitly written with the a priori probability. The probability  $p(c \rightarrow c')$  is split up into two separate parts

$$p(c \rightarrow c') = \mathcal{A}(c \rightarrow c') P(c \rightarrow c'), \quad (\text{B.5})$$

where  $P(c \rightarrow c')$  is the acceptance probability of the move proposed with  $\mathcal{A}(c \rightarrow c')$ . The full detailed balance is

$$\mathcal{A}(c \rightarrow c') P(c \rightarrow c') \omega(c) = \mathcal{A}(c' \rightarrow c) P(c' \rightarrow c) \omega(c'). \quad (\text{B.6})$$

Now, one form for the acceptance probability is

$$P(c \rightarrow c') = \min \left( 1, \frac{\omega(c') \mathcal{A}(c' \rightarrow c)}{\omega(c) \mathcal{A}(c \rightarrow c')} \right). \quad (\text{B.7})$$

### mmmc95

In MMMC95 there is only one move, namely

$$\underbrace{(M, E_M^*) + (N, E_N^*)}_c \rightarrow \underbrace{(P, E_P^*) + (Q, E_Q^*)}_{c'} \quad (\text{B.8})$$

where  $M, N, P$  and  $Q$  are clusters, their mass are respectively indicated by their name,  $M + N = P + Q$ .  $E_M^*, E_N^*, E_P^*$  and  $E_Q^*$  are their respective internal excitation energy.  $M \in \mu(c)$ ,  $N \in \mu(c')$ ,  $N \in \{0\} \cup \mu(c)$  and  $Q \in \{0\} \cup \mu(c')$ , where “0” is a “virtual” vacuum fragment. It has no mass and no excitation energy and does not contribute to the microcanonical weight factor eq. (3.8) on page 47.

This move spans all the ones used in MMMC77 [GRO97], e.g. “split fragment” is now

$$(M, E_M^*) + 0 \rightarrow (P, E_P^*) + (Q, E_Q^*),$$

but also moves that were not proposed (implying a breaking of the detailed balance condition, see sec. 3.4.1), e.g.

$$(1, 0) + (1, 0) \rightarrow (2, 0). \quad (\text{B.9})$$

A move is performed in two steps. First a new mass distribution is generated then the excitation energies ( $E_P^*, E_Q^*$ ) are sampled.

#### B.2.1 Partitioning factor

As in this subsection mass distributions are only considered, the internal excitations energies of eq. (B.8) can be omitted

$$\underbrace{M + N}_c \rightarrow \underbrace{P + Q}_{c'}. \quad (\text{B.10})$$

The only weight that might be changed by (B.10) is the partitioning weight  $\omega_{sym} = \frac{1}{\prod_{i=1}^A \xi_c(i)!}$ , where  $\xi_c(i)$  is the number of cluster of size  $i$  in the event  $c$ . In order to use eq. (B.1) on the page before in the numerical code eq. (B.4) must be satisfied which is an impossibly difficult task. So one must use eq. (B.7) where the a priori probability is explicitly taken into account

$$P(c \rightarrow c') = \min \left( 1, \frac{\omega_{sym}(c') \mathcal{A}(c' \rightarrow c)}{\omega_{sym}(c) \mathcal{A}(c \rightarrow c')} \right). \quad (\text{B.11})$$

In its turn  $\mathcal{A}(c \rightarrow c')$  is split up into two parts, i.e.  $\mathcal{A}(c \rightarrow c') = p(M, N)p(\rightarrow P, Q|M, N)$ , where  $p(M, N)$  is the probability to choose  $M$  and  $N$  and  $p(\rightarrow P, Q|M, N)$  is the probability to sample  $P$  and  $Q$  once  $M$  and  $N$  are chosen.

In order to increase the pass acceptance and to decrease the correlation time,  $M$  is chosen among the clusters in  $\mu(c)$  with a probability proportional to its mass.  $N$  is chosen among the clusters in  $\{0\} \cup \mu(c) \setminus M$  in an equiprobable way, i.e.

$$p(M, 0) = \frac{M\xi_c(M)}{A} \frac{1}{N_f} = \frac{M\xi_c(M)}{AN_f} \quad (\text{B.12a})$$

$$p(M, N \neq M) = \frac{M\xi_c(M)}{A} \frac{\xi_c(N)}{N_f} = \frac{M\xi_c(M)\xi_c(N)}{AN_f} \quad (\text{B.12b})$$

$$p(M, M) = \frac{M\xi_c(M)}{A} \frac{\xi_c(M) - 1}{N_f} = \frac{M\xi_c(M)(\xi_c(M) - 1)}{AN_f} \quad (\text{B.12c})$$

Eq. (B.12a) correspond to the case when a “real” and the vacuum fragments are chosen. Eq. (B.12b) is the general case when two fragments of different masses are chosen whereas in Eq. (B.12c) both fragments have the same mass.

$M + N$ ,  $M \geq N$  are repartitioned in the following way. An integer number  $i$  is chosen in the range  $[-N, \text{floor} \frac{M+N}{2} - N]$ , where  $\text{floor } x$  is the biggest integer less or equal to  $x$ , with a probability proportional to  $\frac{1}{|i-N|+1}$ . The new mass distribution is given by

$$Q = N + i, \quad (\text{B.13a})$$

$$P = M + N - Q, \quad (\text{B.13b})$$

for an illustration see fig. B.1 on the following page. This repartitioning favors small changes in the mass distribution. Moreover it is easy to verify that it ensures  $p(\rightarrow P, Q|M, N) = p(\rightarrow M, N|Q, P)$ . Thus, in eq. (B.11) only the ratio  $\frac{p(P, Q)}{p(M, N)}$  has to be estimated.

Now everything can be collected in order to compute the probability transition. As an example, let us consider the move

$$M + N \rightarrow P + Q,$$

with  $M \neq N$ ,  $M \neq P$ ,  $N \neq Q$ ,  $Q \neq 0$  and  $N \neq 0$ , i.e. no vacuum fragment is involved and all the fragments have different masses. The second argument in the min function in eq. (B.7) on the preceding page becomes

$$\frac{\omega_{sym}(c') \mathcal{A}(c' \rightarrow c)}{\omega_{sym}(c) \mathcal{A}(c \rightarrow c')} = \frac{\xi_c(M)! \xi_c(N)! \xi_c(P)! \xi_c(Q)!}{\xi_{c'}(M)! \xi_{c'}(N)! \xi_{c'}(P)! \xi_{c'}(Q)!} \frac{P \xi_{c'}(P) \xi_{c'}(Q)}{M \xi_c(M) \xi_c(N)} \quad (\text{B.14})$$

$$= \frac{P}{M} \frac{(\xi_c(M) - 1)! (\xi_c(N) - 1)! \xi_c(P)! \xi_c(Q)!}{\xi_{c'}(M)! \xi_{c'}(N)! (\xi_{c'}(P) - 1)! (\xi_{c'}(Q) - 1)!} \quad (\text{B.15})$$

but the proposed move implies that  $\xi_{c'}(M) = \xi_c(M) - 1$ ,  $\xi_{c'}(N) = \xi_c(N) - 1$ ,  $\xi_c(P) = \xi_{c'}(P) - 1$  and  $\xi_c(Q) = \xi_{c'}(Q) - 1$ , and eq. (B.15) becomes

$$\frac{\omega_{sym}(c') \mathcal{A}(c' \rightarrow c)}{\omega_{sym}(c) \mathcal{A}(c \rightarrow c')} = \frac{P}{M}. \quad (\text{B.16})$$

With this sampling, the symmetrization weight factor is *exactly* taken into account.

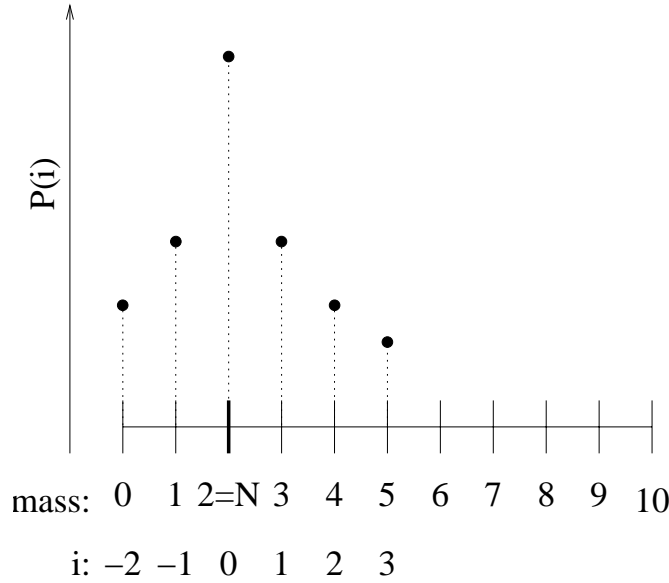


Figure B.1: Illustration of the repartitioning procedure. The initial cluster sizes are  $M = 8$  and  $N = 2$ . The mass of the new smallest fragment  $Q$  is given by  $Q = N + i = 2 + i$  where  $i$  is a number in the range  $[-N, \text{floor} \frac{M+N}{2} - N] = [-2, 3]$ , chosen with a probability proportional to  $\frac{1}{|i-N|+1}$ .

### Example

The simple case of a small system with  $A = 6$  is considered. All the possible partitions are listed in table B.2.1.0 on the facing page along with their respective  $\omega_{sym}$  which can be easily computed.

Using the values in tab. B.2.1.0 one can compute the mean values of several observables

- $\langle N_{fr} \rangle$  mean number of fragments;
- $\langle M_1 \rangle$ ,  $\langle M_2 \rangle$  and  $\langle M_3 \rangle$ , mean size of the first, second and third biggest fragment;
- $\langle N \rangle$ , probability that a fragment of size  $N$  is present in an event (excluding monomers),

and compare them with the results given by MMMC95. The results<sup>a</sup> are listed in table B.2.

The numerical results are in very good agreement with the analytical results. For MMMC77 the results are really bad for such a small system total mass since the algorithm used to estimate the partitioning weight in MMMC77 is valid for large system total mass  $A$  [zZG93].

### B.2.2 Excitation energy sampling

The algorithm for the excitation energy sampling has been developed having in mind the following constraints

---

<sup>a</sup>The results are the averages over  $10^6$  events.

Configurations	$\omega_{sym}$
6	1
5 + 1	1
4 + 2	1
4 + 1 + 1	$1/2! = 1/2$
3 + 3	$1/2! = 1/2$
3 + 2 + 1	1
3 + 1 + 1 + 1	$1/3! = 1/6$
2 + 2 + 2	$1/3! = 1/6$
2 + 2 + 1 + 1	$1/(2!2!) = 1/4$
2 + 1 + 1 + 1 + 1	$1/4! = 1/24$
1 + 1 + 1 + 1 + 1 + 1	$1/6! = 1/720$

Table B.1: List of all the possible mass distributions for  $A = 6$  along with their respective symmetrization weight  $\omega_{sym}$ .

quantities evaluated	analytical results	MMMC95
$\langle N_{fr} \rangle$	$9276/4051 \simeq 2.290$	2.291
$\langle M_1 \rangle$	$16501/4051 \simeq 4.073$	4.071
$\langle M_2 \rangle$	$5791/4051 \simeq 1.430$	1.431
$\langle M_3 \rangle$	$1651/720 \simeq 0.4076$	0.4080
$\langle 6 \rangle$	$24/209 \simeq 0.1148$	0.1147
$\langle 5 \rangle$	$24/209 \simeq 0.1148$	0.1144
$\langle 4 \rangle$	$36/209 \simeq 0.1722$	0.1724
$\langle 3 \rangle$	$52/209 \simeq 0.2488$	0.2488
$\langle 2 \rangle$	$73/209 \simeq 0.3493$	0.3498

Table B.2: Comparison of analytical and numerical results for different observables.

1. it must fulfill the detailed balance equation and therefore be reversible,
2. the new sampled excitation energies must as much as possible lead to a positive remaining energy eq. (3.5) on page 45. This is particularly constraining at small total energy, where, without this constraint nearly 60% of the proposed moves are rejected only because of negative remaining energy.
3. it should favor small steps, e.g, consider  $M \rightarrow P + Q$  with  $P \gg Q$ , then the algorithm should support  $E_P^* \sim E_M^*$ .

To simplify let us consider the following move

$$\underbrace{(M, E_M^*) + (N, E_N^*)}_c \rightarrow \underbrace{(P, E_P^*) + (Q, E_Q^*)}_{c'}, \quad (\text{B.17})$$

with  $P \geq Q \geq 3$ ,  $M \geq N \geq 3$ . The remaining (kinetic) energies in  $c$  and  $c'$  are

$$E_k(c) = \bar{E}(c) - E_M^* - E_N^* - E_{bM} - E_{bN}, \quad (\text{B.18a})$$

$$E_k(c') = \bar{E}(c') - E_P^* - E_Q^* - E_{bP} - E_{bQ}, \quad (\text{B.18b})$$

where  $E_b$  stands for the binding energies.

During the process (B.17)  $\bar{E}$  is conserved, i.e.  $\bar{E}(c) = \bar{E}(c')$ . The first step is to check whether there is enough energy to create  $c'$ , i.e if  $E_k(c') = \bar{E}(c) - E_{bP} - E_{bQ} > 0$ .

Now let us rewrite  $E_i^* = \alpha_i \tilde{E}_{max,i}^*$ ,  $i = M, N, P$  and  $Q$ , where  $\alpha_i \in ]0, 1]$  and  $\tilde{E}_{max,i}^*$  is minimum between

- a.  $E_{max,i}^* = (i - 2)\epsilon_{max}^*$  the maximal allowed excitation energy for clusters  $i$  (see sect. 3.2 on page 40),
- b. the available excitation energy for the move Eq. (B.17) (constraint #2).

The energies are sampled sequentially. First  $P$  (conversely  $M$ ) therefore

$$\tilde{E}_{max,P}^* = \min((P - 2)\epsilon_{max}^*, \bar{E}(c) - E_{bP} - E_{bQ}) \quad (\text{B.19a})$$

$$\tilde{E}_{max,M}^* = \min((M - 2)\epsilon_{max}^*, \bar{E}(c) - E_{bM} - E_{bN}) \quad (\text{B.19b})$$

than  $Q$  (conversely  $N$ )

$$\tilde{E}_{max,Q}^* = \min((Q - 2)\epsilon_{max}^*, \bar{E}(c) - E_{bP} - E_{bQ} - E_P^*) \quad (\text{B.20a})$$

$$\tilde{E}_{max,N}^* = \min((N - 2)\epsilon_{max}^*, \bar{E}(c) - E_{bM} - E_{bN} - E_M^*) \quad (\text{B.20b})$$

Considering the move  $c \rightarrow c'$ ,  $\alpha_M$  and  $\alpha_N$  are known. Their values are both shifted

$$\begin{aligned} \alpha_1 &= \text{mod}(\alpha_M + \Delta\alpha_1) \\ \alpha_2 &= \text{mod}(\alpha_M + \Delta\alpha_2), \end{aligned}$$

where  $\Delta\alpha_1$  and  $\Delta\alpha_2$  are two random numbers sampled in the range  $[-0.05, 0.05]$ . The new  $\alpha_P$  and  $\alpha_Q$  are simply either  $(\alpha_P, \alpha_Q) = (\alpha_1, \alpha_2)$  or  $(\alpha_P, \alpha_Q) = (\alpha_2, \alpha_1)$ , each case has a probability of 1/2.

Now a computation of the a priori probability ratio yields

$$\frac{\mathcal{A}(c \rightarrow c')}{\mathcal{A}(c' \rightarrow c)} = \frac{\tilde{E}_{max,P}^* \tilde{E}_{max,Q}^*}{\tilde{E}_{max,M}^* \tilde{E}_{max,N}^*}. \quad (\text{B.21})$$

### B.3 Multicanonical algorithm

In this section the blocking mechanism used to estimate the  $Bg$  function for the self gravitating system studied in part III (eq. (6.21) on page 92) is presented. The estimate of  $Bg$  is obtained by an algorithm based on multicanonical technics [BIN97, BER96, LEE93, FS89].

The usual multicanonical task is to compute the free energy as a function of the total energy [PAR01]. For the gravitational system presented in part III one has to compute  $Bg$  as a function of the inertial momentum  $I$  and of the potential energy  $\phi$ . The updating scheme presented in [SMI96] is used. One of the reason for this choice is that although it has been given for a one dimensional task it can be trivially extended to bi-variate problems. The other reason is that it is one of the few algorithms to give and use information about the statistical errors on the estimate of the weight  $Bg$  (for another recent algorithm see [BOR01]).

In a multicanonical scheme  $Bg \equiv W$  is built iteratively. To improve the performances of the algorithm blocking mechanism has been added. After an iteration. if it is estimated

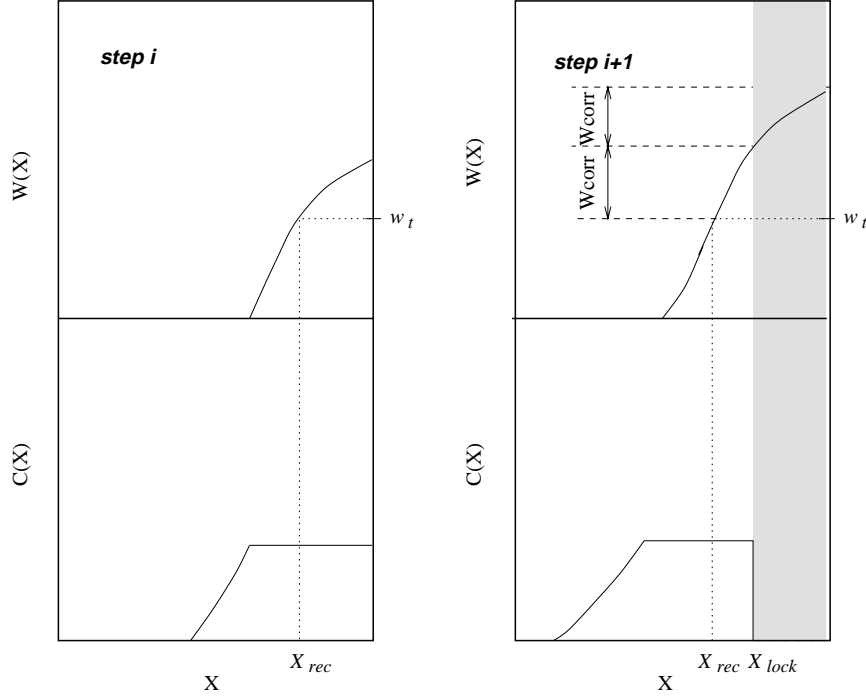


Figure B.2: Schematic illustration of the blocking mechanism. The visited state histogram  $C(X)$  is plotted for the iteration steps  $i$  and  $i + 1$ , the plotted weight  $W(X) \equiv Bg(X)$  is the one obtained *after* the iterations  $i$  and  $i + 1$ , respectively. The region where  $W > W_t$  are tagged to be locked during the next iterations.  $W_t$  is a suitable threshold weight. The consequences of the locking process can be seen in  $C_{i+1}(X)$  where  $C_{i+1}(X) = 0$  for  $X > X_{i+1 \text{ lock}}$ . The weight  $W_{i+1}(X > X_{i+1 \text{ lock}})$  is corrected simply by  $W_{i+1}(X > X_{i+1 \text{ lock}}) = W_i(X > X_{i+1 \text{ lock}}) + W_{\text{corr}}$  where  $W_{\text{corr}} = \frac{1}{\Delta X} \int_{X_{i+1 \text{ lock}} - \Delta X}^{X_{i+1 \text{ lock}}} W_i(X) dX$ , where  $\Delta X$  is a suitable positive constant.

that enough information has been collected on a given region of the parametric space  $(I, \phi)$  then this region is tagged as “locked” so that it will not be visited during next iterations (see fig. B.2). This mechanism enables the program to spread more quickly over the parametric space and save computation time compared to usual multicanonical algorithms.

Figure B.3 on the following page shows a slice of  $Bg(I, \phi)$  for  $I = 3$  at different iteration steps  $i$  for the gravitational system and  $N = 20$  (Fig. B.3(a)). The histogram  $C(I = 3, \phi)$  of the visited region is also plotted in order to illustrate the blocking mechanism (Fig. B.3(b)). As expected  $Bg$  is strongly peaked around the disordered region  $\phi \approx -1$  (this value corresponds to the mean of  $\phi$  over randomly generated spatial configurations). After 10 iterations the ratio between the maximum and the minimum of  $Bg$  is  $\approx \exp 120$ . This ratio increases exponentially with  $N$ , e.g. at  $N = 10$  its value is  $\approx \exp 80$ .

In fig. B.3 the final estimate of  $Bg$  is shown. The CPU-time to compute the whole  $Bg$  but also the observables used in chap. 6 (radial distribution, distance distribution) is around 40 hours on an ALPHA-workstation.

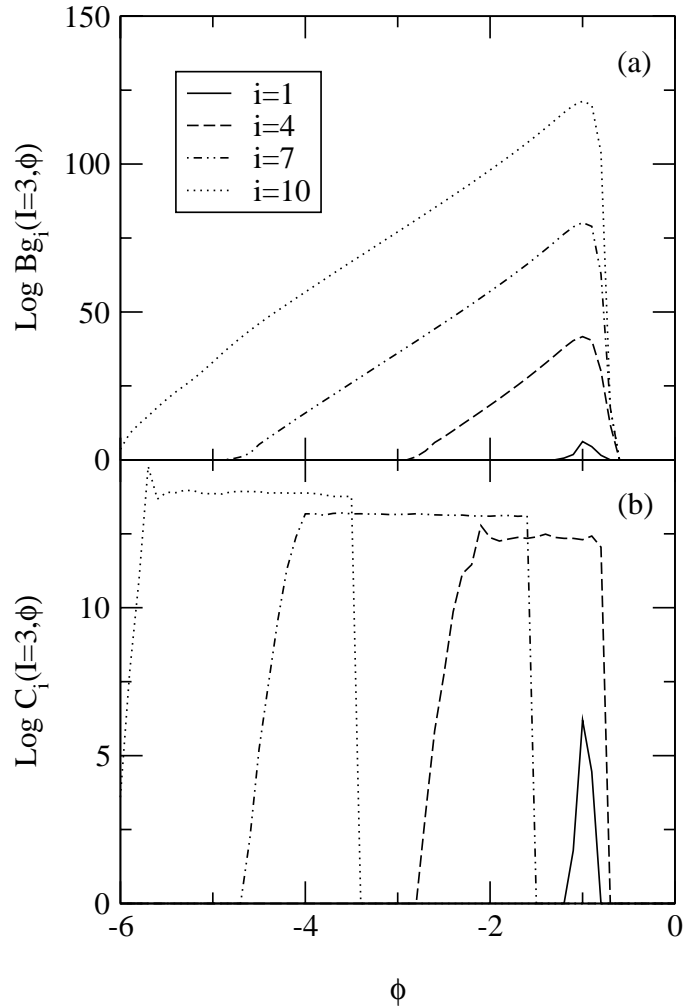


Figure B.3: Estimate of the density of state  $Bg$ , panel (a), and histogram of the visited states  $C$ , panel (b), for  $I = 3$  at different iteration steps  $i$  of the multicanonical algorithm as a function of the potential energy  $\phi$ . Panel (a) shows how  $Bg$  is built step by step.  $Bg$  is an extremely peaked function, the log of the ratio between its maximum and its minimum is about 120. Without the blocking mechanism (see text)  $C_i$  would have been non null for all value of  $\phi$  visited during previous steps  $j < i$ . In panel (b) one sees that the algorithm does no longer visit “well-known” regions ( $\phi \gtrsim -1.5$ ) already after four steps.

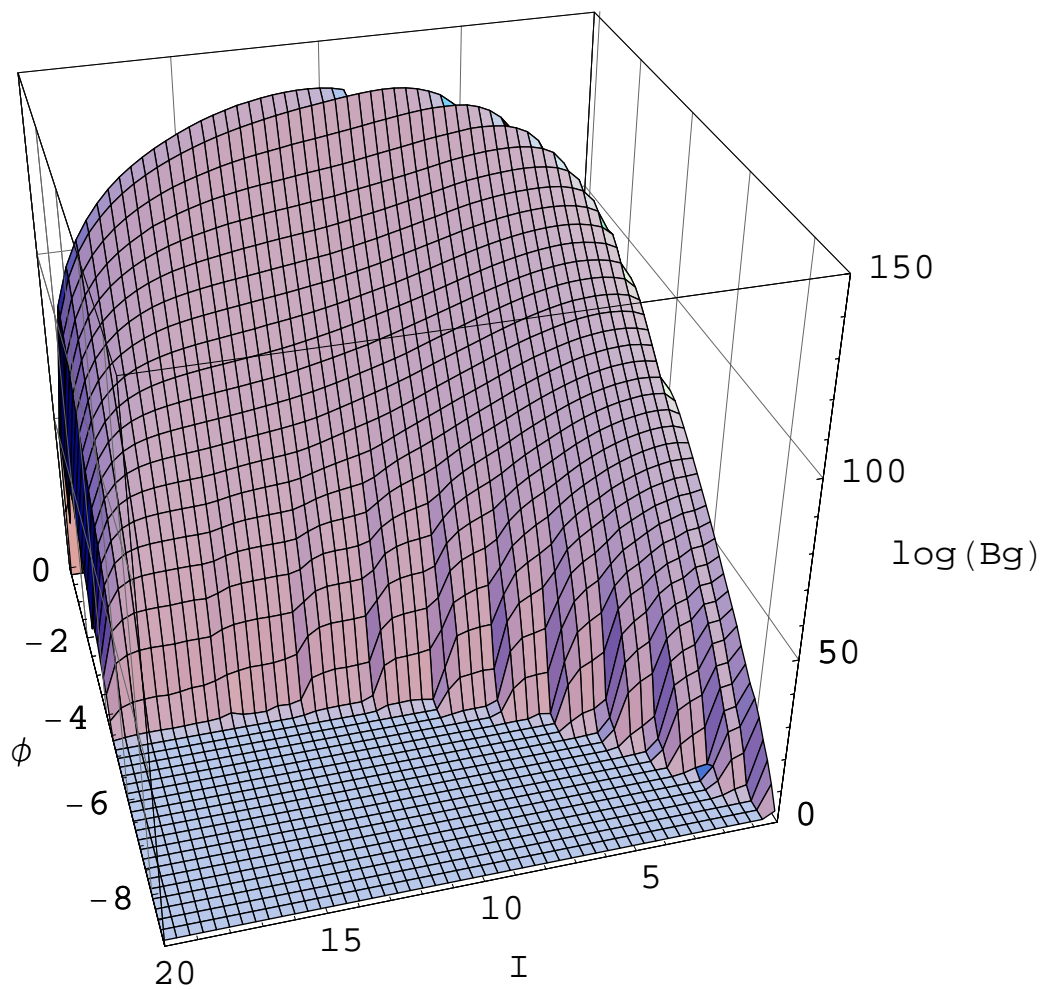


Figure B.4: Final estimate of  $Bg$  for  $N = 20$  as a function of the inertial momentum  $I$  and the potential energy  $\phi$ .



# Appendix C

## Momentum distribution

In this appendix  $\langle \mathbf{p}_k \rangle_{\mathbf{q}_k}$  the average momentum of particle  $k$  at fixed position is computed.

For simplicity  $k$  is set to 1. The  $\alpha$ -component of  $\langle \mathbf{p}_1 \rangle_{\mathbf{q}_1}$  is

$$\begin{aligned} \langle p_1^\alpha \rangle_{\mathbf{q}_1} &= \frac{\int \left( \prod_i d\mathbf{p}_i \prod_{i=2}^N d\mathbf{q}_i \right) p_1^\alpha \delta(E - \mathcal{H}) \delta^2(\sum_i \mathbf{p}_i) \delta(\sum_i \mathbf{q}_i \times \mathbf{p}_i - L) \delta^2(\sum_i \mathbf{q}_i)}{\int \left( \prod_i d\mathbf{p}_i \prod_{i=2}^N d\mathbf{q}_i \right) \delta(E - \mathcal{H}) \delta^2(\sum_i \mathbf{p}_i) \delta(\sum_i \mathbf{q}_i \times \mathbf{p}_i - L) \delta^2(\sum_i \mathbf{q}_i)} \\ &= \frac{\int \left( \prod_{i=2}^N d\mathbf{q}_i \right) \mathcal{P}_1^\alpha \delta^2(\sum_i \mathbf{q}_i)}{\int \left( \prod_{i=2}^N d\mathbf{q}_i \right) W(\mathbf{r}) \delta^2(\sum_i \mathbf{q}_i)}, \end{aligned} \quad (\text{C.1})$$

where  $\mathcal{P}_1^\alpha(E, L, \{\mathbf{q}\}) = \int \left( \prod_i d\mathbf{p}_i \right) p_1^\alpha \delta(E - \mathcal{H}) \delta^2(\sum_i \mathbf{p}_i) \delta(\sum_i \mathbf{q}_i \times \mathbf{p}_i - L)$ ,  $\{\mathbf{q}\}$  is a shorthand for  $\{\mathbf{q}_1, \dots, \mathbf{q}_N\}$  and  $W(\mathbf{q})$  is the microcanonical weight at fixed spatial configuration  $\{\mathbf{q}\}$ , its value is  $W(E, L, \{\mathbf{q}\}) = \mathcal{C} \frac{1}{\sqrt{I}} E_r^{N-5/2}$ , where  $\mathcal{C} = \frac{\prod_i m_i}{M} \frac{1}{(2\pi)^{N+9/2}} \frac{1}{\Gamma(N-3/2)}$  (see eq. (1.11) on page 7).  $\mathcal{H} = \sum_i \frac{\mathbf{p}_i^2}{2m_i} - \phi(\mathbf{q})$  is the Hamiltonian where  $\phi(\mathbf{q})$  is the potential.

The outline of the derivation of  $\mathcal{P}_1^\alpha$  is the same as in [LAL99] for  $W$ .

First  $\mathcal{P}_1^\alpha$  is Laplace transformed  $E' = E + \phi \rightsquigarrow s$

$$\tilde{\mathcal{P}}_1^\alpha(s, L, \{\mathbf{q}\}) = \int_0^\infty dE' e^{-sE'} \mathcal{P}_1^\alpha(E, L, \{\mathbf{q}\}), \quad (\text{C.2})$$

$$\begin{aligned} &= \int \prod_i d\mathbf{p}_i p_1^\alpha \exp \left\{ -s \sum_i \frac{\mathbf{p}_i^2}{2m_i} \right\} \delta^2 \left( \sum_i \mathbf{p}_i \right) \\ &\quad \delta \left( \sum_i \mathbf{q}_i \times \mathbf{p}_i - L \right). \end{aligned} \quad (\text{C.3})$$

Using the integral form of the delta Dirac

$$\delta(x) = \int_{-\infty}^{\infty} \frac{dw}{2\pi} \exp \{ iw \cdot x \}, \quad (\text{C.4})$$

for the conservation of the linear and angular momenta in eq. (C.3) yields

$$\begin{aligned} \tilde{\mathcal{P}}_1^\alpha(s, L, \{\mathbf{q}\}) &= \int \prod_i d\mathbf{p}_i \frac{d\mathbf{w}_1}{(2\pi)^2} \frac{dw_2}{2\pi} p_1^\alpha \\ &\exp \left\{ -s \sum_i \frac{\mathbf{p}_i^2}{2m_i} + i\mathbf{w}_1 \cdot \sum_i \mathbf{p}_i + iw_2 \sum_i \mathbf{q}_i \times \mathbf{p}_i - iw_2 L \right\}, \end{aligned} \quad (\text{C.5})$$

where  $\mathbf{w}_1 = (w_1^1, w_1^2)$  is a two dimensional vector. Now one can write explicitly the vectors components in eq. (C.5)

$$\begin{aligned} \tilde{\mathcal{P}}_1^\alpha(s, L, \{\mathbf{q}\}) &= \int \prod_i d\mathbf{p}_i \frac{d\mathbf{w}_1}{(2\pi)^2} \frac{dw_2}{2\pi} p_1^\alpha \\ &\exp \left\{ -s \sum_i \sum_{\beta=1}^2 \frac{(p_i^\beta)^2}{2m_i} + i \sum_{\beta=1}^2 w_1^\beta \cdot \sum_i p_i^\beta + iw_2 \sum_i \sum_{\gamma, \beta=1}^2 \epsilon_{\gamma\beta} q_i^\gamma p_i^\beta - iw_2 L \right\}, \end{aligned} \quad (\text{C.6})$$

where  $\epsilon$  is the antisymmetric tensor of rank 2.

The integration  $I_1$  over  $\{p_i^\beta\}$   $i = 1, \dots, N$  with  $\beta \neq \alpha$  gives

$$\begin{aligned} I_1 &= \int \prod_i dp_i^\beta \exp \left\{ -s \sum_i \frac{(p_i^\beta)^2}{2m_i} + i \sum_i w_1^\beta p_i^\beta + i \sum_i w_2 \sum_\gamma \epsilon_{\gamma\beta} q_i^\gamma p_i^\beta \right\} \\ &= \frac{(\prod_i m_i)^{1/2}}{(2\pi s)^{N/2}} \exp \left\{ -\frac{1}{2s} \sum_i m_i \left( w_1^\beta + w_2 \sum_{\gamma=1}^2 \epsilon_{\gamma\beta} q_i^\gamma \right)^2 \right\}. \end{aligned} \quad (\text{C.7})$$

The integration  $I_2$  over  $\{p_i^\alpha\}$   $i = 2, \dots, N$  gives

$$\begin{aligned} I_2 &= \int \prod_{i=2}^N dp_i^\alpha \exp \left\{ -s \sum_{i=2}^N \frac{(p_i^\alpha)^2}{2m_i} + i \sum_{i=2}^N w_1^\alpha p_i^\alpha + i \sum_{i=2}^N w_2 \sum_\gamma \epsilon_{\gamma\alpha} q_i^\gamma p_i^\alpha \right\} \\ &= \frac{(\prod_{i=2}^N m_i)^{1/2}}{(2\pi s)^{(N-1)/2}} \exp \left\{ -\frac{1}{2s} \sum_{i=2}^N m_i \left( w_1^\alpha + w_2 \sum_{\gamma=1}^2 \epsilon_{\gamma\alpha} q_i^\gamma \right)^2 \right\}. \end{aligned} \quad (\text{C.8})$$

Finally an integration over  $p_1^\alpha$  yields

$$\begin{aligned} I_3 &= \int dp_1^\alpha p_1^\alpha \left\{ -s \frac{(p_1^\alpha)^2}{2m_1} + iw_1^\alpha p_1^\alpha + iw_2 \sum_\gamma \epsilon_{\gamma\alpha} q_1^\gamma p_1^\alpha \right\} \\ &= \frac{(m_1)^{1/2}}{(2\pi s)^{1/2}} \left\{ -\frac{im_1}{s} \left[ w_1^\alpha + w_2 \sum_{\gamma=1}^2 \epsilon_{\gamma\alpha} q_1^\gamma \right] \right\} \\ &\exp \left\{ -\frac{m_1}{2s} \left( w_1^\alpha + w_2 \sum_{\gamma=1}^2 \epsilon_{\gamma\alpha} q_1^\gamma \right)^2 \right\} \end{aligned} \quad (\text{C.9})$$

One collects the results from eq. (C.7) to eq.(C.9)

$$\begin{aligned} \tilde{\mathcal{P}}_1^\alpha(s, L, \{\mathbf{q}\}) &= \int \frac{d\mathbf{w}_1}{(2\pi)^2} \frac{dw_2}{2\pi} \frac{\prod_i m_i}{(2\pi s)^N} \left\{ -\frac{im_1}{s} \left[ w_1^\alpha + w_2 \sum_{\gamma=1}^2 \epsilon_{\gamma\alpha} q_1^\gamma \right] \right\} \\ &\quad \exp \left\{ -\frac{1}{2s} \sum_i \sum_{\beta=1}^2 m_i \left( w_1^\beta + w_2 \sum_{\gamma=1}^2 \epsilon_{\gamma\beta} q_i^\gamma \right)^2 - iw_2 L \right\}. \end{aligned} \quad (\text{C.10})$$

The first term in the argument of the exponential in eq. (C.10) can be expanded and simplified (using  $\sum_i \mathbf{q}_i = 0$ )

$$\begin{aligned} \tilde{\mathcal{P}}_1^\alpha(s, L, \{\mathbf{q}\}) &= \int \frac{d\mathbf{w}_1}{(2\pi)^2} \frac{dw_2}{2\pi} \frac{\prod_i m_i}{(2\pi s)^N} \left\{ -\frac{im_1}{s} \left[ w_1^\alpha + w_2 \sum_{\gamma=1}^2 \epsilon_{\gamma\alpha} q_1^\gamma \right] \right\} \\ &\quad \exp \left\{ -\frac{M}{2s} \sum_{\beta=1}^2 (w_1^\beta)^2 - \frac{w_2 I}{2s} - iw_2 L \right\}, \end{aligned} \quad (\text{C.11})$$

where  $M = \sum_i m_i$ , and  $I = \sum_i m_i \mathbf{q}_i^2$ .

$\tilde{\mathcal{P}}_1^\alpha(s, L, \{\mathbf{q}\})$  is the sum of two multiple integrals. The one which contains an argument proportional to  $w_1^\alpha \exp((w_1^\alpha)^2)$  is null since this argument is an odd function of  $w_1^\alpha$ . The remaining multiple Gaussian integrals over  $\mathbf{w}_1$  and  $w_2$  can straightforwardly be computed, and the result is

$$\tilde{\mathcal{P}}_1^\alpha(s, L, \{\mathbf{q}\}) = \frac{1}{(2\pi)^4} \frac{L}{MI} \frac{\prod_i m_i}{(2\pi)^N} \frac{\sum_{\gamma=1}^2 \epsilon_{\gamma\alpha} q_1^\gamma}{s^{N-3/2} \sqrt{2\pi I}} \exp \left\{ -s \frac{L^2}{2I} \right\}. \quad (\text{C.12})$$

The inverse Laplace transform of  $\tilde{\mathcal{P}}_1^\alpha(s, L, \{\mathbf{q}\})$  gives [EMOT54]

$$\mathcal{P}_1^\alpha = \mathcal{C} L m_1 I^{-3/2} \sum_{\gamma=1}^2 q_1^\gamma \epsilon_{\gamma\alpha} E_r^{N-5/2}, \quad (\text{C.13})$$

if  $E_r > 0$ , where  $\mathcal{C} = \frac{\prod_i m_i}{M} \frac{1}{(2\pi)^{N+9/2}} \frac{1}{\Gamma(N-3/2)}$  and  $E_r = E' - \frac{L^2}{2I} = E - \frac{L^2}{2I} - \phi(\{\mathbf{q}\})$ . Using (C.13) in (C.1) one gets finally

$$\begin{aligned} \langle p_1^\alpha \rangle_{\mathbf{q}_1} &= \frac{\int \left( \prod_{i=2}^N d\mathbf{q}_i \right) L m_1 I^{-3/2} \sum_{\gamma=1}^2 q_1^\gamma \epsilon_{\gamma\alpha} E_r^{N-5/2} \delta^2(\sum_i \mathbf{q}_i)}{\int \left( \prod_{i=2}^N d\mathbf{q}_i \right) I^{-1/2} \sum_{\gamma=1}^2 q_1^\gamma \epsilon_{\gamma\alpha} E_r^{N-5/2} \delta^2(\sum_i \mathbf{q}_i)} \\ &= L m_1 \langle I^{-1} \rangle_{\mathbf{q}_1} \sum_{\gamma} q_1^\gamma \epsilon_{\gamma\alpha}. \end{aligned} \quad (\text{C.14})$$

Finally

$$\langle \mathbf{p}_1 \rangle_{\mathbf{q}_k} = L m_1 \langle I^{-1} \rangle_{\mathbf{q}_k} \sum_{\gamma, \alpha} q_k^\gamma \epsilon_{\gamma\alpha} \hat{\mathbf{e}}_\alpha, \quad (\text{C.15})$$

where  $\hat{\mathbf{e}}_\alpha$  is the  $\alpha$ -component unit vector.

$\langle \mathbf{p}_k^2 \rangle_{\mathbf{q}_k}$  can be derived in a similar way, and the result is

$$\begin{aligned} \langle \mathbf{p}_k^2 \rangle_{\mathbf{q}_k} &= 2m_k \left( 1 - \frac{m_k}{M} \right) \langle \frac{N-5/2}{E_r} \rangle_{\mathbf{q}_k} \\ &\quad - m_k I_k \langle \frac{N-5/2}{I E_r} \rangle_{\mathbf{q}_k} + I_k L^2 m_k \langle I^{-2} \rangle_{\mathbf{q}_k}, \end{aligned} \quad (\text{C.16})$$

where  $I_k = m_k \mathbf{q}_k^2$ .

## Appendix D

# Temperature at constant pressure

The entropy of a configuration in MMMC can be written as (see sec. 3.3)

$$S = \ln \int_{W'} d\mathbf{x} C(\mathbf{x}) \frac{V^{N_f}}{NCC} E_k^{\tilde{N}}. \quad (\text{D.1})$$

The microcanonical inverse temperature  $\beta$  (at constant *volume*) is

$$\beta = \left\langle \frac{\tilde{N}}{E_k} \right\rangle, \quad (\text{D.2})$$

and the microcanonical pressure is

$$p = \frac{1}{\beta} \left[ \left\langle \frac{N_f}{V} \right\rangle - \left\langle \frac{\partial \ln NCC}{\partial V} \right\rangle \right]. \quad (\text{D.3})$$

The microcanonical inverse temperature at constant *pressure*  $\beta_p$  is given by

$$\beta_p = \beta \left[ 1 - p \frac{\frac{\partial p}{\partial E}|_V}{\frac{\partial p}{\partial V}|_E} \right], \quad (\text{D.4})$$

where

$$\frac{\partial p}{\partial E}|_V = -\beta^{-2} \frac{\partial^2 S}{\partial E^2}|_V \frac{\partial S}{\partial V}|_E + \beta^{-1} \frac{\partial^2 S}{\partial E \partial V}, \quad (\text{D.5})$$

$$\frac{\partial p}{\partial V}|_E = -\beta^{-2} \frac{\partial^2 S}{\partial E \partial V} \frac{\partial S}{\partial V}|_E + \beta^{-1} \frac{\partial^2 S}{\partial V^2}|_E, \quad (\text{D.6})$$

$$\frac{\partial S}{\partial V}|_E = \left\langle \frac{N_f}{V} \right\rangle - \left\langle \frac{\partial \ln NCC}{\partial V} \right\rangle \left\langle \frac{1}{1} \right\rangle, \quad (\text{D.7})$$

$$\frac{\partial S}{\partial E}|_V = \left\langle \frac{\tilde{N}}{E_k} \right\rangle, \quad (\text{D.8})$$

$$\begin{aligned} \frac{\partial^2 S}{\partial V^2}|_E = & - \left( \frac{\partial S}{\partial V}|_E \right)^2 + \left\langle \frac{N_f(N_f - 1)}{V^2} \right\rangle - \left\langle \frac{2N_f}{V} \frac{\partial \ln NCC}{\partial V} \right\rangle \\ & + \left\langle 2 \left( \frac{\partial \ln NCC}{\partial V} \right)^2 \right\rangle - \left\langle \frac{1}{NCC^2} \frac{\partial^2 NCC}{\partial V^2} \right\rangle, \quad (\text{D.9}) \end{aligned}$$

$$\frac{\partial^2 S}{\partial E^2}|_V = -\left(\frac{\partial S}{\partial E}|_V\right)^2 + \left\langle \frac{\tilde{N}(\tilde{N} - 1)}{E_k^2} \right\rangle, \quad (\text{D.10})$$

and

$$\frac{\partial^2 S}{\partial E \partial V} = -\frac{\partial S}{\partial V}|_E \frac{\partial S}{\partial E}|_V - \left\langle \frac{\partial \ln NCC}{\partial V} \frac{\tilde{N}}{E_k} \right\rangle + \left\langle \frac{N_f}{V} \frac{\tilde{N}}{E_k} \right\rangle. \quad (\text{D.11})$$

# Bibliography

- [ALM01] M. P. ALMEIDA, *Generalized entropies from first principles*. e-print arXiv.org/cond-mat/0102112 (Feb. 2001). 36
- [AM76] N. W. ASHCROFT and N. D. MERMIN, *Solid State Physics* (Harcourt Brace College Publishers, Fort Worth, 1976). 73
- [AMPP00] S. ABE, S. MARTINEZ, F. PENNINI and A. PLASTINO, *Ideal gas in nonextensive optimal Lagrange multipliers formalism*. e-print arXiv.org/cond-mat/0006109 (2000). 35
- [ANT62] V. ANTONOV, *Most probable phase distribution in spherical stellar systems and conditions of its existence*. Vestn, Leningr. Gros. Univ. **7(2)**:(1962) p. 135. 87
- [ARH98] V. ARHELGER, *Parameterabhängige dichte Packungen konvexer Körper*. Ph.D. thesis, Universität Siegen (1998). 109
- [AT98] C. ANTENEODO and C. TSALLIS, *Breakdown of exponential sensitivity to initial conditions: role of the range interaction*. Phys. Rev. Lett. **80(24)**:(1998) pp. 5313–5316. 36
- [AW62] B. J. ALDER and T. E. WAINWRIGHT. Phys. Rev. **127**:(1962) pp. 357+. 109
- [BAB98] F. BABALIEVSKI, *Cluster counting: The Hoshen-Kopelman algorithm vs. spanning tree approaches* (1998). Submitted to Intern. J. of Modern Physics C , v.9(1) (1998) 43. 77
- [BAL82] R. BALIAN, *Du microscopique au macroscopique*, vol. 1 and 2 (Ellipses., 1982). Cours de Physique Statistique de l'École Polytechnique. 3
- [BAT98] M. R. BATE, *Collapse of a Molecular Cloud Core to Stellar Densities: The First Three-Dimensional Calculations*. Astrophys. J. Lett. **518**:(1998) p. L95. 87
- [BB96] A. BURKERT and P. BODENHEIMER, *"Fragmentation in a centrally condensed protostar\*\*UCO/Lick Observatory Bulletin, No. #1333"*. Mon. Not. R. Astron. Soc. **280**:(1996) pp. 1190–1200. 87
- [BBG97] P. BLAISE, S. A. BLUNDELL and C. GUET, *Extended Thomas-Fermi molecular dynamics of sodium clusters*. Phys. Rev. B **55(23)**:(1997) pp. 15856–15867. 39

- [BBI<sup>+</sup>95] J. P. BONDORF, A. S. BOTVINAB, A. S. ILJINOV, I. N. MISHUSTINA and K. SNEPPEN, *Statistical multifragmentation of nuclei*. Physics Report **257(3)**:(1995) pp. 133–221. 109
- [BCC<sup>+</sup>90] C. BRÉCHIGNAC, P. CAHUZK, F. CARLIER, M. DE FRUTOS and LEIGNIER. J. Chem. Soc. Faraday Trans **86**:(1990) pp. 2535+. 42, 46
- [BCC<sup>+</sup>95] C. BRÉCHIGNAC, P. CAHUZAC, F. CARLIER, M. DE FRUTOS, J. LEYGNIER, J.-P. ROUX and A. SARFATI, *Dissociation and binding energies of metal clusters*. Comments At. Mol. Phys. **31**:(1995) pp. 361–393. 42, 46
- [BER96] B. A. BERG, *Multicanonical Recursions*. J.Statist.Phys. **82**:(1996) pp. 323–342. 128
- [BH93] B. A. BERG and U. HANSMANN, *Simulation of an ensemble with varying magnetic field: A numerical determination of the order-order interface tension in the  $D = 2$  Ising model*. Phys. Rev. B **47(1)**:(1993) pp. 497–500. 93
- [BIN97] K. BINDER, *Applications of Monte Carlo methods to statistical physics*. Rep. Prog. Phys. **60(5)**:(1997) pp. 487–559. 128
- [BLR] M. BARANGER, V. LATORA and A. RAPISARDA, *Time evolution of thermodynamic entropy for conservative and dissipative chaotic maps*. Talk presented at the Int. Conf. on "Classical and Quantum Complexity and Nonextensive Thermodynamics", Denton (Texas) April 3-6 2000, accepted for publication in Chaos, solitons and fractals. 36
- [BM72] R. BAYER and E. M. MCCREIGHT, *Organization and Maintenance of Large Ordered Indices*. Acta Informatica **1**:(1972) pp. 173–189. 119
- [BMH00] P. BORRMANN, O. MUELKEN and J. HARTING, *Classification of phase transitions in small systems*. Phys. Rev. Lett. **84**:(2000) p. 3511. 33, 34, 35
- [BOR63] G. BORELIUS. Solid State Physics **15**:(1963) p. 1. 44
- [BOR01] J. BORG, *New Monte Carlo Iteration Method for Generalized Ensembles*. e-print arXiv.org/cond-mat/0102140 (2001). Submitted to Phys. Rev. Lett.. 128
- [BRI95] J. BRICMONT, *Science of Chaos or Chaos in Science?* Physicalia Magazine **17(3–4)**:(1995) pp. 159–208. UCL-IPT-96-03. 146
- [BS97] K. J. BÖRÖCZKY and U. SCHNELL, *Quasi-crystals and the Wulff-shape*. Tech. Rep. 284, Universität Siegen — Mathematische Forschungsberichte (May 1997). 109
- [BT87] J. BINNEY and S. TREMAINE, *Galactic dynamics* (Princeton series in astrophysics, Princeton, NJ, 1987). 87
- [BY89] R. A. BAEZA-YATES, *The Expected Behaviour of  $B+$ -Trees*. Acta Informatica **26(5)**:(1989) pp. 439–471. 119

- 
- [CAL85] H. CALLEN, *Thermodynamics and an introduction to thermostatistics* (Wiley, New York, 1985), 2nd edn. 3, 17, 21, 27
- [CGD00] P. CHOMAZ, F. GULMINELLI and V. DUFLOT, *Topology of event distribution as a generalized definition of phase transitions in finite systems*. e-print arXiv.org/cond-mat/0010365 (2000). 12
- [CH88] M. S. S. CHALLA and J. H. HETHERINGTON, *Gaussian ensemble: An alternate Monte Carlo scheme*. Phys. Rev. A **38(12)**:(1988) pp. 6324–6337. 12, 22, 35
- [CHA98] P.-H. CHAVANIS, *Systematic drift experienced by a point vortex in two-dimensional turbulence*. Phys. Rev. E **58(2)**:(1998) pp. R1199–R1202. 87
- [CHA00] P.-H. CHAVANIS, *Trapping of dust by coherent vortices in the solar nebula*. Astron. Astrophys. **356**:(2000) pp. 1089–1111. 105
- [CL98] F. CALVO and P. LABASTIE, *Monte-Carlo simulation of rotating clusters*. Eur. Phys. J. D **3**:(1998) pp. 229–236. 89
- [COM98] F. COMBES, *Fractal Structures Driven by Self-Gravity: Molecular clouds and the Universe*. In C. MECHANICS, ed., *Chaotic Dynamics of Gravitational Systems* (Les Arcs 2000, 1998). 87
- [CP01] P. CIPRIANI and M. PETTINI, *Strong Chaos in the N-body problem and Microcanonical Thermodynamics of collisionless self gravitating systems*. e-print arXiv.org/astro-ph/0102143 (Feb. 2001). Submitted to Cel. Mech. & Dyn. Astron. 6, 11, 87, 88
- [CS89] J. H. CONWAY and N. J. A. SLOANE, *Sphere packings, Lattices and Groups* (Springer-Verlag, Berlin, New York, 1989). 109
- [CS00] F. CALVO and F. SPIEGELMANN, *Mechanisms of phase transitions in sodium clusters: From molecular to bulk behavior*. J. Chem. Phys. **112(6)**:(2000) pp. 2888–2908. 73
- [CT90] D. M. CHRISTODOULOU and J. E. TOHLINE, *Phase transition time scales for cooling and isothermal media*. Astrophys. J. **363**:(1990) pp. 197–205. 87
- [DBB<sup>+</sup>99] M. D'AGOSTINO, A. S. BOTVINA, M. BRUNO, A. BONASERA, J. P. BONDORF, I. N. MISHUSTIN, F. GULMINELLI, R. BOUGAULT, N. L. NEINDRE, P. DESEQUELLES, E. GERACI, A. PAGANO, I. IORI, A. MORONI, G. V. MARGAGLIOTTI and G. VANNINI, *Thermodynamical features of multifragmentation in peripheral Au + Au Collisions at 35 A.MeV*. Nucl. Phys. A **650**:(1999) pp. 329–357. 12
- [DGC<sup>+</sup>00] M. D'AGOSTINO, F. GULMINELLI, P. CHOMAZ, M. BRUNO, F. CANNATA, R. BOUGAULT, N. COLONNA, F. GRAMEGNA, I. IORI, N. L. NEINDRE, G. MARGAGLIOTTI, P. MASTINU, P. MILAZZO, A. MORONI and G. VANNINI, *Negative heat capacity in the critical region of nuclear fragmentation: an experimental evidence of the liquid-gas phase transition*. Phys. Lett. B **473**:(2000) pp. 219–225. 12, 36

- [DGLR89] B. DIU, C. GUTHMANN, D. LEDERER and B. ROULET, *Physique Statistique* (Hermann, 293 rue Lecourbe, 75015 Paris, France, 1989). 3, 4, 12, 13, 14, 90, 91, 112, 113
- [DVS00] H. J. DE VEGA and N. SÁNCHEZ, *The statistical mechanics of the self-gravitating gas: equation of state and fractal dimension*. *Physics Letter B* **490(1–2)**:(2000) pp. 180–186. 100
- [DVSC] H. J. DE VEGA, N. SÁNCHEZ and F. COMBES, *Fractal Structures and Scaling Laws in the Universe: Statistical Mechanics of the Self-Gravitating Gas*. Invited paper to the special issue of the ‘Journal of Chaos, Solitons and Fractals’: ‘Superstrings, M, F, S...theory’, M. S El Naschie and C. Castro, Editors. 87
- [EAG98] E. ENCISO, N. G. ALMARZA and M. A. GONZÁLEZ, *Virial coefficients of hard-sphere mixtures*. *Phys. Rev. E* **57(4)**:(1998) pp. 4486–4490. 113, 115
- [EE12] P. EHRENFEST and T. EHRENFEST, *Begriffliche Grundlagen der statistischen Auffassung in der Mechanik*, vol. IV (Enzycl. d. Mathem. Wissenschaften, 1912). English translation [EE59]. 12
- [EE59] ———, *The Conceptual Foundation of the Statistical Approach in Mechanics* (Cornell University Press, Ithaca NY, 1959). 142
- [EMOT54] A. ERDÉLYI, W. MAGNUS, F. OBERHETTINGER and F. G. TRICOMI, *Tables of Integral Transforms*, vol. 1 of *Bateman manuscript project* (McGraw-Hill, New York, 1954). 135
- [FER65] E. FERMI, *Collected Papers of E. Fermi*, vol. II (Univ. Of Chicago Press, Chicago, 1965). 5
- [FG01] O. FLIEGANS and D. H. E. GROSS, *Effect of angular momentum on equilibrium properties of a self-gravitating system*. e-print arXiv.org/cond-mat/0102062 (2001). Submitted to *Phys. Rev. E*. 10, 17, 87
- [FID<sup>+</sup>83] J. FLAD, G. IGEL, M. DOLG, H. STOLL and H. PREUSS, *A combination of pseudopotentials and density functionals: results for  $Li_n^{m+}$ ,  $Na_n^{m+}$  and  $K_n^{m+}$  clusters ( $n \leq 4; m = 0.1$ )*. *Chemical Physics* **75**:(1983) pp. 331–345. 46
- [Fis65] M. E. FISHER, *Lectures in Theoretical Physics*, vol. 7c (University of Colorado Press, Boulder, 1965). 33
- [FL95] J. K. FINK and L. LEIBOWITZ, *Thermodynamic and transport properties of sodium liquid and vapor* (Argonne National Laboratory, 9700 South Cass Avenue, Argonne, Illinois 60439 (USA), 1995). 39, 43, 46, 52, 69, 70, 82
- [FL00] E. FOLLANA and V. LALIENA, *Thermodynamics of Self-Gravitating Systems with Softened Potentials*. *Phys. Rev. E* **61**:(2000) pp. 6270–6277. 87
- [FS89] A. M. FERRENBURG and R. H. SWENDSEN, *Optimized Monte Carlo data analysis*. *Phys. Rev. Lett.* **63(12)**:(1989) pp. 1195–1198. 93, 128

- 
- [GAM65] G. GAMOW, *Mr Tompkins in Paperback* (Cambridge U. P., Cambridge, 1965). ix
- [GEZ96] D. H. E. GROSS, A. ECKER and X. Z. ZHANG, *Microcanonical Thermodynamics of First Order Phase Transitions studied in the Potts Model*. *Annalen Phys.* **5**:(1996) pp. 446–452. 17, 27
- [GH95] D. H. E. GROSS and P. A. HERVIEUX, *Statistical fragmentation of hot atomic metal clusters*. *Z. Phys. D* **33**:(1995) pp. 295–299. 39, 47
- [GL69] S. GROSSMANN and V. LEHMANN, *Phase transitions and the distribution of temperatures zeros of the partition function II. Applications and examples*. *Z. Phys.* **218**:(1969) pp. 449–459. 17, 33
- [GM87] D. H. E. GROSS and H. MASSMANN. *Nucl. Phys. A* **471**:(1987) pp. 339c–350c. 17, 40, 53
- [GM97] D. H. E. GROSS and M. E. MADJET, *Fragmentation Phase Transition in Atomic Clusters IV — Liquid-gas transition in finite metal clusters and in the bulk —*. *Z. Phys. B* **104(3)**:(1997) pp. 541–551. xiii, 12, 39, 40, 42, 55, 57, 58, 59, 64, 66
- [GMS97] D. H. E. GROSS, M. E. MADJET and O. SCHAPIRO, *Fragmentation phase transition in atomic clusters I — Microcanonical thermodynamics —*. *Z. Phys. D* **39**:(1997) pp. 75–83. 12, 17, 36, 39, 40
- [GR69] S. GROSSMANN and W. ROSENHAUER, *Phase transitions and the distribution of temperatures zeros of the partition function I. General relations*. *Z. Phys.* **218**:(1969) pp. 437–448. 17
- [GROA] D. H. E. GROSS. private communication. xiii, 57, 58
- [GROB] ———, *Microcanonical Thermodynamics, “Fragmentation Phase Transition”, and the Topology of the N-body Phase Space*. CRIS96. 47
- [GRO90] ———, *Statistical decay of very hot nuclei — the production of large clusters*. *Rep. Prog. Phys.* **53**:(1990) pp. 605–658. 12, 17, 36, 39, 53
- [GRO97] ———, *Microcanonical thermodynamics and statistical fragmentation of dissipative systems*. *Physics Report* **279**:(1997) p. 119. ix, 11, 13, 20, 40, 41, 43, 75, 124
- [GRO00A] D. GROSS, *Second Law of Thermodynamics and Macroscopic Observables within Boltzmann’s principle, an attempt*. e-print arXiv.org/cond-mat/0011130 (2000). 36
- [GRO00B] D. H. E. GROSS, *Phase Transitions in “Small” Systems — A Challenge for Thermodynamics*. e-print arXiv.org/cond-mat/0006087 (2000). Invited paper for CRIS2000. 27
- [GRO01] ———, *Microcanonical thermodynamics: Phase transitions in “Small” systems*, vol. 66 of *Lecture Notes in Physics* (World Scientific, Singap., 2001). ix, 5, 17, 22, 27, 30, 36

- [GSSL00] D. GALLI, F. H. SHU, G. LAUGHLIN and S. LIZANO, *Singular Isothermal Disks and the Formation of Multiple Stars*. In T. MONTMERLE and P. ANDRÉ, eds., *Stellar Clusters and Associations*, vol. 198 of *ASP Conference Series* (ASP, 2000). 105
- [GV99] D. H. E. GROSS and E. VOTYAKOV, *Phase transitions in finite systems = topological peculiarities of the microcanonical entropy surface* (1999). E-print arXiv.org/cond-mat/?9904073. 30
- [GV00] ———, *Phase Transitions in "Small" systems*. *Eur. Phys. J. B* **15**:(2000) p. 115. 10, 12, 17
- [HBM97] J. HOSHEN, M. W. BERRY and K. S. MINSER, *Percolation and cluster structure parameters: the enhanced Hoshen-Kopelman algorithm*. *Phys. Rev. E* **56(2)**:(1997) p. 1455. 77
- [HIL56] T. HILL, *Statistical Mechanics* (McGraw-Hill, New York, 1956). 3, 4
- [HK76] J. HOSHEN and R. KOPELMAN, *Percolation and cluster distribution. I. Cluster multiple labeling technique and critical concentration algorithm*. *Phys. Rev. B* **14(8)**:(1976) p. 3438. 77
- [HK77] G. HORWITZ and J. KATZ, *Steepest-descent technique and stellar equilibrium statistical mechanics. I. Newtonian clusters in a box*. *Astrophys. J.* **211**:(1977) pp. 226–243. 6, 87, 88
- [HMCB00] A. HUJEIRAT, P. MYERS, M. CAMENZIND and A. BURKERT, *"Collapse of weakly ionized rotating turbulent Cloud Cores"*. *New Astronomy* **4**:(2000) pp. 601–613. 105
- [HOAK63] R. HULTGREN, R. L. ORR, P. D. ANDERSON and K. K. KELLEY, *Selected Values of Thermodynamic Properties of Metals and Alloys* (Wiley, New York, 1963). 44
- [HT71] P. HERTEL and W. THIRRING, *A Soluble model for a System with Negative Specific Heat*. *Annals of Physics* **63**:(1971) p. 520. 87
- [HÜL94A] A. HÜLLER, *First order phase transition in the canonical and the micro-canonical ensemble*. *Z. Phys. B* **93**:(1994) pp. 401–405. 12, 22
- [HÜL94B] ———. *Z. Phys. B* **95**:(1994) pp. 63–66. 27
- [JG00] J. JELLINEK and A. GOLDBERG, *On the temperature, equipartition, degrees of freedom, and finite size effects: Application to aluminum clusters*. *J. Chem. Phys.* **113(7)**:(2000) pp. 2570–2582. 6
- [JK00] W. JANKE and R. KENNA, *The Strength of First and Second Order Phase Transitions from Partition Function Zeroes*. e-print arXiv.org/cond-mat/0012026 (2000). Accepted for publication in *J. Stat. Phys.* 34
- [KB97] R. S. KLESSEN and A. BURKERT, *Fragmentation of Molecular Clouds: The Initial Phase of a Stellar Cluster*. In *Riken Symposium on Supercomputing* (1997). 87

- 
- [KFMT98] R. I. KLEIN, R. T. FISHER, C. F. MCKEE and J. K. TRUELOVE, *Gravitational Collapse and Fragmentation in Molecular Clouds with Adaptive Mesh Refinement*. In *Proceedings of Numerical Astrophysics 1998* (1998). 87
- [KM00] P. J. KLINKO and B. N. MILLER, *Mean field theory of spherical gravitating systems*. Phys. Rev. E **62(4)**:(2000) pp. 5783–5792. 87, 88, 93, 102
- [KRA98] W. KRAUTH, *Advances in Computer Simulation*, chap. Introduction To Monte Carlo Algorithms. Lecture Notes in Physics (Springer Verlag, 1998). E–print arXiv.org/cond-mat/9612186. 123
- [KRY79] N. S. KRYLOV, *Works on the Foundations of Statistical Mechanics* (Princeton U. P., Princeton, 1979). 3, 4
- [KSR<sup>+</sup>88] M. M. KAPPES, M. SCHÄR, U. RÖTHLISBERGER, G. YERITZIAN and E. SCHUMACHER, *Sodium cluster ionisation potentials revisited: Higher-resolution measurements for Na<sub>x</sub> (x < 23) and their relation to bonding models*. Chem. Phys. Lett. **143**:(1988) p. 251. 41, 42
- [KSS01] E. KUSSELL, J. SHIMADA and E. I. SHAKHNOVICH, *Excluded Volume in Protein Sidechain Packing*. e–print arXiv.org/cond-mat/0103038 (Mar. 2001). Submitted to Journal of Molecular Biology. 109
- [LAL99] V. LALIENA, *Effect of angular momentum on collapsing systems*. Phys. Rev. E **59**:(1999) pp. 4786–4794. 87, 88, 89, 93, 101, 105, 133
- [LB00] D. LYNDEN-BELL, *Rotation, Statistical Dynamics and Kinematics of Globular Clusters*. e–print arXiv.org/astro-ph/0007116 (2000). 87
- [LBRT00] V. LATORA, M. BARANGER, A. RAPISARDA and C. TSALLIS, *The rate of entropy increase at the edge of chaos*. e–print arXiv.org/cond-mat/9907412 (2000). 36
- [LDOP00] A. R. LIMA, P. M. C. DE OLIVEIRA and T. J. P. PENNA, *A comparison between broad histogram and multicanonical methods*. J. Stat. Phys. **99**:(2000) p. 691. 87
- [LEB93] J. L. LEBOWITZ, *Boltzmann’s entropy and time’s arrow*. Physics Today **Sept.**:(1993) pp. 32–38. Replies in November 1994. 146
- [LEE93] J. LEE, *New Monte Carlo algorithm: Entropic sampling*. Phys. Rev. Lett. **71(2)**:(1993) pp. 211–214. 93, 128
- [LGM99] G. B. LIMA NETO, D. GERBAL and I. MÁRQUEZ, *The specific entropy of elliptical galaxies: an explanation for profile-shape distance indicators?* Mon. Not. R. Astron. Soc. **309**:(1999) pp. 481–495. 87
- [LL94] L. LANDAU and E. LIFCHITZ, *Physique statistique*, chap. II.26 (Mir–Ellipses, Moskow, 1994). 3, 4, 7, 12, 13, 21, 30, 91, 112
- [LL96A] C. LAGOUTE and P.-Y. LONGARETTI, *Rotating globular clusters. I. Onset of the gravothermal instability*. Astron. Astrophys. **308**:(1996) pp. 441–452. 87, 105

- [LL96B] ———, *Rotating globular clusters. II. Relaxation and evaporation*. *Astron. Astrophys.* **308**:(1996) pp. 453–464. 87
- [LUD01] S. LUDING, *Global Equation of State of two-dimensional hard sphere systems*. e-print arXiv.org/cond-mat/0103014 (Mar. 2001). 109
- [LW68] D. LYNDEN-BELL and R. WOOD, *The gravo-thermal catastrophe in isothermal spheres and the onset of red-giant structure for stellar systems*. *Mon. Not. R. Astron. Soc.* **138**:(1968) pp. 495+. 87
- [LY52A] T. D. LEE and C. N. YANG, *Statistical Theory of Equations of State and Phase transitions. I. Theory of Condensation*. *Phys. Rev.* **87**(3):(1952) p. 404. 17, 21, 33
- [LY52B] ———, *Statistical Theory of Equations of State and Phase transitions. II. Lattice Gas and Ising model*. *Phys. Rev.* **87**(3):(1952) p. 410. 14, 17
- [LYN67] D. LYNDEN-BELL, *Statistical mechanics of violent relaxation in stellar systems*. *Mon. Not. R. Astron. Soc.* **136**:(1967) pp. 101+. 87
- [MAX] "The Second Law is constantly being violated...in any sufficiently small group of molecule...As the number ...is increased ..the probability of a measurable variation ... may be regarded as practically an impossibility" in [MAX78] quoted in [LEB93] and [BRI95]. 33
- [MAX78] J. C. MAXWELL. *Nature* **17**:(1878) pp. 257+. 146
- [MB01] O. MUELKEN and P. BORRMANN, *Classification of the Nuclear Multifragmentation Phase Transition*. *Phys. Rev. C.* 34
- [MBHS00] O. MUELKEN, P. BORRMANN, J. HARTING and H. STAMERJOHANN, *Classification of phase transitions of finite Bose-Einstein condensates in power law traps by Fisher zeros*. e-print arXiv.org/cond-mat/0006293 (2000). 34
- [MCSL71] G. MANSOORI, N. F. CARNAHAN, K. E. STARLING and T. W. LELAND, *Equilibrium thermodynamic properties of the mixture of Hard spheres*. *The Journal of Chemical Physics* **54**(4):(1971) p. 1523. 48, 113
- [MHGS97] M. E. MADJET, P. A. HERVIEUX, D. H. E. GROSS and O. SCHAPIRO, *Fragmentation Phase Transition in Atomic Clusters II — Symmetry of Fission of Metal Clusters —*. *Z. Phys. D* **39**(4):(1997) pp. 309–316. 12, 39, 40
- [MNPP00] S. MARTÍNEZ, F. NICOLÁS, F. PENNINI and A. PLASTINO, *Tsallis' entropy maximization procedure revisited*. *Physica A* **286**:(2000) p. 489. 35
- [MPRTZ00] E. MARINARI, G. PARISI, F. RICCI-TERSENGHI and F. ZULIANI, *On the Use of Optimized Monte Carlo Methods for Studying Spin Glasses*. e-print arXiv.org/cond-mat/0011039 (2000). 92
- [MRR<sup>+</sup>53] N. METROPOLIS, A. W. ROSENBLUTH, M. N. ROSENBLUTH, A. H. TELLER and E. TELLER, *Equation of State Calculations by fast Computing Machines*. *J. Chem. Phys.* **21**(6):(1953) pp. 1087–1092. 46, 123

- 
- [PAD90] T. PADMANABHAN, *Statistical mechanics of gravitating systems*. Physics Report **188(5)**:(1990) pp. 285–362. 6, 36, 87, 105
- [PAR01] G. PARISI, *Planck's Legacy to Statistical Mechanics*. e–print arXiv.org/cond-mat/0101293 (2001). Historical talk given at the Accademia dei Lincei at the conference on Max Planck. 128
- [PAT72] R. K. PATHRIA, *Statistical mechanics*, vol. 45 of *International series of monographs in natural philosophy* (Pergamon press, Oxford, 1972). 112
- [PCA] I. PAGONABARRAGA, M. E. CATES and G. J. ACKLAND, *Local size segregation in polydisperse hard sphere fluids*. Submitted to Phys. Rev. Lett. 111
- [PLU11] H. C. PLUMMER, *On the Problem of Distribution in Globular Clusters*. Mon. Not. R. Astron. Soc. **71**:(1911) pp. 460+. 89
- [RAD01] A. H. RADUTA, *On the free volume in nuclear multifragmentation*. Nucl. Phys. A **683(1–4)**:(2001) pp. 618–634. 109, 115, 117
- [RB91] R. RODGERS and A. BADDELEY, *Nested Monte Carlo study of random packing on the sphere*. J. Appl. Prob. **28**:(1991) pp. 539–552. 117, 118
- [RFL59] H. REISS, H. L. FRISCH and J. L. LEBOWITZ, *Statistical mechanics of rigid spheres*. J. Chem. Phys. **31(2)**:(1959) pp. 369–381. 111, 113
- [RN93] C. J. REIDL, JR. and M. B. N., *Gravity in one dimension: The critical population*. Phys. Rev. E **48**:(1993) p. 4250. 87
- [ROM97] A. B. ROMEO, *Dynamical effects of softening in N-body simulations of disc galaxies. Method and first applications*. Astron. Astrophys. **324**:(1997) pp. 523–533. 87
- [RR97] A. H. RADUTA and A. R. RADUTA, *Simulation of statistical ensembles suitable for the description of nuclear multifragmentation*. Phys. Rev. C **55(3)**:(1997) pp. 1344+. 47
- [RRS88] J. RANDRUP, M. M. ROBINSON and K. SNEPPEN. Phys. Lett. B **208**:(1988) p. 25. 109
- [RUE63] D. RUELE. Helv. Phys. Acta **36**:(1963) p. 183. 87
- [RUE69] ———, *Statistical mechanics, rigorous results*. (W. A. Benjamin, New York, 1969). 21
- [SAS85] W. C. SASLAW, *Gravitational physics of stellar and galactic systems* (Cambridge University Press, Cambridge, 1985). 3, 6, 87
- [SCH46] E. SCHRÖDINGER, *Statistical Thermodynamics, a Course of Seminar Lectures, delivered in January–March 1995 at the School of Theoretical Physics* (Cambridge University Press, London, 1946). 108

- [SCH97] O. SCHAPIRO, *Microcanonical phase transitions — Fragmentation and coulomb explosion of metal clusters*. Ph.D. thesis, Freien Universität Berlin (1997). 11, 39, 40
- [SIM<sup>+</sup>00] Y. SOTA, O. IGUCHI, M. MORIKAWA, T. TATEKAWA and K. ICHI MAEDA, *The Origin of Fractal Distribution in Self-Gravitating Virialized System and Self-Organized Criticality*. e-print arXiv.org/astro-ph/0009412 (2000). 100
- [SKM<sup>+</sup>97] O. SCHAPIRO, P. J. KUNTZ, K. MÖHRING, P. A. HERVIEUX, D. H. E. GROSS and M. E. MADJET, *Fragmentation Phase Transition in Atomic Clusters III — Coulomb Explosion of Metal Clusters —*. Z. Phys. D **41**:(1997) pp. 219–227. 12, 39, 40
- [SKVIH98] M. SCHMIDT, R. KUSCHE, B. VON ISSENDORF and H. HABERLAND, *Irregular variations in the melting point of size-selected atomic clusters*. Nature **393**:(1998) pp. 238–240. 65
- [SLVH97] J. SOMMER-LARSEN, H. VEDEL and U. HELLSTEN, *The Structure of Isothermal, Self-gravitating Gas Spheres for Softened Gravity*. Astrophys. J. **500**:(1997) p. 610. 87
- [SMI96] G. R. SMITH, *The measurement of Free Energy by Monte-Carlo computer simulation*. Ph.D. thesis, University of Edinburgh (1996). Electronic address <http://indigo1.biop.ox.ac.uk/graham/graham.html>. 93, 128
- [SSHT00] K. SATO, K. SEKIMOTO, T. HONDOU and F. TAKAGI, *Irreversibility resulting from contact with a heat bath caused by the finiteness of the system*. e-print arXiv.org/cond-mat/0008393 (2000). 11, 35
- [SSM87] Y. SONG, R. M. STRATT and E. A. MASON, *The equation of state of hard spheres and the approach to random closest packing*. J. Chem. Phys. **88**:(1987) p. 1126. 111
- [STH00] K. SEKIMOTO, F. TAKAGI and T. HONDOU, *The Carnot Cycle for Small Systems: Irreversibility and the Cost of Operations*. Phys. Rev. E **62**(6):(2000) pp. 7759–7768. E-print arXiv.org/astro-ph/0003064. 11, 35
- [TA99] A. TORCINI and M. ANTONI, *Equilibrium and dynamical properties of two-dimensional N-body systems with long-range attractive interactions*. Phys. Rev. E **59**(3):(1999) pp. 2746–2763. 92
- [THI63] E. THIELE, *Equation of State for Hard Spheres*. J. Chem. Phys. **30**(2):(1963) pp. 474–479. 113
- [THI70] W. THIRRING, *Systems with Negative Specific Heat*. Z. Phys. **235**:(1970) pp. 339–352. 87
- [TSA88] C. TSALLIS, *Possible Generalization of Boltzmann–Gibbs Statistics*. Journal of Statistical Physics **52**:(1988) pp. 479+. 35
- [TSA95] ———, *Comment on "Thermodynamic stability conditions for the Tsallis and Rényi entropies" by J.D. Ramshaw*. Phys. Lett. A **206**(5–6):(1995) pp. 389–391. 36

- 
- [TSA99] ———, *Nonextensive Statistics: Theoretical, Experimental and Computational evidences and connections*. Braz. J. Phys. **29(1)**:(1999) pp. 1–35. 33, 36
- [VH49] L. VAN HOVE, *Quelques propriétés générales de l'intégrale de configuration d'un système de particules avec interaction*. Physica**15**:(1949) p. 951. 5, 12, 28
- [VOT] E. VOTYAKOV. private communication. 83
- [WASBW96] A. P. WHITWORTH, N. F. A. S. BHATTAL and S. J. WATKINS, *Star formation and the singular isothermal sphere*. Mon. Not. R. Astron. Soc. **283**:(1996) pp. 1061–1070. 87
- [WER63] M. S. WERTHEIM, *Exact solution of the Percus–Yvick integral equation for hard spheres*. Phys. Rev. Lett. **10(8)**:(1963) pp. 321–323. Solved the Percu-Yevick (PY) integral equations for pure hard spheres, then derived  $Z$  from the virial equation. 113
- [WHI96] S. D. M. WHITE, *Violent Relaxation in Hierarchical Clustering*. In E. T. R. TERLEVICH, O. LAHAV, ed., *Gravitational Dynamics* (Cambridge Univ. Press, Cambridge, 1996). 87
- [WIL91] J. M. WILLS, *Locally dense finite lattice packings of sphere*. Periodica Mathematica Hungarica **22(3)**:(1991) pp. 139–146. 109
- [WIL98] ———, *Spheres ans sausages, crystals and catastrophes — and a joint packing theory*. The Mathematical Intelligencer **20(1)**:(1998) pp. 16–21. 109
- [YEP97] G. YEPES, *Cosmological Numerical simulations*. In D. VALLS-GABAUD, M. HENDRY, P. MOLARO and K. CHAMCHAM, eds., *From quantum fluctuations to cosmological structures*, vol. 126 of *ASP Conferences*, (p. 279) (Astronomical Society of the Pacific, Provo, Utah USA, 1997). 89
- [YM97] K. R. YAWN and B. N. MILLER, *Ergodic properties and equilibrium of one-dimensional self-gravitating systems*. Phys. Rev. E **56(3)**:(1997) pp. 2429–2436. 87
- [ZGXZ87] X. Z. ZHANG, D. H. E. GROSS, S. Y. XU and Y. M. ZHENG. Nucl. Phys. A **461**:(1987) p. 668. 39, 40
- [zZG93] X. ZE ZHANG and D. H. E. GROSS, *An ergodic monte carlo method for simulating the microcanonical model with finite sizes*. In *THE second international conference on computational physics ICCP-2*, vol. 2, (p. 530) (Beijing, China, 1993). 126



## Abstract

In conventional thermostatics there is no phase transition in “small” systems (“small” systems are those where the range of the forces is of the order of the system size). In fact, these systems do not exhibit the usual signals of phase transitions, i.e. Yang-Lee singularities. These singularities (divergences) can only occur at the thermodynamical limit. Nevertheless it is possible to define phases and phase transitions for “small” systems by means of local properties of their *microcanonical* entropy surface *without* invoking the thermodynamical limit.

In the first part of this thesis, the present status of the theory is summarized. The definitions of phase and phase transitions are recalled. Their relation to the conventional ones is discussed. All these points are illustrated by analytical entropy models.

The two other parts are dedicated to original studies of the microcanonical equilibrium properties of two “small” systems.

First, the liquid-gas phase transition of sodium clusters composed by a few hundreds of atoms is discussed. At low pressure, their caloric curves as functions of the enthalpy show a region characterized by a *negative* specific heat capacity. This is the signal of a first order phase transition in “small” systems. For certain enthalpy-range, their mass distributions have some peculiarities (multifragmentation) which vanish at the thermodynamical limit. High pressures calculations show for the first time the critical point of this first order phase transition. This critical point is located at higher pressure and smaller temperature compared to the critical point of corresponding thermodynamical limit.

The last part deals with self-gravitating systems. Although they are spatially very large they are “small” in the sense given above. These systems are studied in the microcanonical ensemble at constant energy  $E$  and total angular momentum  $L$ . They are studied without any a priori assumption about their spatial mass distributions (symmetry) and with a “realistic” potential. This is relevant for many astrophysical systems: from galaxies to (multiple-)stars formation. The entropy surface, its derivatives (temperature, angular velocity) and observables probing the mass distribution are worked out for the whole parameter space  $(E, L)$ . These systems have a rich phase diagram with first order and several second order phase transitions. It is shown that all the properties of (astro-)physical importance are smeared out and lost if the intensive variables are fixed, i.e. in the canonical ensemble. Worst, for a given choice of intensive parameters, the partition function *diverges* for some microcanonical values of these intensive parameters.

## Zusammenfassung

In der konventionellen Thermostatistik gibt es keine Phasenübergänge in "Kleinen" Systemen. (Systeme mit einer Wechselwirkung von einer Reichweite vergleichbar mit der Systemgrösse.) Diese Systeme zeigen nicht die Yang-Lee Singularitäten in den kanonischen Potentialen. Singularitäten können nur im thermodynamischen Limes auftreten. Dennoch kann man in der mikrokanonischen Statistik Phasen und Phasenuebergänge eindeutig auch für "Kleine" Systeme als lokale Besonderheiten der Entropie definieren.

Im ersten Teil der Doktorarbeit wird der augenblickliche Stand der Theorie zusammengefasst. Die Definition der Phasen und der Phasenübergänge wird genannt und ihre Beziehung zur konventionellen Theorie diskutiert. Dies wird an Hand analytischer Modelle illustriert.

Zwei weitere Teile der Arbeit behandeln die Eigenschaften des mikrokanonischen Gleichgewichts in zwei Beispielen "Kleiner" Systeme:

Zuerst wird der flüssig-gas Übergang in Natriumclustern mit einigen hundert Atomen diskutiert. Bei kleinem Druck zeigt die kalorische Kurve als Funktion der Enthalpie einen Bereich mit negativer spez. Wärme. Das ist das Signal für einen Phasenübergang erster Ordnung in einem "Kleinen" System. In bestimmten Bereichen der Enthalpie gibt es Multifragmentation. Diese verschwindet im thermodynamischen Limes. Simulationen von Systemen unter hohen Drucken zeigen das erstemal den kritischen Endpunkt des Phasenueberganges erster Ordnung. Er liegt bei höherem Druck und niedrigerer Temperatur als im Bulk.

Der letzte Teil behandelt selbstgravitierende Systeme. Obwohl kosmologische Systeme sehr groß sind, gehören auch sie zu den "Kleinen" Systemen wie wir sie oben definiert haben. Diese Systeme müssen im mikrokanonischen Ensemble bei konstanter Energie *und* konstantem totalen Drehimpuls studiert werden, ohne irgendwelche a priori Annahmen über ihre räumliche Massenverteilung (Symmetrie) zu machen. Dieses Beispiel ist relevant für viele astrophysikalische Systeme von (Vielfach-)Sternbildung bis hin zu Galaxien. Die Entropiefläche, ihre Ableitungen, die intensiven Größen (Temperatur, Winkelgeschwindigkeit), sowie Observable, die die Massenverteilung kontrollieren, werden in ihrem ganzen Parameterbereich studiert. Diese Systeme haben ein reiches Phasendiagramm: Es gibt alle Arten von Phasenübergängen, erster Ordnung und mehreren von zweiter Ordnung. Es wird gezeigt, daß all diese Eigenschaften von (astro-)physikalischer Bedeutung in dem kanonischen Ensemble als Funktion der intensiven Parameter verwaschen werden oder sogar völlig verloren gehen. Schlimmer noch, für bestimmte Wahl der intensiven Parameter divergiert die kanonische Zustandssumme sogar.

# Curriculum vitae

## Personal Informations

Name	Olivier Fliegans
Date and Place of Birth	03-08-1972 in Rosheim, France
Marital Status	married, 2 children
Citizenship	French

---

## Education

**Doctorate Thesis in Physics** [since September 1998] Freie Universität Berlin, Berlin, Germany.

Title: **Phase transitions in “small” systems.**

Supervisor: Prof. DHE Groß (Freie Universität Berlin, Germany)

**Post-Graduate Studies: Diploma of Advanced Studies** [June 1997]

“**Treatment and analysis of data in astrophysical contexts**”

Observatoire Astronomique de Strasbourg, Strasbourg, France.

**Maîtrise de Physique** [June 1995]

Université Louis Pasteur, Strasbourg.

**Licence de Physique** [June 1994]

Université Louis Pasteur, Strasbourg.

---

## Military Service

[November 1995 – July 1997] National Service as a conscientious objector at the “Planétarium de Strasbourg”, Strasbourg, France